OPTICAL MOLECULAR IMAGING OF HYPOXIC BREAST CANCER

from Prospect to Preclinical Practice

Financial support for the publication of this thesis was kindly provided by the Department of Pathology UMC Utrecht.

ISBN:	978-90-8891-730-1
Printed by:	Proefschriftmaken.nl || Uitgeverij BOXPress
Published by:	Uitgeverij BOXPress, 's-Hertogenbosch

OPTICAL MOLECULAR IMAGING OF HYPOXIC BREAST CANCER

from Prospect to Preclinical Practice

Optische Beeldvorming van Hypoxie
in Borstkanker
van Idee tot Preklinische Toepassing
(met een samenvatting in het Nederlands)

PROEFSCHRIFT

ter verkrijging van de graad van doctor aan de Universiteit Utrecht op gezag van de rector magnificus, prof. dr. G.J. van der Zwaan, ingevolge het besluit van het college voor promoties in het openbaar te verdedigen op donderdag 19 december 2013 des ochtends te 10.30 uur

door

Aram Steye Auke van Brussel
geboren op 2 december 1984 te Amsterdam

Promotoren:	Prof. dr. P.J. van Diest
	Prof. dr. E. van der Wall
Co-promotoren:	Dr. P.M.P. van Bergen en Henegouwen
	Dr. S. Oliveira

Contents

1

General introduction

In The Netherlands, approximately one third of women is diagnosed with cancer during their life span of which breast cancer is the most common form. Of all breast cancer patients, one third will eventually die of metastatic disease [1]. Due to intrinsic and extrinsic factors, genetic mutations occur daily in epithelial (breast) cells. Most of these are repaired by DNA repair mechanisms but the genes of some cells may remain mutated. This can lead to chromosomal aberrations and subsequent changes in cellular function and behavior. Intrinsic mutagenic factors in breast cancer concern, amongst others that are less prevalent, BRCA1 and BRCA2 germ line mutations [2].

Extrinsic mutagenic factors involve lifestyle and environmental factors such as diet (alcohol and fat consumption), lack of physical exercise and exposure to radiation [3].

It is believed that carcinogenesis involves a complex series of stochastic genetic events that turn normal cells into benign preneoplastic lesions, carcinoma in situ, invasive carcinoma and eventually metastatic carcinoma [4, 5]. Besides genetic changes, also epigenetic changes play an important role in carcinogenesis of the breast [6].

Morphological and molecular classification of breast cancer

Breast cancer consists of a heterogeneous group of lesions of which most are adenocarcinomas. Identification of specific subtypes is important for prognosis and therapy optimization. Most of the adenocarcinomas of the breast can, based on growth pattern and cytologic features, be divided into ductal (70-75%) and lobular (5-15%) carcinomas. Ductal carcinoma typically consists of glandular and/or solid clusters of malignant tumor cells with infiltrating margins [7]. Lobular carcinoma is characterized by a loss of expression of E-cadherin leading to loosely cohesive and individually infiltrating tumor cells [4, 7]. This taxonomy is based on morphological features rather than origin, as both types originate from the terminal duct-lobular unit. Of all adenocarcinomas, 5% is classified as invasive carcinomas with mixed ductal and lobular features. Several other subtypes exist, of which invasive tubular and cribriform carcinoma are the most common ones and have a relatively favorable prognosis [4].

Ductal and lobular carcinomas without invasive component are called ductal and lobular carcinoma in situ (DCIS and LCIS), respectively. DCIS can have an extensive growth pattern which follows the lining of the ducts and local recurrence of DCIS after irradical excision causes a major decrease in tumor-specific survival [8]. LCIS coexists with invasive lobular carcinoma in 70-80% of cases and grows more often diffuse, multifocal and bilateral [4].

In the clinic, prognostic factors are important for therapy optimization. Lymph node status and tumor size are the two most important prognostic factors in breast cancer. Tumors can also be classified according to tumor grade. Most frequently used is the Nottingham combined histological grading system. This system takes the degree of tubule formation, nuclear grade and mitotic rate into account, resulting in grade 1 (low), 2 (intermediate) and 3 (high). Of these, the mitotic activity has been proven to be the dominant prognosticator.

Important for tailored endocrine therapy is determination of estrogen (ER) and progesterone (PR) receptor status. Furthermore, HER2 protein expression and HER2/neu gene amplification status help select patients for treatment with agents that specifically target the HER2-receptor, like the monoclonal antibodies trastuzumab and pertuzumab [9, 10]. Tumors that lack ER, PR and HER2 expression are called triple negative and form a challenge in therapeutic decision making [4].

Gene expression profiling of breast tumor tissue has resulted in a molecular classification of breast cancer. The most common molecular subtypes are luminal A, luminal B, HER2 driven and basal-like [9]. Luminal A cancers are typically ER and/or PR positive and HER2 and KI67 negative. Like luminal A, luminal B cancers are ER and/or PR positive but HER2 or KI67 positive. HER2 driven breast carcinoma is negative for ER and PR but positive for HER2 as opposed to the basal subtype, which is negative for all three markers (triple negative). The latter type often shows expression of basal cytokeratins, EGFR and/or mesenchymal markers [10].

These molecular subtypes are to a certain extent related to grade and histology. Integration of morphological and molecular classification might lead to a better understanding of breast cancer subtypes and optimal tailored therapeutic interventions in the future [4].

Current guidelines for breast cancer: Screening, diagnosis and therapy

For breast cancer screening and diagnosis, mammography, magnetic resonance imaging (MRI) or ultrasound are indicated. However, controversy about population screening programs exists. Some studies warn for false positive results, others show a survival benefit [11]. Mammography has a sensitivity of 78%. MRI has a high sensitivity of about 90% but low specificity (50-70%) [12]. *In situ* lesions that lack micro-calcifications are hard to detect with mammography, leading to 10% of DCIS missed by mammography and up to 33% by MRI [8, 12-15].

In (young) women with dense breasts and/or with a BRCA1/2 germ line mutation, MRI is indicated. Cystic lesions can be well detected with ultrasound. After a positive mammogram (BI-RADS 3, 4 and 5), a biopsy is taken. Pathological evaluation of the biopsy results in the final diagnosis. In the case of pathologically confirmed breast cancer, surgery is the local therapy of choice in most cases [12, 16].

Molecular imaging

As current modalities for breast cancer detection do not only have limited tumor specificity but also generate low contrast images, use ionizing radiation and/or are very expensive, alternative imaging modalities, such as molecular imaging, are needed [11, 12, 17].

Positron emission tomography (PET), single-photon emission computed tomography (SPECT) and optical molecular imaging modalities use targeting moieties such as antibodies or antibody fragments to specifically track single molecules or cells in the body. The use of a targeting moiety specific to a tumor antigen results in higher contrast images, as compared to non-targeted imaging strategies [18-20]. Conventional (IgG) antibodies against HER2 (trastuzumab), EGFR (cetuximab) or VEGF (bevacizumab) have successfully been tested for PET and optical imaging in clinical studies [21-23]. The relatively large molecular size of antibodies (~150 kDa) impedes renal excretion which lead to a broad time window for imaging but also to a slow reduction in background signal from the blood. Therefore, optimal imaging is only possible from ~24h after i.v. injection [23]. To reduce logistics and delay for patients, rapid molecular imaging should be developed. Promising probe candi-

dates for rapid molecular imaging are nanobodies, small targeting proteins derived from the variable domain of heavy-chain-only antibodies (VHH) that naturally occur in camelids. Compared to conventional antibodies, nanobodies possess several advantageous properties. Their small size of 15 kDa allows rapid tumor-uptake and fast clearance from the blood, resulting in high tumor-to-normal tissue ratios within hours after injection [24, 25]. Furthermore, nanobodies are proteins with good stability in aqueous solutions and are easy to produce in bacteria, yeast or mammalian protein expression systems [24, 26, 27].

Optical imaging has been evaluated in clinical studies for detection of breast cancer [18]. This technique assesses optical properties of tissue by using near-infrared (NIR) light [18]. The NIR part of the spectrum (700-900 nm) has the lowest absorption and thus the highest penetration through various types of tissue. Still, the main challenge for successful optical imaging is the limited penetration depth of NIR light through the human body. Several NIR dyes have been developed for use in (pre)clinical studies such as IRDye800CW (clinical grade), IRDye700DX and IRDye680RD (LI-COR). These dyes can be conjugated to proteins via NHS-lysine or Maleimide-cysteine (site-directed) coupling [28].

To optimize tumor contrast with molecular imaging, membrane-bound proteins need to be targeted that are not, or much less, expressed in normal tissues. Although hormonal receptor (ER, PR) status has extensively been determined in breast cancer, hormone receptors are less suitable as tumor markers for molecular imaging as they are expressed intracellularly and thus cannot be targeted by antibodies *in vivo*, but only with small molecules. Besides growth factor hormone receptors (HER2 and EGFR), hypoxia upregulated membrane proteins are interesting tumor markers. During carcinogenesis, proliferating epithelial cells are separated from the basement membrane and vasculature. When the limit of O_2 diffusion (~100 μm) is reached, cells become hypoxic (Fig. 1)[29]. Hypoxia causes stabilization of hypoxia-inducible factor 1α (HIF-1α), a transcription factor that regulates the hypoxia response. HIF-1α induces upregulation of many proteins like carbonic anhydrase IX (CAIX), glucose transporter 1 (GLUT1), vascular endothelial growth factor (VEGF) and CD44v6 [30-33]. Because hypoxia hardly occurs in normal tissues, molecules that can detect low oxygen tensions or that are specific for hypoxia

upregulated proteins are potential molecular imaging candidates.

Pimonidazole (a 2-nitroimidazole derivative), is a well established hypoxia marker that competes with oxygen for electrons. At low oxygen tensions, pimonidazole is reduced and forms intracellular aggregates [34]. Hypoxic tissues can be visualized by indirect labeling with anti-pimonidazole antibodies [35]. However, pimonidazole is currently off the market. For molecular imaging of tumor hypoxia *in vivo*, 2-nitroimidazole derivatives have been radiolabeled in several studies [36-38]. Besides general hypoxia markers, antibodies specific for hypoxia upregulated proteins have been developed as well. Rencarex is a monoclonal antibody against CAIX that was evaluated successfully in a clinical trial as diagnostic tumor marker and as therapeutic imaging agent in renal cell carcinoma patients [39, 40].

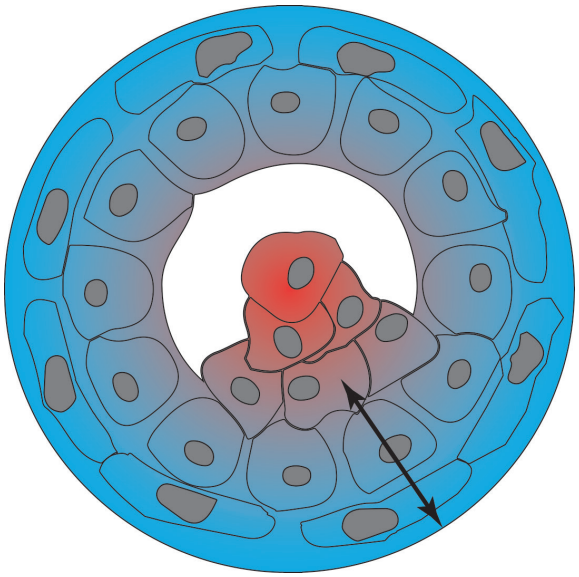

Figure 1: Transection of a mammary duct with myo-epithelial cells (outer lining), luminal cells (inner lining) and malignant cell division in the ductal lumen. The arrow shows the distance between the basal membrane and the diffusion limit of oxygen (~100 µm).

Aims and chapter outline

In this thesis, we evaluate molecular imaging with targeted NIR probes for detection of hypoxic breast cancer. The current knowledge on (immunohistochemistry) expression data of hypoxia-related proteins CAIX, GLUT1, CXCR4 and IGFR was reviewed in chapter 2. This knowledge could direct future probe development. Next to reviewing published data, we further examined expression levels of potential tumor markers for molecular imaging in an immunohistochemistry study (chapter 3). In order to find more hypoxia-specific tumor markers for imaging, nanobodies that bind specifically to hypoxic cells were selected by phage display. By immunoprecipitation and mass spectrometry we determined the (hypoxia-specific) antigen that the nanobodies bound to (chapter 4). Then, we evaluated several hypoxia-targeting probes for optical molecular imaging *in vivo*, starting with the small molecule 2-nitroimidazole. We directly conjugated 2-nitroimidazole to IRDye800CW and tested the conjugate as potential marker for hypoxic breast tumors in a DCIS xenograft mouse model (Chapter 5). Next to 2-nitroimidazole, we conjugated a CAIX-specific antibody (MabCAIX) to IRDye800CW and evaluated the properties of this fluorescent antibody as tumor marker in the same mouse model (chapter 6). In parallel to the MabCAIX antibody, we evaluated a CD44v6-specific antibody for optical molecular imaging in our DCIS mouse model (chapter 7). After evaluating a small molecule and two antibodies, we tested the hypothesis that imaging with nanobodies, compared to conventional antibodies, results in better and faster tumor uptake. We generated CAIX-specific high affinity nanobodies from phage display selections and conjugated them site-directed to IRDye800CW. These fluorescent nanobody conjugates were tested in our DCIS mouse model (chapter 8). Based on the successful imaging with nanobodies we evaluated if co-injections with two nanobodies could increase TNR and solve the problem of tumor heterogeneity (chapter 9). Finally, we discuss the results observed in our studies as the basis for our suggestions for future research in the promising area of optical molecular imaging (chapter 10).

References

1. http://www.cijfersoverkanker.nl/
2. van der Groep P, Bouter A, Menko FH, et al. High frequency of HIF-1alpha overex pression in BRCA1 related breast cancer. Breast Cancer Res Treat 2008; 111: 475-480.
3. Centre NBaOC. Breast cancer risk factors: a review of the evidence. 2009.
4. Corben AD. Pathology of invasive breast disease. Surg Clin North Am 2013; 93: 363-392.
5. Simpson PT, Reis-Filho JS, Gale T, et al. Molecular evolution of breast cancer. J Pathol 2005; 205: 248-254.
6. Huang Y, Nayak S, Jankowitz R, et al. Epigenetics in breast cancer: what's new? Breast Cancer Res 2011; 13: 225.
7. Doshi DJ, March DE, Crisi GM, et al. Complex cystic breast masses: diagnostic approach and imaging-pathologic correlation. Radiographics 2007; 27 Suppl 1: S53-64.
8. Sakorafas GH, Farley DR, Peros G. Recent advances and current controversies in the management of DCIS of the breast. Cancer Treat Rev 2008; 34: 483-497.
9. Sorlie T, Perou CM, Tibshirani R, et al. Gene expression patterns of breast carcino mas distinguish tumor subclasses with clinical implications. Proc Natl Acad Sci USA 2001; 98: 10869-10874.
10. Blows FM, Driver KE, Schmidt MK, et al. Subtyping of breast cancer by im munohistochemistry to investigate a relationship between subtype and short and long term survival: a collaborative analysis of data for 10,159 cases from 12 studies. PLoS Med 2010; 7: e1000279.
11. Verbeek AL, Broeders MJ, Otto SJ, et al. [Effects of the population screening into breast cancer]. Ned Tijdschr Geneeskd 2013; 157: A5218.
12. Smetherman DH. Screening, imaging, and image-guided biopsy techniques for breast cancer. Surg Clin North Am 2013; 93: 309-327.
13. Hubbard RA, Kerlikowske K, Flowers CI, et al. Cumulative probability of false-po sitive recall or biopsy recommendation after 10 years of screening mammography: a cohort study. Ann Intern Med 2011; 155: 481-492.
14. Kerlikowske K, Carney PA, Geller B, et al. Performance of screening mammograhy among women with and without a first-degree relative with breast cancer. Ann Intern Med 2000; 133: 855-863.
15. Berg WA, Zhang Z, Lehrer D, et al. Detection of breast cancer with addition of annual screening ultrasound or a single screening MRI to mammography in wo men with elevated breast cancer risk. JAMA 2012; 307: 1394-1404.
16. Mammacarcinoom, Landelijke richtlijn v2.0.
17. Pages EB, Millet I, Hoa D, et al. Undiagnosed breast cancer at MR imaging: analysis of causes. Radiology 2012; 264: 40-50.
18. van de Ven S, Wiethoff A, Nielsen T, et al. A novel fluorescent imaging agent for diffuse optical tomography of the breast: first clinical experience in patients. Mol Imaging Biol 2010; 12: 343-348.
19. Ntziachristos V, Chance B. Probing physiology and molecular function using optical imaging: applications to breast cancer. Breast Cancer Res 2001; 3: 41-46.
20. Corlu A, Choe R, Durduran T, et al. Three-dimensional in vivo fluorescence diffuse optical tomography of breast cancer in humans. Opt Express 2007; 15: 6696-6716.
21. van Dongen GA, Poot AJ, Vugts DJ. PET imaging with radiolabeled antibodies and tyrosine kinase inhibitors: immuno-PET and TKI-PET. Tumour Biol 2012; 33: 607-

615.
22. Gaykema SB, Brouwers AH, Lub-de Hooge MN, et al. 89Zr-Bevacizumab PET Ima ging in Primary Breast Cancer. J Nucl Med 2013; 54: 1014-1018.
23. Terwisscha van Scheltinga AG, van Dam GM, Nagengast WB, et al. Intraoperative near-infrared fluorescence tumor imaging with vascular endothelial growth factor and human epidermal growth factor receptor 2 targeting antibodies. J Nucl Med 2011; 52: 1778-1785.
24. Oliveira S, van Dongen GA, Stigter-van Walsum M, et al. Rapid visualization of human tumor xenografts through optical imaging with a near-infrared fluorescent anti-epidermal growth factor receptor nanobody. Mol Imaging 2012; 11: 33-46.
25. Kijanka M, Warnders FJ, El Khattabi M, et al. Rapid optical imaging of human breast tumour xenografts using anti-HER2 VHHs site-directly conjugated to IRDye 800CW for image-guided surgery. Eur J Nucl Med Mol Imaging 2013.
26. Hamers-Casterman C, Atarhouch T, Muyldermans S, et al. Naturally occurring antibodies devoid of light chains. Nature 1993; 363: 446-448.
27. Smolarek D, Bertrand O, Czerwinski M. Variable fragments of heavy chain antibo dies (VHHs): a new magic bullet molecule of medicine? Postepy Hig Med Dosw (Online) 2012; 66: 348-358.
28. Marshall MV, Draney D, Sevick-Muraca EM, et al. Single-dose intravenous toxicity study of IRDye 800CW in Sprague-Dawley rats. Mol Imaging Biol 2010; 12: 583-594.
29. Gatenby RA, Smallbone K, Maini PK, et al. Cellular adaptations to hypoxia and acidosis during somatic evolution of breast cancer. Br J Cancer 2007; 97: 646-653.
30. Li XF, O'Donoghue JA. Hypoxia in microscopic tumors. Cancer Lett 2008; 264: 172-180.
31. Bos R, Zhong H, Hanrahan CF, et al. Levels of hypoxia-inducible factor-1 alpha during breast carcinogenesis. J Natl Cancer Inst 2001; 93: 309-314.
32. Bos R, van der Groep P, Greijer AE, et al. Levels of hypoxia-inducible factor-1alpha independently predict prognosis in patients with lymph node negative breast carcinoma. Cancer 2003; 97: 1573-1581.
33. Krishnamachary B, Penet MF, Nimmagadda S, et al. Hypoxia regulates CD44 and its variant isoforms through HIF-1alpha in triple negative breast cancer. PLoS One 2012; 7: e44078.
34. Nunn A, Linder K, Strauss HW. Nitroimidazoles and imaging hypoxia. Eur J Nucl Med 1995; 22: 265-280.
35. Varia MA, Calkins-Adams DP, Rinker LH, et al. Pimonidazole: a novel hypoxia marker for complementary study of tumor hypoxia and cell proliferation in cervical carcinoma. Gynecol Oncol 1998; 71: 270-277.
36. Picchio M, Beck R, Haubner R, et al. Intratumoral spatial distribution of hypoxia and angiogenesis assessed by 18F-FAZA and 125I-Gluco-RGD autoradiography. J Nucl Med 2008; 49: 597-605.
37. Dolbier WR, Jr., Li AR, Koch CJ, et al. [18F]-EF5, a marker for PET detection of hypoxia: synthesis of precursor and a new fluorination procedure. Appl Radiat Isot 2001; 54: 73-80.
38. van Loon J, Janssen MH, Ollers M, et al. PET imaging of hypoxia using [18F]HX4: a phase I trial. Eur J Nucl Med Mol Imaging 2010; 37: 1663-1668.
39. Divgi CR, Pandit-Taskar N, Jungbluth AA, et al. Preoperative characterisation of clear-cell renal carcinoma using iodine-124-labelled antibody chimeric G250 (124I-cG250) and PET in patients with renal masses: a phase I trial. Lancet Oncol 2007; 8: 304-310.
40. Oosterwijk-Wakka JC, Boerman OC, Mulders PF, et al. Application of Monoclonal Antibody G250 Recognizing Carbonic Anhydrase IX in Renal Cell Carcinoma. Int J Mol Sci 2013; 14: 11402-11423.

PART I

Tumor markers for optical molecular imaging of hypoxic breast cancer

Aram S.A. van Brussel*, Arthur Adams*, Jeroen F. Vermeulen, Willem P.Th.M. Mali,
Elsken van der Wall, Paul J. van Diest, Sjoerd G. Elias
*These authors contributed equally

2

The potential of hypoxia markers as target for breast molecular imaging – A systematic review and meta-analysis of human marker expression

Abstract

Background: Molecular imaging of breast cancer is a promising emerging technology, potentially able to improve clinical care. Valid imaging targets for molecular imaging probe development are membrane-bound hypoxia-related proteins, expressed when tumor growth outpaces neo-angiogenesis. We performed a systematic literature review and meta-analysis of such hypoxia marker expression rates in human breast cancer to evaluate their potential as clinically relevant molecular imaging targets.

Methods: We searched MEDLINE and EMBASE for articles describing membrane-bound proteins that are related to hypoxia-inducible factor 1α (HIF-1α), the key regulator of the hypoxia response. We extracted expression rates of carbonic anhydrase-IX (CAIX), glucose transporter-1 (GLUT1), C-X-C chemokine receptor type-4 (CXCR4), or insulin-like growth factor-1 receptor (IGF1R) in human breast disease, evaluated by immunohistochemistry. We pooled study results using random-effects models and applied meta-regression to identify associations with clinicopathological variables.

Results: Of 1,705 identified articles, 117 matched our selection criteria, totaling 30,216 immunohistochemistry results. We found substantial between-study variability in expression rates. Invasive cancer showed pooled expression rates of 35% for CAIX (95% confidence interval (CI): 26-46%), 51% for GLUT1 (CI: 40-61%), 46% for CXCR4 (CI: 33-59%), and 46% for IGF1R (CI: 35-70%). Expression rates increased with tumor grade for GLUT1, CAIX, and CXCR4 (all $p<0.001$), but decreased for IGF1R ($p<0.001$). GLUT1 showed the highest expression rate in grade III cancers with 58% (45-69%). CXCR4 showed the highest expression rate in small T1 tumors with 48% (CI: 28-69%), but associations with size were only significant for CAIX ($p<0.001$; positive association) and IGF1R ($p=0.047$; negative association). Although based on few studies, CAIX, GLUT1, and CXCR4 showed profound lower expression rates in normal breast tissue and benign breast disease ($p<0.001$), and high rates in in situ carcinoma. Invasive lobular carcinoma consistently sho-

wed lower expression rates ($p<0.001$).
Conclusions: Our results support the potential of hypoxia-related markers as breast cancer molecular imaging targets. Although specificity is promising, combining targets would be necessary for optimal sensitivity. These data could help guide the choice of imaging targets for probe development depending on the envisioned clinical application.

Background

In the past decades, conventional breast imaging modalities such as (digital) mammography, breast ultrasound, and more recently dynamic contrast enhanced magnetic resonance imaging (DCE-MRI), have improved detection, characterization, and management of breast cancer. Although these imaging modalities are valuable in clinical practice, novel imaging strategies such as molecular imaging promise additional advantages. With molecular imaging techniques, breast cancer could be detected even before anatomical changes occur that are required for visualization with currently used imaging modalities, making it valuable for early detection or screening. For diagnostic purposes, more informative characterization of breast cancer could result in less unnecessary biopsies. Furthermore, improved imaging of the extent of disease could lead to better preoperative planning and to per-operative guidance, increasing the primary surgery success rate. Molecular imaging could also be applied to demonstrate the presence of appropriate molecular targets in the primary tumor, lymph node and distant metastasis (*in vivo* receptor status determination), and could therefore be useful to tailor therapy to individual patients and to monitor therapy response [1-6]. Molecular imaging of tumor metabolism using ^{18}F-fluorodeoxyglucose Positron Emission Tomography (^{18}FDG-PET) is currently common for imaging and staging of advanced breast cancer. However, it is of limited value in evaluation of early breast cancer because of limited spatial resolution, non-visibility of tumors with low FDG avidity, and low specificity [7]. Imaging of tumor hypoxia could be a feasible alternative strategy for molecular imaging of breast cancer. Hypoxia is a frequent phenomenon in solid tumors that arises due to limited perfusion [8, 9], and might therefore be more specific than FDG imaging. Direct imaging of tumor hypoxia using oxygen mimetics (e.g. with radiolabelled 2-nitroimidazole derivatives (^{18}F-FMISO, ^{18}F-FAZA, ^{18}F-EF5) and other molecules such as Cu-ATSM) has been investigated in several clinical studies [10]. However, the biodistribution properties of these molecules result in images with low contrast.

Molecular imaging using (monoclonal) antibodies or antibody fragments (e.g. single chain variable fragments (scFv), antibody-binding fragments (Fab), variable domains of the heavy chain of heavy-chain-only antibodies (VHH) and affibodies) that have high affinity for markers that are expressed in breast cancer under hypoxic conditions could improve imaging contrast [11-13]. The molecules that are targeted with these antibodies or fragments should ideally be highly prevalent in (breast) cancer, and expression should preferably be already present at the initial stage of tumorigenesis. Expression of these molecules should be absent or low in non-affected tissue and benign breast disease for high specificity, although the relative importance of these properties depends on the envisioned clinical application. For screening purposes, specificity of the target of interest should be high and for application in a diagnostic setting, expression prevalence of the target in breast cancer should be sufficient. For intra-operative guidance, high expression prevalences are less important as pre-operative target selection is possible based on a diagnostic (core) biopsy. However, distribution of the target within the tumor should be homogenous when used for assessment of tumor margins. Furthermore, extracellular membrane-bound molecules are most attractive, as these are more easily accessible for most antibodies or antibody fragments compared to intracellular molecules [14].

Hypoxic conditions result in focal expression of hypoxia-inducible factor 1α (HIF-1α), the key regulator of the hypoxia response [8, 15, 16]. The downstream targets of HIF-1α, carbonic anhydrase IX (CAIX), glucose transporter 1 (GLUT1) and C-X-C chemokine receptor type 4 (CXCR4)[17-20], and insulin-like growth factor 1 receptor (IGF1R) that maintains the hypoxia response via HIF-1α stabilization [21-23], are expressed on the plasma membrane of breast cancer cells and are therefore potentially suitable candidates for molecular imaging of hypoxic tumors with antibodies or antibody fragments.

Despite the apparent potential of these hypoxia-related proteins, expression patterns in human breast cancer, normal breast tissue and benign breast diseases, as well as expression in tumor margins and heterogeneity within tumors are not well established. To evaluate whether molecular imaging using these targets could be clinically relevant, we performed a systematic literature review and meta-analysis

to quantify expression prevalences of these hypoxia markers in breast disease as assessed by immunohistochemistry, investigated relations with clinicopathological characteristics, and assessed the influence of specimen handling on these prevalences. These data could help guide the choice of relevant imaging targets for future probe development towards clinical studies.

Target	**Synonyms used**
CAIX	CAIX OR CA-IX OR "CA IX" OR CA9 OR CA-9 OR "CA 9" OR "carbonic anhydrase IX" OR "carbonic anhydrase 9"
GLUT1	GLUT1 OR GLUT-1 OR "Glucose transporter 1"
CXCR4	CXCR4 OR CXCR-4 OR CXC-R4 OR "CXC chemokine receptor-4"
IGF1R	"insulin like growth factor 1 receptor" OR "insulin like growth factor I receptor" OR IGF1R OR IGF-1R OR IGFR OR IGF-IR OR IGF1-R

Table 1: Search strategy used to identify publications of interest regarding prevalence of hypoxia proteins in benign and malignant breast tissue.
Search terms were combined with 'breast' and 'mamm*'. For MEDLINE, '[tiab]' was added to each search term, and for EMBASE, 'ti;ab;' was added.

Methods

Literature search

We performed a systematic search in the databases of MEDLINE and EMBASE on August 21st, 2012. Search terms included synonyms for the targets of interest (CXCR4, GLUT1, CAIX, and IGF1R), combined with 'breast' and 'mamm*'. The full search syntax can be found in Table 1. We applied no restrictions on publication date. The search in the database of EMBASE was limited to articles that were not indexed with a MEDLINE ID, and conference abstracts were excluded. Duplicate articles were manually removed from the search results.

Article selection

Article eligibility was assessed by three reviewers (AA, AvB, JV) through independent screening of all titles and abstracts from the search result (triple read). We excluded articles based on predefined criteria, disagreements were resolved by discussion. An overview of the selection procedure is shown in Figure 1. Reasons for exclusion of articles based on title or abstract were: (1) non-original data (e.g. reviews, editorials, guidelines, and comments), (2) non-clinical articles (e.g. technical, animal, or *in vitro* studies), (3) case reports, (4) articles investigating other tissues than breast tissue, or (5) articles not written in English. The full texts of the remaining articles were screened for expression prevalence of the targets of interest. Studies were excluded if (1) only lymph node or distant metastases were investigated (N=10), (2) the target of interest was assessed with another method than immunohistochemistry (e.g. quantitative polymerase chain reaction or western blot, N=64), (3) all or a non-definable part of patients received neo-adjuvant therapy (which can profoundly alter biomarker status, N=10), or (4) the prevalence of the target of interest was not reported and could not be derived from the published data (N=20). All references of the remaining articles were reviewed to retrieve articles initially missed in the search syntax.

Data extraction and statistical analysis

We extracted relevant information of each study (e.g. study and population characteristics, patient and tumor characteristics, and immunohistochemistry (IHC) methodology). Then, for each study and per target of interest, we annotated the number of lesions stated as 'target positive' and the total number of lesions, either directly or through recalculation based on the information stated in the article. Lesions of interest were invasive breast cancers, ductal carcinoma in situ (DCIS), benign breast lesions, or normal breast tissue. For invasive cancers, we grouped studies describing similar cut-off levels for marker positivity. When a study described multiple cut-off levels, the level corresponding to the most used cut-off among other included studies was used, as established after collecting all data. If patient data was used in more than one article (i.e. when articles referred to the same study, or assessed a comparable number of patients from the same hospital in a similar inclusion period to evaluate the expression of the same hypoxia marker), then only the article with the largest number of patients was included in the review and meta-analysis. A subgroup was defined for studies investigating membranous staining patterns only. Also, in order to assess applicability of the targets for human molecular imaging studies, we identified articles using a stringent/high cut-off value and preferentially membranous staining localization, as these studies provide the best evidence for high expression levels of the target. Furthermore, subgroups were defined according to tumor size (based on the TNM system), histological grade, histological subtype, and specimen handling method (i.e. if full tissue sections or tissue microarrays (TMA) were investigated), when stated. To assess specificity of the investigated markers, studies were grouped according to tissue types other than invasive breast cancer (normal tissue, benign breast disease, in situ carcinoma).

Then, we pooled prevalence rates across studies using a random-effects model, allowing for between-study heterogeneity. We fitted a linear mixed model using the exact binomial approach with the restricted maximum likelihood method [24]. We tested for subgroup differences using meta-regression analysis with subgroup indicators as fixed effects and the individual studies as random effects in the models. Besides the pooled prevalence estimates, we report predictive intervals as

suggested by Higgins et al. for the evaluation of between-study heterogeneity [25]. We evaluated presence of publication bias with funnel plots and statistically tested for funnel plot asymmetry using Egger's test [26].

Analyses were performed with R (version 2.15.1, R Foundation for Statistical Computing, Vienna, Austria)[27]; with the package 'lme4'[28] and 'meta'[29]. All statistical tests were two-sided and a p-value of 0.05 or less was considered statistically significant. Prevalence estimates are reported with corresponding 95% logit confidence intervals (CI).

Results

The search yielded 1,629 articles in MEDLINE and 270 articles in EMBASE. After removal of 194 duplicates, 1,705 unique articles were left for evaluation. Of these, we excluded 1,476 articles based on title and abstract, and 104 articles based on full text screening (Figure 1). Reference cross-checking of the selected articles yielded two additional studies that were initially missed, as synonyms for breast were not included in the title or abstract [30, 31]. Of the 127 selected articles (CAIX [9, 32-71], GLUT1 [30, 31, 33, 34, 36, 39, 42, 45, 46, 49, 53, 62, 65, 67, 69, 72-91], CXCR4 [92-121], IGF1R [36, 122-156]), we excluded ten articles from the analysis due to (suspected) overlap of study populations [38, 43, 61, 62, 94, 109, 123, 139, 143, 153], and one article [67] because we could not distinguish between in situ and invasive breast cancer. Ten articles [33, 34, 39, 42, 45, 46, 49, 53, 65, 69] described both GLUT1 and CAIX expression, and one study [36] described IGF1R, CAIX, and GLUT1 expression. In three of these studies, co-expression patterns of CAIX and GLUT1 were investigated [42, 45, 69]. Study characteristics of all investigated studies are shown in Additional Information tables S1A-S1D.

IHC methodology varied between the studies. For assessment of CAIX expression, three different antibodies were used, and in 11 (31%) studies only the manufacturer was stated. In articles describing GLUT1 prevalence, six different antibodies were used and in 23 (70%) studies, only the manufacturer was stated. For CXCR4, eight antibodies were used and in seven (25%) studies the antibody data was not reported, and for IGF1R, 11 different antibodies were used, and five (16%) studies did not specify the clone used. In addition, 51 (44%) studies investigated TMAs to evaluate target expression. Only 32 (63%) studies using TMAs reported the number of cores, and 37 (73%) studies reported the diameter of the cores. In 43 (37%) of the studies, no information was available on who assessed staining results, 18 (15%) studies reported evaluation by a single observer and in 56 (48%) studies by more than one observer. In 43 (37%) of the studies, it was explicitly stated that evaluation was performed by one or more pathologists.

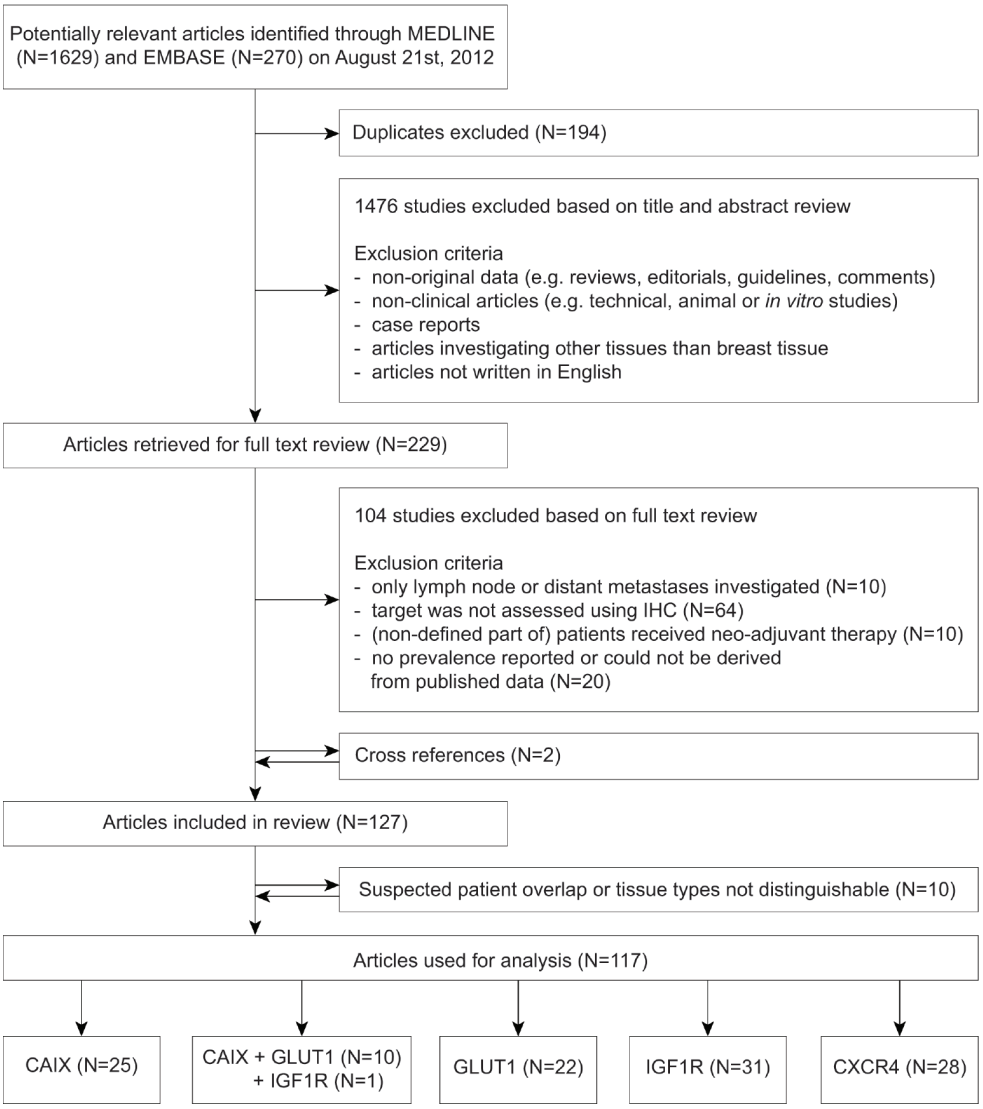

Figure 1: Flowchart for selection of articles describing expression prevalences of the hypoxia markers CAIX, GLUT1, CXCR4, and IGF1R in breast cancer, normal tissue, benign breast disease, and in situ carcinoma, assessed by immunohistochemistry.

CAIX

A total of 36 articles including 10,885 invasive cancers (range of 10 to 3,630 cancers per study) reported on CAIX expression, with prevalence estimates ranging from 7% to 92%. The overall pooled prevalence of CAIX was 35% (CI 26-46%; Figure 2A and Table 2). For studies investigating membranous staining patterns only, we found a pooled expression prevalence of 23% (CI 17-31%, 20 studies; Additional Information Figure S1A) and the studies providing best evidence for evaluation of molecular imaging targets showed a pooled prevalence of 38% (CI 17-65%, 6 studies; Additional Information Figure S1B). Expression prevalence of CAIX increased with histological grade (16% in grade II ($p<0.001$) and 30% in grade III ($p<0.001$) versus 4% in grade I; Additional Information Figure S1C), and tumor size (15% in T2 ($p<0.001$) and 30% in T3 ($p<0.001$) versus 12% in T1; Additional Information Figure S1D). Prevalence of CAIX was also higher in invasive ductal carcinoma (IDC) compared to invasive lobular carcinoma (ILC) (34% versus 1%, $p=0.001$; Additional Information Figure S1E). CAIX expression was more often positive in studies investigating full sections compared to TMA (51% versus 24%, $p=0.002$; Additional Information Figure S1F). In normal breast tissue, the pooled prevalence was 2% (CI 0-50%, $p<0.001$; 4 studies). Pooled prevalence in benign lesions was 6% (CI 2-20%, $p<0.001$; 3 studies), and in in situ carcinoma 49% (CI 31-68%, $p=0.025$; 4 studies) (Figure 2B). Overall, between study-heterogeneity of studies investigating CAIX expression was large, but this decreased when confining analyses to membranous-only and best evidence studies (these study groups largely overlapped). Between-study variation was also lower within subgroups of tumor grade and tumor size.

	CAIX				GLUT1				CXCR4				IGF1R			
	N	Prev.	(CI)	p-value*	N	Prev.	(CI)	p-value*	N	Prev.	(CI)	p-value*	N	Prev.	(CI)	p-value*
Invasive carcinoma																
Overall	36	0.35	(0.26-0.46)	Ref	33	0.51	(0.40-0.61)	Ref	28	0.46	(0.33-0.59)	Ref	31	0.46	(0.35-0.70)	Ref
Membranous localization only	20	0.23	(0.17-0.31)	-	19	0.44	(0.37-0.52)	-	2	0.16	(0.08-0.31)	-	15	0.38	(0.27-0.50)	-
Best evidence studies	6	0.38	(0.17-0.65)	-	17	0.41	(0.35-0.48)	-	7	0.43	(0.25-0.63)	-	10	0.33	(0.22-0.46)	-
Histological grade	12				10				13				5			
I		0.04	(0.02-0.08)	Ref		0.24	(0.18-0.31)	Ref		0.26	(0.13-0.44)	Ref		0.57	(0.51-0.63)	Ref
II		0.16	(0.10-0.24)	**<0.001**		0.33	(0.20-0.50)	**0.012**		0.32	(0.17-0.52)	**0.049**		0.51	(0.49-0.54)	0.093
III		0.30	(0.22-0.39)	**<0.001**		0.58	(0.45-0.69)	**<0.001**		0.44	(0.26-0.63)	**<0.001**		0.41	(0.39-0.43)	**<0.001**
Tumor size	7				6				12				4			
T1		0.12	(0.11-0.14)	Ref		0.37	(0.31-0.42)	Ref		0.48	(0.28-0.69)	Ref		0.45	(0.39-0.51)	Ref
T2		0.15	(0.11-0.20)	**<0.001**		0.36	(0.29-0.43)	0.641		0.52	(0.28-0.74)	0.620		0.47	(0.44-0.49)	0.682
T3		0.30	(0.17-0.47)	**<0.001**		0.30	(0.14-0.53)	0.180		0.68	(0.53-0.80)	0.122		0.39	(0.32-0.47)	**0.047**
Histological type	13				14				10				6			
Invasive Ductal Carcinoma		0.34	(0.20-0.52)	Ref		0.48	(0.32-0.64)	Ref		0.46	(0.22-0.72)	Ref		0.42	(0.28-0.58)	Ref
Invasive Lobular Carcinoma		0.01	(0.00-0.05)	**0.001**		0.09	(0.01-0.40)	**<0.001**		0.35	(0.00-0.98)	**0.001**		0.25	(0.08-0.55)	**<0.001**
Specimen handling	36				32				28				31			
Full sections		0.51	(0.37-0.64)	Ref		0.61	(0.49-0.72)	Ref		0.39	(0.28-0.51)	Ref		0.34	(0.26-0.42)	Ref
Tissue Microarray		0.24	(0.16-0.35)	**0.002**		0.30	(0.18-0.45)	**0.003**		0.61	(0.29-0.85)	0.173		0.57	(0.39-0.73)	**0.032**
Other tissue types	4				5				4				2			
Normal breast tissue		0.02	(0.00-0.50)	**<0.001**		0.03	(0.00-0.22)	**<0.001**		0.03	(0.01-0.07)	**<0.001**		0.74	(0.69-0.78)	0.109
Benign breast diseases		0.06	(0.02-0.20)	**<0.001**		0.04	(0.00-0.42)	**<0.001**		0.04	(0.00-0.80)	**<0.001**		0.73	(0.66-0.79)	0.137
Carcinoma *in situ*		0.49	(0.31-0.68)	**0.025**		0.52	(0.42-0.62)	0.680		0.71	(0.23-0.95)	**<0.001**		0.33	(0.18-0.53)	0.869

Table 2: Systematic review, meta-analysis and meta-regression results of hypoxia membrane protein expression in breast cancer, in situ carcinoma, benign breast disease, and normal breast tissue. *p-values obtained using meta-regression (linear mixed model with subgroup indicators as fixed and the individual studies as random effects); ref: reference category for the meta-regression result; N: Maximum number of studies evaluated for pooled estimate or meta regression.

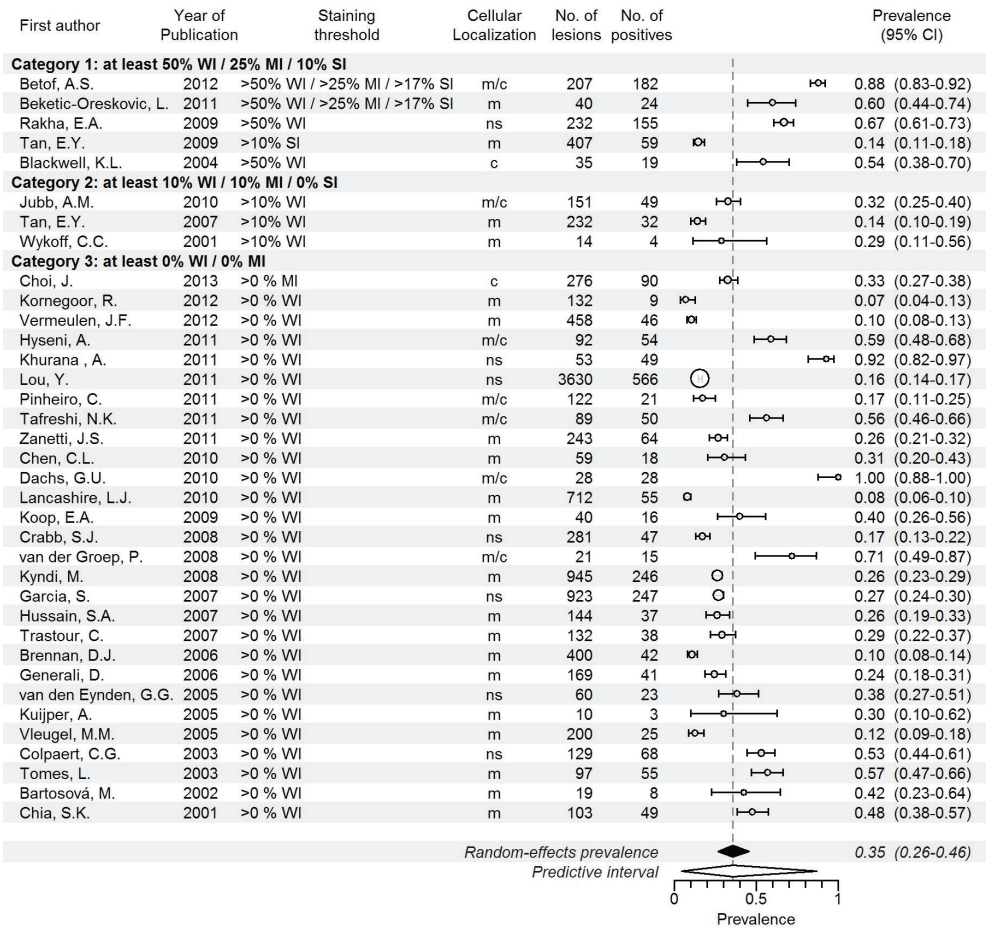

Figure 2A: Systematic literature review of CAIX prevalence in breast cancer assessed by immunohistochemistry, according to reported staining threshold. Dashed gray reference line: overall random-effects prevalence estimate. Abbreviations: Staining threshold: weak intensity (WI), moderate intensity (MI), strong intensity (SI); Localization: cytoplasm (c), membrane (m); confidence interval (CI); not stated (NS).

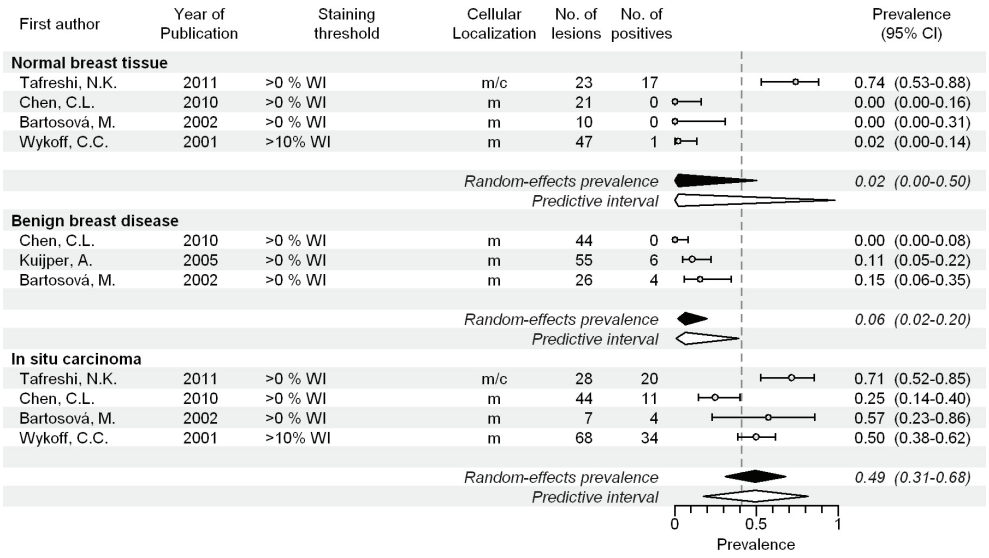

Figure 2B: Systematic literature review of CAIX prevalence in normal breast tissue, benign breast diseases and in situ carcinoma assessed by immunohistochemistry. Dashed line represents random effect summary prevalence estimate for invasive cancer within studies reporting also on normal, benign and/or precancerous breast tissue (N=4). Abbreviations: Staining threshold: weak intensity (WI), moderate intensity (MI), strong intensity (SI); Localization: cytoplasm (c), membrane (m); confidence interval (CI); not stated (NS).

GLUT1

A total of 33 articles including 3,633 invasive cancers reported on GLUT1 expression, with a range of 11 to 458 cancers per study. The overall pooled prevalence of GLUT1 expression was 51% (CI 40-61%; Figure 3A and Table 2), but the reported prevalence varied substantially between studies (range 5% to 100%). For studies investigating membranous staining patterns only, the pooled prevalence was 44% (CI 37-52%, 19 studies; Additional Information Figure S2A) and when the studies providing best evidence for evaluation of molecular imaging targets were selected, this was 41% (CI 35-48%; 17 studies; Additional Information Figure S2B). GLUT1 prevalence was higher for grade III (58%, $p<0.001$) and grade II tumors (33%, $p=0.012$) compared to grade I tumors (24%; Additional Information Figure S2C), but there was no relation with tumor size (Additional Information Figure S2D). Furthermore, as for CAIX, expression prevalence in ILC was lower compared to IDC (9% versus 48%, $p<0.001$; Additional Information Figure S2E). Studies investigating TMAs reported lower prevalence of GLUT1 expression compared to studies using full sections (30% versus 61%, $p=0.003$, Additional Information Figure S2F). In normal breast tissue, the pooled expression prevalence was 3% (CI 0-22%, $p<0.001$; 5 studies). Pooled prevalence in benign lesions was 5% (CI 0-42%, $p<0.001$; 3 studies), and in in situ carcinoma 52% (CI 42-62%, $p=0.680$; 3 studies) (Figure 3B). For GLUT1, the overall between-study variation was large as well, but substantially smaller for studies investigating membranous staining only and the best evidence studies (these study groups again largely overlapped). Furthermore, the between-study variation was markedly lower when taking tumor size into account, and somewhat lower within subgroups of grade. In the studies investigating co-expression patterns of GLUT1 and CAIX, concordant presence or absence of CAIX and GLUT1 was found in 78/118 (66%)[42], 45/59 (76%)[45], and 45/48 (94%)[69] of the cancers, respectively.

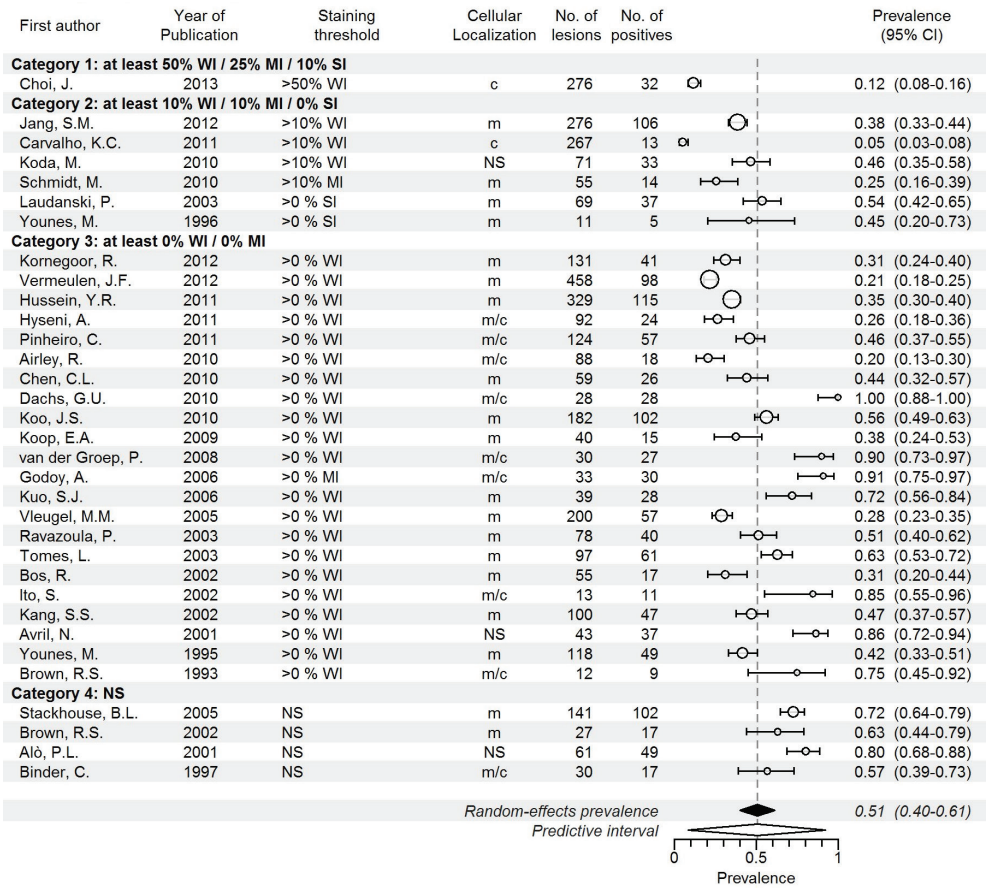

Figure 3A: Systematic literature review of GLUT1 prevalence in breast cancer assessed by immunohistochemistry, according to reported staining threshold. Dashed gray reference line: overall random-effects prevalence estimate. Abbreviations: Staining threshold: weak intensity (WI), moderate intensity (MI), strong intensity (SI); Localization: cytoplasm (c), membrane (m); confidence interval (CI); not stated (NS).

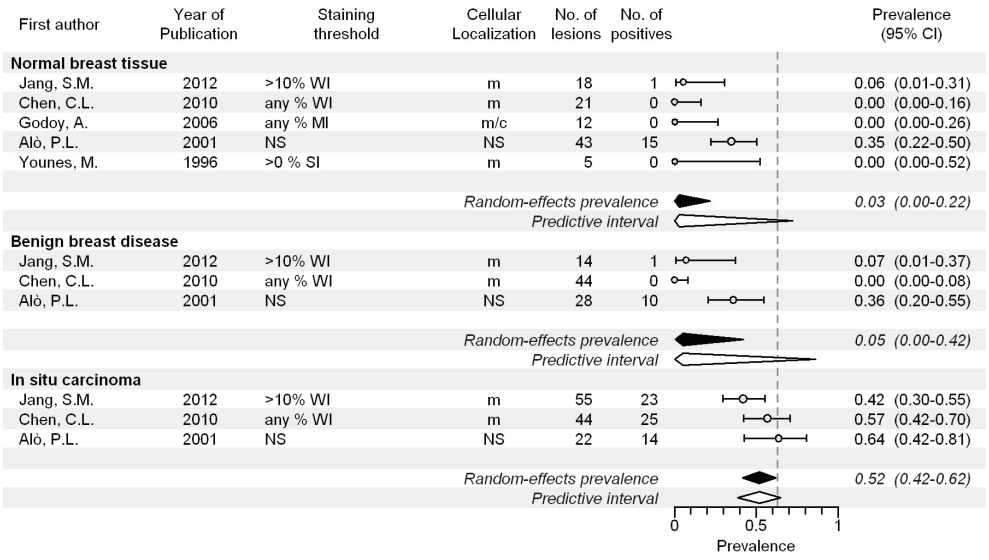

Figure 3B: Systematic literature review of GLUT1 prevalence in normal breast tissue, benign breast diseases and in situ carcinoma assessed by immunohistochemistry. Dashed line represents random effect summary prevalence estimate for invasive cancer within studies reporting also on normal, benign and/or precancerous breast tissue (N=5). Abbreviations: Staining threshold: weak intensity (WI), moderate intensity (MI), strong intensity (SI); Localization: cytoplasm (c), membrane (m); confidence interval (CI); not stated (NS).

CXCR4

A total of 28 articles including 5,583 invasive cancers reported on CXCR4 expression, with a range of 7 to 1,808 cancers per study. The pooled prevalence of CXCR4 expression was 46% (CI 33-59%; Figure 4A and Table 2), with a range between studies of 8 to 100%. For studies investigating membranous staining patterns only, the pooled prevalence was 16% (CI 8-31%; 2 studies; Additional Information Figure S3A) and when the studies providing best evidence for evaluation of molecular imaging targets were selected, this was 43% (CI 25-63%; 7 studies, Additional Information Figure S3B). CXCR4 prevalence increased with histological grade (32% in grade II ($p=0.049$) and 44% in grade III ($p<0.001$), compared to 26% in grade I; Additional Information Figure S3C), but no relation was found with tumor size (Additional Information Figure S3D). Furthermore, the prevalence of CXCR4 was higher in IDC than in ILC (46% versus 35%, $p=0.001$; Additional Information Figure S3E). Expression prevalence was not related to slide construction method (Additional Information Figure S3F). In normal breast tissue, the pooled expression prevalence was 3% (CI 1-7%, $p<0.001$; 4 studies). Pooled prevalence in benign lesions was 4% (CI 0-80%, $p<0.001$; 4 studies), and in in situ carcinoma 71% (CI 23-95%, $p<0.001$; 2 studies) (Figure 4B). Between-study heterogeneity of studies investigating CXCR4 expression was large, both overall and within all subgroups (except for the two studies investigating membranous staining).

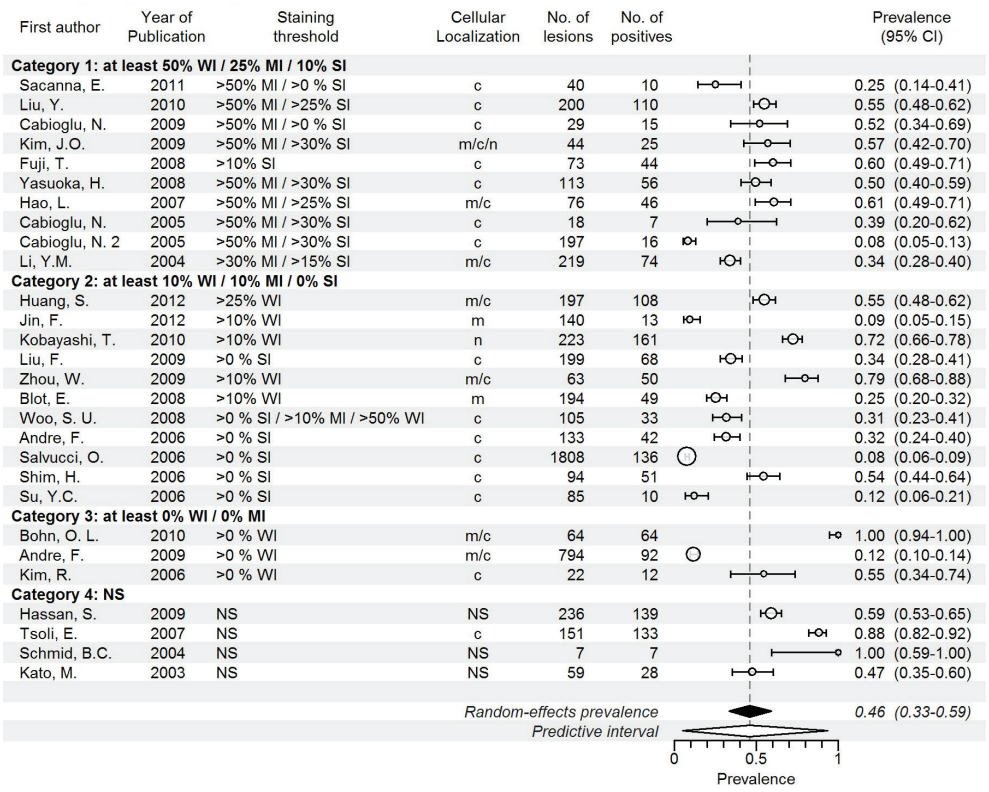

Figure 4A: Systematic literature review of CXCR4 prevalence in breast cancer assessed by immunohistochemistry, according to reported staining threshold. Dashed gray reference line: overall random-effects prevalence estimate. Abbreviations: Staining threshold: weak intensity (WI), moderate intensity (MI), strong intensity (SI); Localization: cytoplasm (c), membrane (m); confidence interval (CI); not stated (NS).

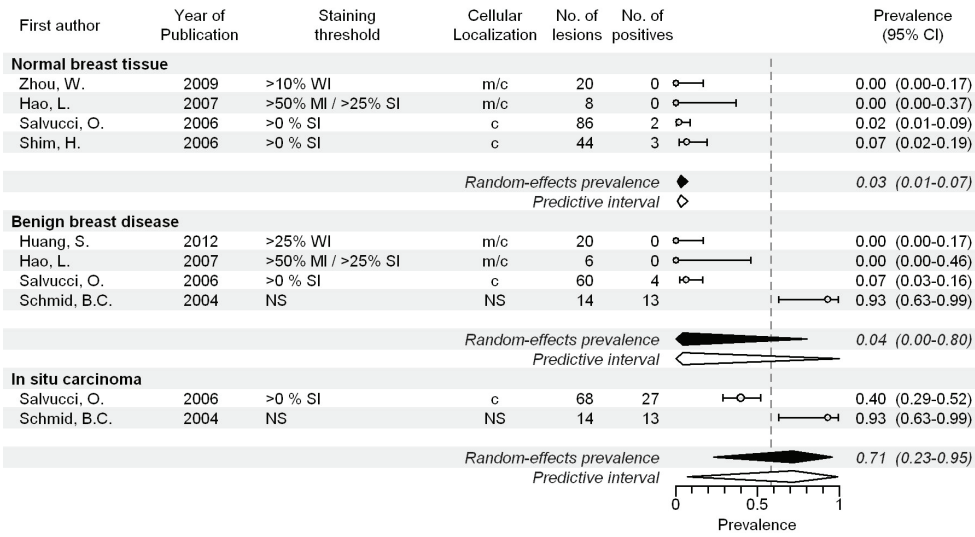

Figure 4B: Systematic literature review of CXCR4 prevalence in normal breast tissue, benign breast diseases and in situ carcinoma assessed by immunohistochemistry. Dashed line represents random effect summary prevalence estimate for invasive cancer within studies reporting also on normal, benign and/or precancerous breast tissue (N=6). Abbreviations: Staining threshold: weak intensity (WI), moderate intensity (MI), strong intensity (SI); Localization: cytoplasm (c), membrane (m); confidence interval (CI); not stated (NS).

IGF1R

We analyzed a total of 31 articles including 8,463 invasive cancers (range of 8 to 2,871 cancers per study). The pooled prevalence of IGF1R expression was 46% (CI 35-57%; Figure 5A and Table 2) with a range between studies of 10% to 99%. For studies investigating membranous staining patterns only, the pooled prevalence was 38% (CI 27-50%; 15 studies, Additional Information Figure S4A) and when the studies providing best evidence for evaluation of molecular imaging targets were selected, this was 33% (CI 22-46%; 10 studies, Additional Information Figure S4B). In contrast to the other investigated markers, the pooled prevalence of IGF1R was lower in grade III versus grade I cancers (41% versus 57%, $p<0.001$; Additional Information Figure S4C), and was lower in T3 cancers compared to T1 cancers (39% versus 45%, $p=0.047$; Additional Information Figure S4D). Prevalence of IGF1R was higher in IDC compared to ILC (42% versus 25%, $p<0.001$; Additional Information Figure S4E), and higher in studies using TMAs than in studies using full sections (57% versus 34%, $p=0.032$; Additional Information Figure S4F). In normal breast tissue, the pooled expression prevalence was 74% (CI 69-78%, $p=0.109$; 2 studies). Pooled prevalence in benign lesions was 73% (CI 66-79%, $p=0.137$; 2 studies), and in in situ carcinoma 33% (CI 18-53%, $p=0.869$; 2 studies) (Figure 5B). Variation in results between studies was large, both overall and within the studies investigating membranous staining only and best evidence studies. Within groups of tumor grade and size, the between-study heterogeneity was very low, but the number of studies in these subgroups was small.

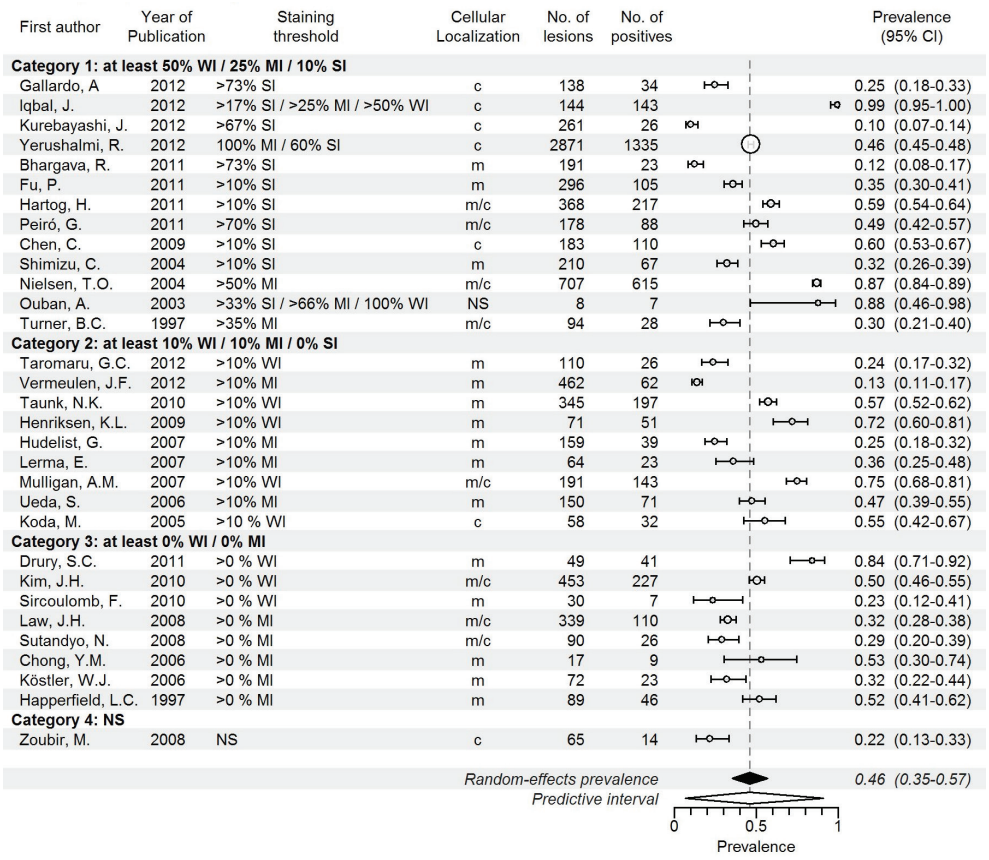

Figure 5A: Systematic literature review of IGF1R prevalence in breast cancer assessed by immunohistochemistry, according to reported staining threshold. Dashed gray reference line: overall random-effects prevalence estimate. Abbreviations: Staining threshold: weak intensity (WI), moderate intensity (MI), strong intensity (SI); Localization: cytoplasm (c), membrane (m); confidence interval (CI); not stated (NS).

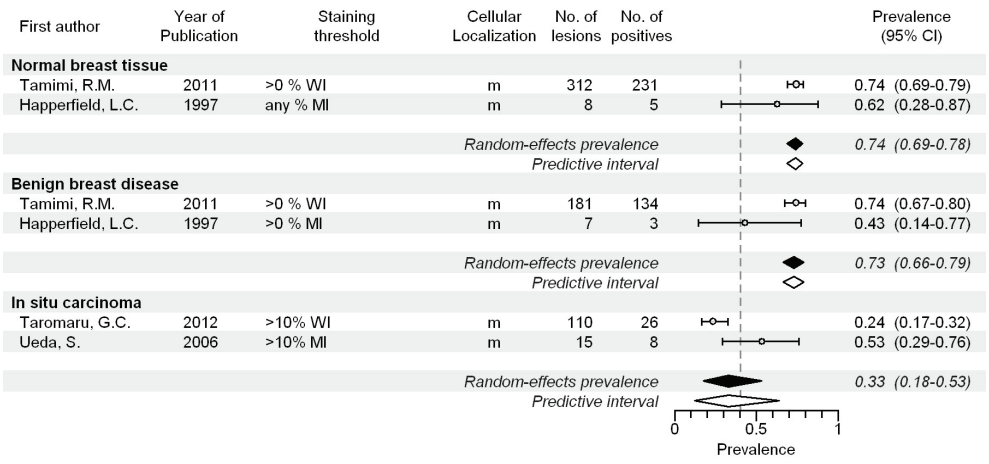

Figure 5B: Systematic literature review of IGF1R prevalence in normal breast tissue, benign breast diseases and in situ carcinoma assessed by immunohistochemistry. Dashed line represents random effect summary prevalence estimate for invasive cancer within studies reporting also on normal, benign and/or precancerous breast tissue (N=3). Abbreviations: Staining threshold: weak intensity (WI), moderate intensity (MI), strong intensity (SI); Localization: cytoplasm (c), membrane (m); confidence interval (CI); not stated (NS).

Evaluation of publication bias

The substantial overall between-study heterogeneity in prevalence estimates was confirmed by examination of the funnel plots (not shown). Furthermore, smaller studies (i.e. with lower precision) were more likely to report higher hypoxia marker prevalence rates (all Egger's tests $p<0.05$, except for IGF1R). Funnel plots evaluating hypoxia marker prevalence rates according to tumor grade showed no evidence for publication bias for GLUT1 and CXCR4 (all Egger's tests $p>0.25$), but indicated that smaller studies showed a larger increase in CAIX prevalence for grade 3 versus 1 and a larger decrease in IGF1R prevalence for grade 2 versus grade 1 tumors (i.e. more extreme effects in small studies; Egger's tests $p=0.044$ and $p=0.023$, respectively). We found no indication for publication bias when evaluating the studies reporting on hypoxia marker prevalence rates according to tumor size (all Egger's tests $P>0.15$, or too few studies for evaluation).

Discussion

In this comprehensive systematic literature review and meta-analysis, we reported on expression prevalence of the hypoxia-related proteins GLUT1, CAIX, CXCR4, and IGF1R in breast cancer and in situ carcinoma, benign breast disease and normal breast tissue. We included a total of 117 articles totaling 30,216 immunohistochemistry results. Hypoxia marker prevalence rates were in the range of other potential targets for molecular imaging with antibodies or antibody fragments, e.g. EGFR [157] or CD44v6 [158], and were higher than for example HER2 [159]. Benign breast disease and non-affected breast tissue showed low expression, but studies were few. The between-study variation of results was substantial and meta-regression showed several clinicopathological features of breast cancer to significantly influence hypoxia marker expression.

CAIX, GLUT1 and CXCR4 prevalence rates significantly increased with histological grade, which is consistent with the hypothesis that high grade tumors have a higher proliferation rate, causing neo-angiogenesis to lag behind tumor growth [160]. The resulting inadequate nutrient and oxygen supply causes activation of the hypoxia pathway [161, 162]. Surprisingly, we found an inverse relation for IGF1R with histological grade. In analogy to histological grade, larger tumors may also express hypoxia markers more frequently, but we only found a significant positive relation for CAIX, and again an unexpected negative significant relation with IGF1R. We further found that hypoxia proteins are infrequently expressed in ILC, suggesting that hypoxia is not a common phenomenon in these cancers. Ercan et al. reported that only 3% of ILC expresses HIF-1α, compared to 39% of IDC [163], suggesting that hypoxia is indeed rare in this subtype. We found significant lower expression prevalences in normal tissue and benign breast diseases compared to invasive breast cancer, showing high cancer-specificity of CAIX, GLUT1 and especially CXCR4. IGF1R was evaluated in few studies with non-significant results, so no conclusions can be drawn with respect to specificity of this target. Pooled expression prevalence rates of in situ carcinoma were at least comparable to (GLUT1 and

IGF1R) or higher than (CAIX and CXCR4) invasive carcinoma, albeit based on few studies.

An increasing number of recent studies evaluated hypoxia marker expression using TMA. Although TMA allows for higher throughput than full section analyses, it may lead to underestimation of marker expression in presence of intra-tumoral heterogeneity. We found that CAIX and GLUT1 prevalence was significantly lower in TMA studies, presumably due to the sampling method used for TMA construction, in which necrotic regions that usually have the highest expression of hypoxia-related proteins are avoided [65]. The lower prevalence of CAIX and GLUT1 in TMA studies could be interpreted as an indication of intratumoral heterogeneity of these markers. Although this interpretation is interesting, the applicability of TMAs for assessment of hypoxia marker expression needs to be reconsidered [164, 165], even if their use has been justified for other markers (e.g. ERα and HER2 [143, 166]).

With a view to molecular imaging, specificity of the imaging target is pivotal for every clinical application. The marked lower expression prevalence of CAIX, GLUT1 and CXCR4 in benign breast disease and normal breast tissue is thus highly promising. The specificity results for IGF1R are less encouraging, albeit based on only two studies. For early detection, a suitable target should be prevalent already in small tumors. Furthermore, evidence is mounting that current X-ray mammography screening may lead to substantial over-diagnosis [167] and picks-up tumors with favorable prognosis [168]. An imaging target that identifies small tumors with poor prognosis, e.g. grade III invasive breast cancers [169], would thus be especially valuable for screening. This combination makes GLUT1 an interesting candidate, with high expression in grade III cancers (58%) and also highest expression in T1 tumors (although the latter not significantly different from T3 tumors). CXCR4 and CAIX also show higher expression in grade III cancers, but for CAIX expression prevalence is markedly lower in smaller lesions. For intra-operative guidance, a high prevalence in invasive cancer is not required, as tissue can be sampled for investigation of target expression pre-operatively. Such a target should ideally show low intratumoral heterogeneity to ascertain radical resection. Although this was not specifically addressed by individual studies, the difference in results between

TMA and full-section studies may indicate that CAIX and GLUT1 have marked intratumoral heterogeneity and might therefore be less suitable for intra-operative application than CXCR4. Risk factors for incomplete tumor resection in current clinical practice include the presence of an extensive intraductal component [170], and the ILC histological subtype [171-175]. Especially CXCR4 shows high expression in DCIS, thus is potentially valuable for imaging of an extensive intraductal component. However, none of the markers show potential for ILC imaging.
None of the investigated markers showed a sufficient expression prevalence to allow sensitive molecular imaging with a single probe only. For successful implementation (especially in a screening or diagnostic setting), a combination of probes would be required to obtain a high sensitivity. However, all of the investigated markers here are expressed via the same (hypoxia-related) oncogenic pathway. The few studies that investigated co-expression patterns found that expression of these markers were indeed closely correlated. It would therefore be more advantageous to combine the hypoxia targets with targets from other oncogenic pathways, such as growth factors (e.g. endothelial growth factor receptor (EGFR) or human epidermal growth factor receptor 2 (HER2)), targets that are expressed in the tumor stroma (e.g. vascular endothelial growth factor (VEGF)), or less tumor-specific targets such as mucin 1 (MUC1), mammaglobin, or CD44v6 [36]. However, the aggregated nature of the obtained data did not allow us to investigate the best combination of targets or to investigate co-expression patterns.
To appreciate the results, one needs to acknowledge that studies employed various immunohistochemistry protocols and assessment methodologies, as no standardized scoring system is established for these markers, in contrast to e.g. HER2 [176]. When we evaluated only studies that used relatively strict cut-offs (i.e. the studies providing best evidence for evaluation of molecular imaging targets) or studies investigating membranous staining only, the results were still comparable to the overall results. Nevertheless, as IHC may not reflect the functionality or availability of a marker in all situations, it remains unclear which or if any cut-off level relates to sufficient marker levels for molecular imaging in humans [177]. However, immunohistochemistry remains the established standard for protein expression estimation since it allows for sensitive detection at the (sub)cellular level, and is more

reliable than assays measuring DNA or RNA levels because of post-translational processing.

Conclusions

We have shown that human expression prevalence and patterns of hypoxia-related markers support their potential as molecular imaging targets, with promising specificity. However, none of the evaluated markers shows sufficient prevalence in invasive cancer to be exploited as the sole target. Future research should focus on the identification of optimal combinations of candidate imaging targets, and dedicated studies are needed to assess the accuracy of such combinations to discriminate between breast cancer (subtypes), and benign breast lesions and normal tissue. The data from this review and such studies could help guide the choice of markers for breast cancer probe development.

References

1. Sampath L, Wang W, Sevick-Muraca EM: Near infrared fluorescent optical imaging for nodal staging. Journal of biomedical optics 2008, 13(4):041312.
2. Goldenberg DM, Nabi HA: Breast cancer imaging with radiolabeled antibodies. Seminars in nuclear medicine 1999, 29(1):41-48.
3. Mann RM, Hoogeveen YL, Blickman JG, Boetes C: MRI compared to conventional diagnostic work-up in the detection and evaluation of invasive lobular carcinoma of the breast: a review of existing literature. Breast cancer research and treatment 2008, 107(1):1-14.
4. Leung JW: New modalities in breast imaging: digital mammography, positron emission tomography, and sestamibi scintimammography. Radiologic clinics of North America 2002, 40(3):467-482.
5. Petralia G, Bonello L, Priolo F, Summers P, Bellomi M: Breast MR with special focus on DW-MRI and DCE-MRI. Cancer imaging : the official publication of the Interna tional Cancer Imaging Society 2011, 11:76-90.
6. Frangioni JV: New technologies for human cancer imaging. Journal of clinical oncology : official journal of the American Society of Clinical Oncology 2008, 26(24):4012-4021.
7. Groheux D, Espie M, Giacchetti S, Hindie E: Performance of FDG PET/CT in the clinical management of breast cancer. Radiology 2013, 266(2):388-405.
8. Bos R, Zhong H, Hanrahan CF, Mommers EC, Semenza GL, Pinedo HM, Abeloff MD, Simons JW, van Diest PJ, van der Wall E: Levels of hypoxia-inducible factor-1 alpha during breast carcinogenesis. Journal of the National Cancer Institute 2001, 93(4):309-314.
9. Wykoff CC, Beasley N, Watson PH, Campo L, Chia SK, English R, Pastorek J, Sly WS, Ratcliffe P, Harris AL: Expression of the hypoxia-inducible and tumor-associ ated carbonic anhydrases in ductal carcinoma in situ of the breast. The American journal of pathology 2001, 158(3):1011-1019.
10. Krohn KA, Link JM, Mason RP: Molecular imaging of hypoxia. Journal of nuclear medicine : official publication, Society of Nuclear Medicine 2008, 49 Suppl 2:129S-148S.
11. Muda M, Gross AW, Dawson JP, He C, Kurosawa E, Schweickhardt R, Dugas M, Soloviev M, Bernhardt A, Fischer D et al: Therapeutic assessment of SEED: a new engineered antibody platform designed to generate mono- and bispecific antibo dies. Protein engineering, design & selection : PEDS 2011, 24(5):447-454.
12. Hamers-Casterman C, Atarhouch T, Muyldermans S, Robinson G, Hamers C, Songa EB, Bendahman N, Hamers R: Naturally occurring antibodies devoid of light chains. Nature 1993, 363(6428):446-448.
13. Feldwisch J, Tolmachev V: Engineering of affibody molecules for therapy and diagnostics. Methods Mol Biol 2012, 899:103-126.
14. Taroni P: Diffuse optical imaging and spectroscopy of the breast: a brief outline of history and perspectives. Photochemical & photobiological sciences : Official journal of the European Photochemistry Association and the European Society for Photobiology 2012, 11(2):241-250.
15. Li XF, O'Donoghue JA: Hypoxia in microscopic tumors. Cancer letters 2008, 264(2):172-180.
16. Bos R, van der Groep P, Greijer AE, Shvarts A, Meijer S, Pinedo HM, Semenza GL, van Diest PJ, van der Wall E: Levels of hypoxia-inducible factor-1alpha

independently predict prognosis in patients with lymph node negative breast carci noma. Cancer 2003, 97(6):1573-1581.
17. Vaupel P, Thews O, Hoeckel M: Treatment resistance of solid tumors: role of hy poxia and anemia. Med Oncol 2001, 18(4):243-259.
18. Vaupel P, Mayer A, Briest S, Hockel M: Hypoxia in breast cancer: role of blood flow, oxygen diffusion distances, and anemia in the development of oxygen depletion. Advances in experimental medicine and biology 2005, 566:333-342.
19. Staller P, Sulitkova J, Lisztwan J, Moch H, Oakeley EJ, Krek W: Chemokine receptor CXCR4 downregulated by von Hippel-Lindau tumour suppressor pVHL. Nature 2003, 425(6955):307-311.
20. Cronin PA, Wang JH, Redmond HP: Hypoxia increases the metastatic ability of breast cancer cells via upregulation of CXCR4. BMC cancer 2010, 10:225.
21. Peretz S, Kim C, Rockwell S, Baserga R, Glazer PM: IGF1 receptor expression protects against microenvironmental stress found in the solid tumor. Radiation research 2002, 158(2):174-180.
22. Treins C, Giorgetti-Peraldi S, Murdaca J, Monthouel-Kartmann MN, Van Obberghen E: Regulation of hypoxia-inducible factor (HIF)-1 activity and expression of HIF hydroxylases in response to insulin-like growth factor I. Molecular endocrinology 2005, 19(5):1304-1317.
23. Riedemann J, Macaulay VM: IGF1R signalling and its inhibition. Endocrine-related cancer 2006, 13 Suppl 1:S33-43.
24. Hamza TH, van Houwelingen HC, Stijnen T: The binomial distribution of meta-analysis was preferred to model within-study variability. Journal of clinical epidemiology 2008, 61(1):41-51.
25. Higgins JP, Thompson SG, Spiegelhalter DJ: A re-evaluation of random-effects meta-analysis. J R Stat Soc Ser A Stat Soc 2009, 172(1):137-159.
26. Egger M, Davey Smith G, Schneider M, Minder C: Bias in meta-analysis detected by a simple, graphical test. BMJ 1997, 315(7109):629-634.
27. R Core Team: R: A language and environment for statistical computing, R Foundation for Statistical Computing, Vienna, Austria 2012.
28. Bates D, Maechleer M, Bolker B: lme4: Linear mixed-effects models using S4 classes. R package version 0.999999-0. 2012.
29. Schwarzer G: meta: Meta-Analysis with R. R package version 2.1-1 2012.
30. Ito S, Fukusato T, Nemoto T, Sekihara H, Seyama Y, Kubota S: Coexpression of glucose transporter 1 and matrix metalloproteinase-2 in human cancers. Journal of the National Cancer Institute 2002, 94(14):1080-1091.
31. Younes M, Lechago LV, Somoano JR, Mosharaf M, Lechago J: Wide expression of the human erythrocyte glucose transporter Glut1 in human cancers. Cancer research 1996, 56(5):1164-1167.
32. Betof AS, Rabbani ZN, Hardee ME, Kim SJ, Broadwater G, Bentley RC, Snyder SA, Vujaskovic Z, Oosterwijk E, Harris LN et al: Carbonic anhydrase IX is a predictive marker of doxorubicin resistance in early-stage breast cancer independent of HER2 and TOP2A amplification. British journal of cancer 2012, 106(5):916-922.
33. Choi J, Jung WH, Koo JS: Metabolism-related proteins are differentially expressed according to the molecular subtype of invasive breast cancer defined by surrogate immunohistochemistry. Pathobiology : journal of immunopathology, molecular and cellular biology 2013, 80(1):41-52.
34. Kornegoor R, Verschuur-Maes AH, Buerger H, Hogenes MC, de Bruin PC, Oudejans JJ, Hinrichs B, van Diest PJ: Fibrotic focus and hypoxia in male breast cancer. Modern pathology : an official journal of the United States and Canadian Academy of Pathology, Inc 2012, 25(10):1397-1404.
35. Tafreshi NK, Bui MM, Bishop K, Lloyd MC, Enkemann SA, Lopez AS, Abrahams D,

Carter BW, Vagner J, Grobmyer SR et al: Noninvasive detection of breast cancer lymph node metastasis using carbonic anhydrases IX and XII targeted imaging probes. Clinical cancer research : an official journal of the American Association for Cancer Research 2012, 18(1):207-219.
36. Vermeulen JF, van Brussel AS, van der Groep P, Morsink FH, Bult P, van der Wall E, van Diest PJ: Immunophenotyping invasive breast cancer: paving the road for molecular imaging. BMC cancer 2012, 12(1):240.
37. Beketic-Oreskovic L, Ozretic P, Rabbani ZN, Jackson IL, Sarcevic B, Levanat S, Maric P, Babic I, Vujaskovic Z: Prognostic significance of carbonic anhydrase IX (CA-IX), endoglin (CD105) and 8-hydroxy-2′-deoxyguanosine (8-OHdG) in breast cancer patients. Pathology oncology research : POR 2011, 17(3):593-603.
38. Fox SB, Generali D, Berruti A, Brizzi MP, Campo L, Bonardi S, Bersiga A, Allevi G, Milani M, Aguggini S et al: The prolyl hydroxylase enzymes are positively associated with hypoxia-inducible factor-1alpha and vascular endothelial growth factor in human breast cancer and alter in response to primary systemic treatment with epirubicin and tamoxifen. Breast cancer research : BCR 2011, 13(1):R16.
39. Hyseni A, van der Groep P, van der Wall E, van Diest PJ: Subcellular FIH-1 expression patterns in invasive breast cancer in relation to HIF-1alpha expression. Cellular oncology 2011, 34(6):565-570.
40. Khurana A, Liu P, Mellone P, Lorenzon L, Vincenzi B, Datta K, Yang B, Linhardt RJ, Lingle W, Chien J et al: HSulf-1 modulates FGF2- and hypoxia-mediated migration and invasion of breast cancer cells. Cancer research 2011, 71(6):2152-2161.
41. Lou Y, McDonald PC, Oloumi A, Chia S, Ostlund C, Ahmadi A, Kyle A, Auf dem Keller U, Leung S, Huntsman D et al: Targeting tumor hypoxia: suppression of breast tumor growth and metastasis by novel carbonic anhydrase IX inhibitors. Cancer research 2011, 71(9):3364-3376.
42. Pinheiro C, Sousa B, Albergaria A, Paredes J, Dufloth R, Vieira D, Schmitt F, Baltazar F: GLUT1 and CAIX expression profiles in breast cancer correlate with adverse prognostic factors and MCT1 overexpression. Histology and histopathology 2011, 26(10):1279-1286.
43. Yan M, Jene N, Byrne D, Millar EK, O'Toole SA, McNeil CM, Bates GJ, Harris AL, Banham AH, Sutherland RL et al: Recruitment of regulatory T cells is correlated with hypoxia-induced CXCR4 expression, and is associated with poor prognosis in basal-like breast cancers. Breast cancer research : BCR 2011, 13(2):R47.
44. Zanetti JS, Soave DF, Oliveira-Costa JP, da Silveira GG, Ramalho LN, Garcia SB, Zucoloto S, Ribeiro-Silva A: The role of tumor hypoxia in MUC1-positive breast carcinomas. Virchows Archiv : an international journal of pathology 2011, 459(4):367-375.
45. Chen CL, Chu JS, Su WC, Huang SC, Lee WY: Hypoxia and metabolic phenotypes during breast carcinogenesis: expression of HIF-1alpha, GLUT1, and CAIX. Virchows Archiv : an international journal of pathology 2010, 457(1):53-61.
46. Dachs GU, Kano M, Volkova E, Morrin HR, Davey VC, Harris GC, Cheale M, Frampton C, Currie MJ, Wells JE et al: A profile of prognostic and molecular factors in European and Maori breast cancer patients. BMC cancer 2010, 10:543.
47. Jubb AM, Soilleux EJ, Turley H, Steers G, Parker A, Low I, Blades J, Li JL, Allen P, Leek R et al: Expression of vascular notch ligand delta-like 4 and inflammatory markers in breast cancer. The American journal of pathology 2010, 176(4):2019-2028.
48. Lancashire LJ, Powe DG, Reis-Filho JS, Rakha E, Lemetre C, Weigelt B, Abdel-Fatah TM, Green AR, Mukta R, Blamey R et al: A validated gene expression profile for detecting clinical outcome in breast cancer using artificial neural networks. Breast cancer research and treatment 2010, 120(1):83-93.
49. Koop EA, van Laar T, van Wichen DF, de Weger RA, Wall E, van Diest PJ: Expressi

on of BNIP3 in invasive breast cancer: correlations with the hypoxic response and clinicopathological features. BMC cancer 2009, 9:175.
50. Rakha EA, Elsheikh SE, Aleskandarany MA, Habashi HO, Green AR, Powe DG, El-Sayed ME, Benhasouna A, Brunet JS, Akslen LA et al: Triple-negative breast cancer: distinguishing between basal and nonbasal subtypes. Clinical cancer research : an official journal of the American Association for Cancer Research 2009, 15(7): 2302-2310.
51. Tan EY, Yan M, Campo L, Han C, Takano E, Turley H, Candiloro I, Pezzella F, Gatter KC, Millar EK et al: The key hypoxia regulated gene CAIX is upregulated in basal-like breast tumours and is associated with resistance to chemotherapy. British journal of cancer 2009, 100(2):405-411.
52. Crabb SJ, Bajdik CD, Leung S, Speers CH, Kennecke H, Huntsman DG, Gelmon KA: Can clinically relevant prognostic subsets of breast cancer patients with four or more involved axillary lymph nodes be identified through immunohistochemical biomarkers? A tissue microarray feasibility study. Breast cancer research : BCR 2008, 10(1):R6.
53. van der Groep P, Bouter A, Menko FH, van der Wall E, van Diest PJ: High frequency of HIF-1alpha overexpression in BRCA1 related breast cancer. Breast cancer research and treatment 2008, 111(3):475-480.
54. Kyndi M, Sorensen FB, Knudsen H, Alsner J, Overgaard M, Nielsen HM, Overgaard J: Carbonic anhydrase IX and response to postmastectomy radiotherapy in high-risk breast cancer: a subgroup analysis of the DBCG82 b and c trials. Breast cancer research : BCR 2008, 10(2):R24.
55. Garcia S, Dales JP, Charafe-Jauffret E, Carpentier-Meunier S, Andrac-Meyer L, Jacquemier J, Andonian C, Lavaut MN, Allasia C, Bonnier P et al: Poor prognosis in breast carcinomas correlates with increased expression of targetable CD146 and c-Met and with proteomic basal-like phenotype. Human pathology 2007, 38(6):830-841.
56. Hussain SA, Ganesan R, Reynolds G, Gross L, Stevens A, Pastorek J, Murray PG, Perunovic B, Anwar MS, Billingham L et al: Hypoxia-regulated carbonic anhydrase IX expression is associated with poor survival in patients with invasive breast cancer. British journal of cancer 2007, 96(1):104-109.
57. Tan EY, Campo L, Han C, Turley H, Pezzella F, Gatter KC, Harris AL, Fox SB: Cytoplasmic location of factor-inhibiting hypoxia-inducible factor is associated with an enhanced hypoxic response and a shorter survival in invasive breast cancer. Breast cancer research : BCR 2007, 9(6):R89.
58. Trastour C, Benizri E, Ettore F, Ramaioli A, Chamorey E, Pouyssegur J, Berra E: HIF-1alpha and CA IX staining in invasive breast carcinomas: prognosis and treatment outcome. International journal of cancer Journal international du cancer 2007, 120(7):1451-1458.
59. Brennan DJ, Jirstrom K, Kronblad A, Millikan RC, Landberg G, Duffy MJ, Ryden L, Gallagher WM, O'Brien SL: CA IX is an independent prognostic marker in premenopausal breast cancer patients with one to three positive lymph nodes and a putative marker of radiation resistance. Clinical cancer research : an official journal of the American Association for Cancer Research 2006, 12(21):6421-6431.
60. Generali D, Fox SB, Berruti A, Brizzi MP, Campo L, Bonardi S, Wigfield SM, Bruzzi P, Bersiga A, Allevi G et al: Role of carbonic anhydrase IX expression in prediction of the efficacy and outcome of primary epirubicin/tamoxifen therapy for breast cancer. Endocrine-related cancer 2006, 13(3):921-930.
61. Generali D, Berruti A, Brizzi MP, Campo L, Bonardi S, Wigfield S, Bersiga A, Allevi G, Milani M, Aguggini S et al: Hypoxia-inducible factor-1alpha expression predicts a poor response to primary chemoendocrine therapy and disease-free

survival in primary human breast cancer. Clinical cancer research : an official journal of the American Association for Cancer Research 2006, 12(15):4562-4568.
62. Vleugel MM, Shvarts D, van der Wall E, van Diest PJ: p300 and p53 levels determine activation of HIF-1 downstream targets in invasive breast cancer. Human pathology 2006, 37(8):1085-1092.
63. Van den Eynden GG, Van der Auwera I, Van Laere SJ, Colpaert CG, Turley H, Harris AL, van Dam P, Dirix LY, Vermeulen PB, Van Marck EA: Angiogenesis and hypoxia in lymph node metastases is predicted by the angiogenesis and hypoxia in the primary tumour in patients with breast cancer. British journal of cancer 2005, 93(10):1128-1136.
64. Kuijper A, van der Groep P, van der Wall E, van Diest PJ: Expression of hypoxia-inducible factor 1 alpha and its downstream targets in fibroepithelial tumors of the breast. Breast cancer research : BCR 2005, 7(5):R808-818.
65. Vleugel MM, Greijer AE, Shvarts A, van der Groep P, van Berkel M, Aarbodem Y, van Tinteren H, Harris AL, van Diest PJ, van der Wall E: Differential prognostic impact of hypoxia induced and diffuse HIF-1alpha expression in invasive breast cancer. Journal of clinical pathology 2005, 58(2):172-177.
66. Blackwell KL, Dewhirst MW, Liotcheva V, Snyder S, Broadwater G, Bentley R, Lal A, Riggins G, Anderson S, Vredenburgh J et al: HER-2 gene amplification correlates with higher levels of angiogenesis and lower levels of hypoxia in primary breast tumors. Clinical cancer research : an official journal of the American Association for Cancer Research 2004, 10(12 Pt 1):4083-4088.
67. Cooper C, Liu GY, Niu YL, Santos S, Murphy LC, Watson PH: Intermittent hypoxia induces proteasome-dependent down-regulation of estrogen receptor alpha in human breast carcinoma. Clinical cancer research : an official journal of the American Association for Cancer Research 2004, 10(24):8720-8727.
68. Colpaert CG, Vermeulen PB, Benoy I, Soubry A, van Roy F, van Beest P, Goovaerts G, Dirix LY, van Dam P, Fox SB et al: Inflammatory breast cancer shows angiogenesis with high endothelial proliferation rate and strong E-cadherin expression. British journal of cancer 2003, 88(5):718-725.
69. Tomes L, Emberley E, Niu Y, Troup S, Pastorek J, Strange K, Harris A, Watson PH: Necrosis and hypoxia in invasive breast carcinoma. Breast cancer research and treatment 2003, 81(1):61-69.
70. Bartosova M, Parkkila S, Pohlodek K, Karttunen TJ, Galbavy S, Mucha V, Harris AL, Pastorek J, Pastorekova S: Expression of carbonic anhydrase IX in breast is associated with malignant tissues and is related to overexpression of c-erbB2. The Journal of pathology 2002, 197(3):314-321.
71. Chia SK, Wykoff CC, Watson PH, Han C, Leek RD, Pastorek J, Gatter KC, Ratcliffe P, Harris AL: Prognostic significance of a novel hypoxia-regulated marker, carbonic anhydrase IX, in invasive breast carcinoma. Journal of clinical oncology : official journal of the American Society of Clinical Oncology 2001, 19(16):3660-3668.
72. Jang SM, Han H, Jang KS, Jun YJ, Jang SH, Min KW, Chung MS, Paik SS: The Glycolytic Phenotype is Correlated with Aggressiveness and Poor Prognosis in Invasive Ductal Carcinomas. Journal of breast cancer 2012, 15(2):172-180.
73. Carvalho KC, Cunha IW, Rocha RM, Ayala FR, Cajaiba MM, Begnami MD, Vilela RS, Paiva GR, Andrade RG, Soares FA: GLUT1 expression in malignant tumors and its use as an immunodiagnostic marker. Clinics 2011, 66(6):965-972.
74. Hussein YR, Bandyopadhyay S, Semaan A, Ahmed Q, Albashiti B, Jazaerly T, Nahleh Z, Ali-Fehmi R: Glut-1 Expression Correlates with Basal-like Breast Cancer. Translational oncology 2011, 4(6):321-327.
75. Airley R, Evans A, Mobasheri A, Hewitt SM: Glucose transporter Glut-1 is detectable in peri-necrotic regions in many human tumor types but not normal tis

sues: Study using tissue microarrays. Annals of anatomy = Anatomischer Anzeiger : official organ of the Anatomische Gesellschaft 2010, 192(3):133-138.
76. Koda M, Kanczuga-Koda L, Sulkowska M, Surmacz E, Sulkowski S: Relationships between hypoxia markers and the leptin system, estrogen receptors in human primary and metastatic breast cancer: effects of preoperative chemotherapy. BMC cancer 2010, 10:320.
77. Koo JS, Jung W: Alteration of REDD1-mediated mammalian target of rapamycin pathway and hypoxia-inducible factor-1alpha regulation in human breast cancer. Pathobiology : journal of immunopathology, molecular and cellular biology 2010, 77(6):289-300.
78. Schmidt M, Voelker HU, Kapp M, Krockenberger M, Dietl J, Kammerer U: Glycolytic phenotype in breast cancer: activation of Akt, up-regulation of GLUT1, TKTL1 and down-regulation of M2PK. Journal of cancer research and clinical oncology 2010, 136(2):219-225.
79. Godoy A, Ulloa V, Rodriguez F, Reinicke K, Yanez AJ, Garcia Mde L, Medina RA, Carrasco M, Barberis S, Castro T et al: Differential subcellular distribution of glucose transporters GLUT1-6 and GLUT9 in human cancer: ultrastructural localization of GLUT1 and GLUT5 in breast tumor tissues. Journal of cellular physiology 2006, 207(3):614-627.
80. Kuo SJ, Wu YC, Chen CP, Tseng HS, Chen DR: Expression of glucose transporter-1 in Taiwanese patients with breast carcinoma--a preliminary report. The Kaohsiung journal of medical sciences 2006, 22(7):339-345.
81. Stackhouse BL, Williams H, Berry P, Russell G, Thompson P, Winter JL, Kute T: Measurement of glut-1 expression using tissue microarrays to determine a race specific prognostic marker for breast cancer. Breast cancer research and treatment 2005, 93(3):247-253.
82. Laudanski P, Koda M, Kozlowski L, Swiatecka J, Wojtukiewicz M, Sulkowski S, Wolczynski S: Expression of glucose transporter GLUT-1 and estrogen receptors ER-alpha and ER-beta in human breast cancer. Neoplasma 2004, 51(3):164-168.
83. Ravazoula P, Batistatou A, Aletra C, Ladopoulos J, Kourounis G, Tzigounis B: Immunohistochemical expression of glucose transporter Glut1 and cyclin D1 in breast carcinomas with negative lymph nodes. European journal of gynaecological oncology 2003, 24(6):544-546.
84. Bos R, van der Hoeven JJ, van der Wall E, van der Groep P, van Diest PJ, Comans EF, Joshi U, Semenza GL, Hoekstra OS, Lammertsma AA et al: Biologic correlates of (18)fluorodeoxyglucose uptake in human breast cancer measured by positron emission tomography. Journal of clinical oncology : official journal of the American Society of Clinical Oncology 2002, 20(2):379-387.
85. Brown RS, Goodman TM, Zasadny KR, Greenson JK, Wahl RL: Expression of hexokinase II and Glut-1 in untreated human breast cancer. Nuclear medicine and biology 2002, 29(4):443-453.
86. Kang SS, Chun YK, Hur MH, Lee HK, Kim YJ, Hong SR, Lee JH, Lee SG, Park YK: Clinical significance of glucose transporter 1 (GLUT1) expression in human breast carcinoma. Japanese journal of cancer research : Gann 2002, 93(10):1123-1128.
87. Alo PL, Visca P, Botti C, Galati GM, Sebastiani V, Andreano T, Di Tondo U, Pizer ES: Immunohistochemical expression of human erythrocyte glucose transporter and fatty acid synthase in infiltrating breast carcinomas and adjacent typical/atypical hyperplastic or normal breast tissue. American journal of clinical pathology 2001, 116(1):129-134.
88. Avril N, Menzel M, Dose J, Schelling M, Weber W, Janicke F, Nathrath W, Schwaiger M: Glucose metabolism of breast cancer assessed by 18F-FDG PET: histologic and immunohistochemical tissue analysis. Journal of nuclear medicine:

official publication, Society of Nuclear Medicine 2001, 42(1):9-16.
89. Binder C, Binder L, Marx D, Schauer A, Hiddemann W: Deregulated simultaneous expression of multiple glucose transporter isoforms in malignant cells and tissues. Anticancer research 1997, 17(6D):4299-4304.
90. Younes M, Brown RW, Mody DR, Fernandez L, Laucirica R: GLUT1 expression in human breast carcinoma: correlation with known prognostic markers. Anticancer research 1995, 15(6B):2895-2898.
91. Brown RS, Wahl RL: Overexpression of Glut-1 glucose transporter in human breast cancer. An immunohistochemical study. Cancer 1993, 72(10):2979-2985.
92. Huang S, Ouyang N, Lin L, Chen L, Wu W, Su F, Yao Y, Yao H: HGF-induced PKCzeta activation increases functional CXCR4 expression in human breast cancer cells. PloS one 2012, 7(1):e29124.
93. Jin F, Brockmeier U, Otterbach F, Metzen E: New insight into the SDF-1/CXCR4 axis in a breast carcinoma model: hypoxia-induced endothelial SDF-1 and tumor cell CXCR4 are required for tumor cell intravasation. Molecular cancer research : MCR 2012, 10(8):1021-1031.
94. Ibrahim T, Sacanna E, Gaudio M, Mercatali L, Scarpi E, Zoli W, Serra P, Ricci R, Serra L, Kang Y et al: Role of RANK, RANKL, OPG, and CXCR4 tissue markers in predicting bone metastases in breast cancer patients. Clinical breast cancer 2011, 11(6):369-375.
95. Sacanna E, Ibrahim T, Gaudio M, Mercatali L, Scarpi E, Zoli W, Serra P, Bravaccini S, Ricci R, Serra L et al: The role of CXCR4 in the prediction of bone metastases from breast cancer: a pilot study. Oncology 2011, 80(3-4):225-231.
96. Bohn OL, Nasir I, Brufsky A, Tseng GC, Bhargava R, MacManus K, Chivukula M: Biomarker profile in breast carcinomas presenting with bone metastasis. International journal of clinical and experimental pathology 2009, 3(2):139-146.
97. Kobayashi T, Tsuda H, Moriya T, Yamasaki T, Kikuchi R, Ueda S, Omata J, Yamamoto J, Matsubara O: Expression pattern of stromal cell-derived factor-1 chemokine in invasive breast cancer is correlated with estrogen receptor status and patient prognosis. Breast cancer research and treatment 2010, 123(3):733-745.
98. Liu Y, Ji R, Li J, Gu Q, Zhao X, Sun T, Wang J, Du Q, Sun B: Correlation effect of EGFR and CXCR4 and CCR7 chemokine receptors in predicting breast cancer metastasis and prognosis. Journal of experimental & clinical cancer research : CR 2010, 29:16.
99. Andre F, Xia W, Conforti R, Wei Y, Boulet T, Tomasic G, Spielmann M, Zoubir M, Berrada N, Arriagada R et al: CXCR4 expression in early breast cancer and risk of distant recurrence. The oncologist 2009, 14(12):1182-1188.
100. Cabioglu N, Sahin AA, Morandi P, Meric-Bernstam F, Islam R, Lin HY, Bucana CD, Gonzalez-Angulo AM, Hortobagyi GN, Cristofanilli M: Chemokine receptors in advanced breast cancer: differential expression in metastatic disease sites with diagnostic and therapeutic implications. Annals of oncology : official journal of the European Society for Medical Oncology / ESMO 2009, 20(6):1013-1019.
101. Hassan S, Ferrario C, Saragovi U, Quenneville L, Gaboury L, Baccarelli A, Salvucci O, Basik M: The influence of tumor-host interactions in the stromal cell-derived factor-1/CXCR4 ligand/receptor axis in determining metastatic risk in breast cancer. The American journal of pathology 2009, 175(1):66-73.
102. Kim J-O, Suh K-S, Lee D-H, Sul H-J, Lee J-U, Song K-S: Expression of CXCR4 and SDF-1α in Primary Breast Cancers and Metastatic Lymph Nodes. Journal of breast cancer 2009, 12(4):249-256.
103. Liu F, Lang R, Wei J, Fan Y, Cui L, Gu F, Guo X, Pringle GA, Zhang X, Fu L: Increased expression of SDF-1/CXCR4 is associated with lymph node metastasis of invasive micropapillary carcinoma of the breast. Histopathology 2009, 54(6):741-

750.
104. Yasuoka H, Kodama R, Tsujimoto M, Yoshidome K, Akamatsu H, Nakahara M, Inagaki M, Sanke T, Nakamura Y: Neuropilin-2 expression in breast cancer: correlation with lymph node metastasis, poor prognosis, and regulation of CXCR4 expression. BMC cancer 2009, 9:220.
105. Zhou W, Jiang Z, Liu N, Xu F, Wen P, Liu Y, Zhong W, Song X, Chang X, Zhang X et al: Down-regulation of CXCL12 mRNA expression by promoter hypermethylation and its association with metastatic progression in human breast carcinomas. Journal of cancer research and clinical oncology 2009, 135(1):91-102.
106. Blot E, Laberge-Le Couteulx S, Jamali H, Cornic M, Guillemet C, Duval C, Hellot MF, Pille JY, Picquenot JM, Veyret C: CXCR4 membrane expression in node-negative breast cancer. The breast journal 2008, 14(3):268-274.
107. Fujii T, Kawahara A, Basaki Y, Hattori S, Nakashima K, Nakano K, Shirouzu K, Kohno K, Yanagawa T, Yamana H et al: Expression of HER2 and estrogen receptor alpha depends upon nuclear localization of Y-box binding protein-1 in human breast cancers. Cancer research 2008, 68(5):1504-1512.
108. Woo SU, Bae JW, Kim CH, Lee JB, Koo BW: A significant correlation between nuclear CXCR4 expression and axillary lymph node metastasis in hormonal receptor negative breast cancer. Annals of surgical oncology 2008, 15(1):281-285.
109. Yasuoka H, Tsujimoto M, Yoshidome K, Nakahara M, Kodama R, Sanke T, Nakamura Y: Cytoplasmic CXCR4 expression in breast cancer: induction by nitric oxide and correlation with lymph node metastasis and poor prognosis. BMC cancer 2008, 8:340.
110. Hao L, Zhang C, Qiu Y, Wang L, Luo Y, Jin M, Zhang Y, Guo TB, Matsushima K: Recombination of CXCR4, VEGF, and MMP-9 predicting lymph node metastasis in human breast cancer. Cancer letters 2007, 253(1):34-42.
111. Tsoli E, Tsantoulis PK, Papalambros A, Perunovic B, England D, Rawlands DA, Reynolds GM, Vlachodimitropoulos D, Morgan SL, Spiliopoulou CA et al: Simultaneous evaluation of maspin and CXCR4 in patients with breast cancer. Journal of clinical pathology 2007, 60(3):261-266.
112. Andre F, Cabioglu N, Assi H, Sabourin JC, Delaloge S, Sahin A, Broglio K, Spano JP, Combadiere C, Bucana C et al: Expression of chemokine receptors predicts the site of metastatic relapse in patients with axillary node positive primary breast cancer. Annals of oncology : official journal of the European Society for Medical Oncology / ESMO 2006, 17(6):945-951.
113. Kim R, Arihiro K, Emi M, Tanabe K, Osaki A: Potential role of HER-2; in primary breast tumor with bone metastasis. Oncology reports 2006, 15(6):1477-1484.
114. Salvucci O, Bouchard A, Baccarelli A, Deschenes J, Sauter G, Simon R, Bianchi R, Basik M: The role of CXCR4 receptor expression in breast cancer: a large tissue microarray study. Breast cancer research and treatment 2006, 97(3):275-283.
115. Shim H, Lau SK, Devi S, Yoon Y, Cho HT, Liang Z: Lower expression of CXCR4 in lymph node metastases than in primary breast cancers: potential regulation by ligand-dependent degradation and HIF-1alpha. Biochemical and biophysical research communications 2006, 346(1):252-258.
116. Su YC, Wu MT, Huang CJ, Hou MF, Yang SF, Chai CY: Expression of CXCR4 is associated with axillary lymph node status in patients with early breast cancer. Breast 2006, 15(4):533-539.
117. Cabioglu N, Sahin A, Doucet M, Yavuz E, Igci A, E OY, Aktas E, Bilgic S, Kiran B, Deniz G et al: Chemokine receptor CXCR4 expression in breast cancer as a potential predictive marker of isolated tumor cells in bone marrow. Clinical & experimental metastasis 2005, 22(1):39-46.
118. Cabioglu N, Yazici MS, Arun B, Broglio KR, Hortobagyi GN, Price JE, Sahin A:

CCR7 and CXCR4 as novel biomarkers predicting axillary lymph node metastasis in T1 breast cancer. Clinical cancer research : an official journal of the American Association for Cancer Research 2005, 11(16):5686-5693.
119. Li YM, Pan Y, Wei Y, Cheng X, Zhou BP, Tan M, Zhou X, Xia W, Hortobagyi GN, Yu D et al: Upregulation of CXCR4 is essential for HER2-mediated tumor metastasis. Cancer cell 2004, 6(5):459-469.
120. Schmid BC, Rudas M, Rezniczek GA, Leodolter S, Zeillinger R: CXCR4 is expressed in ductal carcinoma in situ of the breast and in atypical ductal hyperplasia. Breast cancer research and treatment 2004, 84(3):247-250.
121. Kato M, Kitayama J, Kazama S, Nagawa H: Expression pattern of CXC chemokine receptor-4 is correlated with lymph node metastasis in human invasive ductal carcinoma. Breast cancer research : BCR 2003, 5(5):R144-150.
122. Gallardo A, Lerma E, Escuin D, Tibau A, Munoz J, Ojeda B, Barnadas A, Adrover E, Sanchez-Tejada L, Giner D et al: Increased signalling of EGFR and IGF1R, and deregulation of PTEN/PI3K/Akt pathway are related with trastuzumab resistance in HER2 breast carcinomas. British journal of cancer 2012, 106(8):1367-1373.
123. Fu P, Ibusuki M, Yamamoto Y, Yamamoto S, Fujiwara S, Murakami K, Zheng S, Iwase H: Quantitative determination of insulin-like growth factor 1 receptor mRNA in formalin-fixed paraffin-embedded tissues of invasive breast cancer. Breast cancer 2012, 19(4):321-328.
124. Iqbal J, Thike AA, Cheok PY, Tse GM, Tan PH: Insulin growth factor receptor-1 expression and loss of PTEN protein predict early recurrence in triple-negative breast cancer. Histopathology 2012, 61(4):652-659.
125. Kurebayashi J, Kanomata N, Shimo T, Yamashita T, Aogi K, Nishimura R, Shimizu C, Tsuda H, Moriya T, Sonoo H: Marked lymphovascular invasion, progesterone receptor negativity, and high Ki67 labeling index predict poor outcome in breast cancer patients treated with endocrine therapy alone. Breast cancer 2012.
126. Taromaru GC, VM DEO, Silva MA, Montor WR, Bagnoli F, Rinaldi JF, Aoki T: Interaction between cyclooxygenase-2 and insulin-like growth factor in breast cancer: A new field for prevention and treatment. Oncology letters 2012, 3(3):682-688.
127. Yerushalmi R, Gelmon KA, Leung S, Gao D, Cheang M, Pollak M, Turashvili G, Gilks BC, Kennecke H: Insulin-like growth factor receptor (IGF-1R) in breast cancer subtypes. Breast cancer research and treatment 2012, 132(1):131-142.
128. Bhargava R, Beriwal S, McManus K, Dabbs DJ: Insulin-like growth factor receptor-1 (IGF-1R) expression in normal breast, proliferative breast lesions, and breast carcinoma. Applied immunohistochemistry & molecular morphology : AIMM / official publication of the Society for Applied Immunohistochemistry 2011, 19(3):218-225.
129. Drury SC, Detre S, Leary A, Salter J, Reis-Filho J, Barbashina V, Marchio C, Lopez-Knowles E, Ghazoui Z, Habben K et al: Changes in breast cancer biomarkers in the IGF1R/PI3K pathway in recurrent breast cancer after tamoxifen treatment. Endocrine-related cancer 2011, 18(5):565-577.
130. Fu P, Ibusuki M, Yamamoto Y, Hayashi M, Murakami K, Zheng S, Iwase H: Insulin-like growth factor-1 receptor gene expression is associated with survival in breast cancer: a comprehensive analysis of gene copy number, mRNA and protein expression. Breast cancer research and treatment 2011, 130(1):307-317.
131. Hartog H, Horlings HM, van der Vegt B, Kreike B, Ajouaou A, van de Vijver MJ, Marike Boezen H, de Bock GH, van der Graaf WT, Wesseling J: Divergent effects of insulin-like growth factor-1 receptor expression on prognosis of estrogen receptor positive versus triple negative invasive ductal breast carcinoma. Breast cancer research and treatment 2011, 129(3):725-736.

132. Peiro G, Adrover E, Sanchez-Tejada L, Lerma E, Planelles M, Sanchez-Paya J, Aranda FI, Giner D, Gutierrez-Avino FJ: Increased insulin-like growth factor-1 receptor mRNA expression predicts poor survival in immunophenotypes of early breast carcinoma. Modern pathology : an official journal of the United States and Canadian Academy of Pathology, Inc 2011, 24(2):201-208.
133. Tamimi RM, Colditz GA, Wang Y, Collins LC, Hu R, Rosner B, Irie HY, Connolly JL, Schnitt SJ: Expression of IGF1R in normal breast tissue and subsequent risk of breast cancer. Breast cancer research and treatment 2011, 128(1):243-250.
134. Kim JH, Cho YH, Park YL, Sohn JH, Kim HS: Prognostic significance of insulin growth factor-I receptor and insulin growth factor binding protein-3 expression in primary breast cancer. Oncology reports 2010, 23(4):989-995.
135. Sircoulomb F, Bekhouche I, Finetti P, Adelaide J, Ben Hamida A, Bonansea J, Raynaud S, Innocenti C, Charafe-Jauffret E, Tarpin C et al: Genome profiling of ERBB2-amplified breast cancers. BMC cancer 2010, 10:539.
136. Taunk NK, Goyal S, Moran MS, Yang Q, Parikh R, Haffty BG: Prognostic significance of IGF-1R expression in patients treated with breast-conserving surgery and radiation therapy. Radiotherapy and oncology : journal of the European Society for Therapeutic Radiology and Oncology 2010, 96(2):204-208.
137. Chen C, Zhou Z, Sheehan CE, Slodkowska E, Sheehan CB, Boguniewicz A, Ross JS: Overexpression of WWP1 is associated with the estrogen receptor and insulin-like growth factor receptor 1 in breast carcinoma. International journal of cancer Journal international du cancer 2009, 124(12):2829-2836.
138. Henriksen KL, Rasmussen BB, Lykkesfeldt AE, Moller S, Ejlertsen B, Mouridsen HT: An ER activity profile including ER, PR, Bcl-2 and IGF-IR may have potential as selection criterion for letrozole or tamoxifen treatment of patients with advanced breast cancer. Acta oncologica 2009, 48(4):522-531.
139. Peiro G, Benlloch S, Sanchez-Tejada L, Adrover E, Lerma E, Peiro FM, Sanchez-Paya J, Aranda FI: Low activation of Insulin-like Growth Factor 1-Receptor (IGF1R) is associated with local recurrence in early breast carcinoma. Breast cancer research and treatment 2009, 117(2):433-441.
140. Law JH, Habibi G, Hu K, Masoudi H, Wang MY, Stratford AL, Park E, Gee JM, Finlay P, Jones HE et al: Phosphorylated insulin-like growth factor-i/insulin receptor is present in all breast cancer subtypes and is related to poor survival. Cancer research 2008, 68(24):10238-10246.
141. Sutandyo N, Suzanna E, Haryono SJ, Reksodiputro AH: Signaling pathways in early onset sporadic breast cancer of patients in Indonesia. Acta medica Indonesiana 2008, 40(3):139-145.
142. Zoubir M, Mathieu MC, Mazouni C, Liedtke C, Corley L, Geha S, Bouaziz J, Spielmann M, Drusche F, Symmans WF et al: Modulation of ER phosphorylation on serine 118 by endocrine therapy: a new surrogate marker for efficacy. Annals of oncology : official journal of the European Society for Medical Oncology / ESMO 2008, 19(8):1402-1406.
143. Henriksen KL, Rasmussen BB, Lykkesfeldt AE, Moller S, Ejlertsen B, Mouridsen HT: Semi-quantitative scoring of potentially predictive markers for endocrine treatment of breast cancer: a comparison between whole sections and tissue microarrays. Journal of clinical pathology 2007, 60(4):397-404.
144. Hudelist G, Wagner T, Rosner M, Fink-Retter A, Gschwantler-Kaulich D, Czerwenka K, Kroiss R, Tea M, Pischinger K, Kostler WJ et al: Intratumoral IGF-I protein expression is selectively upregulated in breast cancer patients with BRCA1/2 mutations. Endocrine-related cancer 2007, 14(4):1053-1062.
145. Lerma E, Peiro G, Ramon T, Fernandez S, Martinez D, Pons C, Munoz F, Sabate JM, Alonso C, Ojeda B et al: Immunohistochemical heterogeneity of breast

carcinomas negative for estrogen receptors, progesterone receptors and Her2/neu (basal-like breast carcinomas). Modern pathology : an official journal of the United States and Canadian Academy of Pathology, Inc 2007, 20(11):1200-1207.
146. Mulligan AM, O'Malley FP, Ennis M, Fantus IG, Goodwin PJ: Insulin receptor is an independent predictor of a favorable outcome in early stage breast cancer. Breast cancer research and treatment 2007, 106(1):39-47.
147. Chong YM, Williams SL, Elkak A, Sharma AK, Mokbel K: Insulin-like growth factor 1 (IGF-1) and its receptor mRNA levels in breast cancer and adjacent non-neoplastic tissue. Anticancer research 2006, 26(1A):167-173.
148. Kostler WJ, Hudelist G, Rabitsch W, Czerwenka K, Muller R, Singer CF, Zielinski CC: Insulin-like growth factor-1 receptor (IGF-1R) expression does not predict for resistance to trastuzumab-based treatment in patients with Her-2/neu overexpressing metastatic breast cancer. Journal of cancer research and clinical oncology 2006, 132(1):9-18.
149. Ueda S, Tsuda H, Sato K, Takeuchi H, Shigekawa T, Matsubara O, Hiraide H, Mochizuki H: Alternative tyrosine phosphorylation of signaling kinases according to hormone receptor status in breast cancer overexpressing the insulin-like growth factor receptor type 1. Cancer science 2006, 97(7):597-604.
150. Koda M, Przystupa W, Jarzabek K, Wincewicz A, Kanczuga-Koda L, Tomaszewski J, Sulkowska M, Wolczynski S, Sulkowski S: Expression of insulin-like growth factor-I receptor, estrogen receptor alpha, Bcl-2 and Bax proteins in human breast cancer. Oncology reports 2005, 14(1):93-98.
151. Nielsen TO, Andrews HN, Cheang M, Kucab JE, Hsu FD, Ragaz J, Gilks CB, Makretsov N, Bajdik CD, Brookes C et al: Expression of the insulin-like growth factor I receptor and urokinase plasminogen activator in breast cancer is associated with poor survival: potential for intervention with 17-allylamino geldanamycin. Cancer research 2004, 64(1):286-291.
152. Shimizu C, Hasegawa T, Tani Y, Takahashi F, Takeuchi M, Watanabe T, Ando M, Katsumata N, Fujiwara Y: Expression of insulin-like growth factor 1 receptor in primary breast cancer: immunohistochemical analysis. Human pathology 2004, 35(12):1537-1542.
153. Koda M, Sulkowski S, Garofalo C, Kanczuga-Koda L, Sulkowska M, Surmacz E: Expression of the insulin-like growth factor-I receptor in primary breast cancer and lymph node metastases: correlations with estrogen receptors alpha and beta. Hormone and metabolic research = Hormon- und Stoffwechselforschung = Hormones et metabolisme 2003, 35(11-12):794-801.
154. Ouban A, Muraca P, Yeatman T, Coppola D: Expression and distribution of insulin-like growth factor-1 receptor in human carcinomas. Human pathology 2003, 34(8):803-808.
155. Happerfield LC, Miles DW, Barnes DM, Thomsen LL, Smith P, Hanby A: The localization of the insulin-like growth factor receptor 1 (IGFR-1) in benign and malignant breast tissue. The Journal of pathology 1997, 183(4):412-417.
156. Turner BC, Haffty BG, Narayanan L, Yuan J, Havre PA, Gumbs AA, Kaplan L, Burgaud JL, Carter D, Baserga R et al: Insulin-like growth factor-I receptor overexpression mediates cellular radioresistance and local breast cancer recurrence after lumpectomy and radiation. Cancer research 1997, 57(15):3079-3083.
157. Klijn JG, Berns PM, Schmitz PI, Foekens JA: The clinical significance of epidermal growth factor receptor (EGF-R) in human breast cancer: a review on 5232 patients. Endocrine reviews 1992, 13(1):3-17.
158. Heider KH, Kuthan H, Stehle G, Munzert G: CD44v6: a target for antibody-based cancer therapy. Cancer immunology, immunotherapy : CII 2004, 53(7):567-579.
159. Menard S, Balsari A, Casalini P, Tagliabue E, Campiglio M, Bufalino R, Cascinelli

N: HER-2-positive breast carcinomas as a particular subset with peculiar clinical behaviors. Clinical cancer research : an official journal of the American Association for Cancer Research 2002, 8(2):520-525.
160. Urruticoechea A, Smith IE, Dowsett M: Proliferation marker Ki-67 in early breast cancer. Journal of clinical oncology : official journal of the American Society of Clinical Oncology 2005, 23(28):7212-7220.
161. Brahimi-Horn MC, Chiche J, Pouyssegur J: Hypoxia and cancer. Journal of molecular medicine 2007, 85(12):1301-1307.
162. Semenza GL: Targeting HIF-1 for cancer therapy. Nature reviews Cancer 2003, 3(10):721-732.
163. Ercan C, Vermeulen JF, Hoefnagel L, Bult P, van der Groep P, van der Wall E, van Diest PJ: HIF-1alpha and NOTCH signaling in ductal and lobular carcinomas of the breast. Cellular oncology 2012, 35(6):435-442.
164. van Diest PJ, Vleugel MM, van der Wall E: Expression of HIF-1alpha in human tumours. Journal of clinical pathology 2005, 58(3):335-336.
165. van Diest PJ, Vleugel MM, van der Groep P, van der Wall E: VEGF-D and HIF-1alpha in breast cancer. Journal of clinical pathology 2005, 58(3):335; author reply 336.
166. Zhang D, Salto-Tellez M, Putti TC, Do E, Koay ES: Reliability of tissue microarrays in detecting protein expression and gene amplification in breast cancer. Modern pathology : an official journal of the United States and Canadian Academy of Pathology, Inc 2003, 16(1):79-84.
167. Bleyer A, Welch HG: Effect of three decades of screening mammography on breast-cancer incidence. The New England journal of medicine 2012, 367(21):1998-2005.
168. Mook S, Van 't Veer LJ, Rutgers EJ, Ravdin PM, van de Velde AO, van Leeuwen FE, Visser O, Schmidt MK: Independent prognostic value of screen detection in invasive breast cancer. Journal of the National Cancer Institute 2011, 103(7):585-597.
169. Rakha EA, Reis-Filho JS, Baehner F, Dabbs DJ, Decker T, Eusebi V, Fox SB, Ichihara S, Jacquemier J, Lakhani SR et al: Breast cancer prognostic classification in the molecular era: the role of histological grade. Breast cancer research : BCR 2010, 12(4):207.
170. Luini A, Rososchansky J, Gatti G, Zurrida S, Caldarella P, Viale G, Rosali dos Santos G, Frasson A: The surgical margin status after breast-conserving surgery: discussion of an open issue. Breast cancer research and treatment 2009, 113(2):397-402.
171. Sakr RA, Poulet B, Kaufman GJ, Nos C, Clough KB: Clear margins for invasive lobular carcinoma: a surgical challenge. European journal of surgical oncology : the journal of the European Society of Surgical Oncology and the British Association of Surgical Oncology 2011, 37(4):350-356.
172. Dillon MF, Hill AD, Fleming FJ, O'Doherty A, Quinn CM, McDermott EW, O'Hig gins N: Identifying patients at risk of compromised margins following breast conservation for lobular carcinoma. American journal of surgery 2006, 191(2):201-205.
173. Takehara M, Tamura M, Kameda H, Ogita M: Examination of breast conserving therapy in lobular carcinoma. Breast cancer 2004, 11(1):69-72.
174. Moore MM, Borossa G, Imbrie JZ, Fechner RE, Harvey JA, Slingluff CL, Jr., Adams RB, Hanks JB: Association of infiltrating lobular carcinoma with positive surgical margins after breast-conservation therapy. Annals of surgery 2000, 231(6):877-882.
175. Hussien M, Lioe TF, Finnegan J, Spence RA: Surgical treatment for invasive lobular carcinoma of the breast. Breast 2003, 12(1):23-35.
176. Jacobs TW, Gown AM, Yaziji H, Barnes MJ, Schnitt SJ: Specificity of HercepTest in

determining HER-2/neu status of breast cancers using the United States Food and Drug Administration-approved scoring system. Journal of clinical oncology : offici al journal of the American Society of Clinical Oncology 1999, 17(7):1983-1987.
177. Amos KD, Adamo B, Anders CK: Triple-negative breast cancer: an update on neoadjuvant clinical trials. International journal of breast cancer 2012, 2012:385978.

Additional files

Jeroen F. Vermeulen, Aram S.A. van Brussel, Petra van der Groep, Folkert H.M. Morsink, Peter Bult, Elsken van der Wall and Paul J. van Diest

3

Immunophenotyping invasive breast cancer: paving the road for molecular imaging

Abstract

Background: Mammographic population screening in The Netherlands has increased the number of breast cancer patients with small and non-palpable breast tumors. Nevertheless, mammography is not ultimately sensitive and specific for distinct subtypes. Molecular imaging with targeted probes might increase specificity and sensitivity of detection. Because development of new probes is labor-intensive and costly, we searched for the smallest panel of tumor membrane markers that would allow detection of the wide spectrum of invasive breast cancers.
Methods: Tissue microarrays containing 483 invasive breast cancers were stained by immunohistochemistry for a selected set of membrane proteins known to be expressed in breast cancer.
Results: The combination of highly tumor-specific markers glucose transporter 1 (GLUT1), epidermal growth factor receptor (EGFR), insulin-like growth factor-1 receptor (IGF1-R), human epidermal growth factor receptor 2 (HER2), hepatocyte growth factor receptor (MET), and carbonic anhydrase 9 (CAIX) 'detected' 45.5% of tumors, especially basal/triple negative and HER2-driven ductal cancers. Addition of markers with a 2-fold tumor-to-normal ratio increased the detection rate to 98%. Including only markers with >3 fold tumor-to-normal ratio (CD44v6) resulted in an 80% detection rate. The detection rate of the panel containing both tumor-specific and less tumor-specific markers was not dependent on age, tumor grade, tumor size, or lymph node status.
Conclusions: In search of the minimal panel of targeted probes needed for the highest possible detection rate, we showed that 80% of all breast cancers express at least one of a panel of membrane markers (CD44v6, GLUT1, EGFR, HER2, and IGF1-R) that may therefore be suitable for molecular imaging strategies. This study thereby serves as a starting point for further development of a set of antibody-based optical probes with a high breast cancer detection rate.

Background

In The Netherlands, the lifetime risk to develop breast cancer increased in the last decades from 1 in 10 in 1989 to 1 in 7 in 2003 [1]. In parallel, the annual number of newly diagnosed cases of breast cancer rose to over 13,000 in 2008 [2]. This makes breast cancer the most commonly diagnosed female cancer in The Netherlands. Despite this increase in incidence, the number of deaths due to breast cancer has remained stable in the last decades, with annually around 3,300 deaths in The Netherlands in the period 1989–2008 [3]. Early detection by mammographic population screening has likely contributed to this, leading to diagnosis of smaller, often non-palpable breast cancers and ductal carcinoma in situ (DCIS) lesions [4,5]. Nevertheless, mammography is not optimally sensitive and specific, especially in younger patients and patients with dense breasts [6-11]. Ultrasonography and magnetic resonance imaging (MRI) have been shown to contribute to early detection of breast cancer, as has positron emission tomography (PET) imaging, but these three imaging devices also have their limitations [12].

Optical molecular imaging with near-infrared fluorescent (NIRF) probes holds promise here [13]. First, the spectral properties (emission wavelengths between 700–900 nm) of the fluorescent tracers result in low background (auto)fluorescence [14]. Second, the detection can be highly sensitive and specific and third, it enables to detect tumors up to centimeters deep in tissue [15]. Fourth, no protective measures are required since no ionizing radiation is emitted [16], and fifth, NIRF probes can be conjugated to highly specific targeted molecules such as antibodies, antibody fragments, peptides, or protease activatable substrates to increase the specificity of the signal in the tumor as reviewed by Pleijhuis et al. [17].

Several molecular targets have been suggested to be suitable for optical detection of breast cancer such as the epidermal growth factor receptor (EGFR) [18], vascular endothelial growth factor (VEGF) [13,19], and HER2 [20,21]. In addition, hypoxia up-regulated surface antigens like glucose transporter 1 (GLUT1) and carbonic anhydrase 9 (CAIX) that are expressed in about half of invasive breast cancers [22]

and also in DCIS [23] and therefore might be valuable targets. Since NIRF antibodies will not be easily internalized, intracellular molecular targets relevant for optical detection of breast cancer have so far been ignored.
However, no single molecular target is expressed in all invasive breast cancers and at the same time provides adequate signal-to-noise ratio to the normal breast. For screening purposes a panel of probes, i.e. antibodies or antibody fragments will likely be necessary. Because development of such antibody-based probes is labor intensive and costly, we set out to screen for expression of a selected set of candidate targets on tissue microarrays containing 483 cases of human invasive breast cancer, in search of the minimum antibody panel that would be suitable for detection of most breast cancers *in vivo* by molecular imaging.

Methods

Patients

The study population was derived from the archives of the Departments of Pathology of the University Medical Center Utrecht, Utrecht, and the Radboud University Nijmegen Medical Centre, Nijmegen, The Netherlands. These comprised 483 cases of invasive breast cancer (operated between 1997 and 2007), of which 340 cases were part of a consecutive series (operated between 2003–2007). The series was enriched with a small consecutive series of lobular breast cancers and a consecutive series of 23 cases with a BRCA germline mutation as previously described [24]. Histological grade was assessed according to the Nottingham scheme [25], and mitotic activity index (MAI) was assessed as before [26]. From representative donor paraffin blocks of the primary tumors, tissue microarrays were constructed by transferring tissue cylinders of 0.6 mm (3 cylinders per tumor) from the tumor area, determined by a pathologist based on haematoxylin and eosin stained slides, using a tissue arrayer (Beecher Instruments, Sun Prairie, WI, USA) as described before [27]. Normal breast tissue was obtained from patients that underwent mammoplasty (and thus had no tumor at all). In case of matched tumor and normal tissue, we analyzed normal tissue in paraffin blocks that did not contain any tumor and thus were far away from the tumor. The use of anonymous or coded left over material for scientific purposes is part of the standard treatment contract with patients in The Netherlands [28]. Ethical approval was not required.

Immunohistochemistry

Immunohistochemistry was carried out on 4 μm thick sections for a panel of potential molecular membrane bound targets known to be expressed in a frequency of >10% in breast cancer. These were partly highly tumor-specific, meaning that they have no or low intensity staining of the normal breast tissue (GLUT1, EGFR, insulin-like growth factor-1 receptor (IGF-1R), HER2, CAIX, hepatocyte growth factor receptor (MET)). We also included less tumor-specific, meaning that are known to have moderate or high intensity staining of the normal breast tissue (mucin 1

(MUC1), CD44v6, mammaglobin, transferrin receptor (TfR), carbonic anhydrase 12 (CAXII)), since cancers have usually increased cellularity compared to the normal breast and could thereby also provide adequate signal-to-noise in tumors compared to the normal breast.

After deparaffination and rehydration, endogenous peroxidase activity was blocked for 15 min in a buffer solution pH 5.8 containing 0.3% hydrogen peroxide. After antigen retrieval, i.e. boiling for 20 min in 10 mM citrate pH 6.0 (for progesterone receptor (PR), CD44v6, GLUT1, CAIX, MET, TfR, and CAXII), tris/EDTA pH 9.0 (estrogen receptor α (ERα), HER2, IGF1-R, MUC1, and mammaglobin) or Prot K (0.15 mg/ml) for 5 min at room temperature (EGFR), a cooling off period of 30 min preceded the primary antibody incubation. CD44v6 (clone VFF18, BMS125 Bender MedSystems, Austria) 1:500; ERα (clone ID5, DAKO, Glostrup, Denmark) 1:200; PR (clone PgR636, DAKO) 1:100; HER2 (SP3, Neomarkers, Duiven, The Netherlands) 1:100; GLUT1 (A3536, DAKO) 1:200; CAIX (ab15086, Abcam, Cambridge, UK) 1:1,000; IGF1-R (NB110-87052, Novus Biologicals, Cambridge, UK) 1:400; TfR (13–6800, Invitrogen, Breda, The Netherlands) 1:300; MUC1 (EMA, M1613 clone E29, DAKO) 1:400; mammaglobin (clone 304-1A5, DAKO) 1:100; CAXII (HPA008773, Sigma Aldrich, Zwijndrecht, The Netherlands) 1:200 were incubated for 1h at room temperature. Primary antibodies against EGFR (clone 31 G7, Zymed, Invitrogen) 1:30; MET (18–2257, Zymed, Invitrogen) 1:100 were incubated overnight at 4°C. All primary antibodies were diluted in PBS containing 1% BSA.

The signal was amplified using Powervision poly-HRP anti-mouse, rabbit, rat (DPVO-HRP, Immunologic, Duiven, The Netherlands) or the Novolink kit (Leica, Rijswijk, The Netherlands) (in the case of EGFR) and developed with diaminobenzidine, followed by counterstaining with haematoxylin, dehydration in alcohol and mounting.

Scoring of immunohistochemistry

All stainings were compared to normal breast tissue and scored as positive when a clear membranous staining was seen and when the expression in the tumor was clearly higher than in the normal breast tissue. All stainings were scored using the DAKO/HER2 scoring system for membranous staining. Scores 2+ and 3+ were

considered as positive except for HER2 where only a score of 3+ was considered positive. Due to the strong intratumor heterogeneity of mammaglobin expression, scoring was performed by estimating the percentage of positive tumor cells, considering cancers with more than 35% of the membrane stained tumor cells as positive. All scoring was done by a single experienced pathologist (PJvD) who was blinded to patient characteristics and results of other stainings. To take tumor-heterogeneity between the tumor cores into account, the average score per tumor was calculated and used for analyses. Only in case of GLUT1 and CAIX, the tumor was classified as positive when a single core showed positivity. In this study a maximum of 3 missing stainings per patient was allowed, these stainings were considered as negative in the analyses. This potentially results in underestimation of the percentage positivity of a marker.

Based on ERα, PR, and HER2 immunohistochemistry, tumors were classified as luminal (ERα and/or PR positive), HER2-driven (ERα-, PR-, HER2+), triple negative (ERα-, PR-, HER2-) or basal (ERα-, PR-, HER2-, EGFR+), the immunohistochemical surrogate [29] of the original Sorlie/Perou classification [30].

Immunofluorescence for quantification of protein expression in tumor and normal breast tissue

Several of the evaluated molecular membrane targets (CD44v6, MUC1, TfR, mammaglobin, and CAXII) are known to be expressed to some extent in the normal breast epithelium. In order for these targets to be useful for breast cancer screening by optical imaging, the signal to background ratio needs to be high enough to be discriminative. We therefore performed immunofluorescence with these antibodies to allow quantification of expression ratios between normal breast and cancer tissue of four randomly selected patients by image analysis.

Immunofluorescence was performed as described above for immunohistochemistry, except that the primary antibodies were detected by incubation with Goat-anti-mouse/rabbit Alexa555 (1:1,000, Invitrogen) for 1h at room temperature, followed by 4,6-Diamidine-2-phenylindole dihydrochloride (DAPI) counterstaining and mounting with Immumount (Thermo Scientific, Etten-Leur, The Netherlands). Representative images of normal breast and breast cancers from the same sections

were taken using identical settings at 20x magnification using a Leica DMI4000b inverted bright-field/fluorescence microscope.

Image analysis of tumor expression versus normal breast tissue

Conventional immunohistochemical slides were digitalized for image analysis using a digital slide scanner (Aperio Technologies Inc., Vista, CA, USA). Of each patient four representative areas of normal and tumor tissue were selected and the average membrane intensity was calculated with the IHC membrane algorithm (Aperio, v8.001). As the signal-to-noise ratio *in vivo* is determined by the difference in expression between cancer and normal cells as well as by cellularity, the number of cells in the selected area was obtained from the algorithm. Tumor-to-normal ratio was calculated as (membrane intensity x cellularity/area) of the tumor/(membrane intensity x cellularity/area) of normal tissue.

Tumor-to-normal ratios of the fluorescently labeled antibodies were calculated with ImageJ using the median intensity scores. Values are expressed as the average tumor/normal ratio ± SEM.

Based on experience in radiology with the blood-pool agent indocyanine green in studies assuming a leaky vessel model [31,32], and from studies using NIRF labeled trastuzumab/bevacizumab in mouse models [33], a tumor-to-normal ratio larger than 3 was considered to be sufficient for optical imaging.

Statistics

Statistical analysis was performed using IBM SPSS Statistics version 18.0 (SPSS Inc., Chicago, IL, USA). Associations between categorical variables were examined using the Pearson's Chi-square test. P-values <0.05 were considered to be statistically significant.

Results

To investigate the most promising combination of markers suitable for imaging, we studied the expression of a panel of membrane markers in our study population that comprised 319 (66.0%) invasive ductal, 126 (26.1%) invasive lobular, and 38 (7.9%) invasive breast cancers with other histology. Other clinicopathological characteristics are shown in Table 1.

Feature	**Grouping**	**N or value**	%
Age (years)	Mean	60	
	Range	28 to 88	
Histological type	Invasive ductal cancer	319	66.0
	Invasive lobular cancer	126	26.1
	Others	38	7.9
Tumor size (cm)	≤2	206	42.7
	>2 and ≤5	219	45.3
	>5	49	10.1
	Not available	9	1.9
Histological grade	1	89	18.4
	2	169	35.0
	3	219	45.4
	Not available	6	1.2
Lymph node status	Negative *	225	46.6
	Positive **	232	48.0
	Not available	26	5.4

Table 1: Clinicopathological characteristics of 483 invasive breast cancer patients studied for expression of selected membrane markers.
*: negative = N0 or N0(i+); **: positive = ≥N1mi (according to TNM 7th edition, 2010)

Representative pictures of immunohistochemistry for the highly tumor-specific molecular membrane targets are shown in Figure 1A. The most widely expressed tumor-specific protein in our cohort was GLUT1, positive in 20.3% of the cancers, followed by EGFR (17.4%), IGF-1R (12.8%), HER2 (10.4%), CAIX (9.5%), and MET (8.9%). The less tumor-specific targets MUC1 (90.7%), CD44v6 (63.8%), mammaglobin (16.8%), TfR (14.5%), and CAXII (8.7%) were in general more frequently expressed than the tumor-specific targets (Table 2). Representative pictures of immunohistochemistry for the less tumor-specific molecular membrane targets are shown in Figure 1B.

Staining	Positive		Negative		Missing	
	N	%	N	%	N	%
HER2	50	10.4	432	89.4	1	0.2
EGFR	84	17.4	395	81.8	4	0.8
c-MET	43	8.9	423	87.6	17	3.5
IGF1-R	62	12.8	400	82.8	21	4.3
GLUT1	98	20.3	360	74.5	25	5.2
CAIX	46	9.5	414	85.3	25	5.2
TfR	70	14.5	402	83.2	11	2.3
CD44v6	308	63.8	160	33.1	15	3.1
CAXII	42	8.7	426	88.2	15	3.1
Mammaglobin	81	16.8	382	79.1	20	4.1
MUC1	438	90.7	26	5.4	19	3.9

Table 2: Frequency of expression of tumor-specific and less tumor-specific membrane markers in invasive breast cancers.

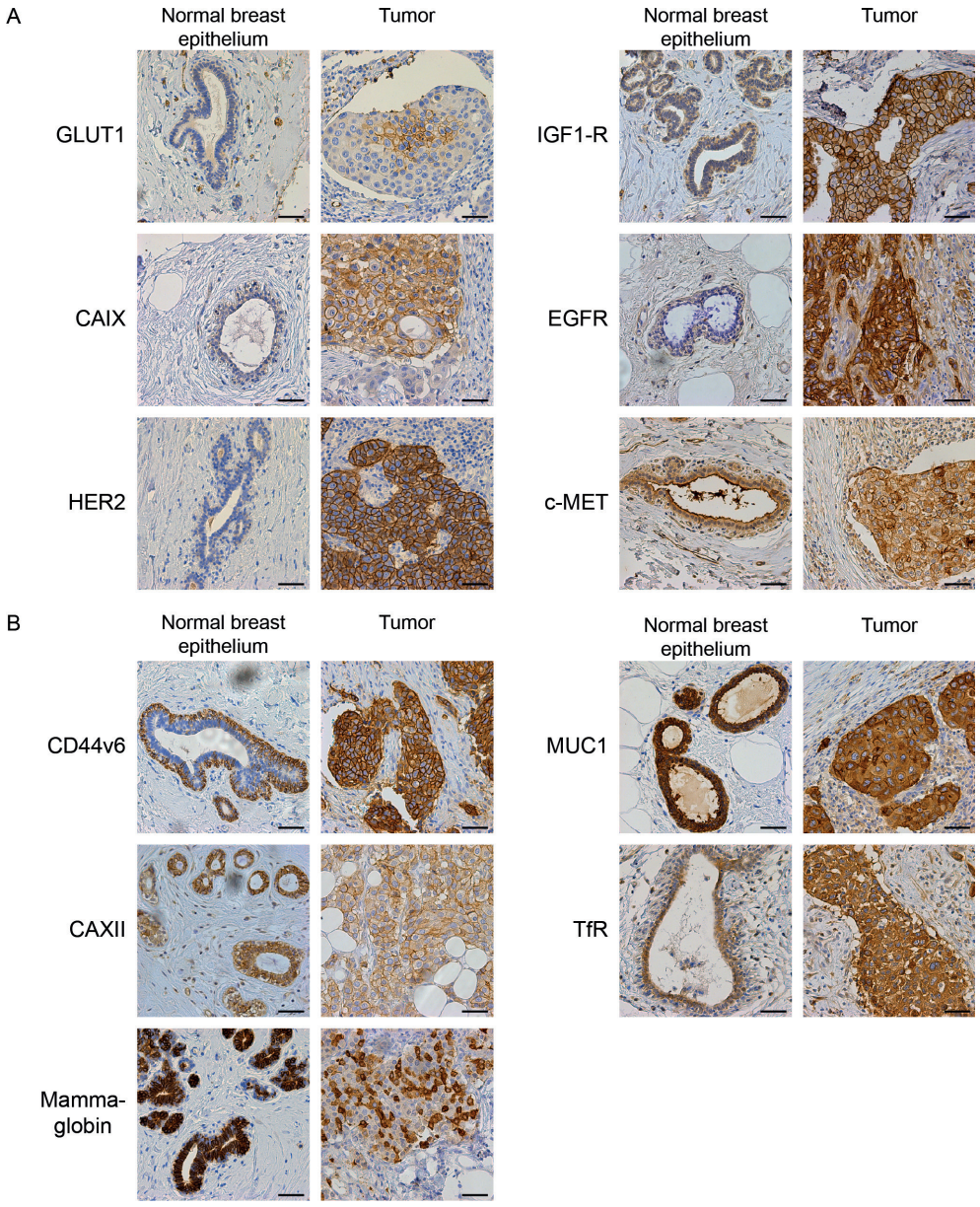

Figure 1: Membrane marker expression in normal breast epithelium and breast cancer. Images of representative breast cancer cases with the corresponding normal breast epithelium that were scored as positive. A. Expression of tumor-specific markers with low or no expression in normal breast epithelium. B. Expression of membrane markers that are also expressed in normal breast tissue. The intensity in the normal breast epithelium was classified as moderate or high. Size bar equals 50 μm.

Detection rate of combinations of highly tumor-specific molecular targets in relation to grade, molecular and histological type

Because the frequency of expression (further denoted 'detection rate') of individual highly tumor-specific markers did not exceed 20.3% of the cases, we examined several combinations of markers by sequential addition of markers to the expression of GLUT1, the most widely expressed highly tumor-specific marker. GLUT1 in combination with EGFR resulted in 30.0% positive cases, GLUT1/IGF1-R in 28.8%, GLUT1/HER2 in 27.7%, GLUT1/MET in 25.2%, and GLUT1/CAIX in 22.3% positive cases. The panel GLUT1, EGFR, HER2, IGF1-R, MET, and CAIX resulted in 45.5% positive cases, although the contribution of CAIX and MET was minimal (Figure 2A).

Clear differences were found between histological subtypes of breast cancer (Table 3). Lobular carcinomas hardly expressed any of the tumor-specific membrane targets present in the panel compared to ductal carcinomas (detection rate 18.3% vs. 55.5%, $p<0.001$).

Target	Ductal (319 cases)		Lobular (126 cases)		Other (38 cases)	
	N	%	N	%	N	%
HER2	43	13.5	4	3.2	3	7.9
EGFR	71	22.3	4	3.2	9	23.7
c-MET	34	10.7	4	3.2	5	13.2
IGF1-R	48	15.0	7	5.6	7	18.4
GLUT1	85	26.6	5	4.0	8	21.1
CAIX	38	11.9	2	1.6	6	15.8
TfR	53	16.6	10	7.9	7	18.4
CD44v6	197	61.8	82	65.1	29	76.3
CAXII	30	9.4	12	9.5	1	2.6
Mammaglobin	44	13.8	34	27.0	3	7.9
MUC1	218	88.1	119	94.4	38	100

Table 3: Expression of a panel of membrane markers in the histological types of breast cancer.

Within the group of lobular carcinomas, pleomorphic lobular carcinomas expressed more membrane targets than classical lobular carcinomas (detection rate 26.8% vs. 8.6%, p = 0.034). Within the group of ductal carcinomas, the basal/triple negative (TN) and HER2-driven ductal cancers expressed more frequently hypoxia markers or growth factor receptors than luminal-type ductal cancers (detection rate 84.2% vs. 45.0%, p<0.001) (Table 4). Therefore the panel EGFR, MET, HER2, GLUT1, CAIX, and IGF1-R detected 84.2% of the basal/TN ductal breast cancers compared to 45.0% of the luminal-type, and 18.3% of the lobular breast cancer cases (Figure 2A, Tables 3 and 4). Because the markers included in our panel are associated with an aggressive phenotype and poor prognosis, we evaluated the detection rate of our panel in relation to grade (Figure 2B). Low grade (grade 1) tumors had a detection rate of 22.5% for this panel, in contrast to 33.7% of grade 2 and 63.9% of grade 3 tumors (p<0.001). This indicates that the panel with tumor-specific antigens is less sensitive for detecting luminal-type, lobular, and low grade/well-differentiated tumors when applied for imaging strategies.

Target	**Luminal (242 cases)**		**HER2-driven (20 cases)**		**Basal/ TN (57 cases)**	
	N	%	**N**	%	**N**	%
HER2	23	9.5	20	100	0	0.0
EGFR	25	10.3	11	55	35	61.4
c-MET	21	8.7	4	20	9	15.8
IGF1-R	41	16.9	2	10	5	8.8
GLUT1	49	20.2	6	30	30	52.6
CAIX	11	4.5	4	20	23	40.4
TfR	33	13.6	5	25	40	70.2
CD44v6	148	61.8	9	45	15	26.3
CAXII	28	11.6	1	5	1	1.8
Mammaglobin	39	16.1	4	20	1	1.8
MUC1	213	88.0	20	100	48	84.2

Table 4: Expression of membrane markers in molecular subtypes of ductal breast cancer.

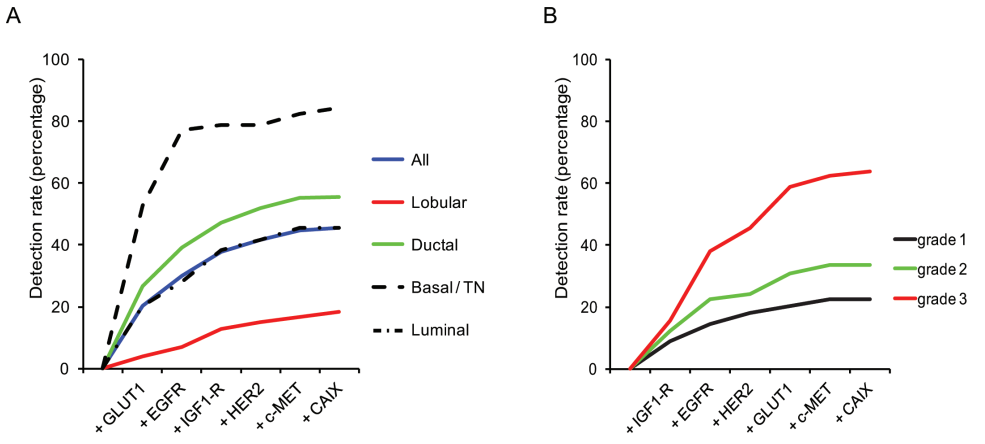

Figure 2: Detection rate of tumor-specific membrane markers for detection of breast cancer. Detection rate of highly tumor-specific membrane markers for detecting luminal, HER2-driven, basal/triple negative ductal breast cancers, and lobular breast cancers. The detection rate of tumor-specific markers for detection of breast cancer plotted as the positivity of the marker in combination with all preceding markers.

Molecular targets that are expressed in normal breast tissue have sufficient signal-to-noise to detect lobular and luminal-type breast cancer

Since lobular and luminal-types of breast cancer appeared to hardly express tumor-specific antigens, antigens that are less tumor-specific are required for their detection. Like with tumor-specific markers, variation between histological and molecular subtypes was observed for TfR, mammaglobin, and CAXII. Luminal-type ductal cancers and lobular cancers expressed significantly more CAXII (10.5% vs. 2.3%, $p = 0.017$) and mammaglobin (19.9% vs. 5.9%, $p = 0.002$) compared to HER2-driven and basal/TN ductal cancers (Tables 3 and 4). TfR expression in lobular and luminal type ductal cancers was significantly lower than in HER2-driven and basal/TN cancers (11.9% vs. 27.9%, $p<0.001$). For MUC1 and CD44v6, no differences in expression were found between lobular and ductal cancer (Tables 3 and 4).

Due to the expression of less tumor-specific antigens in the normal breast epithelium (Figure 1B), the signal-to-noise (or tumor-to-normal) ratio needs to be sufficiently discriminating to be applicable for imaging strategies. We determined therefore the tumor-to-normal ratio in a quantitative manner by image analysis of digital slides, considering a 3-fold tumor-to-normal ratio as sufficient. Image quantification using conventional IHC showed that the intensity of the staining was dependent on the cellularity of the tumor as expected. This resulted in tumor-to-normal ratios of 4.8 ± 0.56, 2.3 ± 0.27, 1.2 ± 0.095, 4.6 ± 0.62, and 2.4 ± 0.88 for CD44v6, MUC1, mammaglobin, CAXII, and TfR, respectively.

Since conventional immunohistochemistry is not necessarily quantitative, we also performed immunofluorescence using directly fluorescently labeled antibodies. The results were comparable with conventional immunohistochemistry (Figure 3) resulting in tumor-to-normal ratios of 3.93 ± 0.14, 2.74 ± 0.46, 1.54 ± 0.11, and 1.66 ± 0.066 for CD44v6, MUC1, mammaglobin, and CAXII, respectively. TfR expression was not detectable using immunofluorescence. Thereby, CD44v6 was the only less tumor-specific marker consistently meeting the required 3-fold tumor-to-normal ratio.

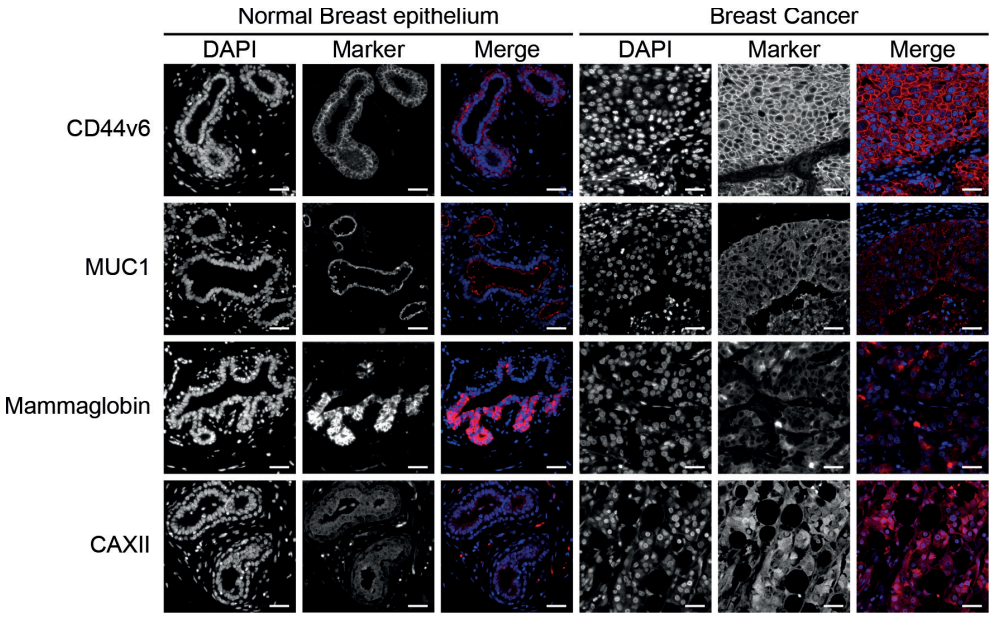

Figure 3: Quantitation of expression levels of less tumor-specific markers using immunofluorescence. Expression levels of less tumorspecific membrane markers (CD44v6, MUC1, mammaglobin, and CAXII) as determined by immunofluorescence resulted in staining patterns in normal breast epithelium and positive tumors comparable to conventional immunohistochemistry (transferrin receptor was not detectable). Size bar equals 25 μm.

Detection rate of combined highly and less tumor-specific molecular targets

Including TfR, mammaglobin, and MUC1 to the panel of highly tumor-specific markers GLUT1, MET, EGFR, IGF1-R, CAIX, and HER2 increased the detection rate from 45.5% to 49.8% (TfR), 56.4% (mammaglobin), and 98.1% (MUC1), respectively. However, of these markers, only CD44v6 reached a sufficiently high tumor-to-normal ratio (see above), so adding CD44v6 to the panel of highly specific markers therefore realistically increased the overall detection rate to 80.1%. When CD44v6 was included, removal of CAIX or MET from the panel had no influence on the detection rate.

Especially the luminal-type ductal and lobular breast cancers were better detected by including CD44v6. Upon addition of CD44v6, the detection rate rose from 45.5% to 78.9% for luminal-type cancers, from 18.3% to 72.2% for the lobular breast cancers, and from 84.2% to 90.0% for basal/TN ductal breast cancers (Figure 4A). Moreover, the detection rate of the panel was not dependent on grade (76.4%, 74.0%, and 84.5% for grade 1, grade 2, and grade 3 tumors, respectively), tumor size (79.1%, 77.6%, and 85.7% for tumors ≤2 cm, >2 and ≤5 cm, and >5 cm, respectively), lymph node status (76.2% for lymph node negative, and 82.7% for lymph node positive cases), or age (78.8% for patients <60 years and 80.1% for patients >60 years) (Figure 4B).

Therefore, the optimal combination of membrane expressed proteins to target by molecular imaging seemed to consist of CD44v6, GLUT1, EGFR, HER2, and IGF1-R by which about 80% of invasive breast cancers are predicted to be detectable.

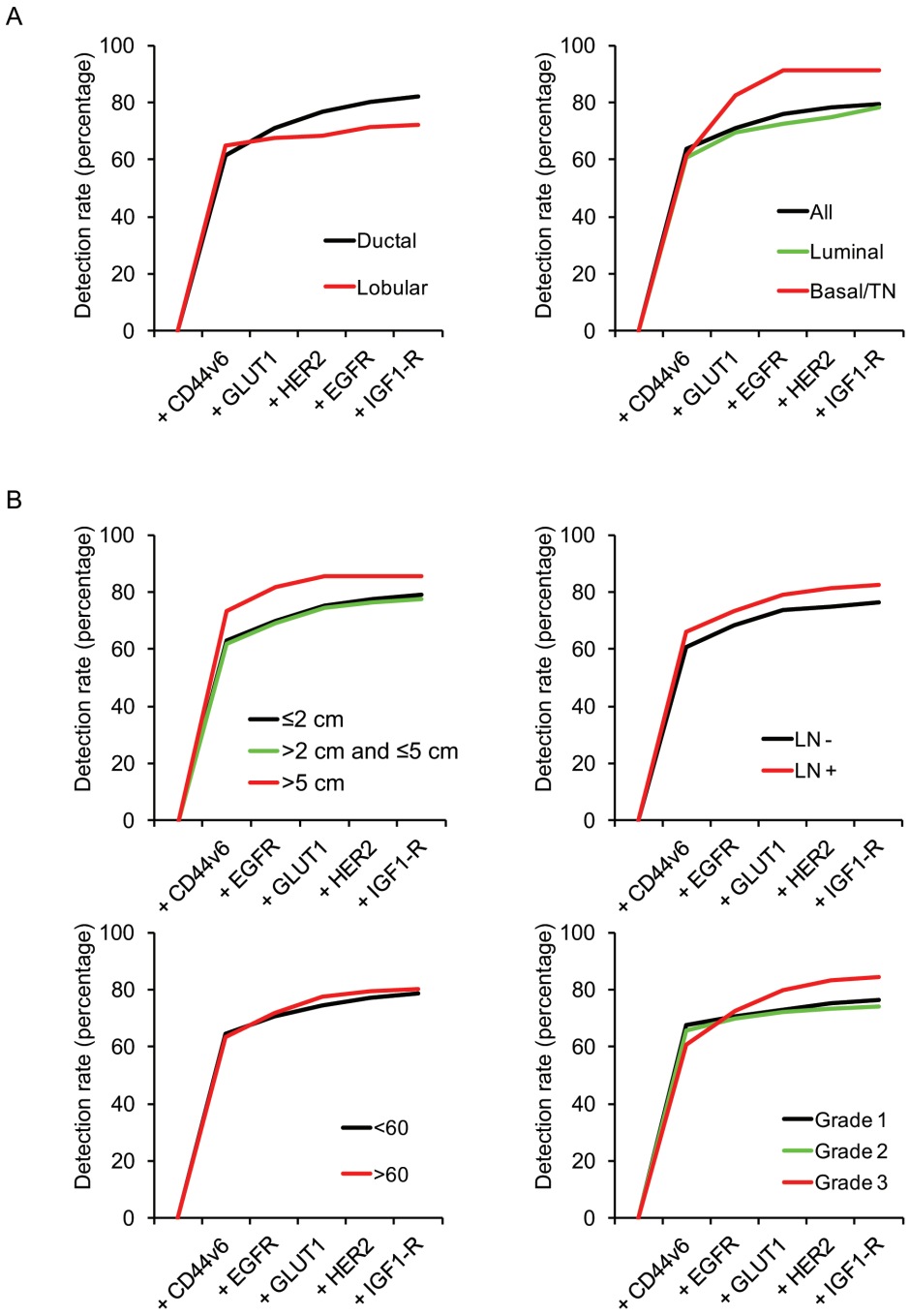

Figure 4: Optimal combination of membrane markers for detection of breast cancer correlated with clincopathological characteristics. A. The contribution of each tumor-specific and less tumor-specific membrane marker in the optimal panel for detection of breast cancer. B. The detection rate of the panel with respect to several clinicopathological features.

Discussion

The aim of this study was to identify the minimum panel of membrane markers that may be suitable for detection of invasive breast cancer by molecular imaging. In order to determine this combination, we stained TMAs consisting of 483 clinical specimens of invasive breast cancer by immunohistochemistry. Based on the expression profiles in the normal breast tissue, we defined highly tumor-specific (no or low staining of the normal breast tissue) and less tumor-specific (moderate or high staining of the normal breast tissue) membrane targets. We found that the expression of highly tumor-specific targets (HER2, EGFR, GLUT1, CAIX, IGF1-R, and MET) is quite dependent on the tumor histology and molecular subtype: ductal cancers and in particular the basal/TN and HER2-driven subtypes express more frequently highly tumor-specific membrane targets than lobular cancers.
Because the individual tumor-specific markers are clearly not sensitive enough, application of a tumorspecific panel of probes is required to detect all types of breast cancer. A panel of tumor-specific markers (GLUT1, EGFR, HER2, IGF1-R, MET, and CAIX) was in the present study able to 'detect' 45.5% of all cancers and 55.6% of ductal cancers. For lobular cancers and low-grade tumors, the panel was not very suitable because of detection rates of 18.3% and 22.5%, respectively. Addition of less tumor-specific markers theoretically increased the detection rate to 98.1% using MUC1, but of the less tumor-specific markers only CD44v6 met the desired 3-fold tumor-to-normal tissue ratio measured by image analysis. When adding CD44v6 to the panel, 80.1% of all cancers could be 'detected' with at least one marker in a panel consisting of HER2, GLUT1, EGFR, IGF1-R, and CD44v6. CAIX and MET had no additional effect on the sensitivity of the panel once CD44v6 had been included. Our estimation of positivity of breast cancers for our panel may have been conservative since we have been very stringent in calling expression positive, explaining why our rates of expression for GLUT1, CAIX, EGFR, MET, TfR, CAXII, and mammaglobin are on the lower side compared to the literature [22,34-43]. Tumors with 1+ membrane staining were consistently considered negative as we expect that this

level of staining provides insufficient signal-to-noise, but only *in vivo* studies can confirm this. Moreover, quantification of expression levels based on image analysis of immunohistochemical stainings may be hampered by the non-linear amplification of the signal during immunohistochemistry. For that reason we applied immunofluorescence of directly labeled antibodies for more reliable quantitation of protein expression. Tumor-to-normal ratios above 3 where only obtained when tumors are scored as DAKO 2+ or 3+ membranous staining. This justifies the predefined thresholds for calling tumors positive. Furthermore, cytoplasmic staining was ignored as imaging antibodies will not be easily internalized and will have to bind to receptors on the outside of the cancer cells. Lastly, using TMAs may have resulted in slight underestimation of GLUT1 and CAIX expression, because the expression is usually limited to hypoxic areas within the tumor [44,45].

Adding further candidate tumor markers may enable to improve the results of our panel of membrane related markers. For instance, biomarkers that are specifically expressed in the stroma of breast cancers like growth factors (e.g. VEGF) may be valuable.

This study provides information on the expression levels of membrane-bound targets for imaging using paraffin-embedded material of invasive breast cancers. To be suitable for breast cancer detection or screening, multiple steps have to be taken before probe development and testing in (pre)clinical trials results in treatment of patients. However, the present study elucidates which targets might be most suitable based on the expression in cancer vs. normal breast tissue. One of the current challenges is specific detection of lobular breast cancers and DCIS, because these lesions are difficult to detect by mammography. DCIS was beyond the scope of the current paper, but for detection of lobular breast cancer CD44v6 is potentially quite useful.

Next to expression of target proteins, tumor perfusion and penetration of the probe into the tumor could influence the signal for imaging. Further, affinity after labeling and half-life of the probe in the human body determine the tumor-to-background ratio and thus the applicability of a probe in a clinical setting. Based on preclinical studies using NIRF labeled trastuzumab and bevacizumab, the maximal tumor-to-background ratio was obtained 6 days post injection [33]. Optimizing this

by reducing the half-life of the probe would be beneficial for clinical practice. The present study underlines that no single membrane marker probe is likely to detect all breast cancers by molecular imaging, and that a panel of least five probes may be required. So far, experience is however limited to maximally two different probes at once. Barrett et al. [46] showed that two antibodies allowed to identify differences in tumor expression of HER2 and EGFR *in vivo*. When aiming to be just discriminative between tumor and normal, a panel of markers can be injected with the same probe attached to simplify imaging. Feasibility and toxicity of injecting a panel of markers require further *in vivo* experiments in mouse models.

Conclusions

We studied which tumor membrane markers are most discriminating between invasive breast cancer and normal breast tissue in order to identify the minimal number of targeted probes needed for the highest possible breast cancer detection rate. We showed that 80% of all breast cancers express at least one of a panel of markers (CD44v6, GLUT1, EGFR, HER2, and IGF1-R) that therefore may be suitable for molecular imaging strategies. The present study thereby serves as a starting point for further development of a set of antibody-based optical probes with high potential for detecting breast cancer.

References

1. Paap E, Broeders MJ, van Schoor G, Otten JD, Verbeek AL: Large increase in a Dutch woman's lifetime risk of developing breast cancer. Eur J Cancer 2008, 44:1485-1487.
2. Incidentie van invasive tumoren naar geslacht en lokalisatie per incidentiejaar (1989-2008) [http://www.ikcnet.nl/page.php?id=2902&nav_id=114]
3. Sterfte aan kanker naar geslacht en lokalisatie en jaar van overlijden (1989-2008) [http://www.ikcnet.nl/uploaded/docs/Landelijk/cijfers/incidentie%202008/B1_NL.xls]
4. Medina-Franco H, Abarca-Perez L, Garcia-Alvarez MN, Ulloa-Gomez JL, Romero-Trejo C, Sepulveda-Mendez J: Radioguided occult lesion localization (ROLL) versus wire-guided lumpectomy for non-palpable breast lesions: a randomized prospective evaluation. J Surg Oncol 2008, 97:108-111.
5. Singletary SE: Surgical margins in patients with early-stage breast cancer treated with breast conservation therapy. Am J Surg 2002, 184:383-393.
6. Brown ML, Houn F, Sickles EA, Kessler LG: Screening mammography in community practice: positive predictive value of abnormal findings and yield of follow-up diagnostic procedures. Am J Roentgenol 1995, 165:1373-1377.
7. Elmore JG, Armstrong K, Lehman CD, Fletcher SW: Screening for breast cancer. JAMA 2005, 293:1245-1256.
8. Kerlikowske K, Grady D, Barclay J, Sickles EA, Eaton A, Ernster V: Positive predictive value of screening mammography by age and family history of breast cancer. JAMA 1993, 270:2444-2450.
9. Lidbrink E, Elfving J, Frisell J, Jonsson E: Neglected aspects of false positive findings of mammography in breast cancer screening: analysis of false positive cases from the Stockholm trial. BMJ 1996, 312:273-276.
10. Moadel RM: Breast cancer imaging devices. Seminars in nuclear medicine 2011, 41:229-241.
11. Brewer NT, Salz T, Lillie SE: Systematic review: the long-term effects of false-positive mammograms. Annals of internal medicine 2007, 146:502-510.
12. Bos R, van der Hoeven JJ, van der Wall E, van der Groep P, van Diest PJ, Comans EF, Joshi U, Semenza GL, Hoekstra OS, Lammertsma AA, Molthoff CF: Biologic correlates of (18)fluorodeoxyglucose uptake in human breast cancer measured by positron emission tomography. J Clin Oncol 2002, 20:379-387.
13. Oude Munnink TH, Nagengast WB, Brouwers AH, Schroder CP, Hospers GA, Lub-de Hooge MN, van der Wall E, van Diest PJ, de Vries EG: Molecular imaging of breast cancer. Breast 2009, 18 Suppl 3:S66-73.
14. Frangioni JV: In vivo near-infrared fluorescence imaging. Curr Opin Chem Biol 2003, 7:626-634.
15. Frangioni JV: New technologies for human cancer imaging. J Clin Oncol 2008, 26:4012-4021.
16. Ntziachristos V: Fluorescence molecular imaging. Annual review of biomedical engineering 2006, 8:1-33.
17. Pleijhuis RG, Graafland M, de Vries J, Bart J, de Jong JS, van Dam GM: Obtaining adequate surgical margins in breast-conserving therapy for patients with early-stage breast cancer: current modalities and future directions. Ann Surg Oncol 2009, 16:2717-2730.
18. Sampath L, Kwon S, Ke S, Wang W, Schiff R, Mawad ME, Sevick-Muraca EM: Du

al-labeled trastuzumab-based imaging agent for the detection of human epidermal growth factor receptor 2 overexpression in breast cancer. J Nucl Med 2007, 48:1501-1510.
19. Viacava P, Naccarato AG, Bocci G, Fanelli G, Aretini P, Lonobile A, Evangelista G, Montruccoli G, Bevilacqua G: Angiogenesis and VEGF expression in pre-invasive lesions of the human breast. J Pathol 2004, 204:140-146.
20. Gee MS, Upadhyay R, Bergquist H, Alencar H, Reynolds F, Maricevich M, Weissleder R, Josephson L, Mahmood U: Human breast cancer tumor models: molecular imaging of drug susceptibility and dosing during HER2/neu-targeted therapy. Radiology 2008, 248:925-935.
21. Lee SB, Hassan M, Fisher R, Chertov O, Chernomordik V, Kramer-Marek G, Gandjbakhche A, Capala J: Affibody molecules for in vivo characterization of HER2-positive tumors by near-infrared imaging. Clin Cancer Res 2008, 14:3840-3849.
22. Bos R, van der Groep P, Greijer AE, Shvarts A, Meijer S, Pinedo HM, Semenza GL, van Diest PJ, van der Wall E: Levels of hypoxia-inducible factor-1alpha independently predict prognosis in patients with lymph node negative breast carcinoma. Cancer 2003, 97:1573-1581.
23. Bos R, Zhong H, Hanrahan CF, Mommers EC, Semenza GL, Pinedo HM, Abeloff MD, Simons JW, van Diest PJ, van der Wall E: Levels of hypoxia-inducible factor-1 alpha during breast carcinogenesis. J Natl Cancer Inst 2001, 93:309-314.
24. van der Groep P, Bouter A, van der Zanden R, Menko FH, Buerger H, Verheijen RH, van der Wall E, van Diest PJ: Re: Germline BRCA1 mutations and a basal epithelial phenotype in breast cancer. J Natl Cancer Inst 2004, 96:712-713; author reply 714.
25. Elston CW, Ellis IO: Pathological prognostic factors in breast cancer. I. The value of histological grade in breast cancer: experience from a large study with long-term follow-up. Histopathology 1991, 19:403-410.
26. van der Groep P, Bouter A, van der Zanden R, Siccama I, Menko FH, Gille JJ, van Kalken C, van der Wall E, Verheijen RH, van Diest PJ: Distinction between hereditary and sporadic breast cancer on the basis of clinicopathological data. J Clin Pathol 2006, 59:611-617.
27. Packeisen J, Korsching E, Herbst H, Boecker W, Buerger H: Demystified...tissue microarray technology. Mol Pathol 2003, 56:198-204.
28. van Diest PJ: No consent should be needed for using leftover body material for scientific purposes. For. BMJ 2002, 325:648-651.
29. Kornegoor R, Verschuur-Maes AHJ, Buerger H, Hogenes MCH, de Bruin PC, Oudejans JJ, van der Groep P, Hinrichs B, van Diest PJ: Molecular subtyping of male breast cancer by immunohistochemistry. Mod Pathol 2011.
30. Sorlie T, Perou CM, Tibshirani R, Aas T, Geisler S, Johnsen H, Hastie T, Eisen MB, van de Rijn M, Jeffrey SS, et al: Gene expression patterns of breast carcinomas distinguish tumor subclasses with clinical implications. Proc Natl Acad Sci U S A 2001, 98:10869-10874.
31. Corlu A, Choe R, Durduran T, Rosen MA, Schweiger M, Arridge SR, Schnall MD, Yodh AG: Three-dimensional in vivo fluorescence diffuse optical tomography of breast cancer in humans. Opt Express 2007, 15:6696-6716.
32. van de Ven S, Wiethoff A, Nielsen T, Brendel B, van der Voort M, Nachabe R, van der Mark M, van Beek M, Bakker L, Fels L, et al: A novel fluorescent imaging agent for diffuse optical tomography of the breast: first clinical experience in patients. Mol Imaging Biol 2010, 12:343-348.
33. Terwisscha van Scheltinga AG, van Dam GM, Nagengast WB, Ntziachristos V, Hollema H, Herek JL, Schroder CP, Kosterink JG, Lub-de Hoog MN, de Vries EG:

Intraoperative near-infrared fluorescence tumor imaging with vascular endothelial growth factor and human epidermal growth factor receptor 2 targeting antibodies. J Nucl Med 2011, 52:1778-1785.
34. Afify A, McNiel MA, Braggin J, Bailey H, Paulino AF: Expression of CD44s, CD44v6, and hyaluronan across the spectrum of normal-hyperplasia-carcinoma in breast. Appl Immunohistochem Mol Morphol 2008, 16:121-127.
35. Bhargava R, Beriwal S, Dabbs DJ: Mammaglobin vs GCDFP-15: an immunohistologic validation survey for sensitivity and specificity. Am J Clin Pathol 2007, 127:103-113.
36. Carracedo A, Egervari K, Salido M, Rojo F, Corominas JM, Arumi M, Corzo C, Tusquets I, Espinet B, Rovira A, et al: FISH and immunohistochemical status of the hepatocyte growth factor receptor (c-Met) in 184 invasive breast tumors. Breast Cancer Res 2009, 11:402.
37. Habashy HO, Powe DG, Staka CM, Rakha EA, Ball G, Green AR, Aleskandarany M, Paish EC, Douglas Macmillan R, Nicholson RI, et al: Transferrin receptor (CD71) is a marker of poor prognosis in breast cancer and can predict response to tamoxifen. Breast Cancer Res Treat 2010, 119:283-293.
38. Klijn JG, Berns PM, Schmitz PI, Foekens JA: The clinical significance of epidermal growth factor receptor (EGF-R) in human breast cancer: a review on 5232 patients. Endocr Rev 1992, 13:3-17.
39. Lacunza E, Baudis M, Colussi AG, Segal-Eiras A, Croce MV, Abba MC: MUC1 oncogene amplification correlates with protein overexpression in invasive breast carcinoma cells. Cancer Genet Cytogenet 2010, 201:102-110.
40. Sasaki E, Tsunoda N, Hatanaka Y, Mori N, Iwata H, Yatabe Y: Breast-specific expression of MGB1/mammaglobin: an examination of 480 tumors from various organs and clinicopathological analysis of MGB1-positive breast cancers. Mod Pathol 2007, 20:208-214.
41. Tafreshi NK, Enkemann SA, Bui MM, Lloyd MC, Abrahams D, Huynh AS, Kim J, Grobmyer SR, Carter WB, Vagner J, et al: A mammaglobin-A targeting agent for noninvasive detection of breast cancer metastasis in lymph nodes. Cancer Res 2011, 71:1050-1059.
42. Watson PH, Chia SK, Wykoff CC, Han C, Leek RD, Sly WS, Gatter KC, Ratcliffe P, Harris AL: Carbonic anhydrase XII is a marker of good prognosis in invasive breast carcinoma. Br J Cancer 2003, 88:1065-1070.
43. Wykoff CC, Beasley N, Watson PH, Campo L, Chia SK, English R, Pastorek J, Sly WS, Ratcliffe P, Harris AL: Expression of the hypoxia-inducible and tumor-associated carbonic anhydrases in ductal carcinoma in situ of the breast. Am J Pathol 2001, 158:1011-1019.
44. van Diest PJ, Vleugel MM, van der Groep P, van der Wall E: VEGF-D and HIF-1alpha in breast cancer. J Clin Pathol 2005, 58:335; author reply 336.
45. van Diest PJ, Vleugel MM, van der Wall E: Expression of HIF-1alpha in human tumours. J Clin Pathol 2005, 58:335-336.
46. Barrett T, Koyama Y, Hama Y, Ravizzini G, Shin IS, Jang BS, Paik CH, Urano Y, Choyke PL, Kobayashi H: In vivo diagnosis of epidermal growth factor receptor expression using molecular imaging with a cocktail of optically labeled monoclonal antibodies. Clin Cancer Res 2007, 13:6639-6648.

Aram S.A. van Brussel, Veronika Ramovs, Reini van der Welle, Sabrina Oliveira, Mohamed El Khattabi, Monique Slijper, Mirjam J.M.A. Damen, Elsken van der Wall, Willem P.Th.M. Mali, Paul J. van Diest, Paul M.P. van Bergen en Henegouwen

4

Subtractive panning of a nanobody phage library reveals DAF as a biomarker for hypoxic breast cancer

Abstract

Introduction: Hypoxic breast tumors tend to be chemo- and radiotherapy resistant. Early detection of hypoxic tumors, e.g. by molecular imaging, is needed to select alternative treatment strategies for patients. Here we used phage-display to select nanobodies against hypoxia-specific membrane-bound targets, and tested a nanobody lead candidate as probe for optical molecular imaging of breast cancer
Methods: Hypoxia-specific nanobodies were isolated by subtractive panning of a nanobody phage library using normoxic and hypoxic HeLa cells. Nanobody specificity was determined by mass spectrometry. After conjugation to the near-infrared dye IRDye700DX (IR), the nanobody lead candidate was tested as targeted probe for optical molecular imaging and image-guided surgery in a mouse model with hypoxic human breast cancer xenografts (MCF10DCIS.com). As a control, the non-specific nanobody R2 was used. Expression levels of the selected target were evaluated by immunohistochemistry.
Results: Two isolated nanobodies, A2A11 and B3C7, showed increased binding to hypoxic HeLa cells, compared to normoxic cells. By mass spectrometry, DAF (decay accelerating factor, or CD55) was identified as binding partner for both nanobodies, which was further confirmed by western blotting. Optical molecular imaging of breast cancer xenografts resulted in a mean tumor-to-normal tissue ratio (TNR) of 1.6±0.05 (±SEM) 2h after injection of A2A11-IRDye700DX compared to 1.4±0.09 for R2-IR control nanobody. During intra-operative imaging of xenografts mean TNR was 1.8±0.07 for A2A11-IR and 1.5±0.06 for R2-IR.
Conclusion: We isolated a high affinity nanobody (A2A11) specific for DAF, a predominant membrane-bound hypoxia marker in HeLa cells which is expressed in breast cancer cells as well. A2A11 can be used to detect hypoxic (breast) cancer non-invasively, during image guided surgery and to identify patients that are likely to show therapy resistance.

Introduction

Unrestricted proliferation of tumors, away from the basal membrane, leads to tumor hypoxia when the diffusion limit of oxygen is exceeded [1]. Hypoxic tumors of the breast (and other origins) show resistance to chemotherapy and radiotherapy, due to limited tumor perfusion of blood-borne chemotherapeutics and diminished formation of free oxygen radicals, which are important for radiation damage [2]. Molecular markers for hypoxic tumors would allow for selection of patients that are likely to show chemo- and radiotherapy resistance and need alternative therapeutic regimens. In addition, molecular markers that specifically bind to hypoxic tumor cells could be used for targeted therapy of hypoxic tumors. In hypoxic cells, HIF-1α, a transcription factor regulating the hypoxia response, is stabilized and subsequently binds hypoxia response elements (HRE) in promoters of many downstream proteins, e.g. carbonic anhydrase IX (CAIX) and glucose transporter 1 (GLUT1). These are currently well known membrane-bound proteins that are upregulated under hypoxia [1]. However, as the expression of none of these downstream proteins is restricted to hypoxic tumors, additional markers are needed, in order to create a panel of hypoxia markers that can be used to identify hypoxic tumors with high sensitivity and specificity.

Early determination of the hypoxic state of solid tumors can be achieved by molecular imaging, for which hypoxia-specific probes, such as antibodies or nanobodies are required. Nanobodies, or VHHs, are antibody fragments obtained from heavy-chain antibodies that are present in animals from the Camelidae family, including llamas. Nanobodies can be conjugated to radioactive or fluorescent probes and used for PET/SPECT or optical imaging [3, 4, 5].

In the present paper, we set out to select novel nanobodies binding to hypoxic markers that have increased or unique expression in the plasma membrane of hypoxic tumor cells. We designed a novel phage display selection strategy, based on subtractive panning and reverse proteomic antibody screening [6, 7]. From a panel of different nanobodies, two nanobodies were selected that could discriminate be-

tween hypoxia and normoxia. The target specificity of these nanobodies was here investigated and identified as the decay accelerating factor (DAF or CD55). Thereafter a lead nanobody was evaluated *in vivo* with a breast cancer xenograft model. Our results demonstrate the successful selection of nanobodies directed against DAF as novel probes for the detection of hypoxic tumor cells.

Material and Methods

Materials

Recombinant human DAF/CD55 was obtained from R&D systems, (MN, USA) and deglycosylated with protein deglycosylation mix (New England Biolabs®, Inc., MA, USA) according to manufacturers' protocol. Rabbit anti-CD55 polyclonal antibody was purchased from Santa Cruz Biotechnology, Inc. (H-319, Heidelberg, Germany). MabCAIX antibody was produced as described before [8].

Cell lines and culture conditions

HeLa cervical cancer (CCL-2) and COS-7 fibroblast cells (ATCC, Wesel, Germany) were grown in Dulbecco's Modified Eagle's Medium (DMEM; Invitrogen, Breda, The Netherlands) supplemented with 10% (v/v) Fetal Calf Serum (FCS), 100 IU/ml penicillin, 100 µg/ml streptomycin, and 2 mM L-glutamine. HeLa HIF-1α knock-down (KD) cells were kindly provided by dr. J. Ivanova (University Medical Center, Utrecht, The Netherlands) and cultured in complete DMEM containing additional 2 µg/ml puromycin. MCF10DCIS.com cells (further referred to as MCF10DCIS; Asterand, Detroit, USA) were cultured according to the supplier's guidelines in DMEM/F12, supplemented with 10% (v/v) FCS, 100 IU/ml penicillin, 100 µg/ml streptomycin and 2 mM L-glutamine. Transient CD55 transfection of COS-7 cells with Myc-DDk-tagged human CD55, transcript variant 1 (OriGene Technologies, Inc., Rockville, MD, USA) was performed using FuGENE® HD transfection agent according to manufacturers' protocol (Promega Benelux BV, Leiden, The Netherlands). Cells were cultured at 37°C in a humidified atmosphere containing 5% CO_2 and 21% using a conventional incubator or 1% O_2 using an INVIVO2 hypoxia workstation (Ruskinn, Pencoed, UK), respectively. All cells were consistently Mycoplasma free.

Phage display selections with subtractive panning

Phages were produced from *E. coli* TG1 harboring HeLa libraries after infection with helper phage VSCM13 (Strategene, Agilent Technologies Netherlands B.V.,

Amstelveen, The Netherlands) and incubating overnight while shaking at 37°C in medium containing ampicillin (100 µg/ml) and kanamycin (25 µg/ml). Next day, phages were precipitated by adding 2% polyethylene glycol (PEG), 250 mM NaCl for 30 min on ice. After spinning down and resuspending the pellet in ice cold phosphate-buffered saline (PBS), PEG precipitation was repeated two times. To enrich for hypoxia-specific binders, 50 µl of phages, blocked by 2% Marvel milk in PBS for 30 min at room temperature, was added to normoxic HeLa HIF-1α KD cells and left incubating head-over-head at 4°C for 1 h. Cells were spun down for 5 min at 1,200 rpm, supernatant was collected and the resulting depleted phage library was used for selections. Hypoxic HeLa cells were detached by incubation with 10 mM Ethylenediamine-tetraacetic acid (EDTA). Detached cells were spun down at 800 rpm for 5 min, resuspended and blocked in 1 ml of cold 2% bovine serum albumin (BSA) in PBS for 30 min at 4°C. Phages were selected through three rounds of panning on variable amounts of hypoxic HeLa cells. After 1.5h of head-over-head incubation at 4°C, cells were spun down for 5 min at 1,200 rpm and cell pellet was collected and washed three times with Hank's Buffered Salt Solution (HBSS) and one time with PBS. Bound phages were eluted by trypsin digestion (1.0 mg/ml) for 20 min. After addition of trypsin inhibitor, phages were recovered by infection of an *E. coli* culture in the exponential phase of the growth for 30 min. After infection, phages were spotted on agar plates (containing 100 µg/ml ampicillin and 2% glucose) to calculate the number of bound phages by titration. Subsequently, the infections were grown overnight in 2x Tryptone Yeast Extract medium (2TY) containing 100 µg/ml ampicillin and 2% glucose, shaking at 37°C. Next day the overnight culture was stored at -80°C.

Periplasmic fraction production and ELISA screening on cells

Single *E. coli* TG1 colonies were picked from agar plates and grown in 100 µl 2TY supplemented with 2% glucose and 100 µg/ml ampicillin in sterile 96-wells plates with v-shaped bottom overnight at 37°C. Next day, 10 µl of TG1 were used to inoculate 1 ml 2TY supplemented with 100 µg/ml ampicillin in 96-well square V-bottom plates (Corning, New York, USA) for 4h at 37°C while shaking. Nanobo-

dy production was induced by adding 1mM isopropyl β-D-1-thiogalactopyranoside (ITPG) and subsequently incubated for 4h at 37°C. Bacteria were spun down at 4,600 rpm for 15 min, and pellets were frozen at -20°C overnight. Next day pellets were thawed and dissolved in 100 µl PBS. After centrifugation at 4,600 rpm for 15 min the supernatant was used for further screening by ELISA.

Twenty thousand HeLa cells were seeded in each well of 96 well plates (96 v shaped, Greiner bio-one, Alphen aan de Rijn, The Netherlands). Next day, cells were placed on ice and medium was replaced by 50 µl/well of PBS with 4% BSA. Cells were incubated for 1.5h on ice with 30 µl of periplasmic fraction, with 50 µl/well of MabCAIX (1:2,000 in 2% BSA PBS) as positive control, or with 4% BSA in PBS as negative control. Then, cells were washed twice with cold PBS and fixed with 4% paraformaldehyde (PFA) for 30 min on ice. Activity of PFA was quenched by addition of 50 mM NH_4Cl in PBS for 10 min at room temperature, after which cells were washed twice with PBS. Nanobodies bound to cells were detected through a rabbit anti-VHH antibody (incubated for 1h at 1:2,000 dilution in 2% BSA PBS). Negative and positive control wells were incubated with rabbit anti-human IgG antibody (1:2,000 in 2% BSA PBS). After washing with PBS, cells were incubated for 1h at room temperature with donkey anti-rabbit-peroxidase (DARPO, 1:5,000 in 2% BSA PBS). After washing in PBS, O-phenyldiamin (OPD) with 0.1% H_2O_2 was added and blocked after 30 min with 1 M H_2SO_4. Absorbance was measured with a microplate reader (model 550, BIO-RAD, Veenendaal, The Netherlands) at 490 nm wavelength with reference filter at 405 nm wavelength. In case of visible inter-well variation in cell number, absorbance was corrected by the number of cells with TO-PRO-3 staining. For this, cells were incubated with TO-PRO-3 (1:5,000 in PBS) for 10 min, after which they were washed twice with PBS. Finally, near-infrared (NIR) signal intensity was measured with the Odyssey imaging system (LI-COR Biosciences, Lincoln, NE) using the 700 nm channel.

Nanobody production, purification and biotinylation

After transformation into AVB101 *E. coli*, overnight cultures were diluted 1/100 in 800 ml 2TY and grown at 37°C, shaking. Biotin (50 µM) was added at optical density of 0.3 at 600 nm (OD600: 0.3) and nanobody production was induced by adding

0.1mM IPTG at OD600 0.5. Cultures were grown overnight shaking at 30°C. Next day, bacteria were harvested by centrifugation. Pellets were frozen at -20°C and next day the periplasmic fraction was obtained by thawing pellets and resuspending them in PBS, by spinning for 2h head-over-head at 4°C, and then centrifugation at 4,600 rpm for 15 min. Nanobodies were purified from the periplasmic fraction by affinity chromatography using a HiTrap protein A HP column (GE Healthcare, Zeist, The Netherlands) using the ÄKTAxpress system (GE Healthcare, Zeist, The Netherlands).

Determination of hypoxia specificity on live HeLa cells by ELISA

HeLa cells were seeded in 96-wells plates (15,000 cells per well) and cultured overnight under normoxic (21% O_2) or hypoxic (1% O_2) conditions. Next day, cells were put on CO_2-independent medium supplemented with 4% BSA and blocked for 30 min at 4°C. Blocked cells were incubated with 2 uM nanobody or MabCAIX anti-CAIX antibody as positive control for hypoxia, for 1.5h at 4°C. After washing twice with PBS, cells were fixed with 4% paraformaldehyde (PFA) for 30 min. PFA was quenched with NH_4Cl for 15 min. After two subsequent washes, nanobodies were detected with rabbit anti-VHH (1/500) and goat anti-rabbit IRDye800CW (1/1,000). MabCAIX was detected with rabbit anti-human IgG (1/500) and goat anti-rabbit IRDye800CW. To correct for cell number, TO-PRO-3 was used as described above. Signal was measured with the Odyssey imaging system (LI-COR) using the 700 nm channel for the TO-PRO-3 stain and the 800 nm channel for IRDye800CW detection.

Characterization of unconjugated nanobodies

Nanobody proteins (1 µg) were size-separated with 15% SDS-PAGE. Gels were stained with Coomassie Brilliant Blue solution (SERVA Electrophoresis GmbH, Heidelberg, Germany) and imaged with the Odyssey imaging system (LI-COR). For affinity determination of, $2.0x10^4$ HeLa cells were seeded per well, one day in advance and incubated at 4°C for 1.5h with dilution series of nanobody in PBS in triplicate. After washing with PBS, incubation with rabbit anti-VHH antibody (1:2,000) and goat anti-rabbit IRDye800CW (1:1,000), bound nanobodies were

detected using the 800 nm channel of the Odyssey imaging system (LI-COR). The dissociation constant (K_D) was derived from the concentration of nanobodies at which half the intensity of B_{max} was found using non-linear regression, of one site specific binding, (Graphpad Prism v.5, GraphPad Software, La Jolla, USA).

Membrane vesicles isolation from HeLa cells

For immunoprecipitation, approximately $3{,}0x10^7$ HeLa cells were cultured under 1% or 21% O_2 for 24 h. Next day, cells were washed 3 times with 20 ml PBS and 1 time with ca/mg-free hypotonic PBS (5%PBS in demi water). Cells were incubated with hypotonic PBS for 15 min at room temperature. Then, cells were washed and incubated with vesiculation buffer (100 mM NaCl, 50 mM Na_2HPO_4, 5 mM KCl, 0,5 mM $MgSO_4$, pH 8,5) for 20 min at room temperature. Cells were placed in a 37°C incubator for 1h. After conformation of vesicle formation by light microscopy (20x), buffer was collected in 50 ml falcon tubes on ice. After centrifugation at 150 g for 5 min at 4°C, supernatant was centrifuged for 1h at 100,000 g in an ultracentrifuge (Beckman Coulter Nederland B.V., Woerden, The Netherlands), using a 70 Ti fixed rotor type. After centrifugation, pellet was resuspended in 10 mM hepes-PBS buffer (pH 7,4).

Immunoprecipitation

Vesicles were lysed in 2 ml PBS/0.1%Triton X-100 with DFO (1/1,000) and protease inhibitors. Lysate was spun down at 1,200 rpm, at 4°C for 5 min and supernatant was aliquoted and stored at 4°C. Two ml of lysate was precleared by incubation with 20 µl M280 Streptavidin Dynabeads (Invitrogen) for 30 min at 4°C, head-over-head. Biotinylated nanobodies (6-8 µg) were prebound to 20 µl streptavidin beads for 90 min at 4°C in a total volume of 500 µl PBS. After blocking with lysis buffer/DFO/2% Chicken Egg white Albumin (CEA) for 30 min and washing with PBS/0.1%Triton, pre-bound nanobody-Dynabeads were added to 1 ml pre-cleared lysate and incubated for 2h at 4°C head-over-head. Beads were washed 4-6x with PBS/0.1%Triton/300 mM NaCl. After the final wash, supernatant was removed completely and 25 µl of sample buffer was added. Sample buffer lysate was boiled for 5 min and cooled on ice. Lysate and 25 µl of unbound fraction was run on

SDS-PAGE (10% gel).

Spectrometry and data analysis

Samples for mass spectrometry were obtained from Coomassie Brilliant Blue (SERVA) stained SDS-PAGE gel. Targeted bands were cut from gel and in-gel digested with trypsin [9]. Additionally, samples were treated with 0.01 units of N-Glycosidase F (Roche Nederland B.V., Woerden, The Netherlands) per sample for 2h at 37°C. The samples were analysed using reversed phase nano-LC-MS/MS. This consisted of an Agilent 1,200 series nanoflow HPLC (Agilent technologies, Amstelveen, The Netherlands) connected to a MS LTQ-Orbitrap XL (Thermo Scientific, Bremen, Germany). The samples were trapped on a 20 mm ReproSil-Pur C18-AQ (Dr. Maisch GmbH, Ammerbuch, Germany) trapping column (packed in-house, i.d., 100 µm; resin, 5 µm) with a flow-rate of 5 µL min^{-1}. Sequential elution of peptides was accomplished using an analytical column (Dr. Maisch GmbH; packed in-house, i.d., 50 µm; resin, 3 µm). with a 35 min gradient of 10–38% buffer B (buffer A, 0.1 M acetic acid; buffer B, 0.1 M acetic acid, 80% (v/v) acetonitrile) followed by 38–100% B in 3 min, 100% B for 2 min. The flow rate was passively split from 0.45 mL/min to 100 nL/min. Nanospray was achieved using a distally coated fused silica emitter (made in-house, o.d. 375 µm; i.d. 20 µm) biased to 1.7 kV. The mass spectrometer was operated in data dependent mode to automatically switch between MS and MS/MS. The high resolution survey full scan was acquired in the Orbitrap analyzer from m/z 350 to 1,500 m/z with a resolution of 30,000 (FHMW) at 400 m/z, whereas MS/MS scans were acquired in the linear ion trap (LTQ) at a resolution of 7,500. The most intense ions at a threshold of above 500 were fragmented in the linear ion trap using collision-induced dissociation at a target value of 10,000. All MS data were processed with Proteome Discoverer (version 1.3; Thermo Scientific) with standard workflows. All generated peak lists were searched against a Swissprot database (version 56.2; taxonomy Homo sapiens) using Mascot version 2.3 (Matrix Science, London, United Kingdom). The search parameters included the use of trypsin as proteolytic enzyme allowing up to a maximum of 2 missed cleavages. Carbamidomethyl-cysteine was set as a fixed modification whereas oxidation of methionines were set as variable modifications. Precursor mass tolerance was set

at 50 ppm, while fragment mass tolerance was set at 0.6 Da.

Fluorescence binding assay of nanobodies on recombinant DAF protein.

Maxisorp wells were coated with recombinant DAF, 0.5 µg protein per well in 50 µl PBS, shaking for 30 min at room temperature and at 4°C overnight. Next day, unbound protein was removed by washing with PBS and wells were blocked with 4% BSA in PBS. Wells were incubated with 2 µM nanobody in 50 µl PBS for 1.5h at room temperature. Wells were washed twice with PBS. Nanobodies were detected as described above. After three washes with PBS, plates were imaged with the Odyssey imaging system at 800 nm (LI-COR).

Immunofluorescence

Cover glasses were coated with 0.2% gelatin in a 12 wells plate and $4.0x10^4$ MCF10DCIS cells were seeded. Next day, cells were blocked in 2% BSA in CO_2-independent medium for 30 min and incubated with 1 µM nanobody for 2h at 4°C. After washing twice with PBS, cells were fixed in 4% PFA, 0.1% Triton/PBS for 20 min and quenched with 100 mM glycin in PBS for 10 min. Nanobodies were detected with a rabbit anti-VHH (1:500) and DAF-FLAG was detected with mouse anti-FLAG M2 (1:500, Sigma Aldrich, Zwijndrecht, The Netherlands). Subsequently, a goat anti-rabbit Alexa488 (Life Technologies Europe BV, Bleiswijk, The Netherlands) was used for detection of anti-VHH and a goat anti-mouse Alexa555 (Life Technologies Europe BV) was used for detection of anti-FLAG M2, using a confocal microscope (Zeiss, Sliedrecht, The Netherlands).

Conjugation of IRDye700DX to nanobodies

As described before for IRDye800CW [4], the NIR fluorophore IRDye700DX (IR) was purchased as an N-hydroxysuccinimide (NHS) ester (LI-COR). The conjugation was performed with a fourfold molar excess of IR to the moles of protein, and the reaction mixture was incubated for 2h at room temperature. After conjugation, the unconjugated IR was removed using two Zeba Spin Desalting columns (Thermo Fisher Scientific, Perbio Science Nederland B.V., Etten-Leur, The Netherlands)

per protein in two sequential steps. IR-conjugated proteins (1 μg) were size-separated with 15% SDS-PAGE. Gels were stained with Coomassie Brilliant Blue solution and imaged with the Odyssey imaging system using the 700 nm channel for IR detection.

In vivo experiments

All animal experiments were approved by the Utrecht University Animal Experimental Committee (DEC no. 2012.III.02.015). The mouse model used in this study was based on a previously described model [10]. Briefly, MCF10DCIS cells were inoculated in 4th mammary glands at both sides of SCID/Beige mice. After tumor formation, mice carrying xenografts with diameters between 0.5 and 1.0 cm were selected for imaging. One week before the first nanobody injections, mice were put on alfalfa-free food in order to reduce background signal in the 700 nm channel. Mice were imaged non-invasively and invasively, after removal of the skin from the xenografts, with the Pearl Impulse Small Animal Imaging System (LI-COR) using the 700 nm channel up to 48h after injection. After drawing regions of interest (ROI) on tumor and normal tissue (hind leg), tumor-to-normal tissue ratios (TNR) were calculated using Pear Impulse Software (v.2.0, LI-COR). Mean intensities of tumor ROIs were divided by mean intensities of background ROI.

Imaging of fluorescent sections

Immediately after resection, tumors were fixed in neutral buffered formalin, routinely processed to paraffin blocks and stored in the dark until further processing. Four μm thick sections were scanned using the Odyssey imaging system at highest (21 μm) resolution and highest quality.

Immunohistochemistry

Immunohistochemistry was carried out on 4 μm thick sections. After deparaffination and rehydration, endogenous peroxidase activity was blocked for 15 min in a buffer solution pH 5.8 containing 0.3% hydrogen peroxide. After antigen retrieval, boiling for 20 min in tris/EDTA pH 9.0, slides were incubated with DAF antibody (1:100) in PBS, containing 1% BSA and sodium azide, at room temperature. Signal

was amplified using Powervision poly-HRP anti-mouse, rabbit, rat (DPVO-HRP, Immunologic, Duiven, The Netherlands) and developed with diaminobenzidine, followed by counterstaining with haematoxylin, dehydration in alcohol and mounting.

Statistics

Statistical analysis was performed using GraphPad Prism (v.5, GraphPad Software). Comparisons of TNRs of injected probes and between xenograft types were performed using the Mann-Whitney U test (two-tailed). P-values of <0.05 were considered to be statistically significant.

Results

Phage display selections

Nanobodies with specificity for hypoxic markers were selected by subtractive panning of an immune library, previously made through immunizations of llamas with hypoxic HeLa cells [11]. Phages were incubated with different numbers of normoxic HeLa cells and subsequently with hypoxic HeLa cells. Non-bound phages were removed by washing while bound phages were eluted by incubation with trypsin. Subsequently, monoclonal periplasmic fractions were isolated and screened for binding to hypoxic cells by cell-based ELISA using hypoxic and normoxic HeLa cells. Incubation with anti-CAIX antibody, as positive control for the hypoxia pathway activation, confirmed the upregulation of CAIX in hypoxic HeLa cells. Two nanobodies (A2A11 and B3C7) were selected and used for further investigations (Fig. 1A).

Nanobody characterization

Sequencing of the two clones revealed differences in CDR2 and CDR3 indicating that both nanobodies originated from different nanobody families. For affinity measurements, hypoxic HeLa cells were incubated with dilution series of both nanobodies. Based on these binding curves, dissociation constants (K_D) were calculated, which were: 14 nM and 1 nM for B3C7 and A2A11, respectively (Fig. 1B). Finally, we showed increased binding of B3C7 and A2A11 to hypoxic HeLa cells by immunofluorescence while no binding was observed after incubation with R2 negative control nanobody (Fig. 1C).

Both nanobodies were C-terminally fused with a biotinylation signal, cloned into an expression plasmid and expressed in AVB101 *E. coli* bacteria, which produce a biotin ligase. Biotinylated nanobodies were produced, purified, and used to determine the binding partners of B3C7 and A2A11. Membrane vesicles from hypoxic and normoxic HeLa cells were isolated and incubated with biotinylated nanobodies prebound to streptavidin beads. After washing, beads were loaded on SDS-PAGE, and Coomassie staining of the gels revealed bands at 55, 70 and 220

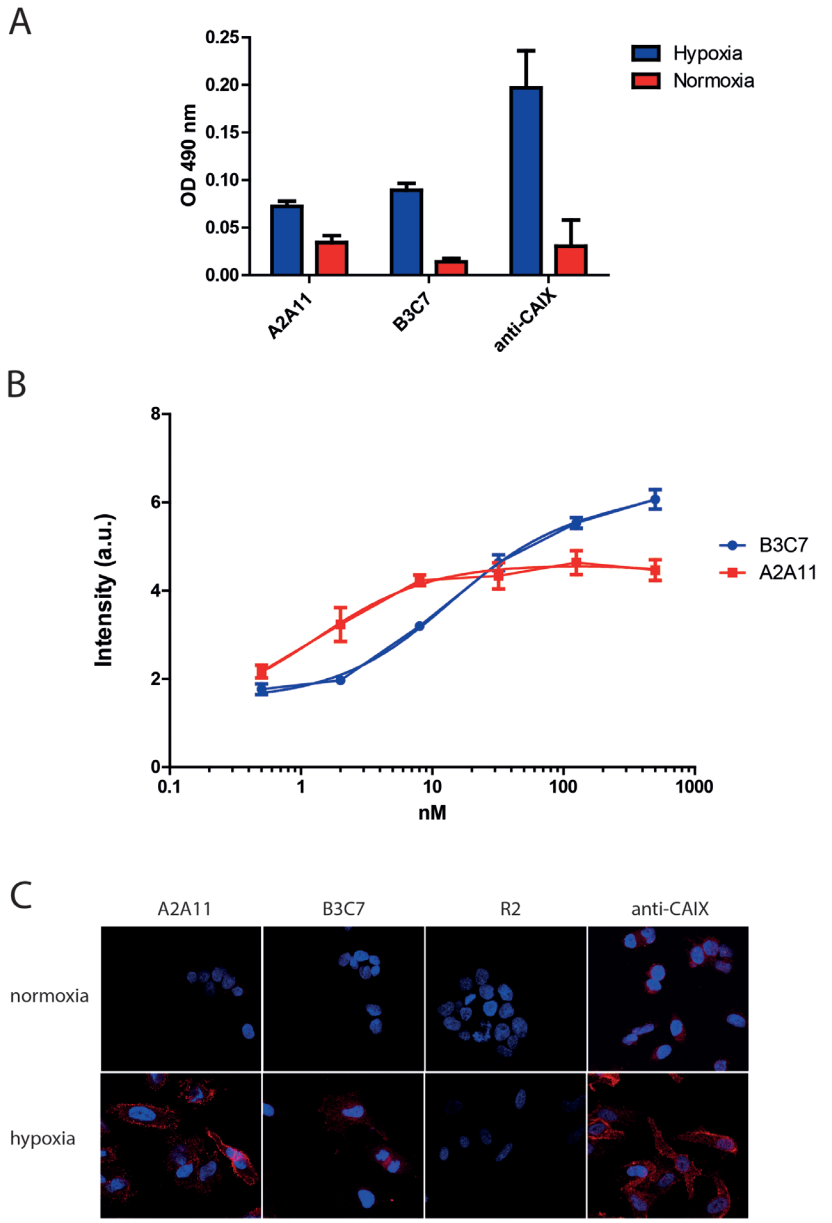

Figure 1: Two hypoxia-specific nanobodies selected by subtractive phage display selections. A. Cell-based ELISA assay using normoxic and hypoxic HeLa cells showed binding of two clones, A2A11 and B3C7 on hypoxic cells. Cells were incubated with an anti-CAIX antibody which served as control for activation of the hypoxia pathway. Bars represent means, error bars represent SEMs. B. Binding assay on hypoxic HeLa cells incubated with a nanobody concentration range in triplicate. Curves represent means, error bars represent SEMs. C. Immunofluorescence of indicated nanobodies on normoxic and hypoxic HeLa cells showing specific binding to hypoxic HeLa cells. Anti-CAIX antibody was used as positive control.

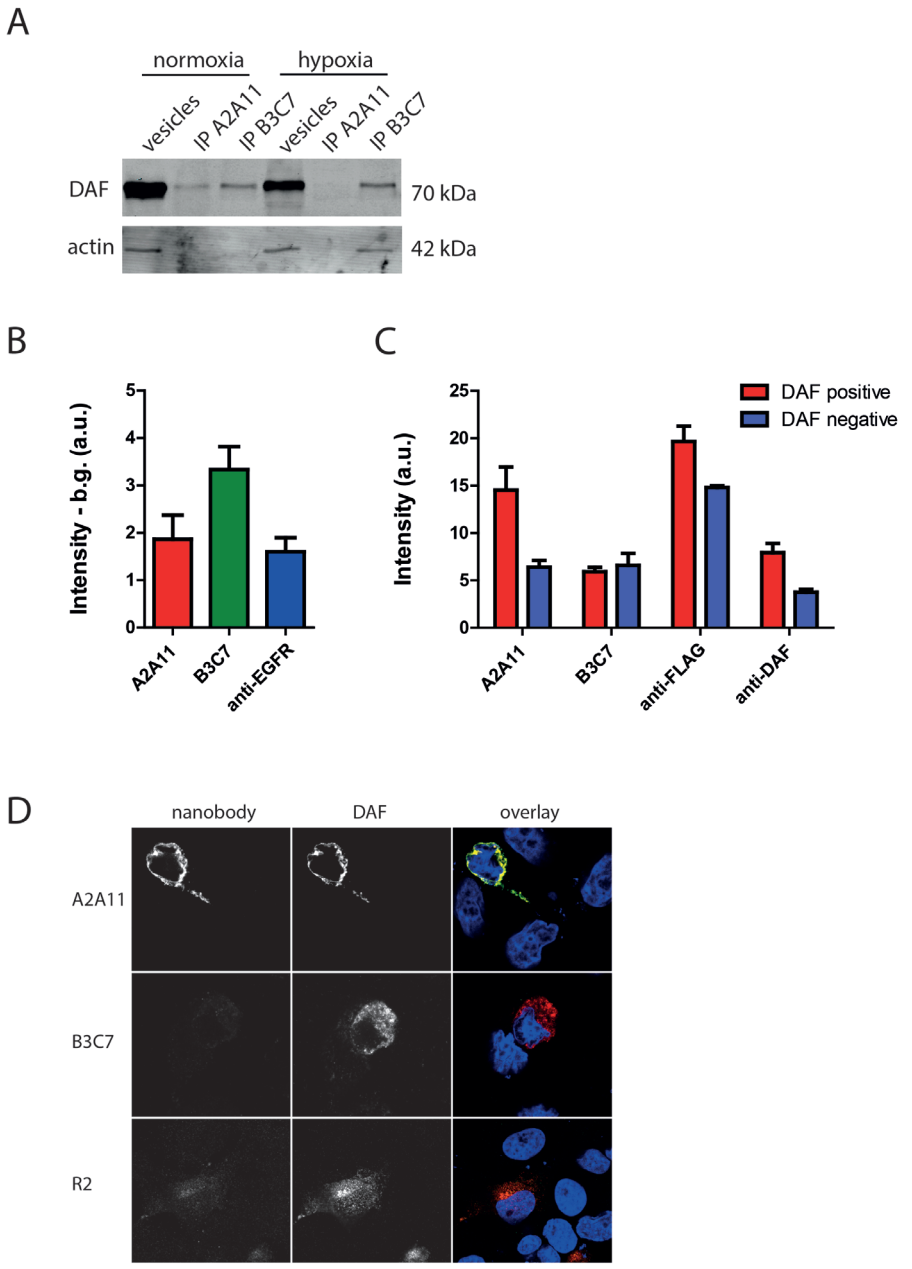

Figure 2: Nanobodies A2A11 and B3C7 recognize DAF. A. DAF western blot of normoxic and hypoxic HeLa membrane vesicles and immunoprecipitated fractions binding to A2A11 and B3C7. B. Fluorescence binding assay on deglycosylated recombinant DAF protein. Anti-EGFR nanobody as aspecific control. Bars represent means, error bars represent SEMs. C. Binding assay on DAF transfected and negative COS-7 cells. Bars represent means, error bars represent SEMs. D. Immunofluorescence of A2A11, B3C7 and R2 as negative control nanobody on mixed DAF positive and negative COS-7 cells.

kDa for both nanobodies (A2A11 and B3C7). Analysis of the predominant band at 70 kDa by mass spectrometry indicated the 'decay accelerating factor' (DAF, also known as CD55) as a strong candidate antigen of both nanobodies. DAF is a single pass transmembrane protein that is easily accessible to nanobodies during selection assays. Several assays were performed to confirm that both nanobodies were binding to DAF. First, we incubated the biotinylated nanobodies with plasma membrane fractions from normoxic and hypoxic cells and performed immunoprecipitation using streptavidin beads. Proteins were separated by SDS-PAGE and western blotting was performed with a mouse anti-DAF antibody (Fig. 2A). Bands were obtained at the expected height of 70 kDa for both nanobodies. B3C7 showed better binding to DAF than A2A11. Surprisingly, no increase in precipitation of DAF was obtained in the hypoxic fraction. Secondly, binding was investigated to the recombinant ectodomain of DAF, with negative results for both nanobodies. However, this recombinant ectodomain was heavily glycosylated and after removal of these sugar chains B3C7 showed binding (Fig. 2B). Again, no binding was observed for A2A11 and anti-EGFR nanobody, which was used as non-relevant control ($p=0.08$). Finally, we transfected COS-7 cells with cDNA encoding FLAG-tagged DAF and performed a fluorescence binding assay (Fig. 2C). Cells were incubated with A2A11, B3C7 and the R2 nanobody as negative control. DAF was detected using anti-FLAG and anti-DAF antibodies. Significantly higher intensity was observed with cells incubated with A2A11 as compared to the nontransfected cells ($p=0.03$). However, no signal was obtained with B3C7. These results were confirmed by confocal microscopy (Fig. 2D). Intense membrane staining was obtained with A2A11 but not with B3C7 (green). No fluorescence labeling was obtained with the negative control nanobody R2, while with an anti-FLAG antibody we showed labeling of cells transfected with the DAF-FLAG construct (red). In conclusion, we have selected two different nanobodies with different properties but both specific for DAF. Most probably these nanobodies recognize different epitopes on DAF. The nanobody denoted B3C7 shows binding to the recombinant, deglycosylated protein and to DAF in the immunoprecipitation. On the other hand, A2A11 performs better for immunofluorescence studies and probably recognizes DAF in its native conformation. The A2A11 nanobody was used for further studies.

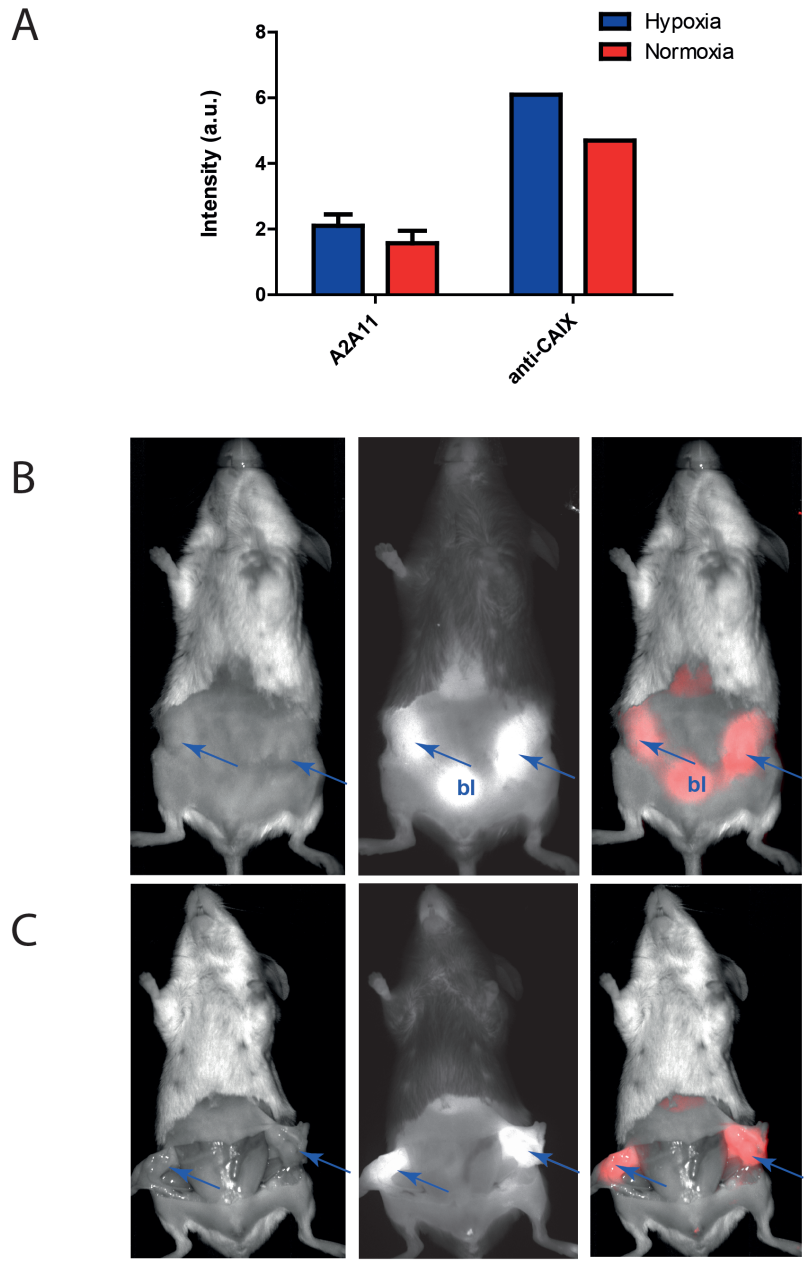

Figure 3: DAF as possible target for breast cancer imaging. A. Fluorescence binding assay on hypoxic and normoxic MCF10DCIS cells showing limited response to hypoxia (anti-CAIX antibody) and limited increased binding of A2A11 on normoxic breast cancer cells. Bars represent means, error bars represent SEMs. B. Non-invasive optical molecular imaging of hypoxic breast xenografts, 3h post injection of A2A11-IR. Left: white channel, middle: fluorescence channel (700 nm), right: overlay(arrow: tumor signal; bl: bladder signal). C. Invasive optical molecular imaging.

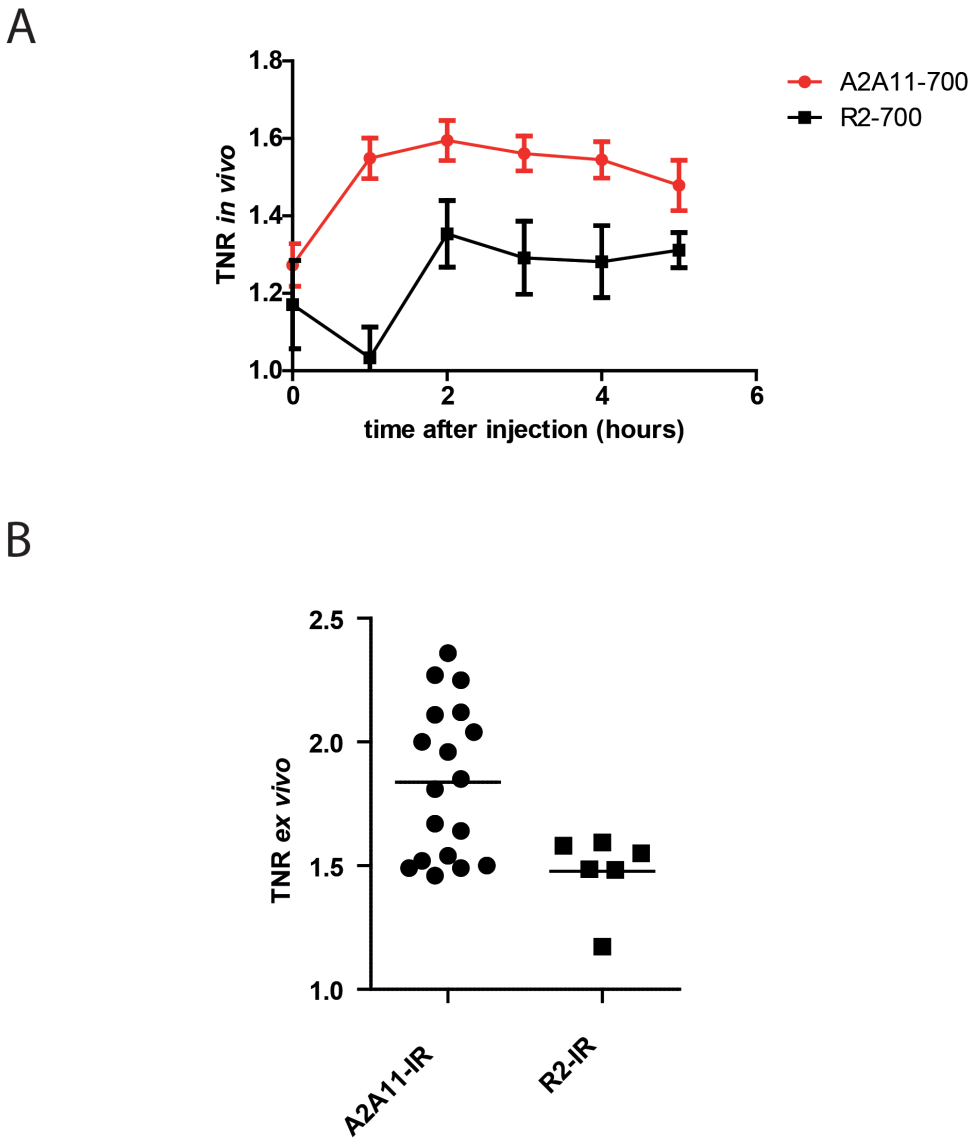

Figure 4: TNRs with molecular imaging using A2A11. A. TNRs in time, obtained by non-invasive optical molecular imaging. Compared to R2-IR, TNRs of A2A11-IR were significantly higher 2h after injection (p=0.046). Curves represent means, error bars represent SEMs. B. Single TNRs obtained with invasive imaging, 5h post injection. Horizontal bars represent means (p=0.03).

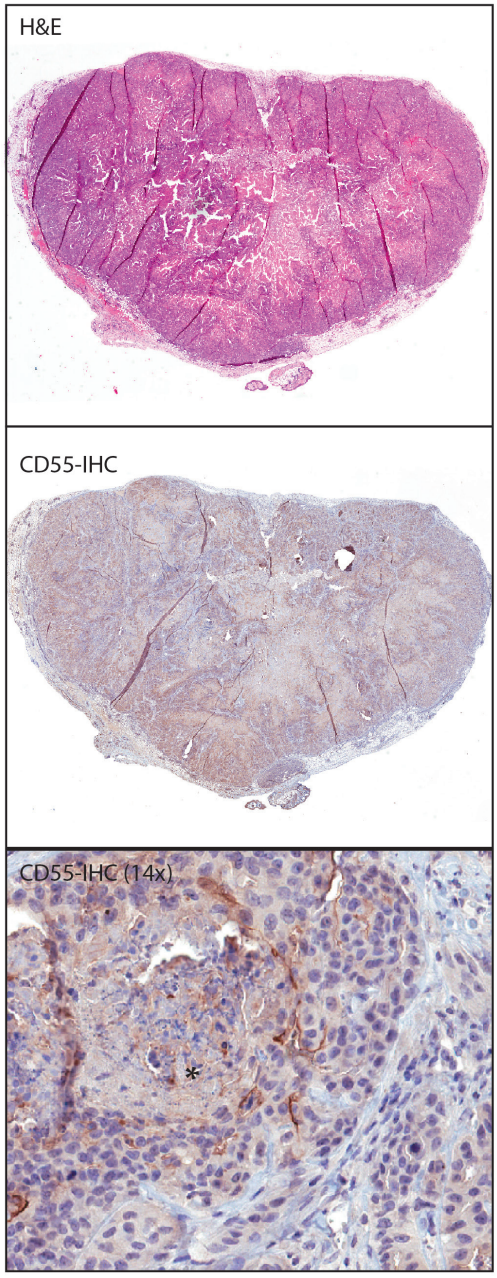

Figure 5: IHC showing DAF focally expressed in MCF10DCIS xenografts. Upper panel: H&E staining of MCF10DCIS xenograft sections. Middle panel: DAF-IHC. Lower panel: 14x magnification of DAF-IHC with necrosis (*).

Molecular imaging using anti-DAF nanobody as marker

To evaluate application of A2A11 in breast cancer, a fluorescence binding assay with normoxic and hypoxic pre-invasive breast cancer cells (MCF10DCIS) was performed. Incubation with an anti-CAIX antibody showed a limited response to hypoxia, compared to HeLa cells (Fig. 3A). A2A11 also showed a limited increase in binding to hypoxic cells (p= 0.4). A2A11 was conjugated to IRDye700DX and tested as targeted probe for optical molecular imaging of mice xenografted with MCF10DCIS cells (in both 4th mammary glands), which resemble ductal carcinoma in situ of the breast. Already 2h post injection, tumors could be delineated through fluorescent nanobody (Fig. 3B). Five hours after injection mice were sacrificed and skin was removed from both xenografts to test A2A11-IR as targeted probe in an 'image-guided surgery' setting. As shown in figure 3C, based on fluorescence signal from A2A11-IR, xenografts could be clearly delineated from surrounding tissue (muscle, fat, gland and peritoneum). TNRs were calculated non-invasively up to 5h post injection and invasively after sacrificing mice and removal of mouse skin and underlying tissue from the xenografts (Fig. 4A). After 2h, mean TNR of A2A11-IR was compared to the mean TNR of R2-IR, which was 1.6±0.05 and 1.4±0.09 (±SEM) respectively (p=0.046). During intra-operative imaging of xenografts 5h post injection, mean TNR was 1.8±0.07 for A2A11-IR, which was significantly higher than for R2-IR (1.5±0.06; p=0.03; Fig. 4B). Finally, to confirm specific uptake of A2A11-IR in the MCF10DCIS xenografts, DAF-IHC was performed showing regions of perinecrotic membranous DAF expression (Fig 5).

Discussion

As tumor hypoxia is a cancer feature and is associated with resistance against chemotherapy, early determination of the hypoxic state of solid tumors would facilitate imaging and help to determine the optimal therapeutic strategy. We set out to search for novel nanobodies binding to hypoxic marker proteins using an immune phage library obtained from immunization of llamas with hypoxic HeLa cells [11]. By subtractive panning of this nanobody phage library using normoxic and hypoxic HeLa cells we isolated two hypoxia-specific nanobodies. Sequencing revealed that especially the CDR3 (complementarity determining region 3) were different, suggesting binding to different epitopes. With immunoprecipitation followed by tryptic digestion and mass spectrometry we were able to identify the target of both nanobodies as the decay accelerating factor DAF or CD55.
Previously, Hsu et al. generated and characterized monoclonal antibodies that bound Hela cells *in vitro* to identify new targets for detection and treatment of cervical cancer. Mass spectrometry revealed DAF as molecular target [12]. Our results show that, in parallel to monoclonal antibodies, also nanobody libraries can be used to detect differences between expression levels of membrane-bound proteins in hypoxic and normoxic cells. Others have also identified DAF as tumor-specific target by subtractive panning of a human single-chain Fv phage library with a lung adenocarcinoma cell line and a non-tumor bronchial epithelial cell line for counter-selection [7]. Our study is in agreement with previous work and shows the upregulation of DAF in hypoxic HeLa cells and MCF10DCIS breast cancer cells. Already in 1987, Medof et al. identified DAF on epithelium of different origins. Also, HeLa cells were found to express DAF more than blood cells [13]. DAF helps cells to escape from complement attack [14] and plays a role in clearance of neutrophils as part of transepithelial neutrophil migration during inflammation. Furthermore, DAF was reported to have a strong relationship with hypoxia by identification of a functional binding site for HIF-1α [15], confirming our findings. In parallel to cervical cancer, it was previously shown that high DAF expression

may be a characteristic of breast cancer stem cells and that presence of cells with high expression of DAF is a sign for aggressiveness and a poor prognostic factor for breast cancer [14].

Different assays were used to demonstrate specific binding of the selected nanobodies to DAF. First, for B3C7 binding was demonstrated to deglycosylated DAF recombinant protein as opposed to glycosylated recombinant DAF. This suggests that the proteoglycans (PG) bound to the PG domain of the recombinant protein prevent binding of B3C7. Immunoprecipitations showed specific binding of both A2A11 and B3C7 to DAF. Again, better binding was observed for B3C7 suggesting that this nanobodies preferably binds to denatured DAF. This suggestion is confirmed by the observations that A2A11 binds better and with higher affinity to DAF on cells. Specificity of A2A11 for DAF was demonstrated by the difference in binding between native DAF negative COS-7 cells and cells transfected with FLAG-tagged DAF. The differences in binding properties of A2A11 and B3C7 can be explained by their differences in the sequence of the CDR2 and 3, resulting in binding to different epitopes on DAF. As A2A11 was found to bind better to the native protein on intact cells, this nanobody was used for further *in vivo* molecular imaging studies.

After identifying DAF as target for hypoxic HeLa cells we tested the applicability of A2A11 as targeted probe for optical molecular imaging of hypoxic breast cancer. We showed that targeting DAF non-invasively with optical molecular imaging results in moderate contrast. Compared to non-invasive imaging, higher TNRs were obtained after resection of the skin, mimicking 'image-guided surgery'. By IHC we showed expression of DAF in MCF10DCIS xenografts. We noticed focal perinecrotic membranous expression confirming upregulation of DAF under hypoxia. This heterogenous expression pattern might hamper the utility of DAF as target for molecular imaging and explains the moderate TNRs that we obtained in our *in vivo* study. However, as DAF is an indicator of bad prognosis in breast cancer, we propose DAF as target for molecular fluorescence pathology [8], which is probably more cost-effective and rapid than conventional IHC.

In conclusion, by performing a novel approach for the selection of nanobodies that specifically bind to hypoxic HeLa cells, we have obtained a nanobody that

specifically recognizes DAF. The lead nanobody A2A11 recognizes the native DAF protein that is predominantly present on the surface of hypoxic breast cancer cells. We have demonstrated that this nanobody can be used both for non-invasive and invasive optical molecular imaging as well as DAF expression status determination. This nanobody may contribute to better detection of tumors and tumor hypoxia, which would help to improve the diagnostic and therapeutic strategy for each individual patient.

References

1. Gatenby RA, Smallbone K, Maini PK, et al. Cellular adaptations to hypoxia and acidosis during somatic evolution of breast cancer. Br J Cancer 2007; 97: 646-653.
2. Ward C, Langdon SP, Mullen P, et al. New strategies for targeting the hypoxic tumour microenvironment in breast cancer. Cancer Treat Rev 2013; 39: 171-179.
3. Kijanka M, Warnders FJ, El Khattabi M, et al. Rapid optical imaging of human breast tumour xenografts using anti-HER2 VHHs site-directly conjugated to IRDye 800CW for image-guided surgery. Eur J Nucl Med Mol Imaging 2013.
4. Oliveira S, van Dongen GA, Stigter-van Walsum M, et al. Rapid visualization of human tumor xenografts through optical imaging with a near-infrared fluorescent anti-epidermal growth factor receptor nanobody. Mol Imaging 2012; 11: 33-46.
5. Xavier C, Vaneycken I, D'Huyvetter M, et al. Synthesis, preclinical validation, dosimetry, and toxicity of 68Ga-NOTA-anti-HER2 Nanobodies for iPET imaging of HER2 receptor expression in cancer. J Nucl Med 2013; 54: 776-784.
6. Groot AJ, El Khattabi M, Sachs N, et al. Reverse proteomic antibody screening identifies anti adhesive VHH targeting VLA-3. Mol Immunol 2009; 46: 2022-2028.
7. Ridgway JB, Ng E, Kern JA, et al. Identification of a human anti-CD55 single-chain Fv by subtractive panning of a phage library using tumor and nontumor cell lines. Cancer Res 1999; 59: 2718-2723.
8. van Brussel AS, Adams A, Vermeulen JF, et al. Molecular imaging with a fluorescent antibody targeting carbonic anhydrase IX can successfully detect hypoxic ductal carcinoma in situ of the breast. Breast Cancer Res Treat 2013; 140: 263-272.
9. Shevchenko A, Wilm M, Vorm O, et al. Mass spectrometric sequencing of proteins silver-stained polyacrylamide gels. Anal Chem 1996; 68: 850-858.
10. Behbod F, Kittrell FS, LaMarca H, et al. An intraductal human-in-mouse transplantation model mimics the subtypes of ductal carcinoma in situ. Breast Cancer Res 2009; 11: R66.
11. van Brussel AS, Adams A, Oliveira S, et al. Hypoxia-targeting fluorescent nanobodies for optical molecular imaging of pre-invasive breast cancer. Submitted, 2013
12. Hsu YT, Mohanty S, Litvinchuk A, et al. Generation and characterization of monoclonal antibodies directed against the surface antigens of cervical cancer cells. Hybrid Hybridomics 2004; 23: 121-125.
13. Medof ME, Walter EI, Rutgers JL, et al. Identification of the complement decay-accelerating factor (DAF) on epithelium and glandular cells and in body fluids. J Exp Med 1987; 165: 848-864.
14. Ikeda J, Morii E, Liu Y, et al. Prognostic significance of CD55 expression in breast cancer. Clin Cancer Res 2008; 14: 4780-4786.
15. Louis NA, Hamilton KE, Kong T, et al. HIF-dependent induction of apical CD55 coordinates epithelial clearance of neutrophils. FASEB J 2005; 19: 950-959.

PART II

Probes for optical molecular imaging of hypoxic breast cancer

Aram S.A. van Brussel, Reini van der Welle, Peter ’t Hart, Veronika Ramovs, Sabrina Oliveira, Elsken van der Wall, Paul J. van Diest, Nathaniel I. Martin, Paul M.P. van Bergen en Henegouwen

5

Hypoxia-specific optical imaging of ductal carcinoma of the breast with a near-infrared 2-nitroimidazole conjugate

Abstract

Background: Tumor-specific contrast agents are a prerequisite for optical imaging to become a successful diagnostic modality. Hypoxia is a tumor-specific condition that can be targeted to discriminate between tumor and healthy tissue. Previously, 2-nitroimidazole, a hypoxia-specific molecule, was conjugated to indocyanine green (ICG) for optical imaging of mice, resulting in limited contrast and high liver uptake. Compared to ICG, near-infrared dye IRDye800CW has much more favourable chemical properties for *in vivo* application. Therefore, we hypothesized that a specific 2-nitroimidazole-IRDye800CW conjugate (here named 2-nitro-IR) can be used to detect pre-invasive breast cancer and allows imaging before and during surgery as well as pathological evaluation after resection.

Methods: We synthesized and purified the 2-nitro-IR conjugate. Specificity for hypoxic cells was tested *in vitro* over a concentration range of both the 2-nitro-IR compound as well as the corresponding carboxylate-IRDye800CW species (carboxy-IR) which was used as a negative control. SCID/Beige mice, orthotopically transplanted with MCF10DCIS breast cancer cells, were imaged with a Pearl imager after i.v. injection of 10 nmol of 2-nitro-IR or carboxy-IR. Absolute and relative fluorescent signals were measured up to 48h. To determine probe distribution within tumors, tumors were excised and tumor sections were scanned with the Odyssey imaging system.

Results: *In vitro*, the mean fluorescent signal from hypoxic cells incubated with 2-nitro-IR was approximately two fold higher than from normoxic cells, which was not observed with the carboxy-IR control. *In vivo*, 24h after injection, mean absolute tumor signal was 0.1±0.01 (a.u.) and 0.03±0.005 for mice injected with 2-nitro-IR and carboxy-IR, respectively ($p<0.0001$). At this time point, mean absolute background signal was 0.06±0.004 and 0.02±0.001 ($p<0.0001$) for mice injected with 2-nitro-IR and carboxy-IR, respectively. Tumor-to-normal tissue ratios were not significantly different between 2-nitro-IR and carboxy-IR. Necrotic tumor sections showed higher uptake of 2-nitro-IR, as compared to carboxy-IR.

Conclusions: The 2-nitroimidazole-IRDye800CW conjugate (2-nitro-IR) specifically binds hypoxic cells. *In vivo*, tumor signals of 2-nitro-IR as well as background were significantly higher compared to control mice ($p<0.0001$) indicating that 2-nitro-IR is a promising novel probe for optical imaging.

Introduction

Breast cancer is the most common cancer among women in the Western world [1]. An important preventive measure is early detection [2]. Ductal carcinoma in situ (DCIS), which is a precursor lesion of invasive breast cancer, is detected by mammography when micro-calcifications are present [3]. However, part of DCIS tumors lack microcalcifications and when present they can be missed, e.g. in dense breast tissue, which necessitates the development of other imaging techniques for DCIS detection [4]. Molecular imaging is a rapidly evolving technology that can track single tumor cells. However, tumor-specific contrast agents are a prerequisite for molecular imaging to become a successful diagnostic imaging modality for DCIS and breast cancer detection.
Hypoxia is in most organs a tumor-specific condition that can be targeted to discriminate between tumor and healthy tissue. In the breast, hypoxia, as measured by expression of hypoxia-related proteins, is cancer-specific. Percentages of DCIS lesions reported to be hypoxic vary between 34 and 82% [5-9].

2-Nitroimidazole derivatives are molecules that form intracellular aggregates under hypoxic conditions and have been tested in clinical studies as PET tracers ([^{18}F]Faza; [^{18}F]FMISO) and as radiosensitizers and for therapy planning [10,11]. Others have conjugated 2-nitroimidazole with indocyanine green (ICG) for optical imaging of advanced solid tumors and determined the probe characteristics in a mouse model [9, 12, 13]. These ICG conjugates were reported to have sub-optimal pharmacological properties, such as high uptake in the liver, moderate optical properties and instability in aqueous media [14].
The near-infrared (NIR) dye IRDye800CW has a similar quantum yield but has favourable chemical properties for *in vivo* application compared to ICG. It shows less nonspecific binding, can be covalently conjugated to biomolecules and is approved for clinical studies [15]. Therefore, we hypothesized that a specific 2-nitroimidazole-IRDye800CW conjugate (2-nitro-IR, Fig. 1) can be used to detect pre-invasive

breast cancer lesions and that the imaging timeframe would allow imaging before and during surgery, as well as pathological evaluation after resection.

Materials and Methods

Synthesis of 2-nitroimidazole-800CW conjugate (see supplemental scheme 1)

tert-Butyl (6-(2-nitro-1H-imidazol-1-yl)hexyl)carbamate. 2-nitroimidazole (250 mg, 2.21 mmol) was dissolved in dry DMF (4.0 mL) and treated with K_2CO_3 (368 mg, 2.66 mmol) and (6-Bromo-hexyl)-carbamic acid tert-butyl ester (746 mg, 2.66 mmol) followed by stirring at 110 °C for 2h. After cooling, the DMF was removed in vacuo and the residue redissolved in EtOAc (10 mL). The EtOAc layer was washed with H_2O (3x10 mL), dried over Na_2SO_4, filtered, and evaporated. The residue was then applied to a silica column eluting with a 1:1 mixture of EtOAc/hexane to yield the desired product as a colourless oil that solidified upon storage at 4 °C (637, 93%). Analytical Data: 1H NMR (300 MHz, CDCl3) δ 7.75 (d, 1H, J = 0.9 Hz), 7.08 (d, 1H, J = 0.9 Hz), 4.52 (br s, 1H), 4.40 (t, 2H, J = 7.5 Hz), 3.10 (q, 2H, J = 6.6 Hz), 1.83 (br p, 2H, J = 7.2 Hz), 1.55-1.30 (m, 15H); 13C NMR (75 MHz, CDCl3) δ 156.0, 128.3, 125.9, 79.0, 50.2, 40.2, 30.4, 29.8, 28.4, 26.1, 26.0; MS (ESI) Calcd for C14H24N4O4Na [M+Na]+, 335.2, found 335.1.

Conjugation of 2-nitroimidazole to IRDye800CW and purification

tert-Butyl (6-(2-nitro-1H-imidazol-1-yl)hexyl)carbamate (2.0 mg, 6.5 µmol, 5 equiv.) was deprotected by treatment with 1:1 TFA/CH_2Cl_2 (5.0 mL) with stirring at room temperature for 2h. After evaporation, the residue was cooled on ice and treated with a pre-cooled 100 µL aliquot of a DMSO a solution containing the IR-Dye800CW-NHS Ester (1.5 mg, 1.3 µmol, 1 equiv.), followed by addition of N-methylmorpholine (1.4 µL, 13.0 µmol, 10 equiv.). The mixture was protected from light and stirred on ice for 4h after which it was directly applied to a preparative-scale C18 high pressure liquid chromatography (HPLC) column (26 mm inner diameter x 300mm length) using 0.1 M triethylammonium acetate buffer (pH 7.3)/acetonitrile (30–60% in 70 min) as an eluent. Following lyophilization of product-containing fractions, the triethylammonium salt of the 2-nitro-IR conjugate was obtained as a dark green solid (1.8 mg, 92%). Analytical HPLC indicated a product purity of

>95% and mass spectrometry confirmed the expected molecular weight: MS (ESI negative mode) Calcd for $C_{55}H_{67}N_6O_{16}S_4$ [M-H]-, 1195.4, found 1195.7.

Cell culture

HeLa cervical carcinoma cells (ATCC, Wesel, Germany) were grown in Dulbecco's Modified Eagle's Medium (DMEM; Invitrogen, Breda, The Netherlands) supplemented with 10% (v/v) Fetal Calf Serum, 100 IU/ml penicillin, 100 µg/ml streptomycin, and 2 mM L-glutamine. MCF10DCIS.com (further referred to as MCF10DCIS) cells (Asterand, Detroit, USA) were cultured according to the supplier's guidelines in DMEM/F12, supplemented with 10% (v/v) FCS, 100 IU/ml penicillin, 100 µg/ml streptomycin and 2 mM L-glutamine. All cells were cultured at 37°C in a humidified atmosphere containing 5% CO_2.

2-Nitro-IR binding assay

HeLa cells were seeded (40,000 cells/well) in twelve-well plates as described previously [13]. Plates were exposed to hypoxic (1% O_2, in INVIVO2 hypoxia workstation, Ruskinn, Pencoed, UK) or normoxic (21% O_2) conditions for 17h. Equal amounts of 2-nitro-IR and carboxy-IR were determined by titration using the Odyssey imaging system (LI-COR Biosciences, Lincoln, Nebraska, USA). Cells were incubated with 1, 3 and 5 µM 2-nitromidazole-IRDye or carboxy-IR in PBS for 30 min. To release unbound probe, cells were put on fresh medium for 1h (normoxic conditions). Cells were washed twice in ice-cold PBS. The detection of 2-nitro-IR and carboxy-IR was performed using the 800 nm channel of the Odyssey imaging system. Cells were incubated with MabCAIX to check for upregulation of carbonic anhydrase IX (CAIX) in hypoxic cells, as control for hypoxia.

Near-infrared fluorescence microscopy

HeLa cells were grown on cover slips for 1 day either at 21% O_2 or at 1% O_2 and 5% CO_2. Cells were washed with sterile, ice-cold PBS and incubated for 1.5h at 4°C with 7 µM 2-nitroimidazole-IR and carboxylate-IR (carboxy-IR), a non-reactive form of IRDye, as negative control, in PBS. Cells were washed with PBS, stained with DAPI (Roche, Almere, The Netherlands) and fixed in 4% paraformaldehy-

de. Cells were imaged using an inverted microscope (TE2000, Nikon Instruments Europe B.V., Ham, UK). For our purposes the Hg-excitation appendage of the microscope was removed. Excitation was achieved by focusing light from a 760nm high-power AlGaAs LED (SMB760-1100-03-I, Epitex Inc. Japan) into a 60x 1.49NA oil-objective of the microscope. Excitation and IRDye-fluorescence were separated using a dedicated dichroic/filter set (set 41037, Chroma Technology, Olching, Germany). Images were recorded with an EMCCD-camera (Ixon+, Andor, Ireland) and a shutter was used to synchronize the excitation-illumination with the recording-interval to minimize bleaching.

In vivo experiments

All animal experiments were approved by the Utrecht University Animal Experimental Committee (DEC no. 2012.III.02.015). The mouse model used in this study was based on a previously described model [16]. Five-week old female SCID/Beige (CB17 Cg-PrkdcSCIDlystBG/Crl) immunodeficient mice (Harlan Laboratories, Horst, The Netherlands) were orthotopically transplanted as described before [17]. Approximately $4x10^4$ luciferase-expressing MCF10DCIS cells were injected using a 10 µl Hamilton syringe in the left 4^{th} (inguinal) mammary fat pad. Tumor growth was monitored on a weekly basis using bioluminescence imaging (Photon Imager, BiospaceLabs, Paris, France). Upon development of palpable tumors, tumor growth was monitored manually on a weekly basis. When tumors reached ~0.5 cm^3, mice were depilated ventrally using Veet depilatory cream (Reckitt Benckiser, The Netherlands) and imaged. To assure equal carboxy-IR and 2-nitro-IR fluorophore levels, probes were calibrated by scanning concentration ranges with the Odyssey imaging system. Ten nmol of 2-nitro-IR and the equivalent of the negative control carboxy-IR was intravenously injected in the tail vein. Imaging was performed with a Pearl imager (LI-COR).

Imaging of fluorescent sections

Immediately after resection, tumors were fixed in neutral buffered formalin, embedded in paraffin and stored in the dark until further processing to sections. Because deparaffination would cause washout of probe, 4 µm thick paraffin sections

were scanned using the Odyssey imaging system at 21 μm resolution and highest quality. In order to show necrotic areas, haematoxylin and eosin (H&E) stainings were performed.

Image analysis for assessment of tumor-to-normal tissue ratios

Regions of interest (ROI) were drawn around the tumor and background regions and tumor-to-normal tissue ratios (TNR) were calculated for each time point and each tumor using Pearl impulse software v2.0 (LI-COR). The hind legs were used as background.

Statistics

Statistical analysis was performed using GraphPad Prism. Comparisons of TNRs of injected probes, were performed using the Mann-Whitney U test (two-tailed). P-values of <0.05 were considered to be statistically significant.

Results

Conjugation of 2-nitroimidazole to IRDye800CW and purification

After synthesis of 2-nitroimidazole with a primary amino group, the 2-nitroimidazole-IRDye conjugate (2-nitro-IR; Fig 1A) was successfully synthesized by linking the IRDye800CW NHS ester to the primary amino group of 2-nitroimidazole. The conjugate was purified by C18 reverse-phase HPLC and the purity and identity of the compound was confirmed by 1H and 13C NMR and negative-mode MALDI MS analysis. As negative control we used carboxylate-IRDye800CW (carboxy-IR; Fig. 1B).

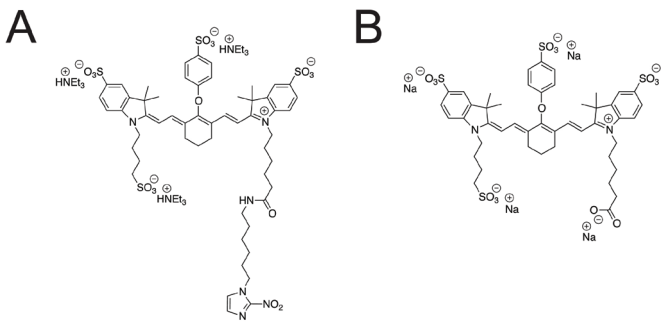

Figure 1: A. Structure of 2-nitroimidazole-IRDye800CW (2-nitro-IR) B. Structure of carboxylate-IRDye800CW (carboxy-IR).

Characterization of 2-nitro-IR

To evaluate 2-nitro-IR as an hypoxia-specific marker, an *in vitro* assay was performed on hypoxic and normoxic HeLa cells. Cells were incubated with different concentrations (1-5 μM) of 2-nitro-IR for 30 min at 37°C. To estimate cellular uptake of the conjugate, the cells were scanned with the Odyssey imager at 800 nm. An increase in signal was observed at higher concentrations of 2-nitro-IR. An approximately 2 fold difference was observed in the mean signal at 5 μM between hypoxic (151.1±31.6; mean±SEM) and normoxic cells (74.8±5.2; $p<0.0001$; Fig. 2A). After determining the optimum concentration, hypoxic and normoxic cells were incubated with 5 μM 2-nitro-IR and the fluorescence signal was compared to that of cells that were incubated with an equal amount of carboxy-IR. Mean fluorescence intensity from hypoxic cells incubated with 2-nitro-IR was significantly higher than the mean intensity from hypoxic cells incubated with carboxy-IR ($p=0.03$). Moreover, at higher concentrations an increase in fluorescence was observed for hypoxic cells after incubation with 2-nitro-IR in contrast to the negative control probe carboxy-IR (Fig. 2B). The anti-CAIX antibody was used as control for the hypoxia response of the HeLa cells (Fig. 2B).

Probe localization was determined with near-infrared fluorescence microscopy. HeLa cells were seeded on coverslips and grown under hypoxic or normoxic conditions. Cells were incubated with 5 μM 2-nitro-IR or carboxy-IR 30 min at 37°C. A perinuclear endosomal-like pattern was observed in hypoxic cells incubated with 2-nitroimidazole, which was hardly visible in normoxic cells. The cells incubated with carboxy-IR showed a diffuse cytoplasmic pattern which was less strong than the signal from cells incubated with 2-nitro-IR (Fig. 2C). In conclusion, we have successfully produced the 2-nitro-IR conjugate and demonstrated the specificity for hypoxic HeLa cells.

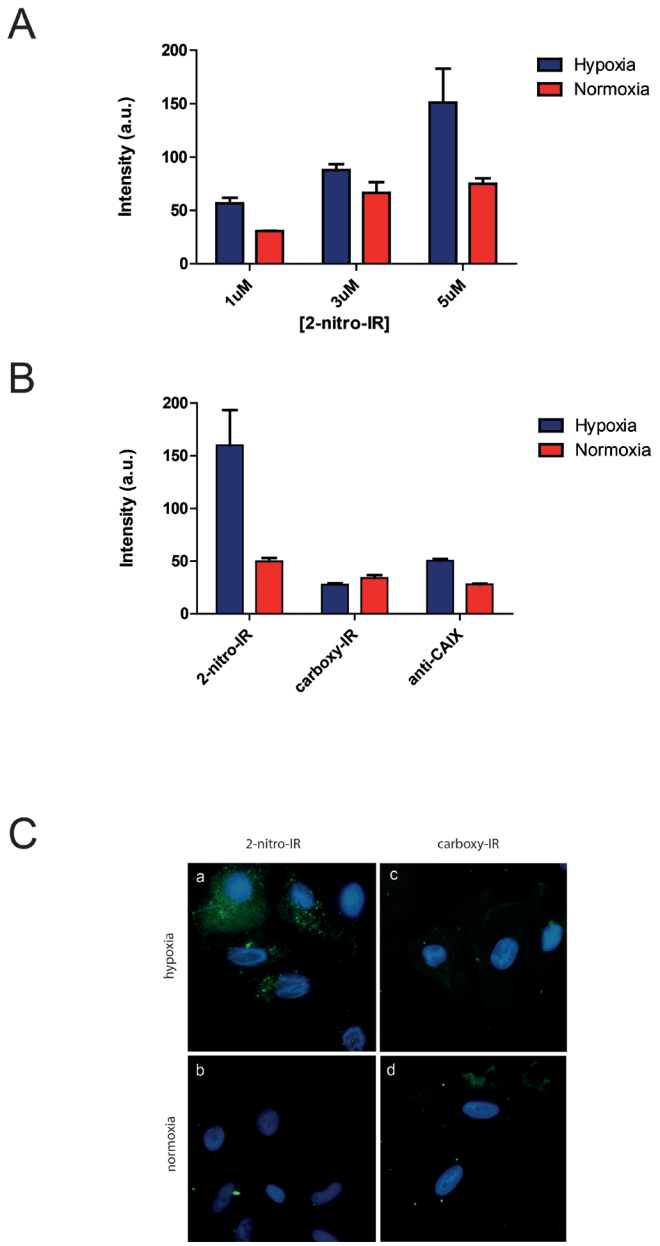

Figure 2: 2-nitro-IR specifically binds to hypoxic cells. A. Hypoxic and normoxic HeLa cells were incubated with a concentration range of 2-nitro-IR and fluorescence intensity was determined. B. Comparison of fluorescent intensities of hypoxic and normoxic HeLa cells incubated with 5 µM 2-nitro-IR, carboxy-IR or a CAIX-specific antibody. C. Near-infrared fluorescence microscopy of hypoxic and normoxic HeLa cells incubated with either 2-nitro-IR (a,b) or carboxy-IR (c,d).

In vivo experiments

SCID/Beige immunodeficient mice were orthotopically transplanted with MCF10DCIS cells in the left and right 4th (inguinal) mammary fat pad. Upon development of palpable tumors, mice were intravenously injected in the tail vein with 2-nitro-IR or carboxy-IR. Mice were imaged regularly up to 72h after injection using the Pearl imager. Tumors of both 2-nitro-IR and carboxy-IR were visible from 24h after injection up to 72h (Fig. 3A). Both tumor and background signals from mice injected with 2-nitro-IR were higher than from mice injected with carboxy-IR. After imaging *in vivo*, mice were sacrificed and the skin was removed from the xenografted mammary glands. Although tumors were visible in both mice 24h after injection with either 2-nitro-IR or carboxy-IR, higher fluorescence intensities were observed in mice injected with 2-nitro-IR (Fig. 3B).

To visualize the distribution of both probes within the tumor, sections were prepared and scanned with the Odyssey imaging system. Tumor sections from mice injected with 2-nitro-IR showed uptake in and around necrotic tumor regions 24h after injection (Fig. 3C, left). Carboxy-IR also showed some tumor uptake (Fig. 3C, right). H&E stainings were performed to show necrotic tumor areas, which colocalized with 2-nitro-IR uptake.

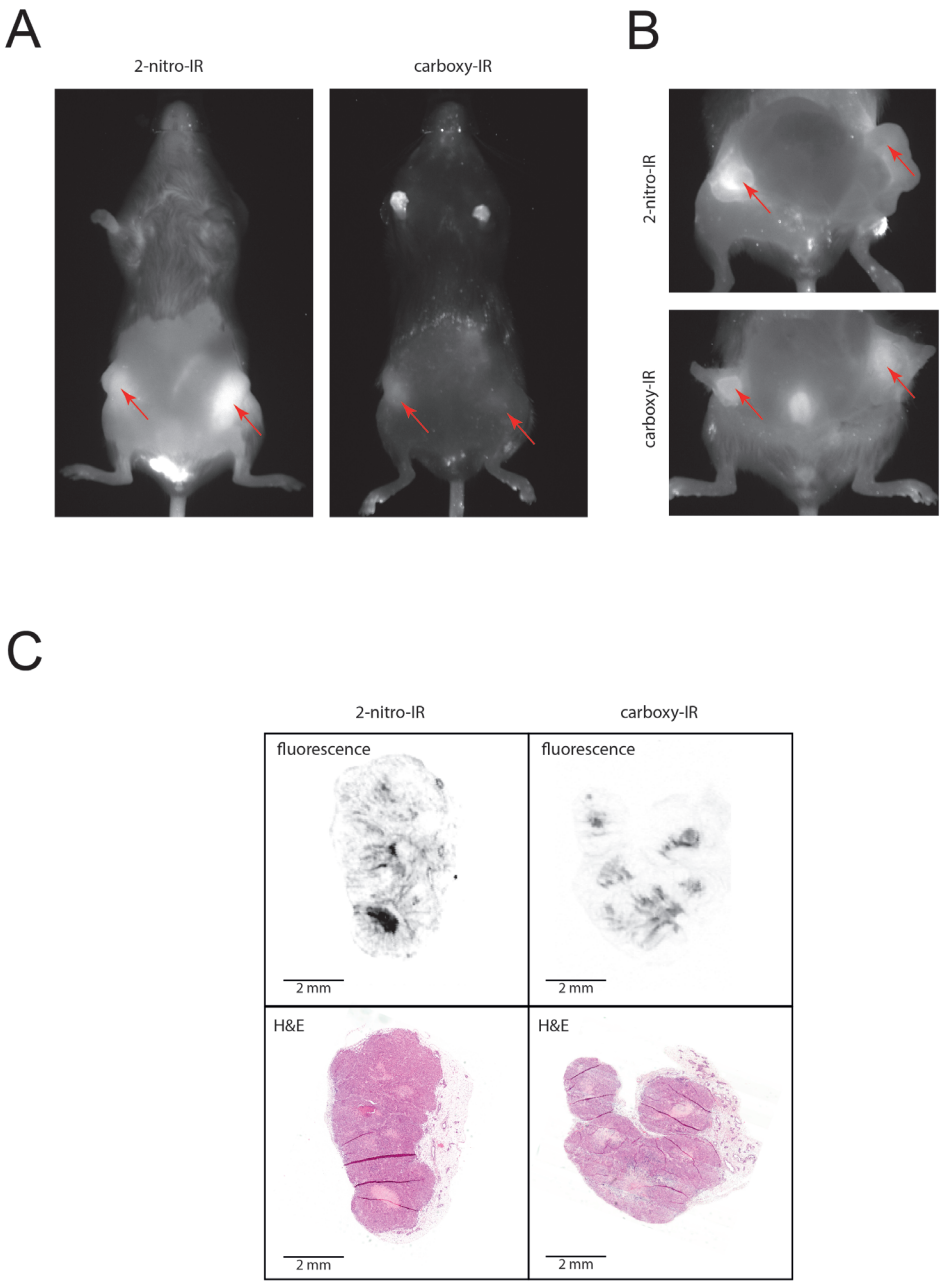

Figure 3: 2-nitro-IR accumulates in human breast cancer xenografts A. Imaging of mice bearing breast cancer xenografts (arrows), 24h after injection of 2-nitro-IR (left) or carboxy-IR (right). B. *Ex vivo* imaging 24h after injection. Skin is removed from the tumors. C. Fluorescent signal and H&E stainings from sections of mice injected with 2-nitro-IR or carboxy-IR.

Image analysis

Mice injected with either 2-nitro-IR or carboxy-IR were imaged up to 72h and the absolute tumor and background signals were determined. Background signals were determined on the hind leg. A significant difference was observed in fluorescence signal between mice injected with 2-nitro-IR and carboxy-IR indicating the specific tumor uptake of 2-nitro-IR (Fig. 4A). At 24h after injection, the mean absolute tumor signal was 0.1±0.01 (a.u.) and 0.03±0.005 for mice injected with 2-nitro-IR and carboxy-IR, respectively ($p<0.0001$). Also at the 24h time point, the mean absolute background signals from mice injected with 2-nitro-IR were significantly higher than from mice injected with carboxy-IR, 0.06±0.004 and 0.02±0.001 ($p<0.0001$) for mice injected with 2-nitro-IR and carboxy-IR respectively (Fig. 4A, B).

The imaging window for 2-nitro-IR and carboxy-IR was estimated by calculating TNRs for each time point after injection. For both probes an increase in TNR was observed during the first 24h. At the 24h time point mean TNR for 2-nitro-IR was 1.7±0.1 and 2.0±0.2 for carboxy-IR (n.s.). After the 24h time point a plateau phase was observed up to 72h after injection (Fig. 4C).

A similar observation was made by *ex vivo* imaging. Mice were sacrificed 24h after injection of 2-nitro-IR or carboxy-IR. Skin was removed from the tumors, tumors were imaged and *ex vivo* TNRs were calculated (Fig. 4D). Mean TNR for 2-nitro-IR was 1.8±0.2 (n=10) and 2.4±0.4 (n=6) for carboxy-IR (n.s.) (Fig. 4D). Although higher tumor signals were observed in mice injected with 2-nitro-IR, higher background signal resulted in TNRs that were not significantly different from the negative control (carboxy-IR).

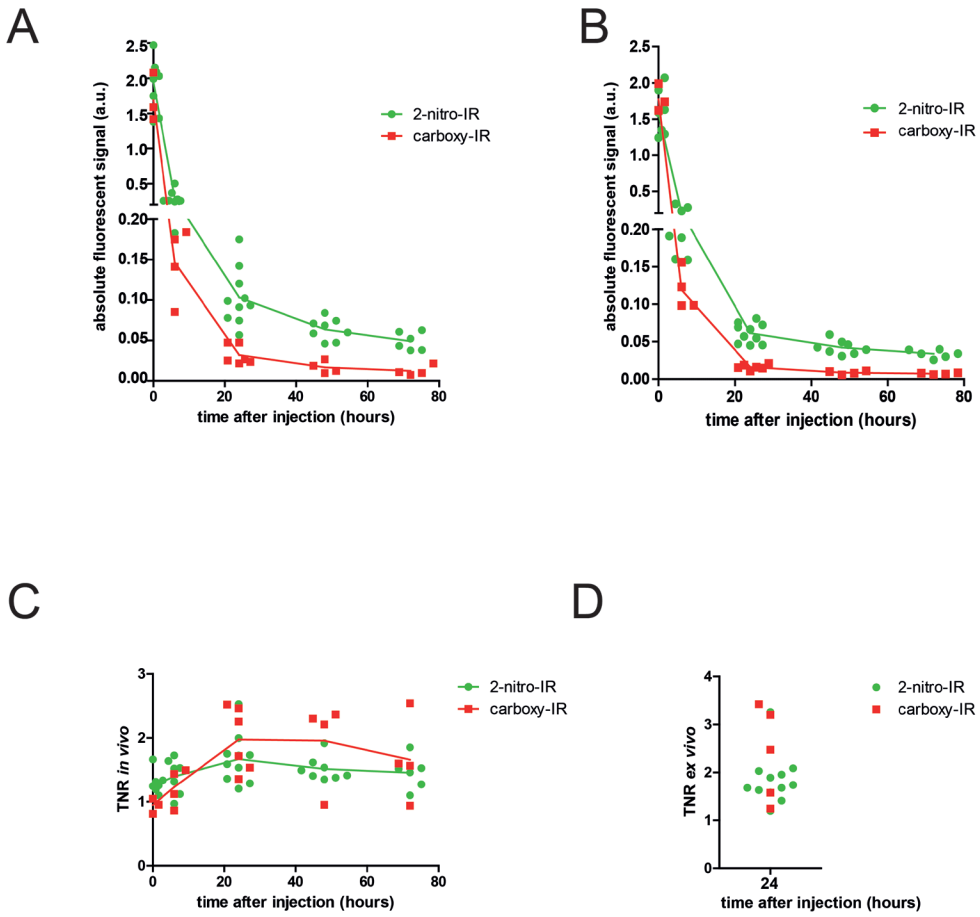

Figure 4: Higher absolute tumor and background signals of 2-nitro-IR result in moderate TNRs Mice were injected with 2-nitro-IR or carboxy-IR and imaged up to 72h. Absolute tumor signals (A) and background signals (B) were determined and TNRs were calculated (C). For *ex vivo* imaging, mice were sacrificed 24h after injection of 2-nitro-IR or carboxy-IR. Skin was removed from the tumors, imaged and *ex vivo* TNRs were calculated by image analysis (D).

Discussion

Optical molecular imaging has recently gained much attention as it may provide tumor information *in vivo*. Successful early detection and subsequent removal of pre-invasive breast lesions can prevent progression to invasive cancer. In addition, adequate surgical removal of invasive cancers and their surrounding precursors reduces the percentage of breast cancer patients that eventually develop recurrence and metastases [18-21]. Molecular imaging of (breast) cancer using optical probes is a rapidly developing field and novel imaging probes are under development.
As hypoxia is a general property of solid tumors, several probes (e.g. antibodies) have been developed that detect hypoxic cells. As general marker for hypoxia, 2-nitroimidazoles have frequently been used to detect hypoxic tumor regions with indirect methods such as immunohistochemistry, and direct methods after conjugation to a radioisotope [10, 11]. Application of 2-nitro-IR as marker for hypoxia is advantageous compared to antibodies because it is not specific for a certain species and could be applied in various small and large animal models. Furthermore, as hypoxia is a general phenomenon across malignancies, 2-nitro-IR could be used to image solid cancers from a different origin as well. Application of radiolabelled 2-nitroimidazoles appeared to be feasible in clinical studies showing effective imaging at non-toxic doses [10, 11]. 2-Nitroimidazoles conjugated to the fluorescent dye ICG were evaluated by others *in vitro* and *in vivo* for their use in optical imaging as well [12, 13, 22].
In the present study, we have successfully labelled 2-nitroimidazole with the NIR fluorescent dye IRDye800CW that has been approved for clinical studies [23]. By *in vitro* studies we demonstrated specific binding of 2-nitro-IR to hypoxic HeLa cells. With near-infrared fluorescence microscopy we showed 2-nitroimidazole binding in a perinuclear endosomal-like pattern, specific for cells cultured under hypoxia. 2-Nitroimidazole is known to bind thiol groups of proteins under hypoxic conditions [24]. The identities of the proteins nor the endosomes stained by 2-nitro-IR are known.

For *in vivo* characterization of 2-nitro-IR we used a SCID/Beige mouse model with MCF10DCIS xenografts as previously described [17, 25]. This mouse model was first described by Behbod et al. [16]. The MCF10DCIS xenografts resemble human ductal carcinoma in situ (DCIS), the recognized form of pre-invasive breast cancer. The absolute fluorescence intensities of 2-nitro-IR injected mice were significantly higher than that of control carboxy-IR injected mice. However, also the 2-nitro-IR background was significantly higher than that of carboxy-IR resulting in moderate TNRs. The reason for this high fluorescence background in mice is not known, especially considering the low signal from normoxic HeLa cells *in vitro*. A likely explanation is that the anesthesia using inhalatory isoflurane might have caused low oxygen tensions, as has been described before in mice and patients [26, 27], causing the 2-nitro-IR to aggregate in non-tumor tissues as well. Furthermore, tumor uptake of carboxy-IR was observed, resulting in relatively high TNRs in the control group. Tumor retention of carboxy-IR was reported earlier by Zhou et al. [28]. In this study, mean TNRs of 1.4 were measured *ex vivo* in a mouse model with brain tumor xenografts 24h after injection with carboxy-IR, confirming aspecific uptake of the dye. This may be caused by the enhanced permeability and retention (EPR) effect, as a result of the better vascularization of the xenografts. Accumulation of 2-nitro-IR may therefore be the result of two phenomena: specific binding to hypoxic cells and better tumor accumulation as a result of the EPR effect.
In conclusion, we have synthesized a hypoxia-specific optical probe by coupling 2-nitroimidazole to IRDye800CW as fluorescent label. We have demonstrated hypoxia-specificity *in vitro*. *In vivo* higher tumor uptake was observed with 2-nitro-IR compared to the control tracer but as the background was also significantly higher, the resulting TNRs were not significantly higher. Coupling multiple 2-nitroimidazole molecules to a single dye might result in higher TNRs. Alternatively, higher TNRs might be obtained when 2-nitro-IR is used in a multispectral approach, in combination with other hypoxia-specific probes such as anti-CAIX nanobodies.

References

1. www.cijfersoverkanker.nl
2. Verbeek AL, Broeders MJ, Otto SJ, et al. [Effects of the population screening into breast cancer]. Ned Tijdschr Geneeskd 2013; 157: A5218.
3. Cho KR, Seo BK, Kim CH, et al. Non-calcified ductal carcinoma in situ: ultrasound and mammographic findings correlated with histological findings. Yonsei Med J 2008; 49: 103-110.
4. Peters G, Jones CM, Daniels K. Why is microcalcification missed on mammograp hy? J Med Imaging Radiat Oncol 2013; 57: 32-37.
5. Bos R, Zhong H, Hanrahan CF, et al. Levels of hypoxia-inducible factor-1 alpha during breast carcinogenesis. J Natl Cancer Inst 2001; 93: 309-314.
6. van der Groep P, van Diest PJ, Smolders YH, et al. HIF-1alpha overexpression in ductal carcinoma in situ of the breast in BRCA1 and BRCA2 mutation carriers. PLoS One 2013; 8: e56055.
7. Wang Z, Shi Q, Gu Y, et al. Clinicopathologic correlation of cancer stem cell markers CD44, CD24, VEGF and HIF-1alpha in ductal carcinoma in situ and invasive ductal carcinoma of breast: an immunohistochemistry-based pilot study. Pathol Res Pract 2011; 207: 505-513.
8. Chen CL, Chu JS, Su WC, et al. Hypoxia and metabolic phenotypes during breast carcinogenesis: expression of HIF-1alpha, GLUT1, and CAIX. Virchows Arch 2010; 457: 53-61.
9. Okada K, Osaki M, Araki K, et al. Expression of hypoxia-inducible factor (HIF-1alpha), VEGF-C and VEGF-D in non-invasive and invasive breast ductal carcinomas. Anticancer Res 2005; 25: 3003-3009.
10. Postema EJ, McEwan AJ, Riauka TA, et al. Initial results of hypoxia imaging using 1-alpha-D: -(5-deoxy-5-[18F]-fluoroarabinofuranosyl)-2-nitroimidazole (18F-FAZA). Eur J Nucl Med Mol Imaging 2009; 36: 1565-1573.
11. Shi K, Souvatzoglou M, Astner ST, et al. Quantitative assessment of hypoxia kinetic models by a cross-study of dynamic 18F-FAZA and 15O-H2O in patients with head and neck tumors. J Nucl Med 2010; 51: 1386-1394.
12. Okuda K, Okabe Y, Kadonosono T, et al. 2-Nitroimidazole-tricarbocyanine conjugate as a near-infrared fluorescent probe for in vivo imaging of tumor hypoxia. Bioconjug Chem 2012; 23: 324-329.
13. Youssif BG, Okuda K, Kadonosono T, et al. Development of a hypoxia-selective near-infrared fluorescent probe for non-invasive tumor imaging. Chem Pharm Bull (Tokyo) 2012; 60: 402-407.
14. Choi HS, Nasr K, Alyabyev S, et al. Synthesis and in vivo fate of zwitterionic near-infrared fluorophores. Angew Chem Int Ed Engl 2011; 50: 6258-6263.
15. Heuveling DA, Visser GW, de Groot M, et al. Nanocolloidal albumin-IRDye 800CW: a near-infrared fluorescent tracer with optimal retention in the sentinel lymph node. Eur J Nucl Med Mol Imaging 2012; 39: 1161-1168.
16. Behbod F, Kittrell FS, LaMarca H, et al. An intraductal human-in-mouse transplantation model mimics the subtypes of ductal carcinoma in situ. Breast Cancer Res 2009; 11: R66.
17. van Brussel AS, Adams A, Vermeulen JF, et al. Molecular imaging with a fluorescent antibody targeting carbonic anhydrase IX can successfully detect hypoxic ductal carcinoma in situ of the breast. Breast Cancer Res Treat 2013; 140: 263-272.

18. Sakorafas GH, Farley DR, Peros G. Recent advances and current controversies in the management of DCIS of the breast. Cancer Treat Rev 2008; 34: 483-497.
19. Cutuli B, Lemanski C, Le Blanc-Onfroy M, et al. Local recurrence after ductal carcinoma in situ breast conserving treatment. Analysis of 195 cases. Cancer Radiother 2013; 17: 196-201.
20. Lee LA, Silverstein MJ, Chung CT, et al. Breast cancer-specific mortality after invasive local recurrence in patients with ductal carcinoma-in-situ of the breast. Am J Surg 2006; 192: 416-419.
21. Shamliyan T, Wang SY, Virnig BA, et al. Association between patient and tumor characteristics with clinical outcomes in women with ductal carcinoma in situ. J Natl Cancer Inst Monogr 2010; 2010: 121-129.
22. Biswal NC, Pavlik C, Smith MB, et al. Imaging tumor hypoxia by near-infrared fluorescence tomography. J Biomed Opt 2011; 16: 066009.
23. Marshall MV, Draney D, Sevick-Muraca EM, et al. Single-dose intravenous toxicity study of IRDye 800CW in Sprague-Dawley rats. Mol Imaging Biol 2010; 12: 583-594.
24. Zhou Z, Wagh NK, Ogbomo SM, et al. Synthesis and In Vitro and In Vivo Evaluation of Hypoxia-Enhanced 111In-Bombesin Conjugates for Prostate Cancer Imaging. J Nucl Med 2013.
25. Vermeulen JF, van Brussel AS, Adams A, et al. Near-infrared fluorescence molecular imaging of ductal carcinoma in situ with CD44v6-specific antibodies in mice: a preclinical study. Mol Imaging Biol 2013; 15: 290-298.
26. Aust H, Eberhart LH, Kranke P, et al. [Hypoxemia after general anesthesia]. Anaesthesist 2012; 61: 299-309.
27. Baudelet C, Gallez B. Effect of anesthesia on the signal intensity in tumors using BOLD-MRI: comparison with flow measurements by Laser Doppler flowmetry and oxygen measurements by luminescence-based probes. Magn Reson Imaging 2004; 22: 905-912.
28. Zhou H, Luby-Phelps K, Mickey BE, et al. Dynamic near-infrared optical imaging of 2-deoxyglucose uptake by intracranial glioma of athymic mice. PLoS One 2009; 4: e8051.

Additional files

Aram S.A. van Brussel*, Arthur Adams*, Jeroen F. Vermeulen, Sabrina Oliveira,
Elsken van der Wall, Willem P.Th.M. Mali, Paul J. van Diest, and
Paul M.P. van Bergen en Henegouwen
* These authors contributed equally

6

Molecular imaging with a fluorescent antibody targeting carbonic anhydrase IX can successfully detect hypoxic ductal carcinoma in situ of the breast

Abstract

Introduction: Ductal carcinoma in situ (DCIS) of the breast is difficult to remove completely during surgery as it is not palpable and can therefore require re-excision. Real-time visualization of DCIS using near-infrared fluorescent probes could help the surgeon during surgery as well as the pathologist post-operatively to distinguish tumor from healthy tissue. As hypoxia-induced necrosis is a common phenomenon in DCIS, we investigated the molecular imaging of DCIS using a fluorescent antibody targeting an hypoxia marker, carbonic anhydrase IX (CAIX), in a preclinical mouse model.

Methods: A monoclonal antibody against human CAIX was fluorescently labelled with the near-infrared dye IRDye800CW and characterized *in vitro*. An *in vivo* study was performed in SCID/Beige mice that were orthotopically transplanted with human breast cancer cells mimicking human DCIS (MCF10DCIS) and MCF10DCIS stably expressing CAIX. A clinically approved fluorescence imaging system was used to monitor probe uptake and to determine tumor-to-normal tissue ratios (TNR).

Results: Mean *in vivo* TNR of CAIX transduced (CAIX+) tumors was 7.5±0.5. Mean *in vivo* TNR of DCIS tumors with hypoxic areas reached a plateau level at 48h after injection of 2.1±0.1 (mean ± SEM) compared to 1.7±0.1 in DCIS without hypoxic areas. Mean intra-operative TNR of DCIS tumors with necrotic regions was higher than of DCIS tumors without necrotic regions 96h after injection: 2.9±0.1 and 1.5±0.1 respectively, while the TNR of CAIX+ tumors was 11.2±1.0. Specific tumor uptake of MabCAIX-IRDye800CW was confirmed by a biodistribution assay, and immunofluorescence imaging on tumor sections showed specific uptake in hypoxic tumor regions, with higher contrast than conventional chromagen based immunohistochemistry.

Conclusions: Molecular fluorescent imaging with MabCAIX-IRDye800CW can be successfully used to detect hypoxic DCIS before and during surgery to facilitate radical resection. Furthermore, it allows for sensitive CAIX specific immunofluores-

cence microscopy of tumor sections, thereby introducing the concept of 'molecular fluorescence pathology'.

Introduction

Ductal carcinoma in situ (DCIS) is difficult to remove completely during surgery as it is not palpable and spreads through the breast following the ever branching ductal tree. This can require re-excision and could lead to recurrence after irradical excision which affects survival, especially in high grade DCIS [1-4]. Therefore, accurate imaging of DCIS could improve detection and subsequent radical resection of DCIS. Molecular imaging allows for tumor detection at (sub)cellular level and can be used for screening, diagnosis, image-guided surgery, and even post-operatively to evaluate expression of tumor markers in tumor specimens [5]. Molecular imaging requires tumor-specific probes, consisting of a tracer (either radioactive isotopes or fluorophores) and a targeting unit, e.g. peptides or antibodies, providing high specificity to molecules that are abundantly present in tumor tissue, but are absent (or rare) in normal tissue. In addition, the target molecule should preferentially be expressed at the plasma membrane (obviating necessity of cellular uptake) in sufficient amounts to allow for successful detection. Optical imaging with tumor-specific probes in different xenograft models (e.g. breast, ovarian, and skin cancer) has been reported, indicating the feasibility of this technique [6-9]. Hypoxia is a condition that solid tumors of various origins have in common and that is absent in healthy tissue [10-15]. Tumor hypoxia arises due to rapid expansion of the tumor mass, combined with limited perfusion [10,16], causing stabilization of hypoxia-inducible factor-1α (HIF-1α), which induces upregulation of several

proteins such as carbonic anhydrase IX (CAIX), glucose transporter 1 (GLUT1) and vascular endothelial growth factor (VEGF) [10,17,18]. CAIX is frequently expressed in perinecrotic regions of DCIS lesions [16,19-21]. Studies comparing CAIX or HIF-1α expression in DCIS and invasive ductal carcinoma (IDC) report equal or even higher levels in DCIS compared to IDC [16,17,21]. Besides hypoxic tumor regions, CAIX is only expressed in epithelial cells of the gastrointestinal tract, which leads to a tumor specificity that is hardly equaled by other tumor markers [22]. Several groups reported on radiolabelled antibodies with specificity for CAIX [23,24]. However, radiolabeling of antibodies is expensive and can be logistically challenging when applied in clinical routine, because of short half lives of the tracers and protective measures that need to be taken during handling and disposal. Labeling with IRDye800CW, a near-infrared dye approved for clinical studies, is less expensive and results in a non-toxic, very stable probe that can be stored for longer periods [6,7,25,26].

In this study, we have investigated whether a CAIX-specific antibody (MabCAIX) conjugated to the near-infrared tracer IRDye800CW can be used for detection of DCIS using optical molecular imaging. We show that this non-immunogenic [27] tracer can be successfully used for imaging purposes and image guided surgery, and for fluorescence guided pathology sampling and direct immunofluorescence microscopy with higher contrast than conventional immunohistochemistry (IHC). As IRDye800CW, a CAIX antibody and the used fluorescence imaging system are approved to be used in humans, we pursue further development of this fluorescent probe towards clinical studies.

Methods

Cell culture

MDA-MB-231, MCF-7 breast cancer cells and HeLa cervical cancer cells (ATCC, Wesel, Germany) were cultured according to the supplier's guidelines in Dulbecco's Modified Eagle's Medium (DMEM; Invitrogen, Breda, The Netherlands). MCF10DCIS.com cells (further referred to as MCF10DCIS; Asterand, Detroit, USA) were cultured in DMEM/F12. Cell lines were validated by short tandem repeat analysis and were consistently Mycoplasma free.

Lentiviral transduction

Luciferase expressing MCF10DCIS cells were generated by introducing the pLV-CMV-Luc2-IRES-GFP vector (gift from A. Martens, University Medical Center Utrecht, Utrecht, The Netherlands) by lentiviral transduction as described before [28]. CAIX-FLAG expressing MCF10DCIS cells were generated using the pLV-CMV-CAIX-IRES-Zeo vector which was introduced by lentiviral transduction. Cells were subsequently cultured in medium containing 2 µg/ml puromycin. To generate CAIX-FLAG positive, Luc2 positive cells, these cells were transduced again with the pLV-CMV-Luc2-IRES-GFP vector as described above.

Antibody production

The sequences of the variable domain of the kappa light chain and variable domain of the heavy chain of a previously developed CAIX antibody were obtained from the US patent 20090274620. DNA of the variable domain fragments was synthesized by Geneart (Regensburg, Germany). Both domains were cloned into a production vector with IgG1 heavy chain for production in HEK cells by U-Protein Express (Utrecht, The Netherlands). MabCAIX was purified and desalted with protein A affinity chromatography using HiTrap protein A HP columns and the ÄKTAxpress system (GE Healthcare, Zeist, The Netherlands). After filter sterilization, MabCAIX IgG was aliquoted and stored at 4^{o}C in PBS.

Conjugation of IRDye800CW to MabCAIX

IRDye800CW-NHS ester (LI-COR Biosciences, Nebraska, USA) was conjugated to MabCAIX following manufacturer recommendations, with three different molar fluorophore to protein ratios: a 2 times or 4 times molar excess of fluorophore per 2.4 mg/ml protein (condition A and B respectively), and a 4 times molar excess of fluorophore per 1.2 mg/ml of MabCAIX (condition C). After labeling, free fluorophore was separated from the conjugate by size exclusion chromatography, performed twice in sequential steps, with Pierce ZebaTM Desalting Spin Columns (Thermo Fisher Scientific, Landsmeer, The Netherlands). Molar fluorophore to protein ratio was calculated as described before [25].

Characterization of IRDye800CW conjugated MabCAIX

SDS-PAGE gel electrophoresis was used to size-separate IRDye800CW-conjugated proteins (1 μg) on 15% SDS-PAGE. Separated proteins were stained with Coomassie Brilliant Blue solution (SERVA Electrophoresis GmbH, Heidelberg, Germany) and the gel was imaged with the Odyssey imaging system (LI-COR Biosciences, NE, USA). For affinity determination of IRDye800CW labelled MabCAIX, 20,000 MCF10DCIS cells were seeded in 96-wells plates (Thermo Fisher Scientific) and allowed to adhere overnight. Next day, medium was aspirated and cells were incubated at 4°C for 1.5 hour with a dilution series of MabCAIX-IRDye800CW in PBS in triplicate. The dissociation constant (K_D) was derived from the concentration of MabCAIX-IRDye800CW at which half the intensity of B_{max} was found (non-linear regression, one site specific binding, Graphpad Prism v.5, GraphPad Software, La Jolla, USA).

Immunofluorescence

CAIX transduced and non-transduced MCF10DCIS, HeLa, MDA-MB-231 and MCF-7 cells were grown on cover slips for 1 day either at 21% O_2 or at 1% O_2. Cells were washed with sterile, ice-cold PBS and incubated for 1.5h at 4°C with 32 nM MabCAIX in PBS with 2% bovine serum albumin (BSA). Non-bound MabCAIX was removed by washing the cells. After fixation with 4% PFA/PBS, rabbit anti-human IgG (1:500, A 0424, DakoCytomation, Glostrup, Denmark) was used for

detection of the bound MabCAIX with goat anti-rabbit Alexa 488 (1:1,000, Invitrogen, Breda, The Netherlands) as secondary antibody. DAPI (Roche, Woerden, The Netherlands) was employed as nucleic acid stain. Cells were imaged using a confocal microscope (Zeiss, Jena, Germany).

In vivo experiments

All animal experiments were approved by the Utrecht University Animal Experimental Committee (DEC no. 2012.III.02.015). The mouse model used in this study was based on a previously described model [29]. Five-week old female SCID/Beige (C.B-17/IcrHsd-PrkdcscidLystbg) immunodeficient mice (Harlan Laboratories, Horst, The Netherlands) were orthotopically transplanted as described before [28], with some modifications. In short, $4x10^4$ luciferase-expressing MCF10DCIS cells with endogenous CAIX expression were injected in the right 4^{th} mammary fat pad (further denoted 'DCIS' tumors) and CAIX-FLAG overexpressing luciferase positive MCF10DCIS cells (further referred to as 'CAIX+' tumors) were injected in the left 4^{th} mammary fat pad using a 10 µl Hamilton syringe. Tumor growth was monitored on a weekly basis using bioluminescence imaging (Photon Imager, BiospaceLabs, Paris, France). Upon development of palpable tumors, eight mice were intravenously (i.v.) injected in the tail vein with 100 µg MabCAIX-IRDye800CW. A real-time intra-operative multispectral fluorescence reflectance imaging (MFRI) system was used to monitor uptake and washout of the fluorescent antibody over time as described earlier [6]. The following imaging parameters were used: distance between object and lens 11.5 cm, zoom 4%, focus 0%, iris 93%. The exposure time for each image was set at 30 or 50 ms and gain at 1,000. The field of view for each image was 106 x 106 mm, corresponding to a resolution of 0.04 mm^2 per pixel. Static images were acquired every 30 minutes in the first 4h post-injection and 8h, 24h, 48h, and 72h post-injection. Intra-operative imaging was performed with the same imaging settings after sacrificing the mice and removing the skin from the tumor bearing mammary glands. Non-reflecting tweezers were used to fix the tumors at the focus of the camera laser. For background measurements *in vivo*, the muscles of the hind leg of each mouse were used.

Biodistribution

Eight mice were sacrificed 96h after injection of MabCAIX-IRDye800CW and biodistribution assays were performed as described before [25]. After disruption of the tumors and organs, dilution series, including pre-defined concentrations of MabCAIX-IRDye800CW for calibration, were made in Nunc 96 well plates (Thermo Fisher Scientific) with PBS and scanned with the Odyssey imaging system. Thereafter, the quantity of each probe in each organ was determined by intra- or extrapolation of the unknown fluorescence values from the respective calibration curves (GraphPad Prism software v.5, GraphPad Software, La Jolla, USA). Values were stated as average ± standard error of the mean.

Imaging of fluorescent tumor sections and immunohistochemistry

Fluorescent tumor sections were prepared and IHC was performed as described before [6]. Tumor slides were scanned with the Scanscope XT 120 scanner (Aperio, Vista, USA). Qualitative analysis of IHC slides was done manually and only the CAIX membrane staining was considered as specific staining.

Image analysis of fluorescent tumor sections

Image analysis was performed by segmenting tumor and normal tissue for each time point using an automated recursive region growing algorithm that is initialized with an user defined seed point in the tumor or background. Average signal intensities were obtained and tumor-to-normal tissue ratios were calculated. Analysis was performed in MatLab (v7.9.0.529, R2009b, The Mathworks, Natick, USA).

Results

Production, labeling and characterization of MabCAIX

Coomassie staining showed the typical heavy chains (HC) and light chains (LC) of MabCAIX, confirming a successful purification (Fig. 1A). After conjugation to IRDye800CW, free fluorophore was removed by chromatography resulting in <5% free fluorophore, with fluorophore-to-protein ratios of 1.0, 1.8 and 1.65 for conditions A, B and C respectively. SDS-PAGE showed the IRDye800CW labeling of the light and heavy chain of the antibody (Fig. 1B). To determine the affinity of the produced IRDye800CW labelled antibodies, MCF10DCIS cells expressing CAIX-FLAG were incubated with increasing concentrations of MabCAIX. The conjugation conditions A, B and C resulted in different binding affinities of the IRDye800CW-labelled probes, which were 23, 47 and 15 nM respectively (Fig. 1C). The labeling conditions of a 4 times molar excess of fluorophore at a 1.2 mg/ml antibody concentration (condition C) resulted in the highest affinity and best B_{max}. This condition was used for further studies.

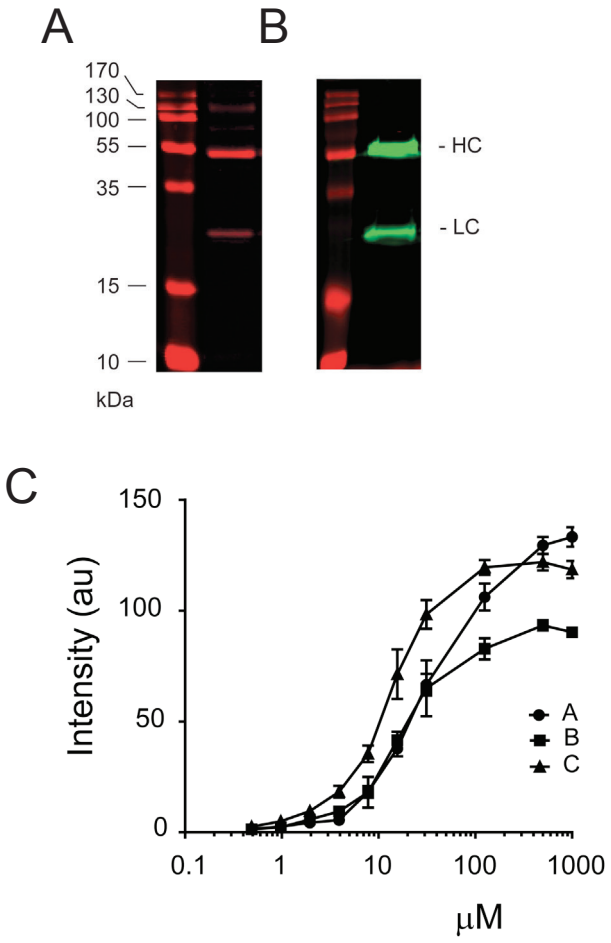

Figure 1: Characterization of MabCAIX. A. MabCAIX-IRDye800CW (1.0 µg) was analyzed on 15% SDS-page under reducing conditions. Gel was stained with Coomassie Brilliant Blue and scanned with the Odyssey imaging system at 700 nm (red). Both heavy chain (50 kDa) and light chain (25 kDa) are visible. B. MabCAIX-IRDye800CW (1.0 µg) on 15% SDS-page under reducing conditions. Gel was scanned with the Odyssey imaging system at 700 nm for the protein ladder (red) and 800 nm channel for the IRDye800CW labelled protein (green). Both heavy and light chain are visible and are fluorescently labelled. C. Affinity determination using MCF10DCIS cells stably transduced with CAIX-FLAG. During labeling, molar fluorophore to protein ratios of 2x and 4x, and two protein concentrations (2.4 or 1.2 µg/µl) were used, resulting in three different labeling conditions (A: 2x2.4; B: 4x2.4 and C: 4x1.2). Values are displayed as mean ± SEM. Experiments were performed in triplicate.

Determining specificity of MabCAIX for CAIX by immunofluorescence

A difference was observed in membrane staining between the MCF10DCIS cells transduced with human CAIX and the MCF10DCIS cells which have no CAIX expression under normoxic conditions (Fig. 2A, B). In addition, immunolabeling was performed on MDA-MB-231 and HeLa cells (expressing CAIX endogenously), and on MCF-7 cells that do not express CAIX under normoxia. HeLa cells showed upregulation of CAIX after culturing under hypoxic conditions (1% O_2) for 24h as compared to HeLa cells cultured under normoxic conditions (21% O_2) (Fig. 2C, D). Also MDA-MB-231 cells showed focal CAIX expression (Fig. 2E) but MCF-7 cells did not show any immunolabeling under hypoxic conditions (Fig. 2F). In summary, our results show the production of an IRDye800CW-labelled monoclonal antibody that is specifically binding with high affinity (15 nM) to CAIX expressed on different cell types.

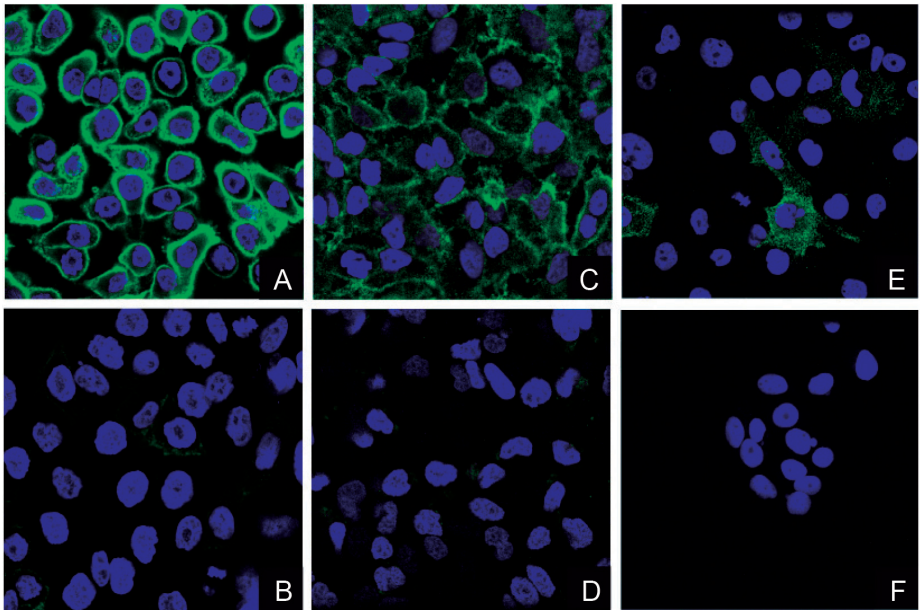

Figure 2: Specificity of MabCAIX for CAIX expressing cells
Immunofluorescence of MabCAIX detected with rabbit anti-human IgG and goat anti-rabbit 488 (green), DAPI in blue, using confocal microscopy. A. MCF10DCIS cells stably transfected with CAIX-FLAG. B. MCF10DCIS cells (non-transfected) C. HeLa cells cultured under hypoxic conditions (1% O_2 for 24h). D. HeLa cells cultured under normoxic conditions (21% O_2 for 24h). E. MDA-MB-231 cells cultured under hypoxic conditions (1% O_2 for 24h). F. MCF-7 cells cultured under hypoxic conditions (1% O_2 for 24h).

In vivo experiments

Already 15 minutes after injection of 100 µg MabCAIX-IRDye800CW in eight mice, a signal was obtained from the CAIX+ and in DCIS tumors, albeit with a stronger signal for the CAIX+ tumor. In some DCIS tumors, no signal was observed 96h after injection and these tumors were indicated as DCIS-, as opposed to tumors in which a signal was observed (DCIS+) (Fig. 3A). Optimal imaging of tumors was obtained from 24h onwards after injection at which time point the DCIS- tumors were also visible (Fig. 3A). At 96h after injection, DCIS+ tumors were clearly visible intra-operatively after removing the skin from the mammary glands (Fig. 3B-D), suggesting that the signal of the DCIS+ tumors is sufficient for the optical imaging system to be detected.

Biodistribution

The weight of all DCIS- tumors was less than 50 mg (approximately 5 mm diameter) while all DCIS+ tumors weighted more than 50 mg (> 5 mm). As expected from the images obtained, tumor uptake was higher for the CAIX+ tumors compared to the DCIS+ tumors, i.e. 56±8.0% and 11±1.1% of the injected dose per gram of tissue (I.D./g) respectively (Fig. 4). Tumor uptake in the DCIS- tumors was on average 4.0±0.9% I.D./g, which was similar to the uptake in other organs (Fig. 4).
Determining the MabCAIX distribution pattern with fluorescent sections and IHC
In CAIX+ tumors, CAIX staining was observed throughout the entire tumor except for connective tissue and necrotic areas (Fig. 5A). Higher magnification indicated that CAIX staining was confined to the cell membranes confirming the membrane localization of CAIX (Fig. 5A, insert). Distribution of the MabCAIX-IRDye800CW fluorescence was comparable to the CAIX staining with IHC. A fluorescent signal from MabCAIX-IRDye800CW was also observed in DCIS+ tumors, while hardly any signal was detected in DCIS- tumors, which is in agreement with the biodistribution data (Fig. 4B, C). In the DCIS+ tumors, CAIX expression by IHC, as well as the MabCAIX-IRDye800CW fluorescence signal was confined to perinecrotic tumor regions, with low signal in surrounding tumor tissue (Fig 5B). Back-to-back slides stained with haematoxylin and eosin (H&E) showed necrotic areas in approximately half of CAIX+ and half of DCIS tumors.

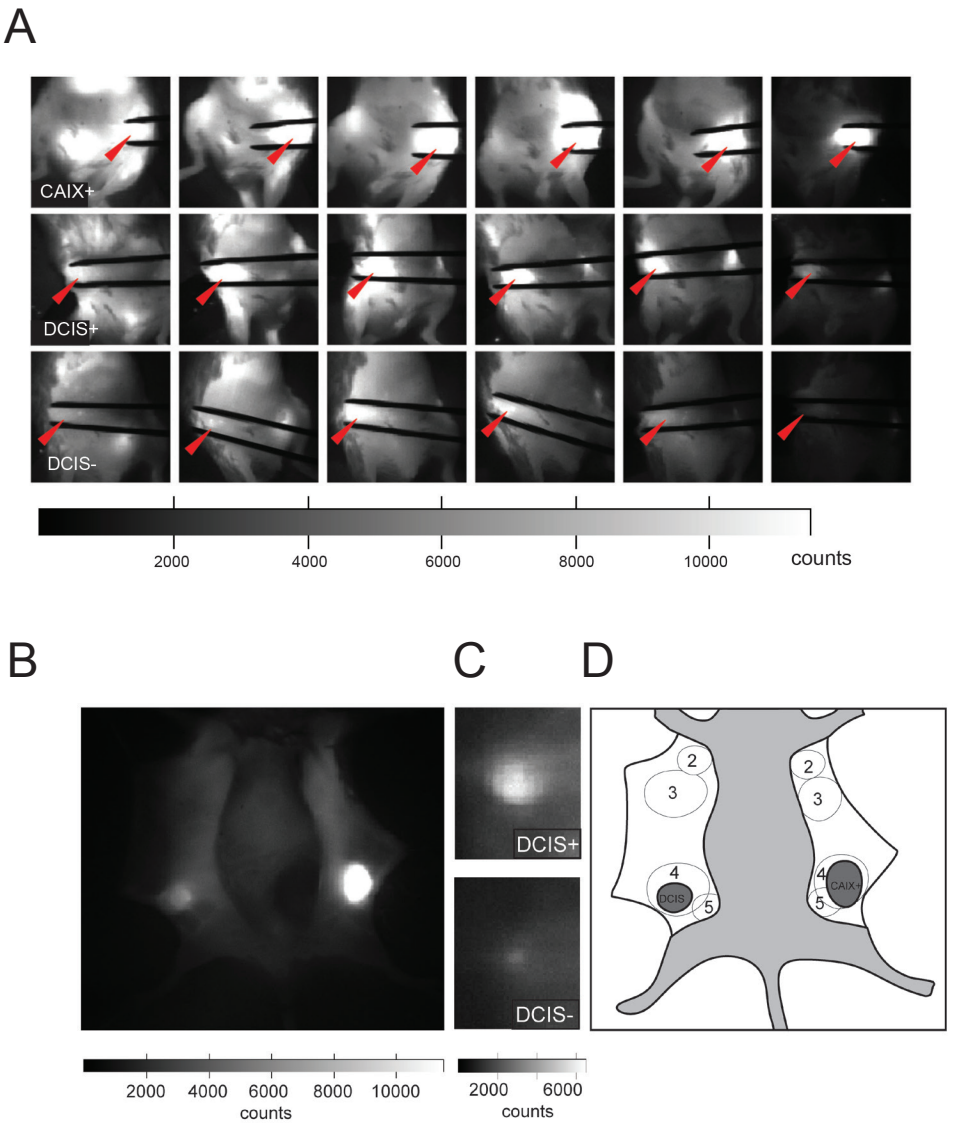

Figure 3: Imaging tumor uptake of MabCAIX-IRDye800CW
A. upper panel: Fluorescence images of SCID/Beige mice with CAIX overexpressing MCF10DCIS tumors (red arrow) held between tweezers, scanned at different time points after injection of 100 µg MabCAIX-IRDye800CW into the tail vein. Middle panel: Fluorescence images of SCID/Beige mice with MCF10DCIS xenografts with necrosis and endogenous CAIX expression (DCIS+). Lower panel: Fluorescence images of SCID/Beige mice with MCF10DCIS xenografts without necrosis and without CAIX (DCIS-). B. intra-operative imaging of CAIX overexpressing and non-overexpressing MCF10DCIS xenografts. C. intra-operative imaging of DCIS tumors with and without necrosis (DCIS+ and -). D. schematic drawing of position of mouse (light gray) and xenograft positions (dark grey) during intra-operative imaging. Skin and mammary glands (2: second mammary gland, 3: third, etc.) in white area.

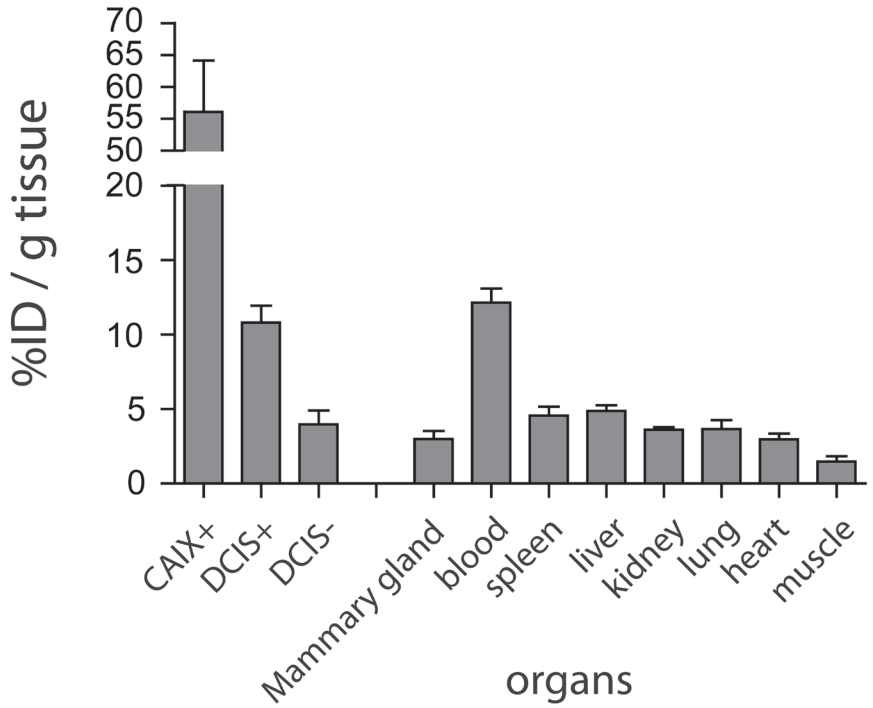

Figure 4: Biodistribution of MabCAIX
Organs were collected 96h after intravenous injection of 100 µg MabCAIX-IRDye800CW (N=8 mice). Biodistribution of MabCAIX-IRDye800CW was expressed as mean percentage of injected dose per gram tissue. Values are displayed as mean ± SEM.

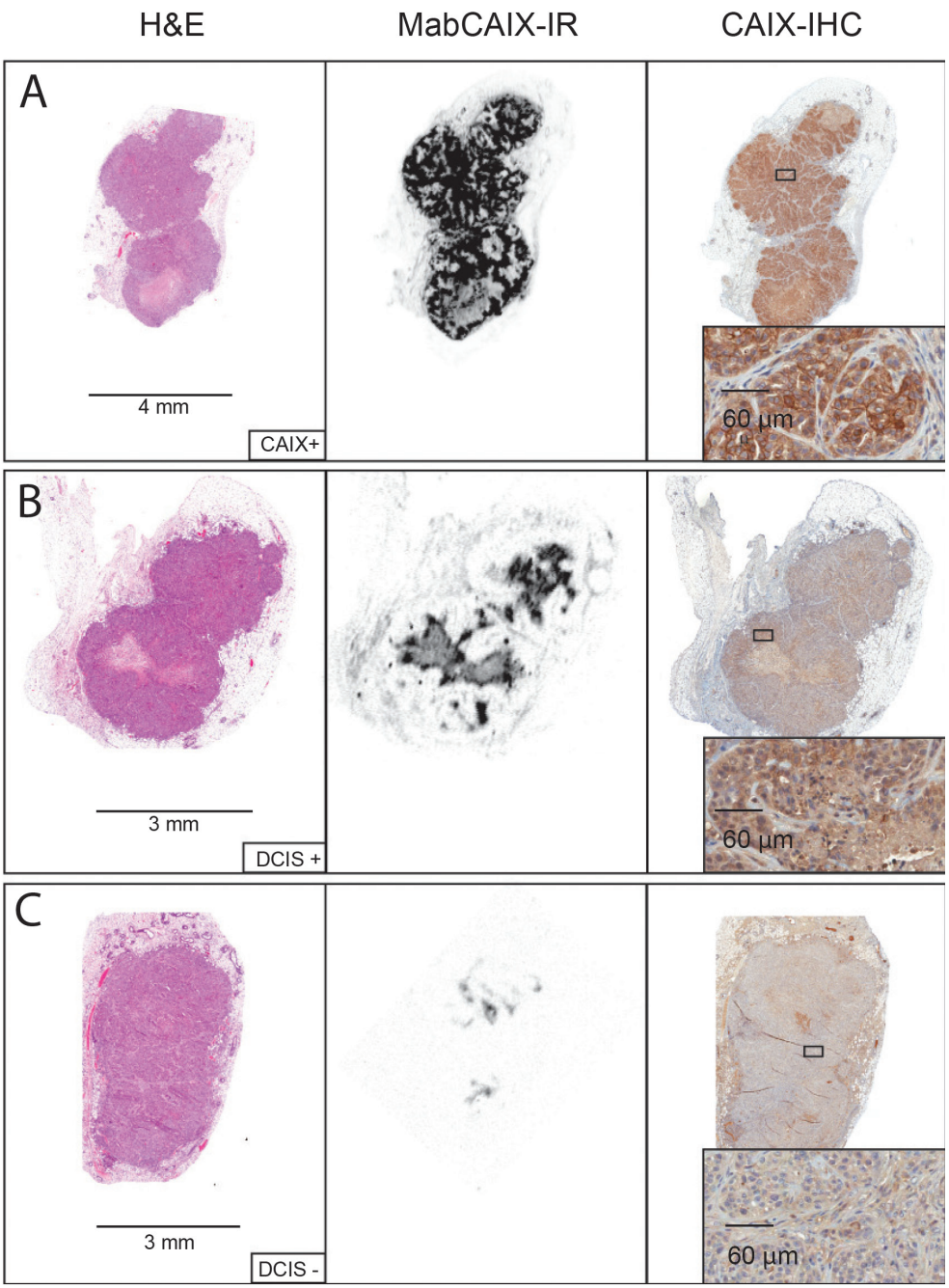

Figure 5: Analysis of tumor sections
Tumors were removed and processed for IHC. Left: H&E staining, middle: fluorescence from MabCAIX-IRDye800CW, right: CAIX staining by IHC. A: CAIX+ tumors B: DCIS tumors with necrosis (DCIS+) C: DCIS tumors without necrosis (DCIS-).

Image analysis

The TNR of the CAIX+ tumors increased gradually in the first three days post injection until a plateau level was reached after 48h. At this time point, the mean TNR was 7.5±0.5. The TNR of the DCIS+ tumors with necrosis also reached a plateau level at 48h, with a mean TNR of 2.1±0.1. The TNR timeline of the DCIS- tumors without necrosis dropped after 48h when the mean TNR was 1.7±0.1 (Fig. 6A). Highest TNR levels were obtained after 96h. At this time point the mean intra-operative TNR of the CAIX+ tumors was 11.2±1.0, 2.9±0.1 in DCIS+ tumors and 1.5±0.1 in DCIS- tumors (Fig. 6B).

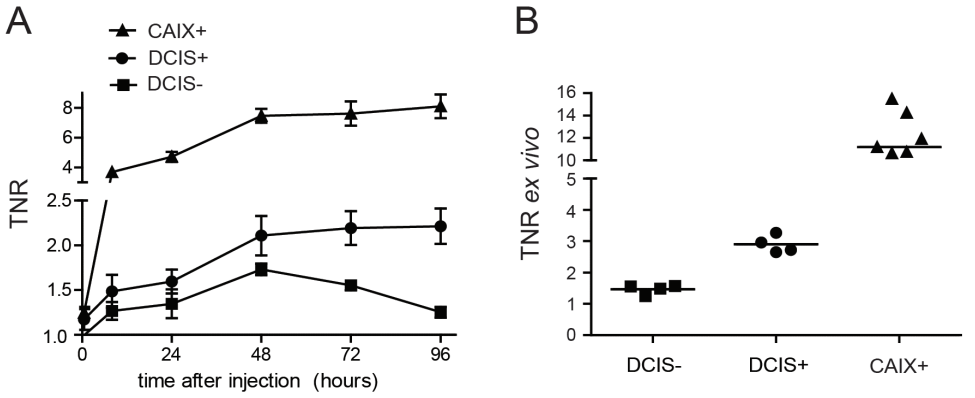

Figure 6: Tumor-to-normal tissue ratios in time. A. Tumor-to-normal tissue ratios measured *in vivo* after i.v. injection of 100 µg MabCAIX-IRDye800CW. Average tumor to normal tissue ratios (TNR) in the CAIX+ group (N=8), DCIS+ (N=4), and DCIS- (N=4) group. Error bars represent SEM. B. Individual values of intra-operative TNR in CAIX+, DCIS+ and DCIS- tumors. Horizontal lines represent the mean value.

Discussion

In this preclinical animal model resembling human DCIS, we investigated a monoclonal antibody directed to IRDye800CW. We showed that hypoxic DCIS can be visualized using a clinically approved multispectral fluorescence reflectance imaging system. Our tumor model resembles the comedo subtype of (high grade) DCIS that is associated with a relatively high risk of local recurrence and progression to invasive cancer [1,30]. CAIX is expressed in perinecrotic regions which are frequently present in human DCIS [10,16] as was the case in our mouse study as well. CAIX is the first hypoxia up-regulated tumor marker used for optical molecular imaging of DCIS. Tumors with hypoxia-induced (perinecrotic) CAIX expression could be distinguished from other organs at 24h after administration, and also from DCIS without necrosis. In tumors without necrosis, no CAIX upregulation or probe accumulation was visible. Absence of necrosis correlated well with tumor size. The TNR timeline for DCIS- tumors was consistent with the human IgG (as negative) control timeline in previous work, in which the same fluorescence camera system and tumor model were used [6]. Specific tumor uptake of MabCAIX-IRDye800CW was confirmed by a biodistribution assay, as well as by IHC for CAIX and its co-localization with the fluorescence in tumor tissue sections. DCIS tumors with hypoxia as small as 5 mm could be distinguished from normal tissue *in vivo* and intra-operatively. However, the sensitivity of this imaging technique is highly dependent on many factors, such as tumor position and depth, tumor size, content of necrosis and specific camera settings.

The heterogeneity of CAIX expression might result in suboptimal detection of DCIS with molecular imaging. Theoretically, molecular imaging targeting growth factor receptors that are more diffusely expressed seems to have advantages here. However, expression of hypoxia proteins in breast carcinoma (in situ) is more common than expression of growth factors. Also, growth factors are present in normal breast tissue as well [31,32]. Comparative clinical studies will have to reveal the best imaging strategies, but it is expected that combinations of probes may be re-

quired for sufficient sensitivity and will provide best results for detection.
The stability of our probe would allow for fluorescence-guided pathology dissection of tumors and even sensitive targeted immunofluorescence microscopy at higher contrast than conventional IHC, thereby introducing the concept of 'molecular fluorescence pathology', which could be applied in a clinical setting as well. To this end dissection rooms and microscopes would need to be equipped for imaging in the near-infrared range, but targeted sampling could allow for optimal assessment of tumor margin status with minimal sampling, which increases cost-effectiveness. Importantly, IRDye800CW can be easily conjugated to any monoclonal antibody, potentially making this a general approach across cancers and tumor targets. Direct immunofluorescence of IRDye800CW already present in the tissue requires no further costly lab processing.
Other hypoxia-specific molecules such as 2-nitroimidazole have proven to be suitable for imaging of hypoxia as well [33-35]. However, due to their small molecular size, these molecules are rapidly cleared from the body, resulting in low tumor uptake and a small window for imaging [36]. Monoclonal antibodies have a longer half-life in the blood pool, providing a wider time window for diagnosis and image-guided surgery. As opposed to other studies [37,38], we used a fluorescent tracer in the near-infrared range (800 nm), which has low absorption properties in human tissues, providing better penetration depth. This is a prerequisite for successful imaging of human tissue. Since IRDye800CW has already been approved for clinical studies and is commercially available, approval of conjugates for clinical studies will be more straightforward.
As the hypoxic state of tumor cells is usually retained during tumor progression, MabCAIX-IRDye800CW could also be useful to detect axillary lymph node metastases and distant metastases as well [37]. Since many different types of cancer are hypoxic and express CAIX [39-41], MabCAIX-IRDye800CW could well be useful for detection of cancers and image-guided surgery in other organs as well.

Conclusions

Molecular fluorescent imaging with MabCAIX-IRDye800CW can be successfully used to detect hypoxic DCIS before and during surgery to facilitate radical resection. Furthermore, it allows for optimized fluorescence-guided sampling during pathology dissection and sensitive targeted immunofluorescence microscopy. Because of the broad applicability of this hypoxia-targeting probe across different cancers, we aim for rapid translation towards the clinic.

References

1. Sakorafas GH, Farley DR, Peros G (2008) Recent advances and current contro versies in the management of DCIS of the breast. Cancer treatment reviews 34 (6):483-497. doi:10.1016/j.ctrv.2008.03.001
2. Cutuli B, Lemanski C, Le Blanc-Onfroy M, de Lafontan B, Cohen-Solal-Le-Nir C, Fondrinier E, Mignotte H, Giard S, Charra-Brunaud C, Auvray H, Gonzague-Casabianca L, Quetin P, Fay R (2013) Local recurrence after ductal carcinoma in situ breast conserving treatment. Analysis of 195 cases. Cancer radiotherapie : journal de la Societe francaise de radiotherapie oncologique. doi:10.1016/j.canrad.2013.01.011
3. Lee LA, Silverstein MJ, Chung CT, Macdonald H, Sanghavi P, Epstein M, Holmes DR, Silberman H, Ye W, Lagios MD (2006) Breast cancer-specific mortality after invasive local recurrence in patients with ductal carcinoma-in-situ of the breast. American journal of surgery 192 (4):416-419. doi:10.1016/j.amjsurg.2006.06.005
4. Shamliyan T, Wang SY, Virnig BA, Tuttle TM, Kane RL (2010) Association between patient and tumor characteristics with clinical outcomes in women with ductal carcinoma in situ. Journal of the National Cancer Institute Monographs 2010 (41):121-129. doi:10.1093/jncimonographs/lgq034
5. Stillebroer AB, Zegers CM, Boerman OC, Oosterwijk E, Mulders PF, O'Donoghue JA, Visser EP, Oyen WJ (2012) Dosimetric analysis of 177Lu-cG250 radioimmunotherapy in renal cell carcinoma patients: correlation with myelotoxicity and pretherapeutic absorbed dose predictions based on 111In-cG250 imaging. Journal of nuclear medicine : official publication, Society of Nuclear Medicine 53 (1):82-89. doi:10.2967/jnumed.111.094896
6. Vermeulen JF, van Brussel AS, Adams A, Mali WP, van der Wall E, van Diest PJ, Derksen PW (2013) Near-Infrared Fluorescence Molecular Imaging of Ductal Carcinoma In Situ with CD44v6-Specific Antibodies in Mice: A Preclinical Study. Molecular imaging and biology : MIB : the official publication of the Academy of Molecular Imaging 15 (3):290-298. doi:10.1007/s11307-012-0605-8
7. Terwisscha van Scheltinga AG, van Dam GM, Nagengast WB, Ntziachristos V, Hollema H, Herek JL, Schroder CP, Kosterink JG, Lub-de Hoog MN, de Vries EG (2011) Intraoperative near-infrared fluorescence tumor imaging with vascular endothelial growth factor and human epidermal growth factor receptor 2 targeting antibodies. Journal of nuclear medicine : official publication, Society of Nuclear Medicine 52 (11):1778-1785. doi:10.2967/jnumed.111.092833
8. Day KE, Beck LN, Heath CH, Huang CC, Zinn KR, Rosenthal EL (2013) Identification of the optimal therapeutic antibody for fluorescent imaging of cutaneous squamous cell carcinoma. Cancer biology & therapy 14 (3):271-277. doi:10.4161/cbt.23300
9. Zhang Y, Hong H, Engle JW, Yang Y, Barnhart TE, Cai W (2012) Positron Emission Tomography and Near-Infrared Fluorescence Imaging of Vascular Endothelial Growth Factor with Dual-Labeled Bevacizumab. American journal of nuclear medicine and molecular imaging 2 (1):1-13
10. Bos R, Zhong H, Hanrahan CF, Mommers EC, Semenza GL, Pinedo HM, Abeloff MD, Simons JW, van Diest PJ, van der Wall E (2001) Levels of hypoxia-inducible factor-1 alpha during breast carcinogenesis. Journal of the National Cancer Institute 93 (4):309-314
11. Greijer AE, de Jong MC, Scheffer GL, Shvarts A, van Diest PJ, van der Wall E (2005)

Hypoxia-induced acidification causes mitoxantrone resistance not mediated by drug transporters in human breast cancer cells. Cellular oncology : the official journal of the International Society for Cellular Oncology 27 (1):43-49
12. Gort EH, Groot AJ, van der Wall E, van Diest PJ, Vooijs MA (2008) Hypoxic regulation of metastasis via hypoxia-inducible factors. Current molecular medicine 8 (1):60-67
13. Seeber LM, Horree N, Vooijs MA, Heintz AP, van der Wall E, Verheijen RH, van Diest PJ (2011) The role of hypoxia inducible factor-1alpha in gynecological cancer. Critical reviews in oncology/hematology 78 (3):173-184. doi:10.1016/j.critrevonc.2010.05.003
14. Jans J, van Dijk JH, van Schelven S, van der Groep P, Willems SH, Jonges TN, van Diest PJ, Bosch JL (2010) Expression and localization of hypoxia proteins in prostate cancer: prognostic implications after radical prostatectomy. Urology 75 (4):786-792. doi:10.1016/j.urology.2009.08.024
15. Kornegoor R, Verschuur-Maes AH, Buerger H, Hogenes MC, de Bruin PC, Oudejans JJ, Hinrichs B, van Diest PJ (2012) Fibrotic focus and hypoxia in male breast cancer. Modern pathology : an official journal of the United States and Canadian Academy of Pathology, Inc 25 (10):1397-1404. doi:10.1038/modpathol.2012.101
16. Wykoff CC, Beasley N, Watson PH, Campo L, Chia SK, English R, Pastorek J, Sly WS, Ratcliffe P, Harris AL (2001) Expression of the hypoxia-inducible and tumor-associated carbonic anhydrases in ductal carcinoma in situ of the breast. The American journal of pathology 158 (3):1011-1019. doi:10.1016/S0002-9440(10)64048-5
17. Li XF, O'Donoghue JA (2008) Hypoxia in microscopic tumors. Cancer letters 264 (2):172-180. doi:10.1016/j.canlet.2008.02.037
18. Bos R, van der Groep P, Greijer AE, Shvarts A, Meijer S, Pinedo HM, Semenza GL, van Diest PJ, van der Wall E (2003) Levels of hypoxia-inducible factor-1alpha independently predict prognosis in patients with lymph node negative breast carcinoma. Cancer 97 (6):1573-1581. doi:10.1002/cncr.11246
19. Wang Z, Shi Q, Gu Y, Shen Y, Sun M, Deng M, Zhang H, Fang J, Zhang S, Xie F (2011) Clinicopathologic correlation of cancer stem cell markers CD44, CD24, VEGF and HIF-1alpha in ductal carcinoma in situ and invasive ductal carcinoma of breast: an immunohistochemistry-based pilot study. Pathology, research and practice 207 (8):505-513. doi:10.1016/j.prp.2011.06.009
20. van der Groep P, van Diest PJ, Smolders YH, Ausems MG, van der Luijt RB, Menko FH, Bart J, de Vries EG, van der Wall E (2013) HIF-1alpha overexpression in ductal carcinoma in situ of the breast in BRCA1 and BRCA2 mutation carriers. PloS one 8 (2):e56055. doi:10.1371/journal.pone.0056055
21. Chen CL, Chu JS, Su WC, Huang SC, Lee WY (2010) Hypoxia and metabolic pheno types during breast carcinogenesis: expression of HIF-1alpha, GLUT1, and CAIX. Virchows Archiv : an international journal of pathology 457 (1):53-61. doi:10.1007s00428-010-0938-0
22. De Simone G, Supuran CT (2010) Carbonic anhydrase IX: Biochemical and crystallographic characterization of a novel antitumor target. Biochimica et biophysica acta 1804 (2):404-409. doi:10.1016/j.bbapap.2009.07.027
23. Ahlskog JK, Schliemann C, Marlind J, Qureshi U, Ammar A, Pedley RB, Neri D (2009) Human monoclonal antibodies targeting carbonic anhydrase IX for the molecular imaging of hypoxic regions in solid tumours. British journal of cancer 101 (4):645-657. doi:10.1038/sj.bjc.6605200
24. Divgi CR, Pandit-Taskar N, Jungbluth AA, Reuter VE, Gonen M, Ruan S, Pierre C, Nagel A, Pryma DA, Humm J, Larson SM, Old LJ, Russo P (2007) Preoperative

characterisation of clear-cell renal carcinoma using iodine-124-labelled antibody chimeric G250 (124I-cG250) and PET in patients with renal masses: a phase I trial. The lancet oncology 8 (4):304-310. doi:10.1016/S1470-2045(07)70044-X
25. Oliveira S, van Dongen GA, Stigter-van Walsum M, Roovers RC, Stam JC, Mali W, van Diest PJ, van Bergen en Henegouwen PM (2012) Rapid visualization of human tumor xenografts through optical imaging with a near-infrared fluorescent anti-epidermal growth factor receptor nanobody. Molecular imaging 11 (1):33-46
26. Marshall MV, Draney D, Sevick-Muraca EM, Olive DM (2010) Single-dose intravenous toxicity study of IRDye 800CW in Sprague-Dawley rats. Molecular imaging and biology : MIB : the official publication of the Academy of Molecular Imaging 12 (6):583-594. doi:10.1007/s11307-010-0317-x
27. Siebels M, Rohrmann K, Oberneder R, Stahler M, Haseke N, Beck J, Hofmann R, Kindler M, Kloepfer P, Stief C (2011) A clinical phase I/II trial with the monoclonal antibody cG250 (RENCAREX(R)) and interferon-alpha-2a in metastatic renal cell carcinoma patients. World journal of urology 29 (1):121-126. doi:10.1007/s00345-010-0570-2
28. Schackmann RC, van Amersfoort M, Haarhuis JH, Vlug EJ, Halim VA, Roodhart JM, Vermaat JS, Voest EE, van der Groep P, van Diest PJ, Jonkers J, Derksen PW (2011) Cytosolic p120-catenin regulates growth of metastatic lobular carcinoma through Rock1-mediated anoikis resistance. The Journal of clinical investigation 121 (8):3176-3188. doi:10.1172/JCI41695
29. Behbod F, Kittrell FS, LaMarca H, Edwards D, Kerbawy S, Heestand JC, Young E, Mukhopadhyay P, Yeh HW, Allred DC, Hu M, Polyak K, Rosen JM, Medina D (2009) An intraductal human-in-mouse transplantation model mimics the subtypes of ductal carcinoma in situ. Breast cancer research : BCR 11 (5):R66. doi:10.1186/bcr2358
30. MacAusland SG, Hepel JT, Chong FK, Galper SL, Gass JS, Ruthazer R, Wazer DE (2007) An attempt to independently verify the utility of the Van Nuys Prognostic Index for ductal carcinoma in situ. Cancer 110 (12):2648-2653. doi:10.1002/cncr.23089
31. Eccles SA (2011) The epidermal growth factor receptor/Erb-B/HER family in normal and malignant breast biology. The International journal of developmental biology 55 (7-9):685-696. doi:10.1387/ijdb.113396se
32. Leone F, Perissinotto E, Cavalloni G, Fonsato V, Bruno S, Surrenti N, Hong D, Capaldi A, Geuna M, Piacibello W, Aglietta M (2003) Expression of the c-ErbB-2/HER2 proto-oncogene in normal hematopoietic cells. Journal of leukocyte biology 74 (4):593-601. doi:10.1189/jlb.0203068
33. Varia MA, Calkins-Adams DP, Rinker LH, Kennedy AS, Novotny DB, Fowler WC, Jr., Raleigh JA (1998) Pimonidazole: a novel hypoxia marker for complementary study of tumor hypoxia and cell proliferation in cervical carcinoma. Gynecologic oncology 71 (2):270-277. doi:10.1006/gyno.1998.5163
34. Picchio M, Beck R, Haubner R, Seidl S, Machulla HJ, Johnson TD, Wester HJ, Reischl G, Schwaiger M, Piert M (2008) Intratumoral spatial distribution of hypoxia and angiogenesis assessed by 18F-FAZA and 125I-Gluco-RGD autoradiography. Journal of nuclear medicine : official publication, Society of Nuclear Medicine 49 (4):597-605. doi:10.2967/jnumed.107.046870
35. Dolbier WR, Jr., Li AR, Koch CJ, Shiue CY, Kachur AV (2001) [18F]-EF5, a marker for PET detection of hypoxia: synthesis of precursor and a new fluorination procedure. Applied radiation and isotopes : including data, instrumentation and methods for use in agriculture, industry and medicine 54 (1):73-80
36. Okuda K, Okabe Y, Kadonosono T, Ueno T, Youssif BG, Kizaka-Kondoh S, Nagasawa H (2012) 2-Nitroimidazole-tricarbocyanine conjugate as a near-infrared

fluorescent probe for in vivo imaging of tumor hypoxia. Bioconjugate chemistry 23 (3):324-329. doi:10.1021/bc2004704

37. Tafreshi NK, Bui MM, Bishop K, Lloyd MC, Enkemann SA, Lopez AS, Abrahams D, Carter BW, Vagner J, Grobmyer SR, Gillies RJ, Morse DL (2012) Noninvasive detection of breast cancer lymph node metastasis using carbonic anhydrases IX and XII targeted imaging probes. Clinical cancer research : an official journal of the American Association for Cancer Research 18 (1):207-219. doi:10.1158/1078-0432.CCR-11-0238
38. Bao B, Groves K, Zhang J, Handy E, Kennedy P, Cuneo G, Supuran CT, Yared W, Rajopadhye M, Peterson JD (2012) In vivo imaging and quantification of carbonic anhydrase IX expression as an endogenous biomarker of tumor hypoxia. PloS one 7 (11):e50860. doi:10.1371/journal.pone.0050860
39. Fillies T, Werkmeister R, van Diest PJ, Brandt B, Joos U, Buerger H (2005) HIF1-alpha overexpression indicates a good prognosis in early stage squamous cell carcinomas of the oral floor. BMC cancer 5:84. doi:10.1186/1471-2407-5-84
40. Horree N, van Diest PJ, van der Groep P, Sie-Go DM, Heintz AP (2007) Hypoxia and angiogenesis in endometrioid endometrial carcinogenesis. Cellular oncology : the official journal of the International Society for Cellular Oncology 29 (3):219-227
41. Seeber LM, Horree N, van der Groep P, van der Wall E, Verheijen RH, van Diest PJ (2010) Necrosis related HIF-1alpha expression predicts prognosis in patients with endometrioid endometrial carcinoma. BMC cancer 10:307. doi:10.1186/1471-2407-10-307

Jeroen F. Vermeulen, Aram S. A. van Brussel, Arthur Adams, Willem P. Th. M. Mali, Elsken van der Wall, Paul J. van Diest, Patrick W. B. Derksen

7

Near-infrared fluorescence molecular imaging of ductal carcinoma in situ with CD44v6-specific antibodies in mice: a preclinical study

Abstract

Purpose: The purpose of this study was to develop a molecular imaging technique using probes specific for ductal carcinoma in situ (DCIS) to improve visualization and localization of DCIS during surgery. As CD44v6 is frequently expressed in DCIS, we used near-infrared fluorescently labeled CD44v6-targeting antibodies for detection of DCIS.

Procedure: Mice bearing orthotopically transplanted CD44v6 positive MCF10DCIS DCIS-like tumors and CD44v6 negative MDA-MB-231 control tumors were intravenously injected with IRDye800CW conjugated to CD44v6-specific antibodies or control IgGs. Non-invasive imaging was performed for 8 days post injection, followed by intraoperative imaging. Antibody accumulation and intratumor distribution were examined.

Results: Maximum accumulation of CD44v6-specific antibodies was obtained 24h post injection. Maximum tumor-to-background ratio for MCF10DCIS tumors was 4.5±0.2, compared to 1.4±0.1 (control tumors, $p=0.006$), and 1.7±0.1 (control IgG, $p=0.014$), for 8 days post injection. *Ex vivo*, tumor-to-background ratios were comparable to those obtained by intraoperative imaging.

Conclusions: We show the applicability of non-invasive and intraoperative optical imaging of DCIS-like lesions *in vivo* using CD44v6-specific antibodies.

Introduction

Molecular imaging of cell surface markers, e.g. growth factor receptors, hypoxia markers, and adhesion molecules, has become an important field for imaging of cancer for diagnosis, assessment of therapy response, or for tumor delineation during surgical resection [1–4]. Achieving radical excision during breast-conserving surgery for ductal carcinoma in situ (DCIS), and diffusely growing or small (T1) breast cancers, is challenging, since these lesions are often not palpable. Molecular imaging with near-infrared fluorescent (NIRF) tracers holds promise when applied as a tool for imageguided surgery. First, detection of lesions can be highly sensitive and specific by using targeted tracers. Second, due to its physical properties, NIRF can penetrate several millimeters in tissue, allowing non-invasive visualization of tumors [5]. Third, no ionizing radiation is used, limiting the need for protective measures. Fourth, the spectral properties (emission wavelengths between 700 and 900 nm) of the fluorescent tracers result in low background (auto) fluorescence [6]. Previously, we examined the expression of membrane markers in breast cancer to identify the most sensitive and specific molecular markers for optical imaging. The expression rate of tumor-specific markers did not exceed 20% of all breast cancers, whereas tumor markers expressed by normal breast epithelium (i.e., with a lower tumor specificity) were expressed in the majority of breast cancers. CD44v6 was expressed in 64% of breast cancers and thereby the most frequently expressed marker achieving a threefold tumor-to-normal ratio (predefined as sufficient for molecular imaging). Therefore, CD44v6 was considered the most promising tumor marker for molecular imaging of breast cancer [7].

The glycoprotein CD44 is a hyaluronic acid-binding adhesion molecule that facilitates binding of epithelial cells to the extracellular matrix. Due to alternative splicing, CD44 is expressed as multiple isoforms that structurally and functionally differ as a result of changes in the extracellular stem region of the receptor [8, 9]. The standard CD44 variant (CD44s) is widely expressed in epithelial tissues and has been used to mark stem cells, but the expression of these variants is mainly

restricted to neoplastic lesions [8–10]. Although the most widely studied variant of CD44, CD44v6, is abundantly expressed in invasive cancers, benign tumors do not express the v6 isoform [10–13]. Despite the high expression in invasive cancer, the relation between aggressiveness, invasiveness, and CD44v6 expression is not clear [14]. A possible role for CD44v6 in tumor progression may lie in its function as co-receptor and scaffolding platform. CD44v6 contains a heparin sulfate side chain able to bind and present glycosylated growth factors to their cognate receptors, thereby potentiating receptor tyrosine kinase signaling [15–19].

In studies investigating radioactively labeled antibodies targeting CD44v6 for detection of head and neck cancer, it was shown that administration was safe and allowed specific tumor detection [20, 21]. Furthermore, imaging of breast cancer with CD44v6 antibodies was only described by one group for detection of T1 cancers with SPECT and showed that 66% of breast cancers could be correctly assigned [22].

To study the applicability of NIRF-labeled antibodies for non-invasive and intraoperative optical imaging of DCIS *in vivo*, we examined NIRF-labeled CD44v6-specific antibodies in a transplantation-based model of DCIS. Our data indicate that detection of pre-invasive lesions with NIRF-labeled antibodies is feasible and not hampered by limited vascularization .

Methods

Cell culture, virus generation, and cell transduction

MCF10DCIS.com cells (further referred to as MCF10DCIS) were obtained from Asterand Inc. (Detroit, MI, USA) and cultured according to the supplier's guidelines. MDA-MB-231/Luc+ [23] (gift of G. van der Pluijm, Leiden University Medical Center, Leiden, The Netherlands) were cultured in DMEM containing 10% FCS supplemented with 100 IU/ml penicillin, and 100 µg/ml streptomycin. Both cell lines were confirmed negative for estrogen receptor-α, progesterone receptor, and HER2. CD44v6 and E-cadherin were expressed in MCF10DCIS only. All cell lines were validated by STR analysis and routinely checked for Mycoplasma infection. All lines were consistently Mycoplasma free.

To generate luciferase-expressing MCF10DCIS cells, pLV-CMV-Luc2-IRES-GFP vector (gift from A. Martens, UMC Utrecht, The Netherlands) was introduced by lentiviral transduction as described before [24]. Transduction efficiency was 100% (determined by expression of GFP) after two rounds of infection.

Antibody production, fluorescent labeling, and binding affinity measurements after labeling

The sequences of the variable domain of the heavy and light chains of humanized VFF18, directed against CD44v6, were obtained from the patent WO2002/094879. DNA of the variable domain fragments was synthesized by GeneArt (Life Technologies, Bleiswijk, The Netherlands). Variable domains were cloned into human IgG expression constructs and produced by U-protein Express (Utrecht, The Netherlands). IgG purification was performed by chromatography on proteinase A columns and eluted with sodium citrate (pH 3.6) followed by desalting and buffer exchange to phosphate-buffered saline (PBS) using the automated ÄKTAxpress system (GE Healthcare, Hoevelaken, The Netherlands). Protein concentration was determined using a NanoDrop spectrophotometer (Thermo Fisher Scientific, Breda, The Netherlands), and purity was confirmed by Coomassie stain of a SDS-PAGE gel. Human IgG from serum was obtained from Sigma-Aldrich (I4506,

Zwijndrecht, The Netherlands) and served as a negative control (further referred to as control IgG). Labeling of IgG antibodies was performed as described before [25]. The NIRF dye IRDye800CW, purchased as an N-hydroxysuccinimide ester (LI-COR Biosciences, Lincoln, NE, USA), was incubated in a fourfold molar excess of dye to IgG for 2h at room temperature. After conjugation, free dye was removed using Zebra Spin Desalting Columns (Thermo Fisher Scientific). Dye-to-protein ratio was determined with the following equation: IR/protein = $(A_{774}/\varepsilon_{IRDye\ 800CW})$ = $(A_{280} - (0.03 \times A_{774} / \varepsilon_{protein})$, where the molar extinction coefficient of IRDye800CW is 240,000 $M^{-1}cm^{-1}$ and the molar extinction coefficient for IgG is 210,000 $M^{-1}cm^{-1}$.
For affinity measurements, 15,000 MDA-MB-231 and MCF10DCIS cells were seeded in 96-well plates (Thermo Fischer Scientific) and allowed to adhere overnight. Next, medium was aspirated, cells were blocked with 4% Marvel (skimmed milk powder) in PBS, and cells were incubated for 2h at 4 °C with IRDye800CW-labeled IgG in 2% Marvel in PBS in the dark. Cells were washed three times with PBS, and bound IgG was detected using an Odyssey imaging system (LI-COR) at 800 nm. The dissociation constant (K_D) was derived from the concentration of IgG at which half the intensity of B_{max} was found. GraphPad Prism 5 software (nonlinear regression—one site-specific binding) was used for computational analyses.

Mouse studies

Five-week-old female SCID Beige (C.B-17/IcrHsd- PrkdcscidLystbg) immunodeficient mice (Harlan Laboratories, Horst, The Netherlands) were orthotopically transplanted as described before [24], with some modifications. Approximately 4×10^4 luciferase-expressing MCF10DCIS and 1×10^5 luciferase-expressing MDA-MB-231 cells were injected using a 10-µl Hamilton syringe in the fourth (inguinal) and third (thoracic) mammary fat pad, respectively. Tumor growth was monitored on a weekly basis using bioluminescence imaging (PhotonIMAGER, Biospace Lab, Paris, France). Upon development of palpable tumors (typically 2–3 mm in diameter), mice were intravenously injected in the tail vein with 100 µg fluorescently labeled IgG. All animal experiments were approved by the Utrecht University Animal Experimental Committee (DEC no. 2011.III.03.027).

Imaging and image analysis

Probe distribution was visualized and quantified based on the fluorescent signal from the labeled CD44v6 and control IgGs. A real-time intraoperative multispectral fluorescence imaging system, developed by the group of Ntziachristos et al., was used for the measurements [26]. In summary, the system consists of a charge-coupled digital iXon3 DU888 camera (Andor Technology, Belfast, UK), cooled at -80 °C for sensitive fluorescence signal detection, and a continuous wave laser with an excitation wavelength of 750 nm for optimal excitation of IRDye800CW. The following imaging parameters were used: distance between object and lens 30–32 cm, zoom 43%, focus 0%, and iris 93%. The exposure time for each image was set at 150 ms and gain at 1,000. The field of view for each image was 125×125 mm, corresponding to a resolution of 0.25×0.25 mm per pixel. Static images were acquired every 30 min in the first 2h post injection and subsequently 3, 4, and 8h post injection. After the first day, images were acquired daily until 8 days post injection.
After image acquisition, a region of interest (ROI) was drawn around each tumor, and the average signal intensity was determined. For each time point, the same size of the ROI was used. Also, an equal-sized ROI was drawn in a representative region without tumor tissue to determine background fluorescence levels and to be able to calculate tumor-to-background ratios. All values are displayed as mean ± standard error of the mean (SEM).

Biodistribution of IRDye800CW-labeled antibodies

One week post injection of the CD44v6 or control IgGs, mice were sacrificed and organs were collected, weighted, and snapfrozen in liquid nitrogen and stored at -80°C. Tissues and tumors were homogenized in RIPA buffer supplemented with protease inhibitors using a TissueLyser II system (QIAGEN, Venlo, The Netherlands). A dilution series of homogenized organs was made in order to measure the intensity in the linear range at 800 nm with the Odyssey Imager (LI-COR). The quantity of IRDye800CW was determined by intra- and extrapolation of the fluorescent value from a calibration curve that consisted of serial dilutions of the injected probe as described before [25, 27].

Immunohistochemistry

Immediately after resection, the tumors were fixed in neutral buffered formalin, paraffin-embedded, and stored in the dark. Immunohistochemistry was performed on 4-µm-thick sequential sections. Following deparaffinization and rehydration, endogenous peroxidase activity was blocked for 15 min in buffer solution containing 0.3% hydrogen peroxide. The different antigen retrieval methods used were as follows: boiling for 20 min in 10 mM citrate pH 6.0 (CD44v6), tris/EDTA pH 9.0 (p63), or pepsin (1 mg/ml) for 15 min at 37 °C (human IgG). A cooling period of 30 min preceded the primary antibody incubation: p63 (clone 4A4, Neomarkers) 1:400, human IgG specific for gamma chains (A0423, DAKO, Glostub, Denmark) 1:500, or CD44v6 (clone VFF18, BMS125 Bender MedSystems, Vienna, Austria) 1:500. The signal was amplified using BrightVision poly-HRP anti-mouse/rabbit/rat (DPVO-HRP, Immunologic, Duiven, The Netherlands) and developed with diaminobenzidine, followed by counterstaining with hematoxylin, dehydration in alcohol, and mounting. Appropriate negative and positive controls were used throughout. For detection of IRDye800CW, tumor slides were deparaffinized, mounted with Immumount (Thermo Fisher Scientific), and scanned using the Odyssey imaging system.

Statistics

Statistical analysis was performed using IBM SPSS Statistics version 18.0 (SPSS Inc., Chicago, IL, USA). Comparison of tumor-to-background levels of injected probes was performed using Mann–Whitney U test. Wilcoxon signed-rank test was performed to compare the fluorescent intensity of non-invasive with intraoperative imaging. P-values < 0.05 were considered to be statistically significant.

Results

Characterization of CD44v6 antibodies for non-invasive imaging of breast cancer

The potential of CD44v6-specific antibodies (further referred to as CD44v6 Ab) as probes for optical imaging was examined in a model for pre-invasive breast cancer. Labeling efficiency, expressed as IRDye800CW-to-protein ratio, was 1.43 and 1.57 for CD44v6 Ab and human serum IgG (further referred to as control IgG), respectively. After purification, 5.6% free dye remained present, which was comparable to previous studies [25]. The apparent affinity (K_D) of labeled CD44v6 Ab was 10 nM and 17 μM on MCF10DCIS (CD44v6 positive) and MDA-MB-231 (CD44v6 negative) cells, respectively. Control IgG had an apparent affinity of approximately 40 nM (MCF10DCIS) and 90 nM (MDA-MB-231), but with maximum binding (B_{max}) 13 times smaller than CD44v6 Ab on MCF10DCIS cells.

Mice bearing MCF10DCIS and MDA-MB-231 tumors (used as a CD44v6 negative control) were intravenously injected with IRDye800CW-conjugated CD44v6 Ab or control IgG. Accumulation of CD44v6 Ab in the MCF10DCIS tumor became detectable 4h post injection, whereas control IgG was not (Fig. 1A). A clear signal of the MCF10DCIS tumor was obtained from 3 days onwards, due to accumulation of the probe in the tumor and decreased background signal from circulating probe. In contrast, accumulation of free IRDye800CW was not observed (data not shown), while levels of control IgG were similar in MCF10DCIS vs. MDA-MB-231 tumors (Fig. 1A). The maximal fluorescence intensity in the MCF10DCIS tumor was reached after 8h (control IgG) and 24h (CD44v6 Ab) and decreased to background levels in 8 days (control IgG) or stabilized after 5 days (CD44v6 Ab) (Fig. 1B). These differences are most likely caused by dissimilar pharmacokinetics of the antibodies used. Fluorescence intensity of control IgG and CD44v6 Ab in the MDA-MB-231 control tumor was lower than the MCF10DCIS tumor, while the background levels and the decrease in fluorescent signal were comparable (Fig. 1B). As a result, tumor-to-background ratio for CD44v6 Ab increased from 2.41±0.39 3 days

post injection to 2.78±0.31 7 days post injection and tended to increase further in MCF10DCIS (Fig. 1C). In contrast, tumor-to-background ratio of control IgG declined to 1.31±0.06 8 days post injection and was significantly lower than CD44v6 Ab ($p=0.004$) in the MCF10DCIS tumor. The tumor-to-background ratio of CD44v6 Ab in the MDA-MB-231 tumor was comparable to control IgG (1.41±0.11, $p=0.201$) and significantly lower than in the MCF10DCIS tumor ($p=0.011$).

Because the antibody levels 8 days post injection were relatively low and positioning of the mice and localization of the tumor could influence the accuracy of the fluorescent signal levels obtained (and thus the tumor-to-background ratio), we determined the coefficient of variation of the optical imaging technique. Four mice were imaged four times each, with readjustment of the imaging device, repositioning of the mice, and reassessing the volume and location of the ROI. The coefficient of variation was 6.1%, supporting the reproducibility of the optical imaging technique.

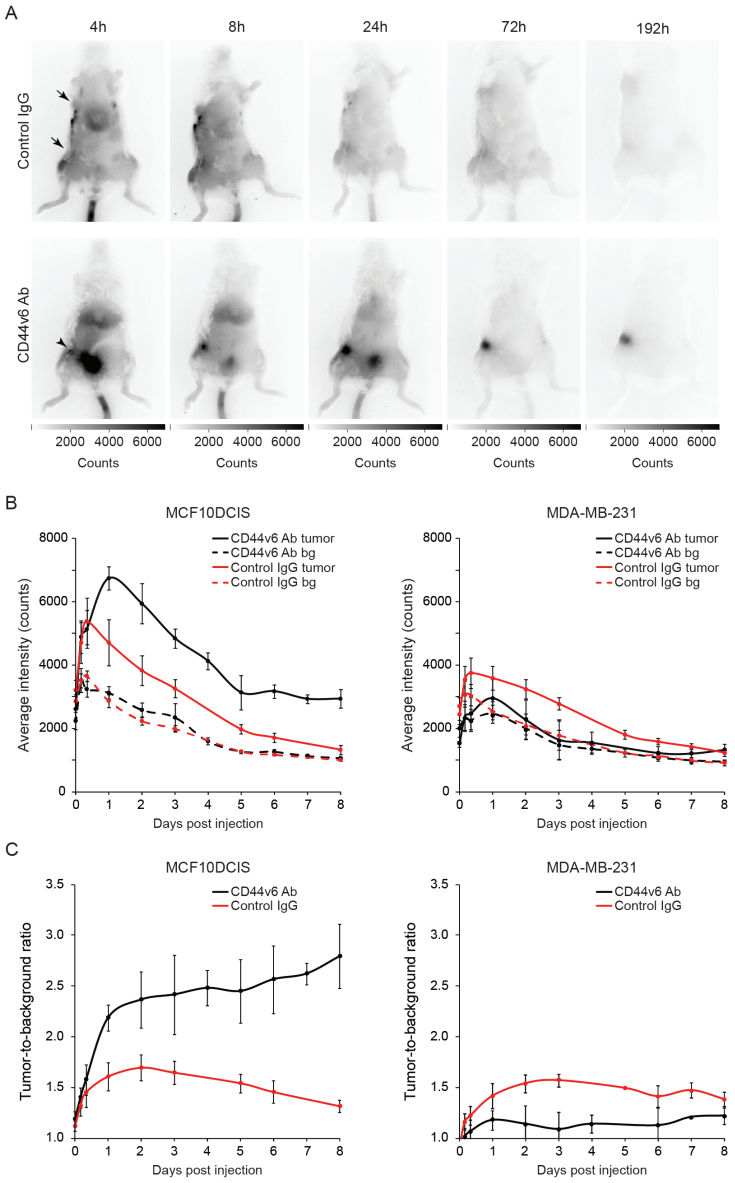

Figure 1: Non-invasive optical molecular imaging of breast cancers. A. Representative SCID Beige mice bearing orthotopically transplanted MCF10DCIS (inguinal) and MDA-MB-231 (thoracic) tumors. Mice were intravenously injected in the tail vein with CD44v6 Ab or control IgG. At 4h post injection, tumor accumulation of CD44v6 Ab was observed in the MCF10DCIS tumors (arrowhead), whereas no accumulation of control IgG was observed in MCF10DCIS or MDA-MB-231 tumors (arrows). B. Fluorescence intensity of MCF10DCIS tumors (left panel) or MDA-MB-231 tumors (right panel) and background of mice injected with CD44v6 Ab or control IgG over time. Data are displayed as average ± SEM (n=6). (bg= background). C. Tumor-to-background ratio of CD44v6 Ab and control IgG in MCF10DCIS and MDA-MB-231 tumors. Data are displayed as average ± SEM (n=6).

Performance of the intraoperative camera system for non-invasive imaging

Since the camera system used is intended for intraoperative image-guided surgery rather than for non-invasive imaging and quantification of probe accumulation, we examined whether the performance differed between these applications. Non-invasive imaging was performed on day 8, directly followed by intraoperative imaging, using identical imaging parameters. Specific accumulation of the CD44v6 Ab was observed in the MCF10DCIS tumor (Fig. 2A). As expected, we neither detected accumulation of the CD44v6 Ab in the MDA-MB-231 tumor nor was control IgG observed in the MCF10DCIS tumor. Tumor intensity of MCF10DCIS and MDA-MB-231 tumors compared to the surrounding tissue (skin and abdomen) was higher, independent of the injected IgG (Fig 2A, B), most likely due to probe retention caused by enhanced tumor vascularization. MCF10DCIS tumor signals were significantly higher in CD44v6 Ab-injected mice intraoperatively, compared to the MDA-MB-231 tumors in the same mouse and compared to the MCF10DCIS tumors in mice injected with control IgG ($p=0.014$ and $p=0.006$, respectively; Fig. 2B). Accordingly, the resulting tumor-to-background ratios were significantly higher for CD44v6 Ab in MCF10DCIS vs. MDA-MB-231 (4.5±0.18 vs. 1.4±0.11, $p=0.006$) and for CD44v6 Ab vs. control IgG in the MCF10DCIS tumor (4.5±0.18 vs. 1.7±0.05, $p=0.014$), indicating specific accumulation of CD44v6 Ab in the MCF10DCIS tumors (Fig. 2C).

To test the performance of the imaging system, we quantified all MCF10DCIS tumors using non-invasive and intraoperative imaging after CD44v6 Ab treatment. Compared to intraoperative imaging, fluorescence intensity of MCF10DCIS lesions with non-invasive imaging was significantly lower in CD44v6 Ab-injected (5,083 vs. 2,900 counts, $p=0.043$) and in IgG injected mice (2,135 vs. 1,537 counts, $p=0.028$). In conclusion, NIRF intraoperative imaging yields a superior tumor-tobackground ratio compared to non-invasive imaging.

Biodistribution of NIRF-labeled antibodies

To quantitate the tumor uptake of CD44v6 and control IgG, liver, kidneys, blood, spleen, and muscle of individual mice were collected directly after intraopera-

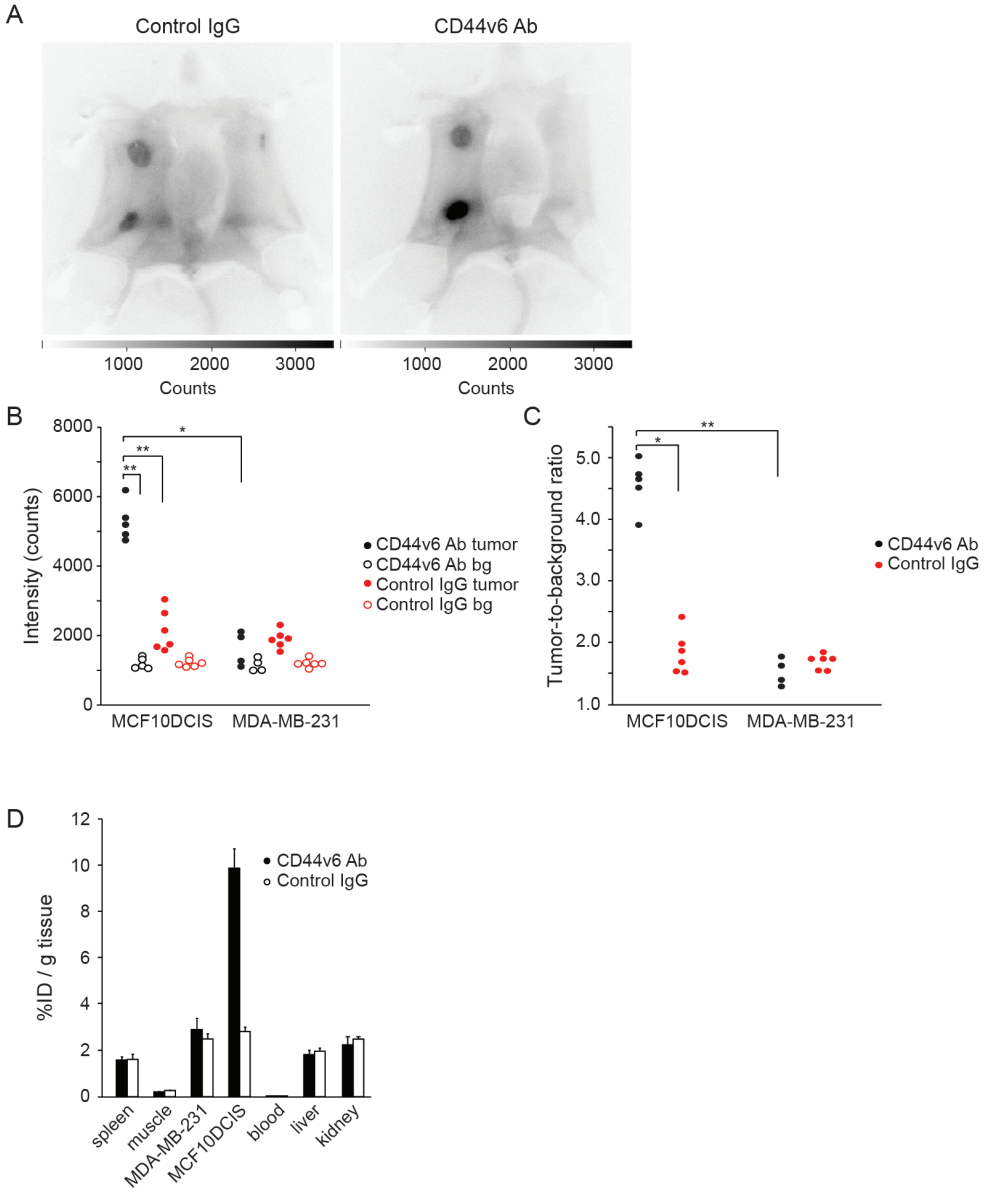

Figure 2: Intraoperative imaging of breast cancers. A. Representative intraoperative fluorescence images of mice bearing MDA-MB-231 tumors and MCF10DCIS tumors 8 days post injection with control IgG and CD44v6 Ab. Clear accumulation of CD44v6 Ab was observed in the MCF10DCIS tumor compared to control IgG. Higher signals in both tumors compared to the background were found, independent of the injected antibody due to enhanced perfusion and retention of the tumor. B. Fluorescence intensity of MCF10DCIS and MDA-MB-231 tumors and the corresponding background (bg) in individual mice (*p<0.05; **p<0.01). C. Tumor-to-background ratio of CD44v6 Ab and control IgG in MCF10DCIS and MDA-MB-231 tumors displayed for individual mice (*p<0.05; **p<0.01). D. Biodistribution of CD44v6 Ab and control IgG 8 days post injection. Tissue levels are expressed as percentage injected dose per gram tissue (%ID/g) as average ± SEM (n=6).

tive imaging. Eight days post injection, the levels of CD44v6 and control IgG in blood were very low (2‰ of the injected dose (ID) per gram tissue) (Fig. 2D). The levels of IgG in muscle was low (approximately 0.2% ID/g tissue), while 9.9±0.8% ID/g of the CD44v6 Ab and 2.8±0.2%ID/g tissue of the control IgG were present in the MCF10DCIS tumor. The percentage of the injected dose per gram tissue of the CD44v6 Ab or the control IgG in the MDA-MB-231 tumor (2.9±0.5 vs. 2.5±0.3% ID/g, respectively) was slightly higher compared to spleen, kidney, and liver. Furthermore, no difference was found between the injected dose per gram tissue of control IgG in the MDA-MB-231 and MCF10DCIS tumors (Fig. 2D). In conclusion, our data indicate that NIRF signals measured with intraoperative imaging (8 days post injection) reflect the actual levels of NIRF probe in the tumors and can be used as a surrogate measure for biodistribution.

Heterogeneous CD44v6 antibody uptake in pre-invasive breast cancer lesions

As shown in Fig. 3A, no accumulation of control IgG was observed in both MDA-MB-231 and MCF10DCIS tumors, while CD44v6 Ab specifically accumulated in the MCF10DCIS lesion, which is in line with the imaging results. Similar to human DCIS, p63 staining of the myoepithelial cells surrounding the MCF10DCIS lesion confirmed the non-invasive phenotype of the MCF10DCIS lesion. Staining for the injected probes by immunohistochemistry revealed a clear difference in tumor distribution; low levels of control IgG were present in the stroma surrounding the tumor cells (Fig. 3B), while CD44v6 Ab was exclusively bound to the epithelial cells of the MCF10DCIS lesion and correlated with CD44v6 expression. Furthermore, staining suggested that tumor penetration of CD44v6 Ab was limited to the first two cell layers aligning blood vessels or stroma (Fig. 3B). These results show that tumor penetration of antibodies is limited and resulted in heterogeneous tumor distribution. Further, detection of DCIS-like lesions using NIRF probes was not hampered by the non-invasive phenotype of the DCIS, suggesting that molecular imaging is suitable for detection of DCIS *in vivo*.

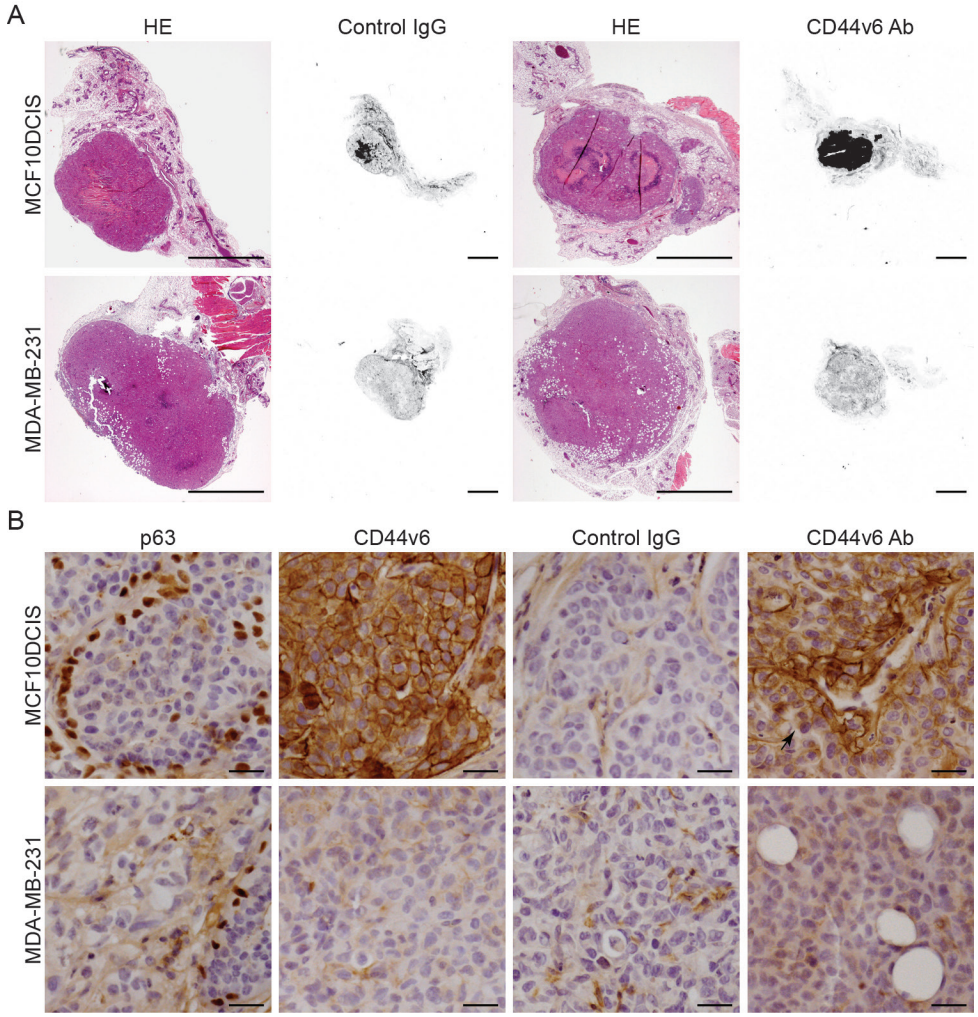

Figure 3: Tumor-specific accumulation of fluorescent probes in breast cancer. A. Representative sections of MDA-MB-231 tumors and MCF10DCIS tumor of mice injected with control IgG or CD44v6 Ab. Hematoxylin and eosin (HE)-stained sections show the non-invasive character of the MCF10DCIS tumor maintaining the preexisting ductal structures intact, whereas the MDA-MB-231 tumors are invading in the mammary fat pad. Accumulation of IRDye800CW-labeled antibodies was detected for CD44v6 Ab in the MCF10DCIS tumor (fluorescence in control IgG was caused by necrosis for unknown reasons). Size bar equals 2 mm. B. Immunohistochemical characterization of breast cancers and evaluation of intratumor distribution of injected antibodies. The non-invasive (DCIS) phenotype of MCF10DCIS lesions was shown by p63 staining of the myoepithelial cells surrounding the MCF10DCIS lesion, which was absent in the MDA-MB-231 tumor. CD44v6 was homogeneously expressed in the MCF10DCIS lesion, which correlated with tumor accumulation of injected CD44v6 Ab. In addition, no accumulation of control IgG was observed in the MCF10DCIS and MDA-MB-231 lesions, whereas CD44v6 Ab accumulation in MCF10DCIS lesions was mainly restricted to the first two cell layers aligning blood vessels or stroma (arrow). Size bars equal 50 µm.

Discussion

There is increasing interest in molecular imaging of breast cancer. Multiple membrane markers, e.g. growth factor receptors and hypoxia upregulated membrane markers, are currently investigated as candidates for molecular imaging of breast cancer [4]. We showed previously that CD44v6 might be required as tumor marker to achieve sufficient sensitivity for molecular imaging, since growth factor receptors and hypoxia upregulated membrane markers alone are too infrequently expressed in breast cancer [7].

In the present study, we show that optical imaging with IRDye800CW-labeled humanized antibodies directed to CD44v6 is feasible in a model of pre-invasive breast cancer. We could assess the specific uptake of the probe *in vivo* and demonstrate application of this probe for intraoperative surgery purposes. Tumor accumulation of IRDye800CW-labeled CD44v6 antibodies in our study (9.9±0.8% ID/g) was comparable to studies using radiolabeled CD44v6 antibodies, which reported a tumor accumulation of 12.9–15.4% ID/g in human or 15.3% ID/g using A431 xenografts in mice [21, 28]. This indicates that biodistribution of IRDye800CW-labeled CD44v6-specific antibodies is comparable to radiolabeled CD44v6 antibodies, which was also recently shown for epidermal growth factor receptor (EGFR)-specific antibodies [27]. In comparison with previous studies using bevacizumab and trastuzumab as probes for optical imaging of breast cancer (tumor-to-background ratios of 1.93±0.40 and 2.92±0.29, respectively) [29], the tumor-to-background ratios of CD44v6 Ab were higher after 6–8 days. Whether these differences were caused by differences in pharmacokinetics or related to target expression remains unclear. Furthermore, using a control IgG, we were able to determine the contribution of perfusion/nonspecific accumulation to the tumor-to-background ratio, which attributed as much as 50% to the tumor-to-background ratio in the first 2 days.

In the present study, non-invasive imaging underestimated fluorescence signal intensities of the tumors by approximately 50%, which might be caused by absorption of fluorescence signal by the skin and the subcutaneous and mammary

fat. This directly affected the minimal tumor size we could detect, i.e., DCIS lesions of approximately 3 mm were detectable *in vivo*, while submillimeter DCIS lesions could be detected with intraoperative imaging. Therefore, non-invasive imaging of breast cancer may significantly underestimate the tumor size, tumor uptake, and/or tumor-to-background ratios of injected probes. More importantly, it might even falsify the conclusions drawn regarding the suitability of a probe for molecular imaging. Given these potential disadvantages of optical imaging, detection of small breast cancer and in situ lesions in patients (e.g., when molecular imaging is applied for screening purposes) might become problematic due to limited excitation power of the laser, localization of the breast tumor, absorption by breast tissue/tumor, and size of the breast. Upcoming clinical trials with IRDye800CW-conjugated antibodies will demonstrate the value of optical molecular imaging for screening purposes.

We showed previously that within normal breast epithelium, myoepithelial cells express low levels of CD44v6. Therefore, the choice of CD44v6 as an imaging target might result in increased background signal from normal breast epithelium and thereby diminished sensitivity and specificity for detection of breast cancer or DCIS lesions. In our preclinical model, the normal (mouse) mammary epithelium did not express CD44v6 and thus did not influence the specificity and sensitivity of detection. Although the uptake of the normal human breast tissue was comparable to that of tumors, Koppe et al. showed that while SPECT imaging of T1 tumors using CD44v6 antibodies had sufficient sensitivity to detect the majority of breast cancers due to increased cellularity of the tumor tissue, the limited resolution of the camera was likely hampering the detection of the cancer in the remaining patients. In addition, when less than 20% of tumor cells were positive for CD44v6, SPECT imaging was not able to detect the lesion [22]. For optical imaging methods, the influence of heterogeneous target expression on the tumor detection is not described, but our unpublished data reveal a similar pattern using optical imaging.

Another parameter attenuating imaging sensitivity was intratumor distribution of the probes. We found that diffusion of IgGs from tumor-associated blood vessels was limited to the aligning first two to three cell layers of the lesion, probably due to size-limited diffusion. Tumor accumulation, expressed as injected dose per gram

tissue of CD44v6 Ab after 8 days, was not different from previous studies performed with Erbitux after 24h [25]. This suggests that maximum tumor accumulation is achieved 1 day post injection and that increased tumor-to-background ratios are solely achieved by clearance of circulating antibodies. Increasing tumor accumulation by size reduction of the probes could enhance the sensitivity of optical imaging for small breast cancers and DCIS. In the case of EGFR, improved tumor uptake and intratumor distribution were achieved by using VHHs (15 kDa antibody fragments consisting of only the Vh domain of the heavy-chain-only antibodies from camelids). In the study of Oliveira et al., VHH-based probes showed a maximum uptake after 2h resulting in homogeneous distribution, suggesting a better tumor penetration [25]. For detection of DCIS and other poorly vascularized lesions, application of VHHs and other small tumor-specific probes for optical imaging might be the preferred option for optical imaging.

Conclusions

Using CD44v6-specific antibodies, we show that near-infrared optical molecular imaging has sufficient sensitivity for non-invasive and intraoperative imaging of DCIS lesions *in vivo*. This opens the way to clinical image-guided surgery trials in humans. In parallel, further improvements may be achieved by better tumor penetration through size reduction of probes.

References

1. Stillebroer AB, Zegers CM, Boerman OC et al (2012) Dosimetric analysis of 177Lu-cG250 radioimmunotherapy in renal cell carcinoma patients: correlation with myelotoxicity and pretherapeutic absorbed dose predictions based on 111In-cG250 imaging. J Nucl Med: Off Publ Soc Nucl Med 53:82–89
2. Hirche C, Murawa D, Mohr Z et al (2010) ICG fluorescence-guided sentinel node biopsy for axillary nodal staging in breast cancer. Breast Cancer Res Treat 121:373–378
3. Murawa D, Hirche C, Dresel S, Hunerbein M (2009) Sentinel lymph node biopsy in breast cancer guided by indocyanine green fluorescence. Br J Surg 96:1289–1294
4. Oude Munnink TH, Nagengast WB, Brouwers AH et al (2009) Molecular imaging of breast cancer. Breast 18(Suppl 3):S66–S73
5. Frangioni JV (2008) New technologies for human cancer imaging. J Clin Oncol 26:4012–4021
6. Frangioni JV (2003) In vivo near-infrared fluorescence imaging. Curr Opin Chem Biol 7:626–634
7. Vermeulen JF, van Brussel AS, van der Groep P et al (2012) Immunophenotyping invasive breast cancer: paving the road for molecular imaging. BMC Cancer 12:240
8. Fox SB, Fawcett J, Jackson DG et al (1994) Normal human tissues, in addition to some tumors, express multiple different CD44 isoforms. Cancer Res 54:4539–4546
9. Ponta H, Wainwright D, Herrlich P (1998) The CD44 protein family. Int J Biochem Cell Biol 30:299–305
10. Afify A, McNiel MA, Braggin J et al (2008) Expression of CD44s, CD44v6, and hyaluronan across the spectrum of normal-hyperplasiacarcinoma in breast. Appl Immunohistochem Mol Morphol 16:121–127
11. Foekens JA, Dall P, Klijn JG et al (1999) Prognostic value of CD44 variant expression in primary breast cancer. Int J Cancer 84:209–215
12. Schumacher U, Horny HP, Horst HA et al (1996) A CD44 variant exon 6 epitope as a prognostic indicator in breast cancer. Eur J Surg Oncol: J Eur Soc Surg Oncol Br Assoc Surg Oncol 22:259–261
13. Morris SF, O'Hanlon DM, McLaughlin R et al (2001) The prognostic significance of CD44s and CD44v6 expression in stage two breast carcinoma: an immunohistochemical study. Eur J Surg Oncol: J Eur Soc Surg Oncol Br Assoc Surg Oncol 27:527–531
14. Heider KH, Kuthan H, Stehle G, Munzert G (2004) CD44v6: a target for antibody-based cancer therapy. Cancer Immunol Immunother: CII 53:567–579
15. Orian-Rousseau V, Chen L, Sleeman JP et al (2002) CD44 is required for two consecutive steps in HGF/c-Met signaling. Genes Dev 16:3074–3086
16. Wobus M, Kuns R, Sheyn I et al (2002) Endometrial carcinoma cells are nonpermissive for CD44-erbB2 interactions. Appl Immunohistochem Mol Morphol 10:242–246
17. Kaufmann M, Heider KH, Sinn HP, von Minckwitz G, Ponta H, Herrlich P (1995) CD44 isoforms in prognosis of breast cancer. Lancet 346:502
18. Marhaba R, Zoller M (2004) CD44 in cancer progression: adhesion, migration and growth regulation. J Mol Histol 35:211–231
19. van der Voort R, Taher TE, Wielenga VJ et al (1999) Heparan sulfatemodified CD44 promotes hepatocyte growth factor/scatter factor-induced signal transduction through the receptor tyrosine kinase c-Met. J Biol Chem 274:6499–6506

20. Postema EJ, Borjesson PK, Buijs WC et al (2003) Dosimetric analysis of radioimmunotherapy with 186Re-labeled bivatuzumab in patients with head and neck cancer. J Nucl Med: Off Publ Soc Nucl Med 44:1690–1699
21. Colnot DR, Roos JC, de Bree R et al (2003) Safety, biodistribution, pharmacokinetics, and immunogenicity of 99mTc-labeled humanized monoclonal antibody BIWA 4 (bivatuzumab) in patients with squamous cell carcinoma of the head and neck. Cancer Immunol Immunother: CII 52:576–582
22. Koppe M, Schaijk F, Roos J et al (2004) Safety, pharmacokinetics, immunogenicity, and biodistribution of (186)Re-labeled humanized monoclonal antibody BIWA 4 (bivatuzumab) in patients with earlystage breast cancer. Cancer Biother Radiopharm 19:720–729
23. Wetterwald A, van der Pluijm G, Que I et al (2002) Optical imaging of cancer metastasis to bone marrow: a mouse model of minimal residual disease. Am J Pathol 160:1143–1153
24. Schackmann RC, van Amersfoort M, Haarhuis JH et al (2011) Cytosolic p120-catenin regulates growth of metastatic lobular carcinoma through Rock1-mediated anoikis resistance. J Clin Invest 121:3176–3188
25. Oliveira S, van Dongen GA, Stigter-van Walsum M et al (2011) Rapid visualization of human tumor xenografts through optical imaging with a near-infrared fluorescent anti-epidermal growth factor receptor nanobody. Mol Imaging. doi:10.2310/7290.2011.00025
26. Themelis G, Yoo JS, Soh KS et al (2009) Real-time intraoperative fluorescence imaging system using light-absorption correction. J Biomed Opt 14:064012
27. Oliveira S, Cohen R, Stigter-van Walsum M et al (2012) A novel method to quantify IRDye800CW fluorescent antibody probes ex vivo in tissue distribution studies. EJNMMI Res 2:50
28. Heider KH, Sproll M, Susani S et al (1996) Characterization of a highaffinity monoclonal antibody specific for CD44v6 as candidate for immunotherapy of squamous cell carcinomas. Cancer Immunol Immunother:CII 43:245–253
29. Terwisscha van Scheltinga AG, van Dam GM et al (2011) Intraoperative near-infrared fluorescence tumor imaging with vascular endothelial growth factor and human epidermal growth factor receptor 2 targeting antibodies. J Nucl Med: Off Publ Soc Nucl Med 52:1778–1785

Aram S.A. van Brussel, Arthur Adams, Sabrina Oliveira, Mohamed El Khattabi, Jeroen F. Vermeulen, Elsken van der Wall, Willem P.Th.M. Mali, Patrick W.B. Derksen, Paul J. van Diest, Paul M.P. van Bergen en Henegouwen

8

Hypoxia-targeting fluorescent nanobodies for optical molecular imaging of pre-invasive breast cancer

Abstract

Introduction: Optical molecular imaging is a novel strategy in diagnosis and therapy of breast cancer. To arrive at high tumor-to-normal tissue ratios (TNR), tumor-specific probes are required that rapidly accumulate in the tumor. Most tumor markers are however expressed in the minority of tumors. Hypoxia is common in solid tumors and induces carbonic anhydrase IX (CAIX) expression. Here we show development and application of novel CAIX-specific nanobodies (15 kDa) that have a faster tumor uptake and body clearance than conventional antibodies, and can be used for molecular imaging of pre-invasive breast cancer.
Methods: High affinity CAIX-specific nanobodies were selected using a modified phage display technology and conjugated site-specifically to IRDye800CW. Mice bearing orthotopically transplanted MCF10DCIS (DCIS) and CAIX-overexpressing (DCIS+CAIX) xenografts were injected with labelled CAIX-specific nanobody (B9-IR) and non-relevant control nanobody (R2-IR) and imaged up to 48h. Tumors were resected under image-guidance. Nanobody uptake was assessed in tissue sections and quantified with a biodistribution assay.
Results: Two hours after injection, a mean DCIS+CAIX TNR of 4.3±0.6 (±SEM) was observed. Mean DCIS TNR was 1.8±0.1 compared to 1.4±0.2 in tumors from mice injected with a non-relevant control nanobody. In mice injected with B9-IR, uptake was 4.6±0.8% of injected dose per gram DCIS tumor tissue (%I.D./g), compared to 2.0±0.2%I.D./g with R2-IR. After 3h, probe accumulation in perinecrotic regions of DCIS tumors was sufficient to allow image-guided tumor resection.
Conclusion: We have developed novel IRDye800CW-labeled nanobodies specific for CAIX. These highly tumor-specific probes can be used for rapid imaging of (pre-)invasive breast cancer.

Introduction

Molecular imaging modalities such as PET, SPECT and optical imaging use antibodies or antibody fragments to specifically track molecules or cells [1]. The use of a targeting moiety, specific to a tumor antigen, results in higher contrast images, as compared to imaging strategies with non-targeted contrast agents [2-6]. Molecular imaging with fluorescent tracers (optical molecular imaging) has recently gained more interest [7-9], since it does not require expensive imaging equipment or protective measures due to the presence of ionizing radiation, and because it could be broadly applied in diagnosis, surgery and monitoring of therapy response of cancer.

Hypoxia is a condition that is present in the majority of solid tumors and absent in healthy (breast) tissue [10-12]. Carbonic anhydrase IX (CAIX) expression is under regulatory control of HIF-1α, a transcription factor that is stabilized under hypoxic conditions [13, 14]. We selected CAIX as target for molecular imaging, as it is one of the most tumor-specific membrane-bound proteins expressed in hypoxic tumors. CAIX can therefore be considered as a suitable marker that can be used to discriminate cancer from non-cancerous tissues [15, 16].

In a previous study, we showed successful optical imaging of pre-invasive breast cancer of the breast (ductal carcinoma in situ, DCIS) with a CAIX-specific conventional antibody (MabCAIX) [17]. However, slow clearance of the antibody resulted in suboptimal contrast during the first 24h post injection, and only 72h post injection optimal tumor-to-normal tissue ratios (TNR) were observed. The use of probes with molecular sizes below the renal glomerular filtration threshold of ~50 kDa will allow faster clearance and subsequent faster image acquisition with higher contrast. Rapid imaging results in lower costs, less logistic procedures, and less discomfort for the patient and healthcare workers. Furthermore, the fast renal clearance will even allow sequential injections of probes with different specificities. Importantly, because of this rapid renal clearance, small probes should have very high affinity for the target molecule, in order to guarantee sufficient tumor accu-

mulation within the first hours post injection [18].

Promising probes for rapid molecular imaging are VHH (Variable domain of Heavy chain of Heavy-chain-only antibodies), also named nanobodies, which are small immune system proteins that naturally occur in camelids. Compared to conventional antibodies, nanobodies possess several advantageous properties. First, nanobodies are ten times smaller (15 kDa vs. 150 kDa), which results in rapid clearance via the kidneys. Second, they can easily be produced and third, are very stable [19]. As shown earlier, these properties result in increased tumor penetration and earlier tumor uptake [9, 20-22].

In the present study, we describe phage display selections for nanobodies that specifically bind to CAIX with high affinity. These nanobodies were selected from a library derived from llamas immunized with hypoxic HeLa cells. A sub-library was produced on basis of PCR using CDR3 sequences from two initial anti-CAIX nanobodies, and from this library high affinity binders for CAIX were obtained. To avoid affinity loss after random conjugation, the nanobodies were site-directed conjugated to IRDye800CW and used for optical molecular imaging of CAIX expressing xenografts in mice. Our data support application of anti-CAIX nanobodies for early detection of hypoxic tumors in general, and breast cancer in particular. The CAIX-specific nanobodies can be used for pre-, intra-, and postoperative optical imaging of (pre-invasive) breast cancer, and hypoxic tumors from other sites, and hold promise for broader applications such as clinical PET or SPECT imaging.

Material and Methods

Antibody production, cell lines and cell culture

MabCAIX antibody was produced as described before [17]. A431 epidermoid cancer (CRL-1555), HeLa cervical cancer (CCL-2) and MDA-MB-231 breast cancer cells (HTB-26, ATCC, Wesel, Germany) were grown in Dulbecco's Modified Eagle's Medium (DMEM; Invitrogen, Breda, The Netherlands) supplemented with 10% (v/v) Fetal Calf Serum (FCS), 100 IU/ml penicillin, 100 µg/ml streptomycin, and 2 mM L-glutamine, at 37°C in a humidified atmosphere containing 5% CO_2. MCF10DCIS.com (further referred to as MCF10DCIS) cells (Asterand, Detroit, USA) and MCF-10A cells (CRL-10317, ATCC, Wesel, Germany) were cultured according to the supplier's guidelines in DMEM/F12, supplemented with 10% (v/v) FCS, 100 IU/ml penicillin, 100 µg/ml streptomycin and 2 mM L-glutamine. Generation of luciferase, and CAIX overexpressing MCF10DCIS cells was described by Van Brussel et al. [17]. All cells were cultured at 37°C in a humidified atmosphere containing 5% CO_2 and were consistently Mycoplasma free.

Cell-based enzyme-linked immunosorbent assay (ELISA)

A431, MCF-10A, MDA-MB-231 and HeLa cells were seeded in 96-wells plates (15,000 cells per well) and cultured overnight under normoxic (21% O_2) or hypoxic (1% O_2) conditions. Next day, cells were put on CO_2-independent medium supplemented with 4% marvel (dried skimmed milk) and blocked for 30 min at 4°C. Next, hypoxic cells were treated with 100 µM deferoxamine (DFO, Sigma Aldrich, Zwijndrecht, The Netherlands). After washing twice with phosphate buffered saline (PBS), cells were incubated with rabbit anti-CAIX antibody (1:2,000; clone ab15086, Abcam, Cambridge, UK) for 1.5h and fixed with 4% paraformaldehyde (PFA) for 30 min. PFA was quenched with NH_4Cl for 15 min. Primary antibody was detected with donkey anti-rabbit conjugated to peroxidase, after incubation with o-Phenylenediaminedihydrochloride (OPD) with 0.1% H_2O_2 used as chromogen and 1 M sulfuric acid was used to stop the peroxidase reaction. Signal was measu-

red using a microplate reader (Bio-Rad model 550, Bio-Rad Laboratories, Veenendaal, The Netherlands).

Immunization and immune response determination

Immunizations were approved by the Utrecht University animal ethics committee (DEC no. 2007.III.01.013). For immunization, $8.0x10^8$ HeLa cells were cultured under hypoxia (1% O_2) overnight in an INVIVO2 hypoxia workstation (Ruskinn, Pencoed, UK) and afterwards divided into 8 vials and stored at -80°C in medium containing FCS with 10% DMSO and DFO. Two llamas (Llama glama) were injected 4 times in the pectoral muscle, with intervals of 2 weeks. Blood was drawn before the first and after the second injection to measure the immune response, and after 8 weeks for construction of the phage library. To measure the immune response, HeLa cells were seeded in two 96-wells plates ($1.5x10^4$ per well) and grown for 24h under 21% or 1% O_2. Cells were incubated with serial dilutions of immune or pre-immune llama serum for 2h at 4°C. After washing twice with 1% BSA in PBS, cells were fixed in 4% PFA for 20 min, followed by quenching of reactive amine groups with 50mM NH_4Cl in PBS for 15 min. Bound heavy-chain antibodies were detected with anti-VHH polyclonal rabbit serum (1:1,000), and a donkey anti-rabbit antibody coupled to peroxidase (1:5,000). As positive control for hypoxia, MabCAIX was produced as described earlier [17], which was detected with a donkey anti-mouse antibody coupled to a peroxidase. OPD with 0.1% peroxide was used as chromogen, and 1 M sulfuric acid was used to stop the peroxidase reaction.

Library construction

Construction of phagemid libraries was performed as described before [23]. In short, peripheral B-lymphocytes were isolated from llama blood. RNA was purified by phenol chloroform extraction, and cDNA was generated by reverse transcriptase PCR (SuperScript III, Life Technologies Europe BV, Bleiswijk, The Netherlands). VHH DNA was amplified with PCR using IgG-specific primers and cloned in the pUR8100 phagemid vector. *Escherichia coli* strain TG1 [supEhsd_5 thi (lac-proAB) F(traD36 proAB_ lacIqlacZ_M15)] was used for the transformation with VHH-phage libraries and for the production of phages.

Phage display selections

Maxisorp plates were coated with 1.00, 0.50, 0.10, 0.05 and 0.00 µg recombinant CAIX (R&D systems, Minneapolis, USA). Phages were produced from *E. coli* TG1 harboring the library after infection with helper phage VSCM13 (Strategene, Agilent Technologies Netherlands B.V., Amstelveen, The Netherlands) and incubating overnight while shaking at 37°C in medium containing ampicillin (100 µg/ml) and kanamycin (25 µg/ml). Next day, maxisorp wells were washed three times with PBS and blocked with 4% marvel in PBS. Phages were precipitated by adding 2% polyethylene glycol (PEG), 250 mM NaCl for 30 min on ice. After spinning down and resuspending the pellet in ice cold PBS, PEG precipitation was repeated two times. After resuspension, phages were incubated in the blocked maxisorp wells for 2h at room temperature, while shaking. Non-specific phages were removed by washing twenty times with PBS containing 0.05% Tween, every fifth time shaking for ten min. Bound phages were eluted by trypsin digestion (1.0 mg/ml) for 20 min and infection of an *E. coli* culture in the exponential phase of the growth for 30 min after adding trypsin inhibitor. After infection, phages were titrated, spotted on agar plates (containing 100 µg/ml ampicillin and 2% glucose) to calculate the number of bound phages. Subsequently, the infections were grown overnight in 2TY medium containing 100 µg/ml ampicillin and 2% glucose, shaking at 37°C. Next day the overnight culture was used for phage production. On the third day a second round of selections was performed by incubating output phages from the first round of selections in wells coated with a concentration range of 0.01 to 1.00 µg recombinant CAIX.

Periplasmic fraction production and ELISA screening on cells

Single *E. coli* TG1 colonies were picked from agar plates and grown in 100 µl 2TY supplemented with 2% glucose and 100 µg/ml ampicillin in sterile 96-wells plates with v-shaped bottom overnight at 37°C. Next day, 10 µl of TG1 were used to inoculate 1 ml 2TY supplemented with 100 µg/ml ampicillin in 96-well square V-bottom plates (Corning, New York, USA) for 4h at 37°C while shaking. Nanobody production was induced by adding 1mM isopropyl β-D-1-thiogalactopyranoside (ITPG) and subsequently incubated for 4h at 37°C. Bacteria were spun down at

4,600 rpm for 15 min, and pellets were frozen at -20°C overnight. Next day pellets were thawed and dissolved in 100 µl PBS. After centrifugation at 4,600 rpm for 15 min the supernatant was used for further screening in an ELISA format.
CAIX overexpressing and non-overexpressing MCF10DCIS cells were plated in 96-wells at 12,000 cells per well. Next day, cells were put on CO_2-independent medium with 4% marvel and blocked for 30 min at 4°C. Monoclonal periplasmic fractions (30 µl) were added to the wells and incubated for 2h at 4°C. After washing twice with PBS, cells were fixed with 4% PFA for 30 min and PFA was quenched with NH_4Cl/PBS for 15 min. Nanobodies were detected with a rabbit anti-VHH serum and donkey anti-rabbit peroxidase. OPD with 0.1% H_2O_2 was used as chromogen.

Nanobody production and purification

Nanobodies were re-cloned from the pUR8100 phagemid vector into the pQVQ72 expression vector (kindly provided by QVQ BV, Utrecht, The Netherlands), which introduces a C-terminal cysteine, flanked by a FLAG-tag to enable site-directed conjugation of IRDye800CW-Maleimide (LI-COR Biosciences, Lincoln, NE). After transformation into *E. coli* TG1, 800 ml cultures were grown in 2x Tryptone Yeast Extract Medium (2TY), until optical density of 0.5 at 600 nm (OD600: 0.5) was reached. Nanobody production was induced by adding 1mM IPTG and 4h after induction bacteria were harvested by centrifugation. Pellets were frozen at -20°C and next day the periplasmic fraction was obtained by thawing, resuspension in PBS, followed by spinning for 2h head-over-head at 4°C, and centrifugation at 4,600 rpm for 15 min. Nanobodies were purified from the periplasmic fraction by affinity chromatography using a HiTrap protein A HP column (GE Healthcare, Zeist, The Netherlands) using the ÄKTAxpress system (GE Healthcare).

Immunofluorescence

Cover glasses were coated with 0.25% gelatin and seeded with $2.0x10^4$ MCF10DCIS cells. Cells were incubated with 1 µM nanobodies for 2h at 4°C. After washing twice with PBS, cells were fixed in 4% PFA for 30 min and quenched with 100 mM glycin in PBS for 10 min. Nanobodies were detected with a rabbit anti-VHH at

1:500 and CAIX-FLAG was detected with mouse anti-FLAG M2 (1:500, Sigma Aldrich, Zwijndrecht, The Netherlands). Subsequently, a goat anti-rabbit Alexa488 and a goat anti-mouse Alexa555 (Life Technologies Europe BV, Bleiswijk, The Netherlands) were used for detection, using a confocal microscope (Zeiss, Sliedrecht, The Netherlands).

Generation of family-specific phage sub-library ('family approach')

Based on the sequence of two anti-CAIX nanobodies, two family-specific sub-libraries were made following the procedure previously described [24], with a few modifications. A unique degenerate reverse primer extending into the entire CDR3 loop region was designed and used in conjunction with the plasmid-based primer (M13 rev) to PCR VHH gene fragments with the same CDR3 present in the library. Amplification was carried out with Phusion High-Fidelity DNA Polymerase (Thermo Fisher Scientific, Landsmeer, The Netherlands), and a 350-bp band was excised after separation on an agarose gel. Following restriction enzyme digestion with BstEII and SfiI and gel purification, the digested DNA fragments were ligated into the phagemid vector pUR8100 for display on filamentous bacteriophage and transferred to *E. coli* TG1 competent cells by electroporation. The resulting two family libraries were used for phage display selections as described above.

Conjugation of IRDye800CW to CAIX nanobodies

Before labeling, nanobodies were reduced by adding 70-fold molar excess of tris (2-carboxyethyl) phosphine hydrochloride (TCEP). IRDye800CW-Maleimide (further referred to as IR; LI-COR) was conjugated to nanobodies following manufacturer recommendations, with molar dye to protein ratios of 4:1. After labeling, free dye was separated from the conjugate using two passages through Pierce ZebaTM Desalting Spin Columns (Thermo Fisher Scientific, Landsmeer, The Netherlands). The degree of labeling (DOL) was calculated using the absorbance at 280 nm (A280) and 774 nm (A774) with a NanoDrop spectrophotometer (NanoDrop Technologies, Wilmington, Delaware, USA). DOL was calculated with the formula: dye/protein=($A_{774}/\varepsilon_{dye}$) / ($A_{280}$-(0.03 x A_{774}) / ε_{prot}), where the molar extinction coefficient of IRDye800CW (ε_{dye}) is 240,000 M^{-1} cm^{-1} and the molar extinction coef-

ficients for the protein (ε_{prot}) is 31,400; 25,900; 31,400; 31,400 and 30,940 M^{-1} cm^{-1} for CAIX1, E4, B9, C5 and R2 nanobodies respectively.

Characterization of IR-conjugated nanobodies

IR-conjugated proteins (1 μg) were size-separated with 15% SDS-PAGE. Gels were stained with Coomassie Brilliant Blue solution (SERVA Electrophoresis GmbH, Heidelberg, Germany) and imaged with the Odyssey imaging system (LI-COR Biosciences, Lincoln, NE) using the 700 nm channel for the Coomassie stain and the 800 nm channel for IR detection. For affinity determination of IR-labelled nanobodies, $2.0x10^4$ MCF10DCIS cells were seeded per well, one day in advance and incubated at 4°C for 1.5h with dilution series of IR-labelled nanobody in PBS in triplicate. The detection of bound IR-labelled nanobody was performed using the 800 nm channel of the Odyssey imaging system. The dissociation constant (K_D) was derived from the concentration of nanobodies at which half the intensity of B_{max} was found using non-linear regression, of one site specific binding (Graphpad Prism v.5, GraphPad Software, La Jolla, USA).

In vivo experiments

All animal experiments were approved by the Utrecht University Animal Experimental Committee (DEC no. 2012.III.02.015). The mouse model used in this study was based on a previously described model [25, 26]. A real-time intra-operative multispectral fluorescence reflectance imaging (MFRI) system (SurgOptix, Groningen, The Netherlands) was used to monitor uptake and washout of the fluorescent nanobody over time as described before [17, 26, 27]. TNR analysis was performed using GraphPad Prism (v.5, GraphPad Software). TNRs, obtained during optimal imaging time points after injections with B9 nanobody or non-relevant R2 nanobody, were compared using the Mann-Whitney U test (two-tailed).

Imaging of fluorescent sections and immunohistochemistry

Immediately after resection, tumors were fixed in neutral buffered formalin, routinely processed to paraffin blocks and stored in the dark until further processing. Following deparaffination and rehydration, 4 μm thick sections were mounted in

Vectashield Mounting Medium (Vector Laboratories, Burlingame, CA, USA) and scanned using the Odyssey imaging system at highest (21 μm) resolution and highest quality. Immunohistochemistry (IHC) for CAIX and haematoxylin and eosin (H&E) stainings were performed as described before [26]. Slides were scanned with the Scanscope XT 120 scanner (Aperio, Vista, CA, USA).

Biodistribution

Quantification of IR-conjugated nanobodies in tumors and tissues was done as previously described [20]. Briefly, tumors and organs collected 3h after probe injection were weighed, snap-frozen in liquid nitrogen and stored at -80°C until further processing. After homogenization and lysis of the organs, dilution series, including pre-defined concentrations of nanobody-IR for calibration, were made in Nunc 96-well plates (Thermo Fisher Scientific, Landsmeer, The Netherlands) with PBS and scanned with the Odyssey imaging system. Thereafter, the quantity of each probe in each organ (in percentage of injected dose per gram of tissue) was determined by intra- or extrapolation of the unknown fluorescence values from the respective calibration curves using the GraphPad Prism software (v.5, GraphPad Software, La Jolla, CA, USA).

Results

Immunization, library construction, phage display selections and screening

To enable llama immunization with cells showing high CAIX expression, we first tested CAIX expression levels of several cell lines cultured under normoxic and hypoxic conditions. Cell lines included A431, MCF-10A, MDA-MB-231 and HeLa. HeLa cells showed the highest CAIX upregulation and were therefore used for immunization (Fig. 1A). Sera obtained from pre- (day 0) and post-immunization (day 28 and 43) were used to follow the development of an immune response against CAIX. Heavy-chain-only antibodies in serum were detected by ELISA, and serum from both llamas showed increased binding at the lower dilution range (1:10,000), indicating a successful immune response (data not shown). Subsequently, we generated a VHH phagemid library as described previously [23]. Various phage display selections were performed using either directly coated recombinant CAIX, captured recombinant CAIX or hypoxic HeLa cells with or without specific elution with anti-CAIX mAb (Fig. 1B).

After two rounds of biopanning, monoclonal periplasmic fractions, containing VHHs provided with a his- and myc-tag, were used for screening on CAIX positive or negative MCF10DCIS cells [17]. From these screenings, two CAIX-specific nanobodies were isolated, indicated as: CAIX1 and CAIX4.

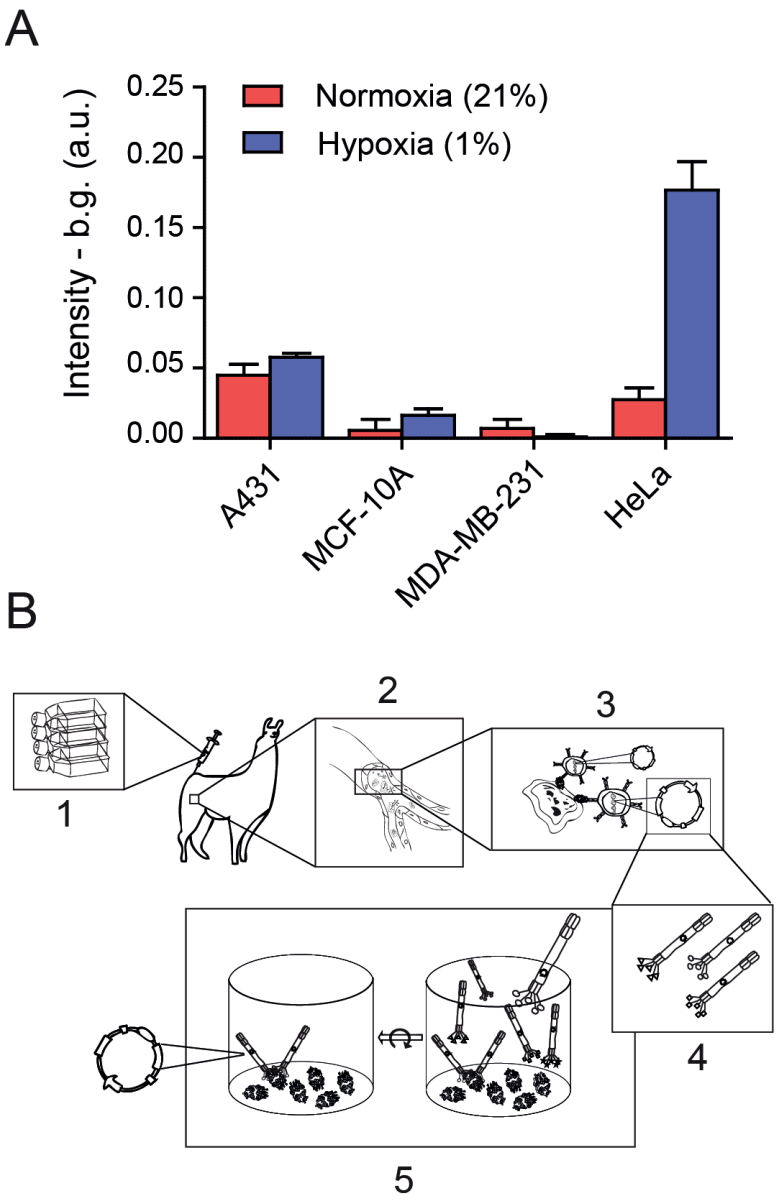

Figure 1: Hypoxic HeLa cells can be used for generation of a hypoxia-specific phage library. A. Indicated cells were grown under normoxic (21% O_2) and hypoxic (1%) conditions for 24h, and CAIX levels were determined by a cell-based ELISA. B. Workflow of phage-display selections: 1. Llamas were immunized with hypoxic HeLa cells; 2. During the immune response peripheral B-lymphocytes generate CAIX specific heavy-chain only antibodies; 3. peripheral B-lymphocytes are isolated and RNA is extracted. After reverse transcriptase PCR, antibody specific DNA is ligated into a phagemid vector; 4. Phages expressing nanobodies at their surface are produced in *E. coli* bacteria; 5. Two rounds of phage display selections are performed in a 96-wells format coated with recombinant CAIX.

Nanobody characterization and generation of a CAIX1 and CAIX4 family-specific phage library

To analyze the specificity of CAIX1 and CAIX4 nanobodies, immunofluorescence studies were performed using co-cultures of CAIX-overexpressing and CAIX negative MCF10DCIS cells. Cells were incubated with CAIX1 or CAIX4 nanobodies, which were detected with antibodies directed against VHH (Fig. 2A, green). In order to visualize CAIX-FLAG, anti-FLAG antibodies were used (Fig. 2A, red). The overlay showed nanobodies binding to the CAIX positive cells. CAIX negative cells did not show any nanobody binding (Fig. 2A, arrows). Subsequently, binding experiments were performed to determine affinities (K_D) of the unconjugated nanobodies for CAIX, which were 11 nM for CAIX1 and 45 nM for CAIX4.

To obtain anti-CAIX nanobodies with higher affinities, a new second-generation family-specific library was made, a method previously described by Koh et al. [24]. Primers were designed based on the N-terminal framework sequence and on the CDR3 sequence of both nanobodies and a PCR was performed using the original library as a template (Fig. 2B). With this novel CAIX library, phage display selections were performed using recombinant CAIX, resulting in the isolation of three additional anti-CAIX nanobodies indicated as C5, B9 (based on the CAIX1) and E4 (based on the CAIX4). Affinities of these unconjugated VHHs were determined on CAIX expressing MCF10DCIS cells. CAIX1-based nanobodies showed an improvement in affinity: from the original 11 nM to 6 and 7 nM for C5 and B9 respectively. Major gain in affinity was obtained with the CAIX4-based family approach: from 45 nM for the CAIX4 nanobody, to 2 nM, which was the affinity of the novel anti-CAIX nanobody E4.

Characterization of IR-conjugated CAIX nanobodies

Four anti-CAIX nanobodies were randomly conjugated to NHS-IRDye800CW and the affinities were checked by a binding assay using CAIX expressing MCF10DCIS cells. Affinities of all nanobodies were considerably reduced (data not shown) and thus we decided to conjugate the dye by site-directed conjugation via a C-terminal cysteine residue as described previously [9]. After C-terminal conjugation of the nanobodies with Maleimide-IRDye800CW, the degree of labeling (DOL) was ap-

proximately 0.6 for all nanobodies. Subsequently, the binding affinity of the nanobodies was determined and showed K_D of 19, 17, 13 and 8 nM for CAIX1-IR, C5-IR, B9-IR and E4-IR, respectively (Fig. 2C). The labeling procedure had detrimental effects on the affinity of CAIX4-IR. The B_{max} of all nanobodies was comparable to CAIX1-IR (~80 a.u.), except of E4-IR, which had a lower B_{max} (~40 a.u.). We selected B9-IR as lead nanobody for further *in vivo* studies because of the best binding affinity in combination with a high B_{max}.

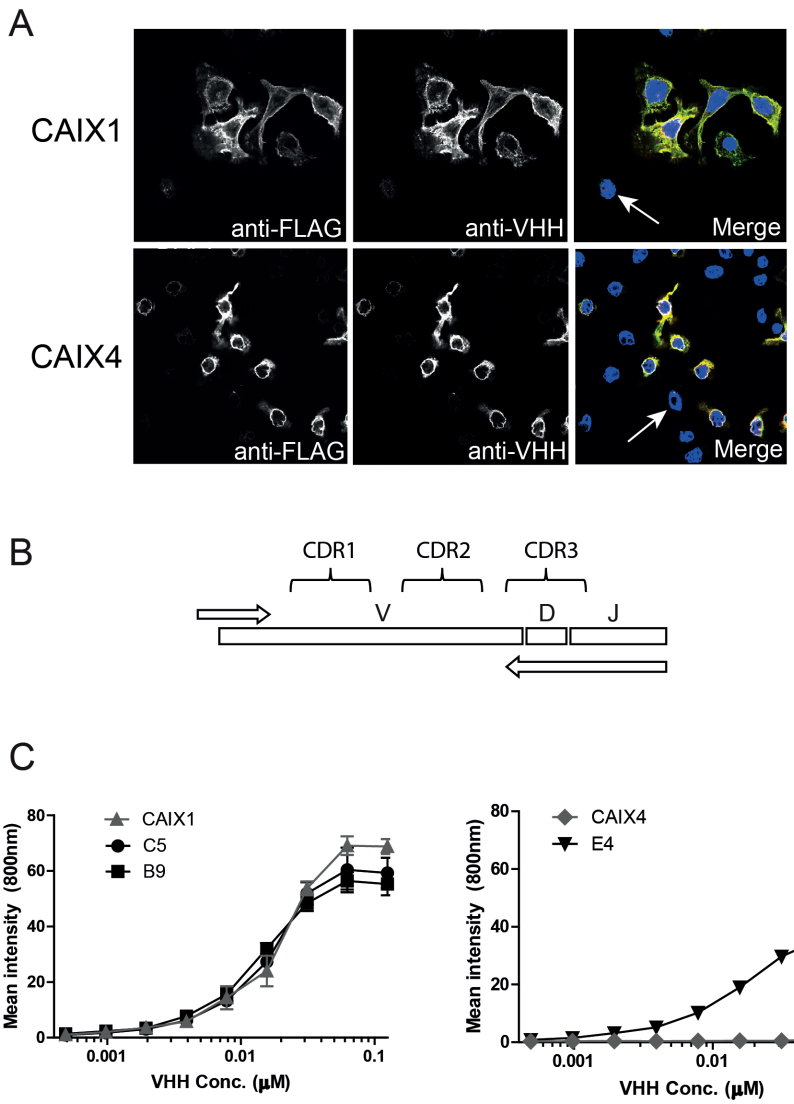

Figure 2: CAIX1 is a high affinity CAIX-specific nanobody and additional nanobodies were selected with the family approach using CAIX1- and CAIX4-based primers. A. Co-cultures of CAIX-FLAG expressing and CAIX negative cells were incubated with either CAIX1 and CAIX4 nanobody. Nuclei were stained with DAPI (blue). Bound nanobodies were detected with Alexa-488 (green) and CAIX-FLAG with Alexa-555 (red). The overlay is shown in the right panels. Arrows indicate cells without CAIX expression. B. DNA of the original phage library is used as template in a PCR reaction with family-specific reverse primers covering the 3rd complementarity determining region (CDR3). The PCR product is ligated in a phagemid vector resulting in a family-specific phage library. C. Cells expressing CAIX were incubated with a dilution range of nanobody conjugated to IRDye800CW: CAIX1(left, gray) and CAIX4 (right, gray) and the nanobodies derived from the family-specific library (black), based on CDR3 of either CAIX1 (C5 and B9) or CAIX4 (E4). The y-axis shows intensity values as measured by the Odyssey system.

In vivo experiments

To test functionality of the B9-IR CAIX-specific nanobody for optical molecular imaging in a preclinical setting, SCID/Beige mice were orthotopically transplanted with MCF10DCIS cells ('DCIS' tumors) and MCF10DCIS cells stably expressing exogenous CAIX ('DCIS+CAIX' tumors). We used the non-relevant R2 nanobody as a negative control [20]. All cells were transduced with a cDNA encoding luciferase, which allowed longitudinal monitoring of tumor growth using bioluminescence imaging. Upon development of palpable tumors, mice were injected in the tail vein with 50 µg B9-IR. Probe distribution was visualized at several time points up to 48h post injection with the fluorescence imaging camera. Already after 2-3h we could delineate both the DCIS+CAIX and DCIS tumors from the background non-invasively (Fig. 3A) and invasively (Fig. 3B, C), based on the fluorescent signal.

TNRs were calculated by dividing absolute fluorescent signal from the tumor by the signal from the hind leg (used as normal tissue) for each time point up to 48h. The mean *in vivo* DCIS+CAIX TNR increased in the first hour until a plateau level was reached that persisted for 8h (Fig. 4A). At this time point, the mean *in vivo* DCIS+CAIX TNR was 5.1±1.3 (standard error of the mean (SEM), n=5). At 2h post injection, a difference was found between the mean DCIS TNR in mice injected with B9-IR (1.8±0.1; n=8) and mice injected with R2-IR non-relevant control nanobody (1.4±0.2; p=0.07; n=4; Fig. 4B). DCIS tumors with a diameter starting from 2 mm could be detected.

After these studies, mice were sacrificed and the skin was removed to enable *ex vivo* tumor imaging. The mean intra-operative TNR of the CAIX-overexpressing tumors was 5.2±0.9, 3h post injection (Fig. 4C). Mean TNR of the DCIS tumors from mice injected with B9-IR or R2-IR was 2.1±0.2 and 1.3±0.1, respectively (p=0.04). The maximum intra-operative TNR of the DCIS tumors obtained from mice injected with B9-IR or R2-IR was 2.7 and 1.5, respectively.

These results show that, beside the (positive control) DCIS+CAIX tumors, native CAIX expressing DCIS tumors could be detected *in vivo* and intra-operatively 2-3h post injection with B9-IR nanobody.

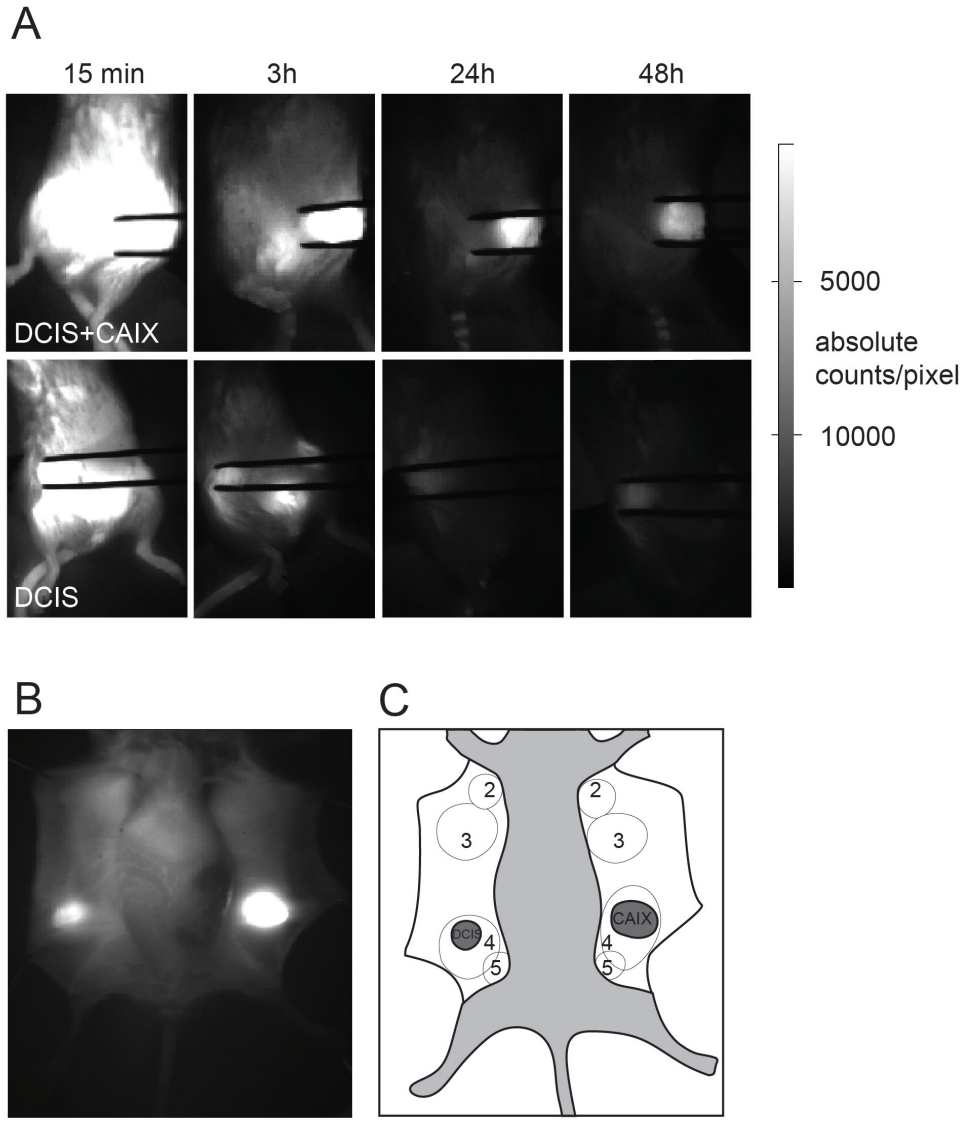

Figure 3: Detection of hypoxic pre-invasive breast tumors *in vivo* and intra-operatively, using the B9-IR nanobody. A. DCIS+CAIX (upper panel) and DCIS (lower panel) xenografts were imaged at several time points post injection of 50 µg B9-IR nanobody. Tumors were held between tweezers. B. Intra-operative imaging of DCIS and DCIS+CAIX tumors, 3h post injection of B9-IR. C. Schematic overview of mammary glands (2-5) and tumors as seen intra-operatively. DCIS+CAIX tumor indicated as 'CAIX'.

Biodistribution

To quantify fluorescent probe signals from the tumors and organs, we performed an *ex vivo* biodistribution study. This technology was specifically designed for this purpose and circumvents effects of scattering and quenching of the fluorescent signal [20, 28]. To determine the biodistribution of both the B9-IR anti-CAIX and the R2-IR non-relevant control nanobodies, organs and tumors of nine mice were excised and their weight was determined. DCIS+CAIX tumors of mice injected with B9-IR and R2-IR had a probe uptake of 14.0±1.1% injected dose per gram tissue (I.D./g) and 1.9±0.5%I.D./g respectively (p=0.01), confirming CAIX-specificity of B9-IR *in vivo*. In DCIS tumors B9-IR probe uptake was 4.6±0.8% I.D./g, compared to 2.0±0.2% I.D./g in mice injected with R2-IR (p=0.2). The difference between B9-IR uptake in DCIS+CAIX and DCIS tumors is caused by the low perinecrotic CAIX content in DCIS tumors compared to the CAIX overexpressing DCIS+CAIX tumors. Compared to other organs, kidney uptake was high due to kidney retention of the nanobodies, confirming biodistribution assays performed by Oliveira et al. [20] (Fig. 4D).

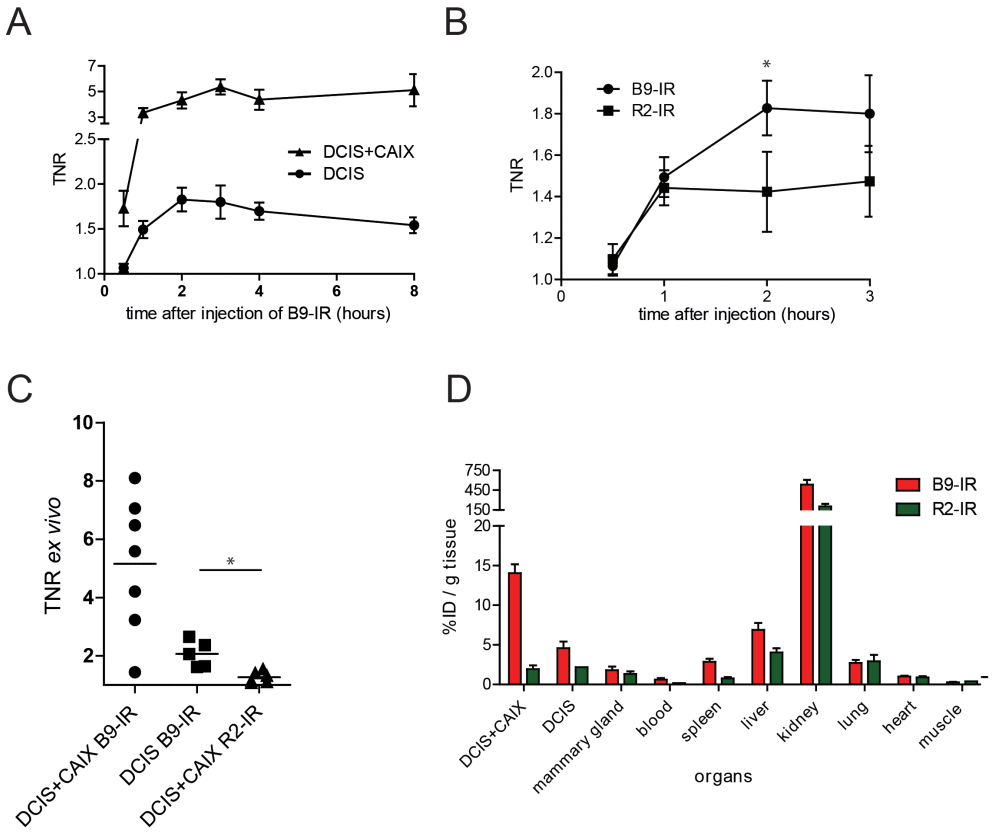

Figure 4: Optimal imaging with B9-IR nanobody 2h post injection. A. Mean TNR of CAIX-overexpressing tumors (DCIS+CAIX, 10 mice), and DCIS tumors (10 mice) determined during the first 8h post injection of B9-IR nanobody. Error bars represent SEM. B. Mice xenografted with DCIS tumors were injected with 50 µl B9-IR (10 mice) or R2-IR (4 mice) non-relevant control nanobody, mean TNR values were determined at indicated time points. (*p=0.07) C. DCIS+CAIX (7 mice) and DCIS (7 mice) were injected with 50 µl B9-IR and DCIS+CAIX tumors (6 mice) were injected with R2-IR non-relevant control nanobody. Single values of intra-operative TNRs were determined 3h post injection. Bar represents the mean (*p= 0.04). D. For a biodistribution assay, mice (n=9) were injected with B9-IR or R2-IR non-relevant control nanobody. Tumors and organs were collected 3h post injection. Error bars represent SEMs.

Imaging of tumor sections and immunohistochemistry

To confirm hypoxia-specific binding of the anti-CAIX nanobodies, tumors were collected 3h post injection of either B9-IR or R2-IR. Tumors were fixed in formalin and embedded in paraffin. Sections of the tumors were scanned with the Odyssey imaging system to detect IR fluorescence. Uptake of B9-IR in perinecrotic areas was visible, which was not the case for R2-IR, all in agreement with the expected specificity of B9-IR for CAIX. DCIS+CAIX tumors showed a more homogeneous tumor distribution compared to DCIS tumors (Fig. 5). IHC confirmed the pattern of intra-tumoral probe distribution of the fluorescent sections. Perinecrotic and membranous CAIX expression was observed in DCIS tumors from mice injected with B9-IR or R2-IR, compared to a more heterogeneous membrane staining in DCIS+CAIX tumors (Fig. 5).

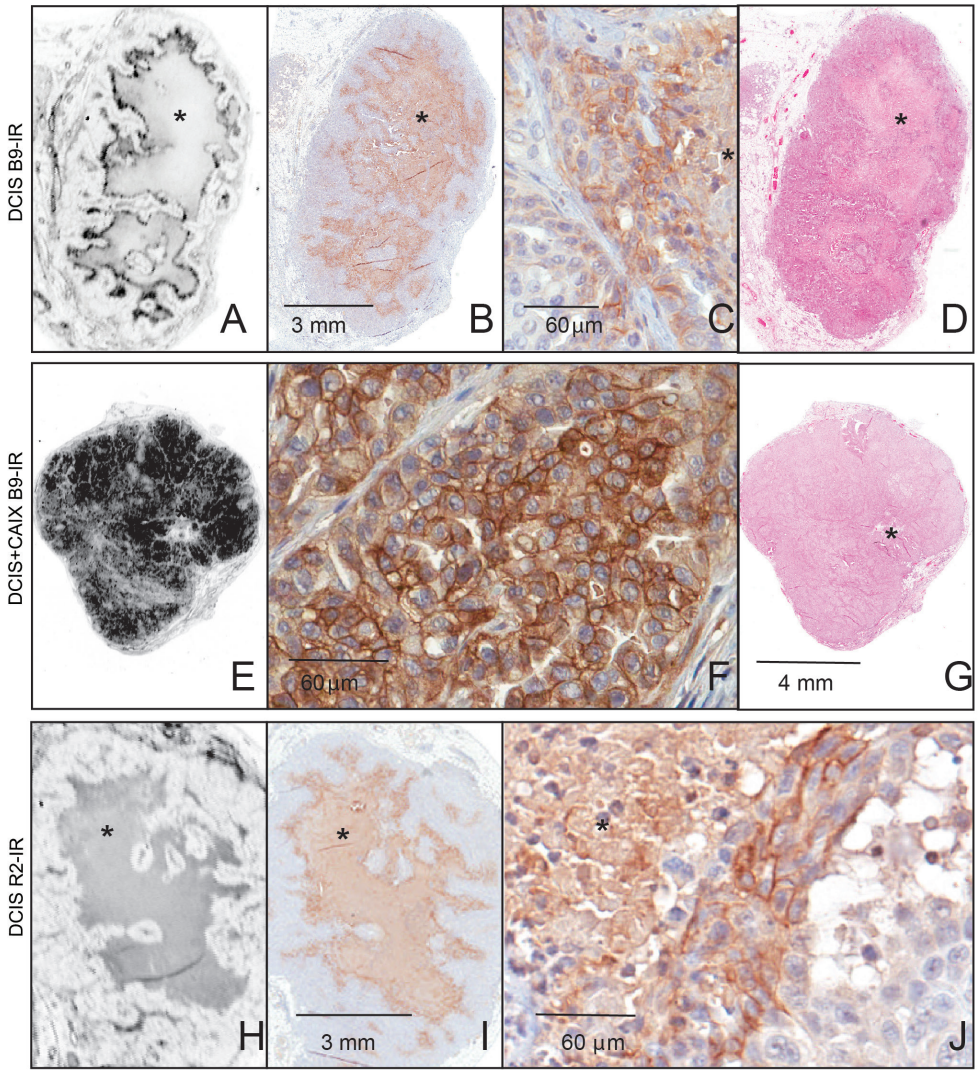

Figure 5: B9-IR binds to perinecrotic CAIX in hypoxic DCIS tumors. A-D. DCIS tumor from a mouse injected with B9-IR nanobody. E-G. DCIS+CAIX tumor from a mouse injected with B9-IR. H-J. DCIS tumor from a mouse injected with R2-IR (non-relevant control nanobody). A. Fluorescence scan of DCIS tumor with central necrosis (*). B. CAIX-IHC. C. Magnification showing perinecrotic CAIX upregulation. D. H&E showing necrosis (*). E. Fluorescence scan of DCIS+CAIX tumor. F. Magnification of CAIX-IHC. G. H&E showing necrosis (*). H. Fluorescence scan of DCIS tumor with central necrosis (*). I. CAIX-IHC. J. magnification of CAIX-IHC with perinecrotic upregulation of CAIX.

Discussion

To allow rapid imaging of (pre-invasive) tumors in general and breast cancer in particular, we generated hypoxia-specific nanobodies. Nanobodies specifically binding to the hypoxia marker CAIX were selected by a phage display family approach using an immune sub-library. The affinities of these nanobodies were better than the affinities from the nanobodies selected from the original immune library, demonstrating the success of this family approach.

An orthotopic xenograft mouse model was obtained by inoculation of MCF10DCIS cells in the mammary glands of SCID/Beige mice. The B9-IR conjugate was used to image hypoxic pre-invasive breast tumors in a non-invasive and intra-operative setting using a camera system approved for clinical studies. Various parameters, such as TNR, that are important for molecular imaging were investigated. Two factors are important for an optimal TNR: high probe accumulation in the tumor in combination with a rapid clearance of non-bound probe from the body. The biodistribution study demonstrated that 14% of the injected dose of B9-IR accumulated in DCIS+CAIX tumor tissue while only 0.25% was observed in muscle 3h post injection. This confirms not only the specificity but also the rapid clearance of the probe. Rapid renal clearance was confirmed by the high accumulation of B9-IR in kidneys, reflecting the clearance of molecules with a low molecular weight (<50 kDa). At 2h post injection, the observed TNR of the DCIS tumors was 1.8±0.1 for B9-IR and 1.4±0.2 for the non-relevant control R2-IR nanobody. The TNR of R2-IR was higher than expected, probably due to non-specific binding of R2-IR to mouse mammary gland tissue, as can be seen in figure 5H. Importantly, the *in vivo* contrast allowed us to successfully detect tumors with a diameter starting from 2 mm. The mean TNR of the DCIS tumors increased to 2.1±0.2 in an intra-operative setting, after removal of the skin, 3h post injection of B9-IR. The difference between *in vivo* and *ex vivo* TNR can be explained by the limited penetration of light through the skin and subcutaneous tissue, making optical imaging especially suitable for image-guided surgery.

An important advantage of the application of nanobodies as targeted probes in optical molecular imaging, is the short time interval between probe injection and imaging procedures. As previously described, tumor-specific nanobodies accumulate in the tumor within 2h post injection [9]. At that time point, the mean TNR of the B9-IR nanobody reaches a plateau level in the tumor, which remained stable for at least 8h. In our previous study, employing the same animal model of pre-invasive human breast tumors, we showed that hypoxic DCIS can also be visualized with a monoclonal antibody directed to CAIX [17]. However, optimal contrast was obtained between 24 and 96h, which is more than 10 times longer compared to the nanobody system. The nanobody system offers a reduction in logistical burden when applied in a clinical setting, as probe injection and operation can be performed on the same day. Further improvement of this system can be expected from the conjugation of several IRDye800CW molecules to the same nanobody, which will require different conjugation strategies.

A promising novel application of molecular imaging in the field of pathology was previously indicated as 'molecular fluorescence pathology' [17]. Analysis of tumor sections is normally done with conventional IHC. However, our strategy allows direct analysis of the tumors on tissue sections using fluorescence microscopy. As shown in figure 5, B9-IR accumulated very well in the perinecrotic areas of the DCIS tumor. CAIX expression was high in perinecrotic regions but low in surrounding normoxic tumor tissue. As with fluorescence microscopy various NIR-dyes can be detected at the same time, the problem of heterogenous tumor binding of CAIX-specific nanobodies can be solved by injection of two or multiple probes, with specificities to other tumor markers, simultaneously. Also, dual labeling allows molecular characterization of tumors and can be advantageous for a better delineation of the tumor, which is essential for imaging of tumor margins. We are currently testing co-injection of nanobodies with other specificities.

As opposed to other (radionuclide) studies [21, 29] we used an optical tracer for molecular imaging of tumors. Compared to optical tracers with other wavelengths, we used a tracer in the near-infrared range (800 nm), which has low absorption properties in human tissue, resulting in a higher penetration depth. This is a prerequisite for successful imaging in tissues like the human breast. Since IRDye800CW

has already been approved for human application and is available as clinical grade compound, approval of conjugates for clinical studies will be more straightforward. Since many different solid tumors are hypoxic and express CAIX [11, 14, 30], B9-IR nanobody could also be useful for imaging of tumors with a different origin than the breast.

In conclusion, the fluorescent CAIX-specific nanobody B9-IR can be used as probe for molecular imaging to detect hypoxic pre-invasive breast cancer before and during surgery. A major advance of using nanobodies is the fast renal clearance, resulting in a low background signal already after 2 hours. Because of this rapid clearance, probe injection and surgical procedure can be performed on the same day. Furthermore, the stability of the conjugate allows for 'molecular fluorescence pathology', which might results in better contrast than conventional CAIX-IHC at the pathology department. Molecular fluorescence pathology might be useful for patient-tailored therapeutic decision making in the future. The selected anti-CAIX nanobody should also be evaluated in preclinical immuno-PET studies. Because of the potential broad applicability of this probe for many different (hypoxic) tumors, we aim for rapid translation of B9-IR towards clinical studies.

References

1. Oude Munnink TH, Nagengast WB, Brouwers AH, et al. Molecular imaging of breast cancer. Breast 2009; 18 Suppl 3: S66-73.
2. van de Ven S, Wiethoff A, Nielsen T, et al. A novel fluorescent imaging agent for diffuse optical tomography of the breast: first clinical experience in patients. Mol Imaging Biol 2010; 12: 343-348.
3. Poellinger A, Persigehl T, Mahler M, et al. Near-infrared imaging of the breast using omocianine as a fluorescent dye: results of a placebo-controlled, clinical, multicenter trial. Invest Radiol 2011; 46: 697-704.
4. Schneider P, Piper S, Schmitz CH, et al. Fast 3D Near-infrared breast imaging using indocyanine green for detection and characterization of breast lesions. Rofo 2011; 183: 956-963.
5. Ntziachristos V, Yodh AG, Schnall M, et al. Concurrent MRI and diffuse optical tomography of breast after indocyanine green enhancement. Proc Natl Acad Sci U S A 2000; 97: 2767-2772.
6. Corlu A, Choe R, Durduran T, et al. Three-dimensional in vivo fluorescence diffuse optical tomography of breast cancer in humans. Opt Express 2007; 15: 6696-6716.
7. Terwisscha van Scheltinga AG, van Dam GM, Nagengast WB, et al. Intraoperative near-infrared fluorescence tumor imaging with vascular endothelial growth factor and human epidermal growth factor receptor 2 targeting antibodies. J Nucl Med 2011; 52: 1778-1785.
8. Cohen G, Lecht S, Oron-Herman M, et al. Near Infrared Optical Visualization of Epidermal Growth Factor Receptors Levels in COLO205 Colorectal Cell Line, Orthotopic Tumor in Mice and Human Biopsies. Int J Mol Sci 2013; 14: 14669-14688.
9. Kijanka MMW, F.; El Khattabi, M.; Lub-de Hooge, M.N.; van Dam, G.M.; Ntziachristos, V., de Vries, E.G.E..; Oliveira, S.; van Bergen en Henegouwen, P.M.P. Rapid Optical Imaging of human Xenografts using anti-HER2 nanobodies site-directly conjugated to IRDye800CW for Image-guided Surgery. in press (European Journal of Nuclear Medicine and Molecular Imaging).
10. Chen CL, Chu JS, Su WC, et al. Hypoxia and metabolic phenotypes during breast carcinogenesis: expression of HIF-1alpha, GLUT1, and CAIX. Virchows Arch 2010; 457: 53-61.
11. Goethals L, Debucquoy A, Perneel C, et al. Hypoxia in human colorectal adenocar cinoma: comparison between extrinsic and potential intrinsic hypoxia markers. Int J Radiat Oncol Biol Phys 2006; 65: 246-254.
12. Wouters BG, Weppler SA, Koritzinsky M, et al. Hypoxia as a target for combined modality treatments. Eur J Cancer 2002; 38: 240-257.
13. Bos R, Zhong H, Hanrahan CF, et al. Levels of hypoxia-inducible factor-1 alpha during breast carcinogenesis. J Natl Cancer Inst 2001; 93: 309-314.
14. Bos R, van der Groep P, Greijer AE, et al. Levels of hypoxia-inducible factor-1alpha independently predict prognosis in patients with lymph node negative breast carci noma. Cancer 2003; 97: 1573-1581.
15. Vermeulen JF, van Brussel AS, van der Groep P, et al. Immunophenotyping invasive breast cancer: paving the road for molecular imaging. BMC Cancer 2012; 12: 240.
16. De Simone G, Supuran CT. Carbonic anhydrase IX: Biochemical and crystallo graphic characterization of a novel antitumor target. Biochim Biophys Acta 2010; 1804: 404-409.
17. van Brussel AS, Adams A, Vermeulen JF, et al. Molecular imaging with a fluores-

cent antibody targeting carbonic anhydrase IX can successfully detect hypoxic ductal carcinoma in situ of the breast. Breast Cancer Res Treat 2013.
18. Schmidt MM, Wittrup KD. A modeling analysis of the effects of molecular size and binding affinity on tumor targeting. Mol Cancer Ther 2009; 8: 2861-2871.
19. Hamers-Casterman C, Atarhouch T, Muyldermans S, et al. Naturally occurring antibodies devoid of light chains. Nature 1993; 363: 446-448.
20. Oliveira S, van Dongen GA, Stigter-van Walsum M, et al. Rapid visualization of human tumor xenografts through optical imaging with a near-infrared fluorescent anti-epidermal growth factor receptor nanobody. Mol Imaging 2012; 11: 33-46.
21. Xavier C, Vaneycken I, D'Huyvetter M, et al. Synthesis, Preclinical Validation, Dosimetry, and Toxicity of 68Ga-NOTA-Anti-HER2 Nanobodies for iPET Imaging of HER2 Receptor Expression in Cancer. J Nucl Med 2013.
22. Movahedi K, Schoonooghe S, Laoui D, et al. Nanobody-based targeting of the macrophage mannose receptor for effective in vivo imaging of tumor-associated macrophages. Cancer Res 2012; 72: 4165-4177.
23. Roovers RC, Laeremans T, Huang L, et al. Efficient inhibition of EGFR signaling and of tumour growth by antagonistic anti-EFGR Nanobodies. Cancer Immunol Immunother 2007; 56: 303-317.
24. Koh WW, Steffensen S, Gonzalez-Pajuelo M, et al. Generation of a family-specific phage library of llama single chain antibody fragments that neutralize HIV-1. J Biol Chem 2010; 285: 19116-19124.
25. Behbod F, Kittrell FS, LaMarca H, et al. An intraductal human-in-mouse transplan tation model mimics the subtypes of ductal carcinoma in situ. Breast Cancer Res 2009; 11: R66.
26. Vermeulen JF, van Brussel AS, Adams A, et al. Near-Infrared Fluorescence Molecular Imaging of Ductal Carcinoma In Situ with CD44v6-Specific Antibodies in Mice: A Preclinical Study. Mol Imaging Biol 2013; 15: 290-298.
27. Themelis G, Yoo JS, Soh KS, et al. Real-time intraoperative fluorescence imaging system using light-absorption correction. J Biomed Opt 2009; 14: 064012.
28. Oliveira S, Cohen R, Walsum MS, et al. A novel method to quantify IRDye800CW fluorescent antibody probes ex vivo in tissue distribution studies. EJNMMI Res 2012; 2: 50.
29. Divgi CR, O'Donoghue JA, Welt S, et al. Phase I clinical trial with fractionated radioimmunotherapy using 131I-labeled chimeric G250 in metastatic renal cancer. J Nucl Med 2004; 45: 1412-1421.
30. van der Groep P, van Diest PJ, Smolders YH, et al. HIF-1alpha overexpression in ductal carcinoma in situ of the breast in BRCA1 and BRCA2 mutation carriers. PLoS One 2013; 8: e56055.

Aram S.A. van Brussel*, Marta Kijanka*, Reini van der Welle, Mohamed El Khattabi, Elsken van der Wall, Willem P.Th.M. Mali, Paul J. van Diest, Paul M.P. van Bergen en Henegouwen, Sabrina Oliveira

*equal contributions

9

Dual-spectral optical imaging of breast cancer with a combination of nanobodies targeting CAIX and HER2

Abstract

Introduction: Optical molecular imaging is a relatively novel technology that is becoming an additional strategy employed for both diagnosis of breast cancer and for image-guided surgery. To arrive at high tumor-to-normal tissue ratios (TNR), tumor-specific probes are required that specifically and rapidly accumulate in the tumor. Combinations of probes with different specificities might overcome low tumor marker expression prevalence and tumor heterogeneity and increase TNR. In this feasibility study, we performed optical molecular imaging of breast cancer xenografts using combinations of CAIX- and HER2-specific nanobodies conjugated to the same fluorophore to evaluate TNR, compared to the TNR obtained with injections of each of the single tumor-specific nanobodies together with an irrelevant nanobody. In addition, we evaluated the expression status of CAIX and HER2 simultaneously, through dual-fluorescence detection *in vivo*, *ex vivo* on tumor sections, and by immunohistochemistry (IHC).
Methods: The anti-HER2 nanobody 11A4 was site-specifically conjugated to IRDye800CW or IRDye680RD; the anti-CAIX nanobody B9 was site-specifically conjugated to IRDye800CW; and the irrelevant nanobody R2 was randomly conjugated with either IRDye800CW or IRDye700DX. SCID/Beige mice were orthotopically inoculated with MCF10DCIS cells in the 4th mammary glands, or intravenously injected with these cells to develop lung metastases. After tumor development, mice were divided into two groups and then injected with different combinations of nanobody conjugates, either with the same or with different fluorescent tags, allowing for single or dual-spectral optical imaging, performed up to 48h after injection using the Pearl imaging system. Tumors were then collected and imaged once again, thereafter tumors were fixed and sectioned and the distribution of the nanobody conjugates was assessed by dual-spectral fluorescence imaging of sections. In parallel, mice with MCF10DCIS lung metastases were sacrificed at 5h post-injection of the nanobody conjugates and lungs were imaged after being exposed.
Results: All the fluorescent nanobodies had a degree of labeling of approximately

50% and the binding affinities of 11A4 and B9 were not affected by fluorophore conjugation. *In vivo*, imaging of mice after injections of combined HER2 and CAIX nanobodies (i.e. HER2-IRDye800CW and CAIX-IRDye800CW) did not result in higher TNRs, compared to injections with each of the single tumor-specific nanobodies together with the irrelevant nanobody. Nevertheless, the expression status of CAIX and HER2 was successfully assessed simultaneously *in vivo* (i.e. after injection of HER2-IRDye680DX and CAIX-IRDye800CW) as well as on tumor sections, as confirmed by IHC.

Conclusion: Dual-spectral optical molecular imaging with a combination of two nanobodies allowed successful simultaneous determination of the expression status of CAIX and HER2 in MCF10DCIS xenografts. In the future, the use of nanobody cocktails and multispectral molecular imaging might improve early tumor detection, the delineation of tumor tissue during image-guided surgery, non-invasive molecular assessment of target expression status of tumors and metastases, and also direct tumor characterization at the pathology department.

Introduction

Although conventional breast cancer imaging strategies have been improved in the past decade, highly sensitive and tumor-specific imaging modalities are still needed in the clinic. Molecular imaging, an emerging technique that detects tumor-specific probe uptake *in vivo*, might fulfill this need. Several probes have been tested or approved for clinical use, however, most of these are radioactively labelled and depend on PET or SPECT imaging modalities that have limited spatial resolution, involve high costs, and their ionizing radiation restricts their repetitive usage [1, 2]. With optical molecular imaging, emitted light from fluorophores is detected by a high resolution fluorescence camera system, making it a cost-effective, non-radioactive, high resolution imaging solution for detection of breast cancer, either for screening or during surgery. To overcome the problem of limited penetration of light to (excitation) and from (emission) structures deeper in the body, fluorophores that absorb and emit light in the near-infrared (NIR) spectrum are employed to improve imaging results. Compared to other wavelengths, NIR light is less absorbed by blood and tissue components, and auto-fluorescence is minimal, resulting in deeper tissue penetration and higher sensitivity. Besides optimal tumor detection, high tumor specificity can be obtained by targeting tumor markers that ideally are (over)expressed in malignant tumors only and not in benign tumors or normal tissues. In some cases, unfortunately, these markers are expressed heterogeneously or in a limited percentage of tumors. As we reported earlier [3], due to the limited expression prevalence of conventional tumor markers, co-injections of targeting agents with different specificities ('cocktails') could circumvent this issue and thereby target the whole tumor in the screening setup. Previously, we reported molecular imaging with fluorescently labelled nanobodies in pre-invasive breast cancer xenografts [4]. Nanobodies are derived from the Variable domain of the Heavy chain of Heavy-chain-only antibodies (VHH), which naturally occur in camelids and sharks [5]. Already 2-4h after injection of these fluorescent nanobodies, optimal imaging was possible. Here, we performed a preclinical imaging

study with rapid optical molecular imaging of pre-invasive breast cancer, using combinations of fluorescently labelled nanobodies. We co-injected nanobodies against carbonic anhydrase IX (CAIX), a marker for tumor hypoxia and prognosis [6, 7], and against HER2, a member of the epidermal growth factor receptor family. By conjugating these nanobodies with a) the same fluorophore, we evaluated the tumor-to-normal tissue ratios (TNR) obtained after co-injections of these two nanobodies, compared to injections of each of the single nanobodies combined with an irrelevant nanobody. In addition, by conjugating these nanobodies with b) different fluorophores of the NIR spectrum, we evaluated the expression status of these two clinically relevant tumor markers, *in vivo* and *ex vivo*.

Material and Methods

Cell lines and cell culture conditions

MCF10DCIS.com (further referred to as MCF10DCIS) cells (Asterand, Detroit, USA) were cultured according to the supplier's guidelines in DMEM/F12, supplemented with 10% (v/v) FCS, 100 IU/ml penicillin, 100 µg/ml streptomycin and 2 mM L-glutamine. Generation of Luciferase overexpressing MCF10DCIS cells has been described by Van Brussel et al. [8]. All cells were cultured at 37°C in a humidified atmosphere containing 5% CO_2 and were consistently Mycoplasma free.

Nanobody production and purification

The HER2-specific nanobody 11A4 and the CAIX-specific nanobody B9 were produced as described earlier [4, 9]. Briefly, nanobodies were re-cloned from the pUR8100 phagemid vector into the pQVQ72 expression vector (kindly provided by QVQ BV), which introduces a C-terminal cysteine, flanked by a FLAG-tag to enable site-directed conjugation of IRDye680RD-Maleimide and IRDye800CW-Maleimide (LI-COR Biosciences, Nebraska, USA). After transformation into *E. coli* TG1, 800 ml cultures were grown in 2x Tryptone Yeast Extract Medium (2TY), until optical density of 0.5 at 600 nm (OD600: 0.5) was reached. Nanobody production was induced by adding 1 mM IPTG and after 4h or overnight induction, bacteria were harvested by centrifugation. Pellets were frozen at -20°C and next day these were thawed and the periplasmic fraction was obtained through resuspension of the pellet in PBS, followed by incubation for 2h under continuous rotation at 4°C, and centrifugation at 4,600 rpm for 15 min. Nanobody R2 was produced as previously described by Oliveira et al. [10]. 11A4 and B9 nanobodies were purified from the periplasmic fraction by protein A affinity chromatography using a HiTrap protein A HP column (GE Healthcare, Zeist, The Netherlands) in the ÄKTAxpress system (GE Healthcare, Zeist, The Netherlands) and the nanobody R2 was purified through immobilized metal affinity chromatography (IMAC; Talon; Takara Bio Europe/Clontech, Saint-Germain-en-Laye, France).

Nanobody labeling

The conjugation of the fluorophores was performed as described earlier [4, 9]. Briefly, before the site-directed conjugation, nanobodies 11A4 and B9 were reduced by adding 20 mM TCEP. 11A4 was either conjugated to IRDye680RD-Maleimide (further referred to as HER2-680) or IRDye800CW-Maleimide ('HER2-800'), while B9 was only conjugated to IRDye800CW-Maleimide ('CAIX-800'), following manufacturers' recommendations, with molar dye-to-protein ratios of 3:1 and overnight incubation. The irrelevant nanobody R2 was randomly conjugated to either the fluorophore IRDye800CW or IRDye700DX (R2-800 and R2-700, respectively) which were purchased from LI-COR as N-hydroxysuccinimidine (NHS) esters. Conjugations were performed with a 2-fold excess of fluorophore to R2 nanobody ratio in PBS and these were incubated for 2h at room temperature. After conjugation of the fluorophores, remaining free dyes were separated from the conjugates using two (for IRDye800CW) or three (for IRDye680RD or IRDye700DX) sequential size exclusion chromatography steps through Pierce ZebaTM Desalting Spin Columns (Thermo Fisher Scientific, Landsmeer, The Netherlands).
The degree of labeling (DOL) was calculated using the absorbance at 280 nm and 774 nm (for IRDye800CW), 672 nm (for IRDye680RD), or 690 (for IRDye700DX) with a NanoDrop spectrophotometer (NanoDrop Technologies, Wilmington, Delaware, USA), according to the instructions given by the provider for each of the fluorophores. After conjugation of the fluorophores to the nanobodies, these conjugates were assessed for their purity and specificity as described in our previous studies [4, 9, 10].

In vivo experiments

All animal experiments were approved by the Utrecht University Animal Experimental Committee (DEC no. 2012.III.02.015). The mouse model used in this study was based on a previously described model [11]. Briefly, 4 x 10^4 MCF10DCIS cells, mimicking ductal carcinoma in situ of the breast (DCIS), were inoculated in 4^{th} mammary glands at both sides of SCID/Beige mice. Six to seven weeks after inoculation, mice were put on alfalfa-free food in order to reduce background

signal in the 700 nm channel. After tumor formation (approximately 8-9 weeks after inoculation), mice carrying xenografts with diameters between 0.5 and 1.0 cm were included for imaging in one of the two studies: a) Mice were divided into 3 different groups injected with combinations of nanobodies (50 µg of each thus 100 µg in total): HER2-800 and CAIX-800, HER2-800 and R2-800, or CAIX-800 and R2-800. b) Three groups of mice were injected with combinations of nanobodies (50 µg of each thus 100 µg in total): HER2-680 and CAIX-800, HER2-800 and R2-700, or CAIX-800 and R2-700. After the injections, mice were imaged with the Pearl Impulse Small Animal Imaging System (LI-COR) using the 700 nm channel for detection of IRDye680RD and IRDye700DX and the 800 nm channel for detection of IRDye800CW. Imaging took place at different time points, up to 48h post injection. For the development of a lung metastasis model, 1×10^5 cells were injected in the tail vein of the mice. After confirmation of the presence of metastasis at the lungs through non-invasive bioluminescence imaging (Photon Imager, Biospace Labs, Paris, France), mice were injected with the combination HER2-680 and CAIX-800. As controls, a mouse was injected with R2-800 and R2-700 and another mouse without lung metastases was injected with HER2-680 and CAIX-800. After drawing regions of interest (ROI) on tumor and normal tissue (hind leg), TNRs were calculated using Pearl Impulse Software (v.2.0, LI-COR Biosciences). Mean intensities of tumor ROIs were divided by mean intensities of background ROI.

Imaging of fluorescent sections and immunohistochemistry

At the end of the imaging study, mice were sacrificed and their tumors collected. These were first imaged (i.e. *ex vivo*) and immediately after, tumors were fixed in neutral buffered formalin, routinely processed to paraffin blocks and stored in the dark until further processing. Four µm thick sections were scanned using the Odyssey imaging system at highest (21 µm) resolution and highest quality. Immunohistochemistry (IHC) for detection of CAIX and HER2 combined with haematoxylin and eosin (H&E) stainings were performed as described before [3]. Slides were scanned with the Scanscope XT 120 scanner (Aperio, Vista, USA).

Statistics

Statistical analysis was performed using GraphPad Prism. Comparisons of TNRs of injected probes and between xenograft types were performed using the Mann-Whitney U test (two-tailed). P-values of <0.05 were considered to be statistically significant.

Results

Preparation of fluorescent nanobodies

In order to assess whether the combination of two probes that target independent tumor markers could a) improve the detection of tumors through an increase in tumor-to-normal tissue ratio (TNR) and b) allow for the detection of individual tumor markers *in vivo* and *ex vivo* through dual-spectral imaging, a set of near-infrared (NIR) fluorescent nanobodies was prepared. We previously described the development of the anti-HER2 nanobody 11A4 and the anti-CAIX nanobody B9 [4, 9]. These two tumor targets were selected as they are likely present in tumors in independent areas, i.e. CAIX is likely confined to hypoxic regions of the tumors, whereas 11A4 is expected to be homogenously distributed throughout the tumors. For comparison of the combination of these two targeted probes, combinations of each of the single fluorescent probes with the irrelevant nanobody R2 were employed. Both 11A4 and B9 were expressed with a C-terminal cystein for site-directed conjugation, in order to avoid affinity loss upon conjugation of the fluorophore. 11A4 was site-directed conjugated to IRDye800CW or IRDye680RD (named HER2-800 and HER2-680, respectively). B9 was site-directed conjugated to IRDye800CW (named CAIX-800) and R2 was randomly conjugated to either IRDye800CW or IRDye700DX (denoted R2-800 and R2-700, respectively). After purification of the conjugates, routine quality control tests were performed that revealed for all conjugates a degree of labeling (DOL) of approximately 50%, and showed that the binding properties of HER2- and CAIX-targeted nanobodies were not affected by the conjugation of the fluorophores. In fact, the affinities of HER2-800, HER2-680 and CAIX-800 were in accordance with previous studies [4, 9], and the nanobodies R2-800 and R2-700 showed no binding to cells (data not shown). These fluorescent nanobodies were therefore considered suitable to proceed with the *in vivo* studies in the pre-invasive breast cancer (MCF10DCIS xenograft) mouse model.

In vivo single-spectrum imaging of combinations of fluorescent nanobodies

To determine whether the combination of anti-HER2 and anti-CAIX fluorescent nanobodies could improve the detection of tumors through an increase in TNR, mice bearing MCF10DCIS breast cancer xenografts with diameters between 0.5 and 1.0 cm were divided into three groups which were injected with the following combinations of fluorescent nanobodies: HER2-800 and CAIX-800, HER2-800 and R2-800, or CAIX-800 and R2-800. Mice were imaged up to 48h after intravenous injection of these combinations, with the Pearl imaging system (LI-COR) using 800 nm channel for detection of the IRDye800CW fluorophore (Fig. 1A). As could be expected, tumors were clearly visible at early time points after injection of the probes, i.e. 2-3h post-injection, enough contrast allowed for the precise delineation of the tumors. Due to the rapid renal clearance of nanobodies, already during the first imaging time points, fluorescent signals were clearly visible from the bladder. TNRs for all three groups were calculated for each time point, after drawing regions of interest (ROIs) around each single tumor and neighboring normal tissue. No increase in TNR was observed in mice injected with CAIX-800 and HER2-800 compared to the control groups that were injected with CAIX-800 and R2-800 or HER2-800 and R2-800 (Fig. 1B).

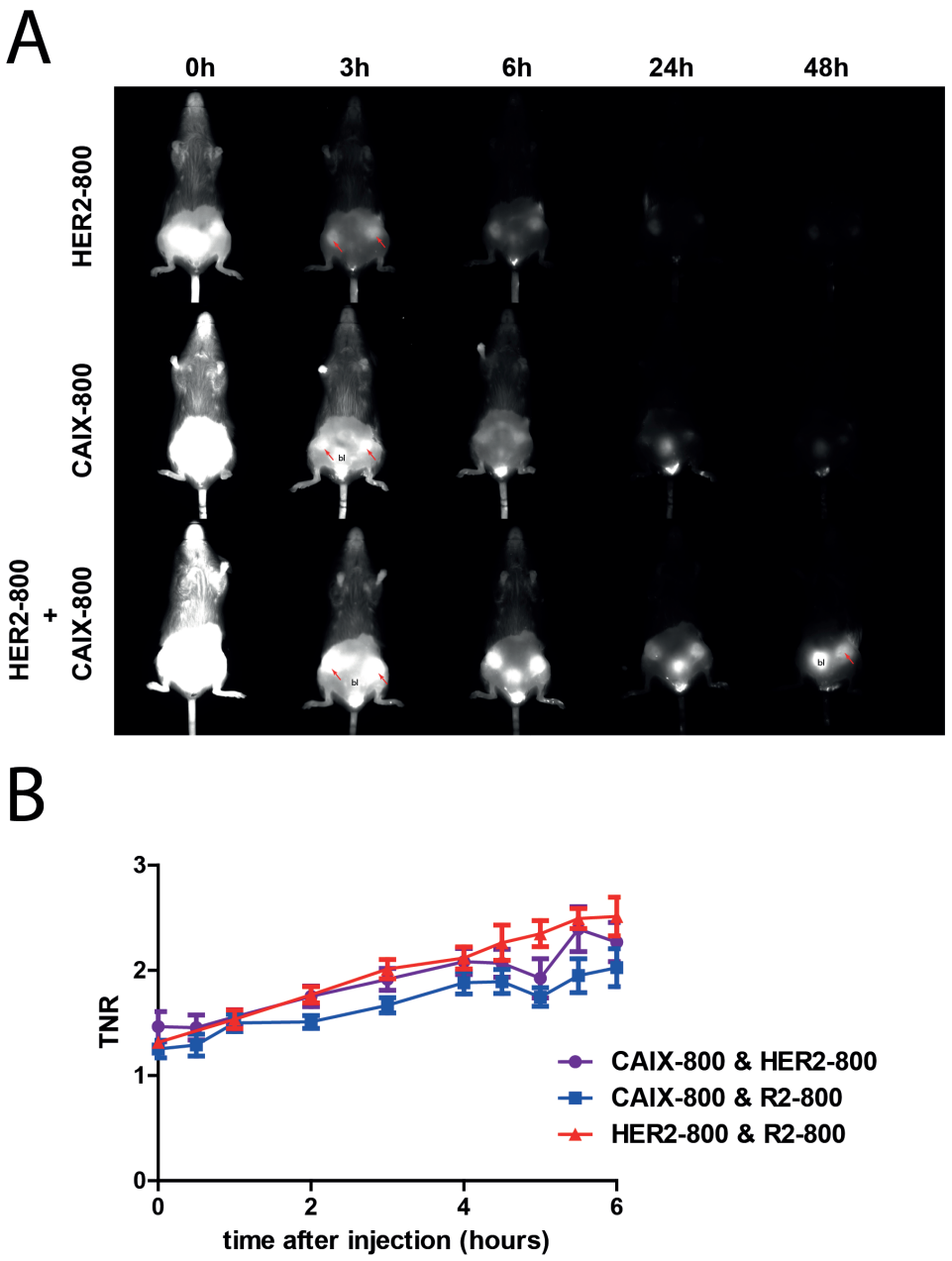

Figure 1: No TNR increase in molecular imaging with two tumor-specific nanobodies compared to a single specific nanobody. A. Optical imaging of mice xenografted with MCF10DCIS cells in time, after injection of HER2-800 nanobody in combination with non-specific R2-800 (upper panel), of CAIX-800 in combination with R2-800 (middle panel), or of both HER2-800 and CAIX-800 specific nanobodies (lower panel). B. TNR in time (7 mice per group). Graphs represent means, error bars represent SEM.

In vivo dual-spectral imaging of combinations of fluorescent nanobodies

To evaluate whether injections of two independent nanobodies with different fluorescent tags would allow for *in vivo* expression status determination of two clinically relevant tumor markers through dual-spectral imaging, mice were injected in the tail vein with equal amounts of two nanobodies: CAIX-800 and HER2-680, and as controls CAIX-800 and R2-700, or HER2-680 and R2-700. Tumor xenografts were again visible and could be clearly delineated from 2-3h up to 48h after injection. In the 700 nm channel (red), intestines were sometimes visible as well. Stronger fluorescent signals were observed at the tumors through the 800 nm channel compared to the 700 nm channel in mice injected with HER2-800 and R2-700 irrelevant control (Fig. 2A) as well as in mice injected with CAIX-800 and R2-700 (Fig. 2B) suggesting specific uptake of both HER2-800 and CAIX-800 nanobodies. Xenografts of mice that were injected with the combination of the two specific nanobodies, i.e. CAIX-800 and HER2-680, were clearly visible in both the 700 nm (red) and 800 nm (green) nm channel, resulting in yellow signals in the overlay (Fig. 2C).
From each individual mouse and individual tumor, TNRs were calculated in time showing optimal contrast in all groups 5-6h after injection. A non-significant difference between HER2-680 and CAIX-800 (Fig. 3A; $p=0.4$) was obtained, whereas significant differences were observed between HER2-800 or CAIX-800 and R2-700 irrelevant control nanobody at 5h after injection (Fig. 3B and 3C; $p=0.04$ and $p=0.01$ respectively). In our previous studies, optimal TNRs were observed 2-3h after injection of single nanobodies. In this study, however, with injections of combinations of nanobodies at twice the dose of the earlier studies, a relatively higher background signal was observed in the first hours after injection, resulting in optimal TNRs from 5h after injection, further increasing up to 48h (data not shown).

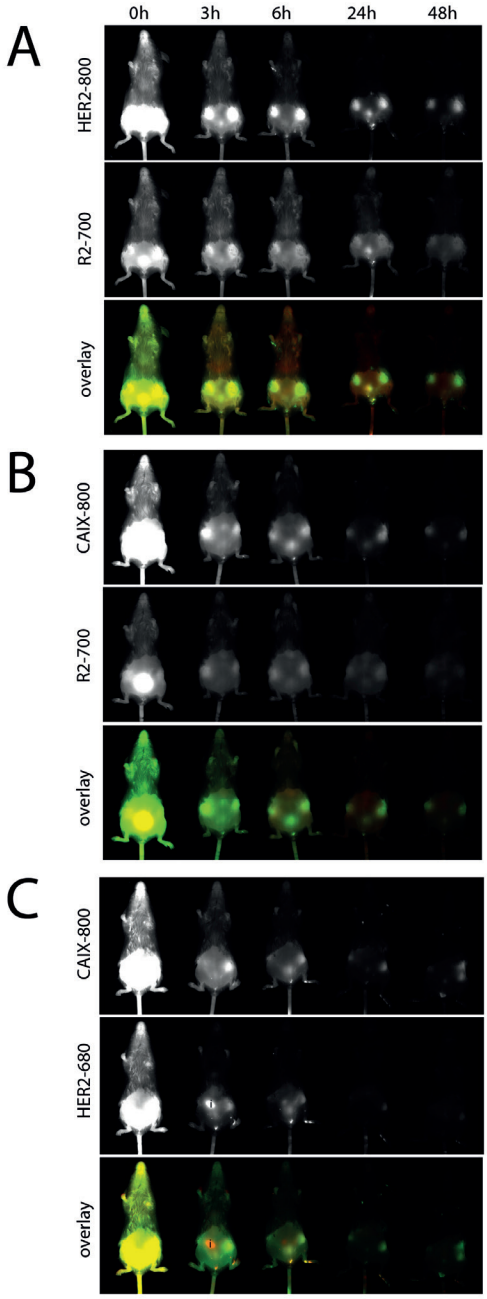

Figure 2: Dual-spectral molecular imaging in the near-infrared range allows for expression status determination of two different tumor markers. A. Mice xenografted with MCF10DCIS cells, imaged up to 48h after injection of HER2-800 (green) in combination with the irrelevant nanobody R2-700 (red). B. Mice injected with CAIX-800 in combination with R2-700 irrelevant nanobody. C. Injections with a combination of CAIX-800 and HER2-680. Aspecific signal from the intestines (i) was mainly observed in the 700 nm channel (red). The observed yellow color originates from the overlay of green and red colors.

Dual-spectral imaging in the surgical setting

To assess the value of detecting both targeted probes through dual-spectral imaging for image-guided surgery, a number of mice were injected with the same combinations of dual-fluorescent nanobodies. At 5h post-injection these mice were sacrificed, the skin was removed from the xenografts and optical imaging was performed with the Pearl imaging system. As could be anticipated, tumor xenografts were clearly visible in these conditions, while background levels of fluorescence were low, except for the intestines that were still visible in the 700 nm channel. Mean TNRs were calculated which were 3.2±0.3 (±SEM) for CAIX-800 compared to 2.0±0.1 for the control R2-700 (Fig. 4B; p=0.003). The calculated mean TNR for HER2-800 was 2.7±0.1 compared to 1.6±0.1 for R2-700 (Fig. 4C; p=0.0002) and 3.1±0.4 for CAIX-800 compared to 3.8±0.7 for HER2-680 (Fig. 4D; p=0.7). Overall, these TNRs are slightly higher than the TNRs obtained non-invasively.

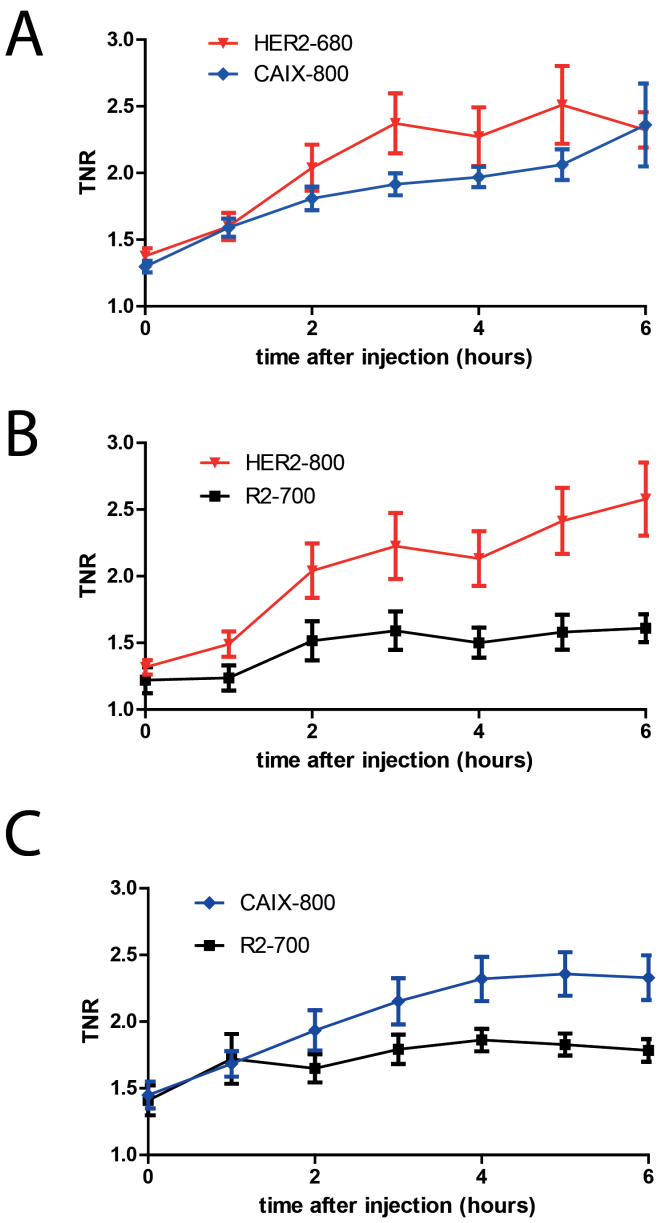

Figure 3: Optimal imaging 5-6h after injection of a nanobody cocktail. TNR increase in the first 6h after injection of HER2-680 in combination with CAIX-800 (A), of HER2-800 in combination with R2-700 (B) and of CAIX-800 in combination with R2-700 irrelevant nanobody (C). Graphs represent means, error bars represent SEM.

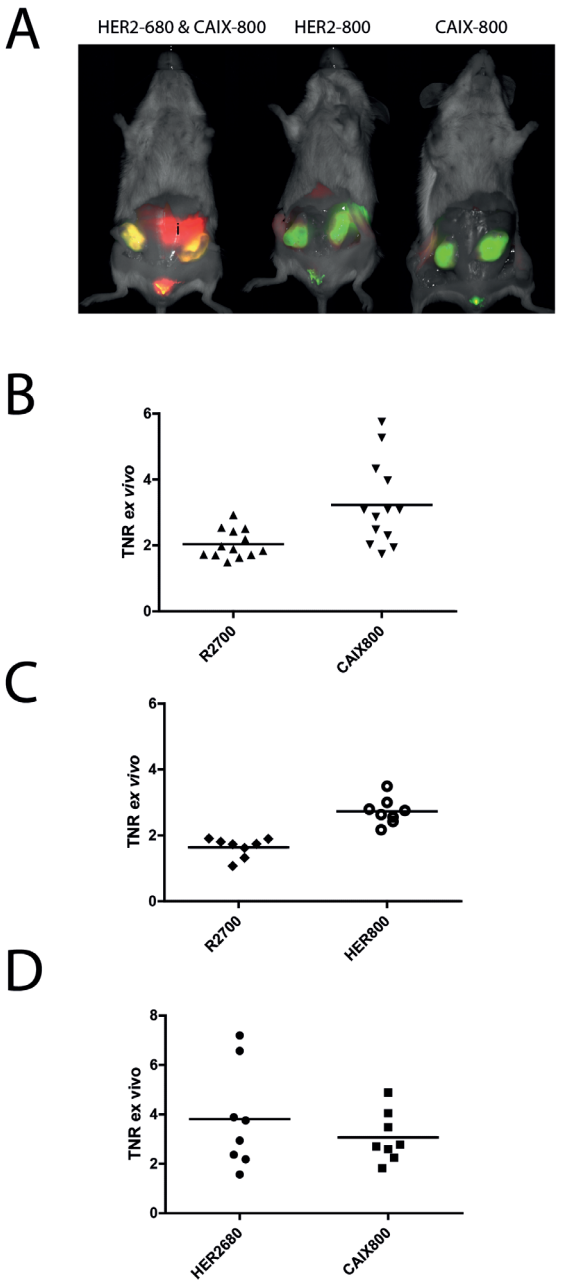

Figure 4: Invasive optical imaging allows evaluation of expression levels of HER2 and CAIX simultaneously. A. Five hours after injection of HER2-680 and CAIX-800 (1:1, left), or HER2-800 with irrelevant control nanobody R2-700 (1:1, middle), or CAIX-800 with the control nanobody R2-700 (1:1, right), mice were sacrificed and skin was removed from the xenografts, mimicking 'image-guided surgery'. Yellow color corresponds to the overlay of red and green colors. Intestines (i) were autofluorescent in the 700 nm channel (red). B-D. TNRs were calculated with ROIs drawn around tumors and normal tissues. Bars represent mean TNR.

Dual-spectral imaging of lung metastases in the surgical setting

In order to investigate whether the combination of anti-HER2 and anti-CAIX nanobodies was suitable for detection of lung metastases in the surgical setting, mice were injected with MCF10DCIS cells in the tail vein. After development of lung metastases, as followed in time by bioluminescence imaging, mice were injected with CAIX-800 in combination with HER2-680. As controls, one mouse with lung metastases was injected with R2-800 and R2-700 and another mouse without metastases was injected with CAIX-800 and HER2-680. Five hours after the injections the mice were sacrificed and their chest wall was removed, in order to facilitate imaging of the lungs. Compared to both controls, a substantial increase of fluorescent signal was observed in all lung metastases (2-5 mm diameter) of mice that were injected with HER2-680 and CAIX-800 (Fig. 5).

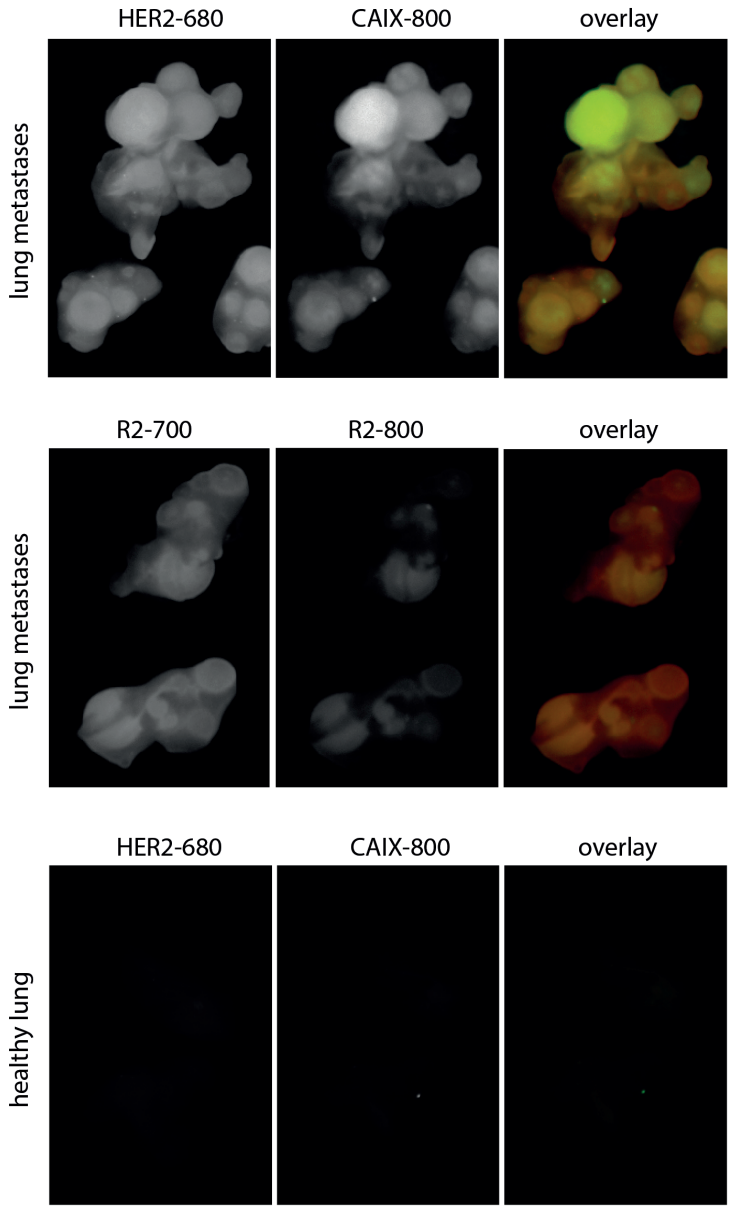

Figure 5: Invasive optical molecular imaging with mixed HER2 and CAIX nanobodies allows detection of lung metastases. MCF10DCIS lung metastases formed after injection of cells via the tail vein. Five hours after injection with mixed HER2-680 and CAIX-800 nanobodies, mice were sacrificed and their lungs exposed for imaging. In parallel, a mouse was injected with the irrelevant control nanobodies R2-700 and R2-800 (middle panel) and a healthy mouse without lung mestastases was injected with HER2-680 and CAIX-800 nanobodies (lower panel).

Dual-fluorescence imaging of tumor sections and immunohistochemistry

To investigate the possibility of expression status assessment *ex vivo*, as could be done at the pathology department, dual-fluorescence imaging was conducted on sections of tumors that were processed after imaging in the surgical setting. Tumor sections were scanned using the 700 nm and 800 nm channels of the Odyssey imaging system. A unique probe distribution was observed for each of the nanobodies: HER2-680 was observed throughout the tumor, while CAIX-800 was confined to perinecrotic areas (Fig. 6A upper panel; necrosis indicated with *). Tumor sections obtained from mice that were injected with a single tumor-specific nanobody (either HER-800 or CAIX-800) in combination with R2-700 control nanobody, only presented fluorescence signal in the 800 nm channel, with a similar distribution pattern as observed earlier for HER2-680 and CAIX-800 (Fig. 6A middle and lower panel). In parallel, IHC was performed on equivalent tumor sections for detection of HER2 and CAIX expression. The first showed 2+ HER2 positivity according to the DAKO scoring system, while CAIX-IHC showed perinecrotic expression (Fig. 6B). These results are in agreement with the images obtained through direct fluorescence detection of the nanobodies (Fig. 6A). These results confirmed specific uptake of both HER2- and CAIX-targeting nanobodies. Importantly, we showed that the expression status of two clinically relevant tumor markers, i.e. HER2 and CAIX, can be assessed on tumor sections after a single injection of the combination of the two fluorescent nanobodies.

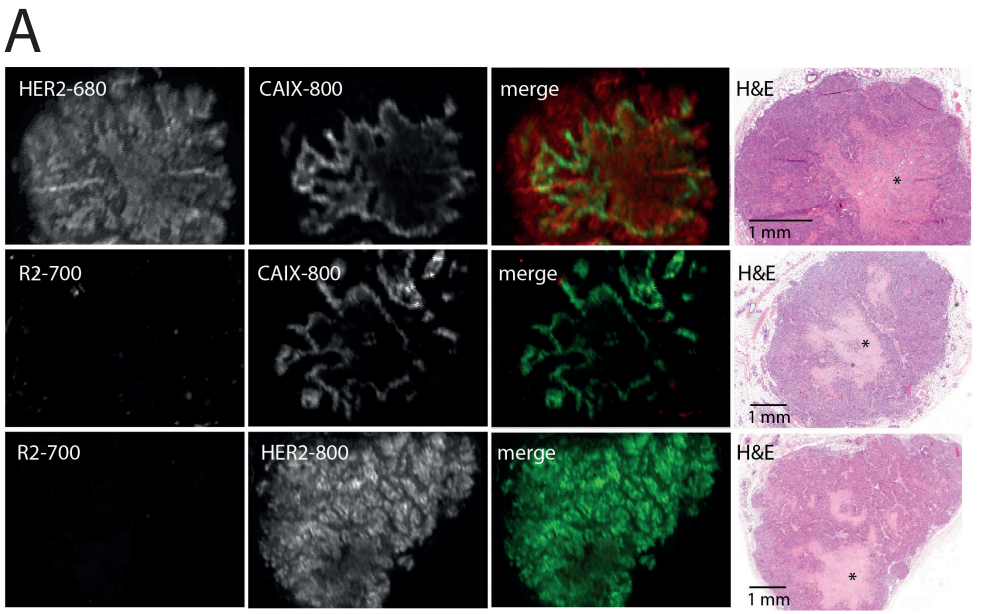

Figure 6: Dual-spectral fluorescence molecular pathology allows simultaneous determination of HER2 and CAIX expression status. A. Upper panel: Distribution of HER2-680 (red) and CAIX-800 (green) nanobodies in MCF10DCIS xenografts, 5h after injection. H&E showing central necrosis (*). Middle panel: Perinecrotic distribution of CAIX-800 nanobodies in MCF10DCIS xenografts. Lower panel: Distribution of HER2-800 nanobodies in MCF10DCIS xenografts. B. IHC on sections from xenografts confirmed expression of HER2 and CAIX. HER2 (left) was homogenously expressed (2+) and CAIX (right) was expressed perinecrotically.

Discussion

Despite the many efforts made over the years to facilitate early breast cancer detection, improvements are still eagerly awaited. Recent developments in the field of optical molecular imaging have raised many hopes in this direction. For reliable detection, high tumor-to-normal tissue ratios (TNR) are necessary, for which tumor-specific probes have been developed. Unfortunately, the tumor markers to which these probes are specific, are in many cases not homogenously distributed. Further, prevalence of tumor-specific markers is limited. Combinations of probes ('cocktails') with different specificities might overcome low tumor marker expression prevalences and tumor heterogeneity.

In the present study we addressed two main research questions: first, whether the detection of breast cancer xenografts can be facilitated by a combination of CAIX- and HER2-specific nanobodies conjugated to the same fluorophore. All mice were injected with the same amount of fluorophores in a 1:1 molar ratio of the nanobodies to exclude possible influences of aspecific residualization of the NIR fluorophores. After comparing TNRs in time, we did not find any significant difference between test and control groups. The increased dose of nanobodies, and thus the increased amount of fluorophores compared to earlier studies (i.e. 100 μg instead of 50 μg), resulted in relatively high background signals, which may have influenced the resulting contrast more than the overall increase in fluorescent signal from specific tumor binding. These results probably depend on tumor-type and animal model, increasing the degree of difficulty to actually draw general conclusions. Nevertheless, tumors were always visible shortly after administration of CAIX-800, which is in agreement with our previous studies [4]. Furthermore, the nanobody targeting HER2 was for the first time here employed to successfully delineate xenografts of a particularly relevant orthotopic breast cancer model. In future studies, combinations of nanobodies, specific for other tumor markers than HER2 and CAIX, should be evaluated. Also, testing probe cocktails for optical molecular imaging in a xenograft mouse model with higher tumor marker expression levels

might show an increase in TNR compared to single probe injections.
Secondly, we evaluated whether the expression status of the two tumor markers CAIX and HER2 could be determined after a single injection by dual-spectral optical molecular imaging using 700 nm and 800 nm detection channels.
In a pilot study, spectral bleed-through of 700 nm and 800 nm channels was confirmed to be minimal/acceptable when the channel of 700 nm was used to detect IRDye800CW and the channel of 800 nm for the detection of IRDye680RD or IRDye700DX.
As opposed to PET and SPECT, which are monochromatic imaging techniques, optical molecular imaging is polychromatic, which is a prerequisite for imaging studies in which cocktails of probes are used [12]. *In vivo* we showed successful dual-imaging of CAIX and HER2 positive MCF10DCIS xenografts, as confirmed by IHC (Fig. 6D). Simultaneous determination of the expression status of multiple tumor markers could be a cost-effective, time-efficient way to characterize tumors non-invasively and by molecular fluorescence pathology, as described before [8]. Imaging of multiple probes is important for optimal delineation of tumor tissue which could also be very useful during image-guided surgery, as no single tumor marker is expressed in 100% of tumor cells. Therefore we performed optical molecular imaging in an invasive setting as well. After removal of the skin from the 4th mammary glands, mice were imaged and higher TNRs were obtained compared to non-invasive imaging. Furthermore we showed specificity of the nanobody mixture for MCF10DCIS xenografts as little signal was observed from surrounding tissues, except for intestinal autofluorescence in the 700 nm channel. These observations highlight the potential of dual or even multi-spectral imaging in the surgical setting, where cameras currently under development could enable the detection of several tumor markers, providing more confidence to the surgeon during tumor resection.
As lungs are a common site for breast cancer metastases, we have also evaluated our imaging approach in a MCF10DCIS lung metastases model. For the first times, both nanobodies were employed in this setting and with these we were able to detect and distinguish metastases from healthy lung tissue, which covered a wide range of sizes.

Few have evaluated multispectral optical imaging of cancer using targeted probes. Xie et al. compared four different NIRF probes, imaged 24h after injection, to bioluminescence and IHC data in a subcutaneous xenograft mouse model, showing that optical molecular imaging is a feasible approach to detect different tumor features simultaneously [13]. Barret et al. used anti-EGFR and anti-HER2 antibodies, labelled with Cy5.5 and Cy7 respectively, for molecular imaging of EGFR or HER2 overexpressing xenografts [12]. By spectral unmixing, optimal contrast was obtained 24h after injection. By using nanobodies instead of antibodies, we were able to detect tumors already from 3h after injection, reducing logistical burden in future clinical application.

In conclusion, we showed successful dual-spectral optical molecular imaging of CAIX and HER2 positive DCIS xenografts *in vivo*, in the surgical setting, as well as in tumor sections. Simultaneous determination of expression status of multiple, clinically relevant tumor markers will lead to a better tumor detection and optimal tumor delineation during surgery under image-guidance, and allows for non-invasive assessment of target expression status in tumors and metastases. Furthermore, multispectral optical imaging is one step forward towards implementation of the concept of molecular fluorescence pathology in the clinic as a cost-effective, time-efficient and sensitive alternative to conventional IHC.

References

1. van Dongen GA, Poot AJ, Vugts DJ. PET imaging with radiolabeled antibodies and tyrosine kinase inhibitors: immuno-PET and TKI-PET. Tumour Biol 2012; 33: 607-615.
2. Smetherman DH. Screening, imaging, and image-guided biopsy techniques for breast cancer. Surg Clin North Am 2013; 93: 309-327.
3. Vermeulen JF, van Brussel AS, van der Groep P, et al. Immunophenotyping invasive breast cancer: paving the road for molecular imaging. BMC Cancer 2012; 12: 240.
4. van Brussel AS, Adams A, Oliveira S, et al. Hypoxia-targeting fluorescent nanobodies for optical molecular imaging of pre-invasive breast cancer. Submitted 2013
5. Hamers-Casterman C, Atarhouch T, Muyldermans S, et al. Naturally occurring antibodies devoid of light chains. Nature 1993; 363: 446-448.
6. Pinheiro C, Sousa B, Albergaria A, et al. GLUT1 and CAIX expression profiles in breast cancer correlate with adverse prognostic factors and MCT1 overexpression. Histol Histopathol 2011; 26: 1279-1286.
7. Ward C, Langdon SP, Mullen P, et al. New strategies for targeting the hypoxic tumour microenvironment in breast cancer. Cancer Treat Rev 2013; 39: 171-179.
8. van Brussel AS, Adams A, Vermeulen JF, et al. Molecular imaging with a fluorescent antibody targeting carbonic anhydrase IX can successfully detect hypoxic ductal carcinoma in situ of the breast. Breast Cancer Res Treat 2013; 140: 263-272.
9. Kijanka M, Warnders FJ, El Khattabi M, et al. Rapid optical imaging of human breast tumour xenografts using anti-HER2 VHHs site-directly conjugated to IRDye800CW for image-guided surgery. Eur J Nucl Med Mol Imaging 2013.
10. Oliveira S, van Dongen GA, Stigter-van Walsum M, et al. Rapid visualization of human tumor xenografts through optical imaging with a near-infrared fluorescent anti-epidermal growth factor receptor nanobody. Mol Imaging 2012; 11: 33-46.
11. Behbod F, Kittrell FS, LaMarca H, et al. An intraductal human-in-mouse transplantation model mimics the subtypes of ductal carcinoma in situ. Breast Cancer Res 2009; 11: R66.
12. Barrett T, Koyama Y, Hama Y, et al. In vivo diagnosis of epidermal growth factor receptor expression using molecular imaging with a cocktail of optically labeled monoclonal antibodies. Clin Cancer Res 2007; 13: 6639-6648.
13. Xie BW, Mol IM, Keereweer S, et al. Dual-wavelength imaging of tumor progression by activatable and targeting near-infrared fluorescent probes in a bioluminescent breast cancer model. PLoS One 2012; 7: e31875.

PART III

Summarizing chapters

10

Summarizing discussion and future perspectives

Although the relative breast cancer mortality rate has substantially reduced over the past two decades, absolute mortality has remained fairly stable in The Netherlands (1989: 3,293; 2011: 3,261 women) [1]. Since most cancer-related deaths are due to metastatic disease [2], the mortality rate might be reduced considerably if invasive tumors or even pre-invasive lesions could be detected and completely resected before having metastasized. Sensitive imaging techniques for screening and intraoperative surgery should thus be carefully evaluated [3, 4]. Molecular imaging techniques hold great promise here.

Molecular imaging, nuclear versus optical

Traditional imaging techniques such as magnetic resonance imaging (MRI), computed tomography (CT) and ultrasound (US) use physical (e.g. absorption, scattering, proton density and relaxation rates) and physiologic (e.g. blood flow) properties as the main source of contrast for detection and characterization of tumors. Molecular imaging is based on these imaging techniques (nuclear, optical imaging) but uses, instead of nonspecific physical sources, specific molecular sources for image contrast (specific biomolecules or tumor markers) [5, 6].

For nuclear molecular imaging, probes such as antibodies or small molecules conjugated to isotopes (e.g. ^{89}Zr-Trastuzumab or ^{18}FDG) [7, 8] specifically target tumors and radioactive probe uptake is measured by positron emission tomography (PET) or single-photon emission computed tomography (SPECT). Nuclear (PET/SPECT) imaging is sensitive and has a high penetration depth but the resolution is limited. Other drawbacks are high costs of tracer production, logistic infrastructure and the need for protective measures against ionizing radiation [9, 10]. Optical molecular imaging requires no ionizing radiation, requires less expensive equipment and has high resolution. However, a limited tissue penetration depth is one of the biggest challenges for successful implementation in the clinic [11].

Fluorescent contrast agents, targeted versus non-targeted

Molecular imaging with near-infrared (NIR) non-targeted contrast agents has been evaluated in patients. Omocianine was tested as non-targeted agent for breast cancer detection with diffuse optical tomography [12]. Only five out of ten malignant lesions could be detected and tumor-to-normal tissue ratios (TNR) were limited suggesting that targeted contrast agents are needed.

Tumor markers in hypoxia

For molecular imaging with targeted agents, validated tumor markers are needed. Ideally, a tumor marker would be homogeneously expressed in 100% of tumors and none of normal tissues or benign tumors. Although many tumor markers have been evaluated, either tumor-specificity or tumor expression levels are limited. Special interest exists for hypoxia upregulated tumor markers. Hypoxia is a condition that solid tumors of various origins have in common and that is absent in most healthy tissues. Tumor hypoxia arises due to rapid expansion of the tumor mass away from the basal membrane and vasculature. Low oxygen tensions result in HIF-1α stabilization and upregulation of several downstream proteins. In chapter 2 we performed a meta-analysis of reported expression rates of four hypoxia upregulated proteins, carbonic anhydrase IX (CAIX), glucose transporter 1 (GLUT1), C-X-C chemokine receptor type-4 (CXCR4) and insulin-like growth factor 1 receptor (IGF1-R), in human breast cancer and benign breast disease. Of these four proteins, GLUT1 showed the highest prevalence: membranous localization in ~44% of tumors. Expression levels of all four markers were comparable or higher in carcinoma in situ compared to invasive carcinoma. However, as none of the evaluated markers shows sufficient prevalence in invasive cancer to be exploited as the single target, we identify in chapter 3 the minimal number of combined targeted probes needed for the highest possible breast cancer detection rate, and determine expression levels and discriminating power between invasive breast cancer and normal breast tissue. We show that 80% of all human breast cancers express at least one of a panel of markers (CD44v6, GLUT1, EGFR, HER2, and IGF1-R) that therefore may be suitable for molecular imaging strategies. In chapter 4 we search for other hypoxia upregulated tumor markers, using a modified reverse phage display

selection technology, and describe the selection of nanobodies with specificity for hypoxic cells. High affinity nanobody A2A11 was isolated and characterized. Mass spectrometry results revealed specificity for DAF, which was confirmed in binding assays and *in vivo* in our DCIS mouse model. DAF was convincingly reported by others to have a strong relationship with hypoxia by identification of a functional binding site for HIF1α [13]. Others have shown that high DAF expression might be a characteristic of breast cancer stem cells and presence of cells with high expression of DAF is a sign for aggressiveness and a poor prognostic factor for breast cancer [14].

Molecular size of probe

A range of targeted probes with varying molecular weights, e.g. 150 kDa IgG antibodies, antibody fragments (80 kDa minibodies, 50 kDa Fabs, 27 kDa scFvs, 15 kDa nanobodies) small molecules and nanoparticles, have preclinically and clinically been evaluated for molecular imaging by others [15-18]. In this thesis we tested small molecules, antibody fragments as well as IgG antibodies for optical molecular imaging of hypoxic breast cancer (Fig. 1)

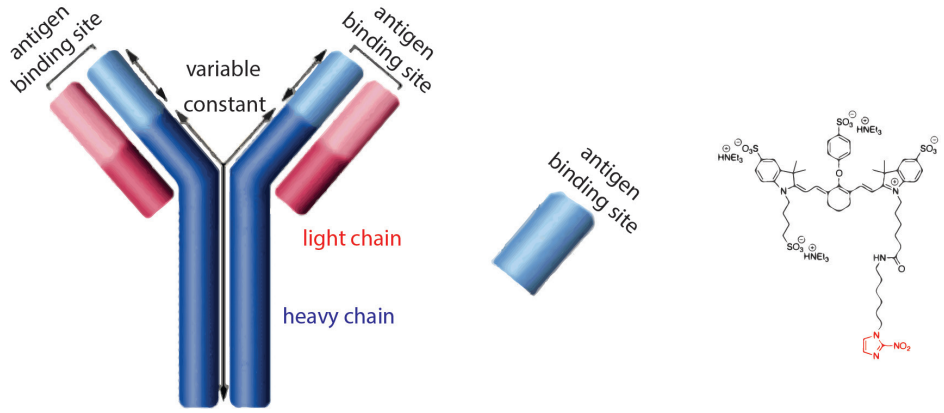

Figure 1: Left: IgG antibody of 150 kDa. Middle: nanobody of 15 kDa. Right: structure of the small molecule 2-nitroimidazole-IRDye800CW. (red: 2-nitroimidazole, 0.13 kDa)

In chapter 5 we report synthesis of small molecule 2-nitroimidazole and conjugation to IRDye800CW (2-nitro-IR) to detect pre-invasive breast cancer. Specificity for hypoxic cells was confirmed *in vitro*. Evaluation in a preclinical mouse model for DCIS, showed that tumor signals of 2-nitro-IR as well as background were higher compared to control mice, resulting in moderate contrast. Based on our present results, we conclude that targeted, e.g. antibody-based probes, rather than small molecules are needed for successful tumor detection with high contrast images. Traditionally, tumor targeting has focused on the use of IgG monoclonal antibodies, which have a molecular weight of 150 kDa. In chapter 6 we investigate the molecular imaging of DCIS using a NIR fluorescent antibody targeting CAIX (MabCAIX-IR) in a preclinical mouse model for DCIS (MCF10DCIS xenografts). We showed that from 24h after injection of MabCAIX-IR, hypoxic DCIS can be successfully detected with molecular fluorescence imaging before and also during surgery, to facilitate radical resection. By sensitive targeted molecular fluorescence microscopy we showed perinecrotic CAIX expression 96h after injection. Furthermore, we suggest that this imaging technique would allow for optimized fluorescence-guided sampling during pathology dissection.

In chapter 7 we label a CD44v6-targeting antibody with IRDye800CW and evaluate tumor uptake and biodistribution in mice bearing orthotopically transplanted, CD44v6 positive MCF10DCIS xenografts and CD44v6 negative MDA-MB-231 control xenografts. As with MabCAIX-IR, maximum accumulation of CD44v6-specific antibodies was obtained from 24h after injection. We conclude that the use of antibodies as targeted probes for optical molecular imaging, due to limited tumor penetration and slow plasma clearance, results in high background levels and subsequent low TNRs during the first 24h after injection. After 24h, antibodies have a broad optimal time window for imaging that can last up to weeks after injection. To arrive at high TNRs, tumor-specific probes are required that rapidly accumulate in the tumor. As size and affinity alone largely account for the targeting properties of most macromolecules, smaller probes need high affinities to evade rapid washout from the tumor [18]. In chapter 8 we show development and application of novel CAIX-specific nanobodies (15 kDa) which have a faster tumor uptake and body clearance than conventional antibodies and can be used for rapid molecu-

lar imaging of pre-invasive breast cancer. We selected high affinity CAIX-specific nanobodies using a modified phage display technology and conjugated site-specifically to IRDye800CW. Already after 2h, high TNRs were observed. We tested the lead compound, B9-IR, *in vivo* and 2h after injection we show detection of hypoxic DCIS before and during surgery. As was the case for MabCAIX-IR, the stability of the B9-IR conjugate allowed for molecular fluorescence pathology, which results in better contrast than conventional CAIX-IHC at the pathology department.
Finally, in chapter 9 we evaluate a cocktail of HER2- and CAIX-specific nanobodies for multispectral optical molecular imaging of DCIS tumors in mice and we show successful determination of expression status of CAIX and HER2 in MCF10DCIS xenografts simultaneously.

Future perspectives

Optical molecular imaging in its present form is especially interesting for image-guided surgery or molecular fluorescence pathology. For image-guided surgery, high tumor specificity of molecular imaging probes is of great importance. Although the expression status of many tumor markers in human (breast) tissues has been evaluated by others, few groups reported expression levels in normal tissues, which poses a problem for the determination of tumor specificity. Therefore, future immunohistochemistry studies should always include normal tissues as reference.
Next to surgery, molecular fluorescence pathology is a novel method to evaluate expression levels in resected tissue without the need for immunohistochemistry and resulting in high contrast images. Molecular fluorescence pathology might speed up the diagnostic process and tumor characterization and can facilitate patient-tailored therapy planning.
For non-invasive imaging, the limited penetration of (NIR) light remains a problem. Future studies should clarify whether stronger lasers, alternative light sources, such as LEDs, or more sensitive cameras might improve detection of deep-seated tumors. Another approach can be conjugation of nanobodies or antibodies to multiple fluorophores in order to increase strength of signal. Nanobodies should therefore be expressed with multiple C-terminal cysteins and solutions for possible quenching of the fluorescent signals should be evaluated.

In this thesis we evaluated nanobodies as probes for rapid molecular imaging, next to other molecules (a small molecule and antibodies). The rapid uptake and clearance of nanobodies might especially be interesting in case of urgent surgery or when rapid evaluation of expression status is needed, for which antibody clearance is too slow. As high sensitivity of tumor detection will only be possible with cocktails of probes, molecular imaging studies should focus on dual- or even multispectral imaging. As radioisotopes are monochromatic, optical probes should be used for these types of imaging. At present, to our knowledge, available imaging systems that are capable of detecting NIR signals can only separate two different wavelengths (700 and 800 nm) without experiencing any bleed-through effect. Future imaging systems might be able to detect and separate more than two wavelengths at the same time, allowing expression status evaluation of many relevant tumor markers simultaneously.

As we showed, hypoxic tumors can be targeted either by probes specific to membrane proteins that are upregulated in an hypoxic environment (e.g. CAIX) or by probes that form intracellular aggregates under hypoxia (e.g. 2-nitroimidazoles). Our 2-nitroimidazole-IR conjugate seemed to form aggregates in normoxic tissues as well, resulting in high background fluorescent signals. Chemical modifications (>1 dye molecule per 2-nitroimidazole molecule or bi- or trivalent 2-nitroimidazole molecules) might improve fluorescence signal intensity and specificity of the probe, thereby decreasing background and/or increasing tumor signal in future studies. Although most downstream proteins of HIF-1α are either not membrane-bound (e.g. vascular endothelial growth factor, VEGF) or not tumor-specific (GLUT1), CAIX remains an interesting target with high specificity for tumor tissue. As CAIX is expressed in less than half of all breast cancers, CAIX should be used in combination with other tumor markers for image-guided surgery or pathology. However, as prognostic marker or for non-invasive detection of (breast) cancer, CAIX is also very interesting as single target, as complete tumor delineation is not necessary for these applications.

References

1. Zhou H, Luby-Phelps K, Mickey BE, et al. Dynamic near-infrared optical imaging of 2-deoxyglucose uptake by intracranial glioma of athymic mice. PLoS One 2009; 4: e8051.
2. Weigelt B, Peterse JL, van 't Veer LJ. Breast cancer metastasis: markers and models. Nat Rev Cancer 2005; 5: 591-602.
3. Gibbs SL. Near infrared fluorescence for image-guided surgery. Quant Imaging Med Surg 2012; 2: 177-187.
4. van Dam GM, Themelis G, Crane LM, et al. Intraoperative tumor-specific fluorescence imaging in ovarian cancer by folate receptor-alpha targeting: first in-human results. Nat Med 2011; 17: 1315-1319.
5. Weissleder R. Molecular imaging: exploring the next frontier. Radiology 1999; 212: 609-614.
6. Phelps ME. PET: the merging of biology and imaging into molecular imaging. J Nucl Med 2000; 41: 661-681.
7. Dijkers EC, Oude Munnink TH, Kosterink JG, et al. Biodistribution of 89Zr-trastuzumab and PET imaging of HER2-positive lesions in patients with metastatic breast cancer. Clin Pharmacol Ther 2010; 87: 586-592.
8. Warning K, Hildebrandt MG, Kristensen B, et al. Utility of 18FDG-PET/CT in breast cancer diagnostics--a systematic review. Dan Med Bull 2011; 58: A4289.
9. Smetherman DH. Screening, imaging, and image-guided biopsy techniques for breast cancer. Surg Clin North Am 2013; 93: 309-327.
10. Fleming IN, Regel SJ, Pike LC, et al. Positron emission tomography oncology research in the UK: a comparison with USA and Europe. Nucl Med Commun 2012; 33: 341-348.
11. Kovar JL, Simpson MA, Schutz-Geschwender A, et al. A systematic approach to the development of fluorescent contrast agents for optical imaging of mouse cancer models. Anal Biochem 2007; 367: 1-12.
12. van de Ven S, Wiethoff A, Nielsen T, et al. A novel fluorescent imaging agent for diffuse optical tomography of the breast: first clinical experience in patients. Mol Imaging Biol 2010; 12: 343-348.
13. Louis NA, Hamilton KE, Kong T, et al. HIF-dependent induction of apical CD55 coordinates epithelial clearance of neutrophils. FASEB J 2005; 19: 950-959.
14. Ikeda J, Morii E, Liu Y, et al. Prognostic significance of CD55 expression in breast cancer. Clin Cancer Res 2008; 14: 4780-4786.
15. Joshi BP, Wang TD. Exogenous Molecular Probes for Targeted Imaging in Cancer: Focus on Multi-modal Imaging. Cancers (Basel) 2010; 2: 1251-1287.
16. Oliveira S, van Dongen GA, Stigter-van Walsum M, et al. Rapid visualization of human tumor xenografts through optical imaging with a near-infrared fluorescent anti-epidermal growth factor receptor nanobody. Mol Imaging 2012; 11: 33-46.
17. Terwisscha van Scheltinga AG, van Dam GM, Nagengast WB, et al. Intraoperative near-infrared fluorescence tumor imaging with vascular endothelial growth factor and human epidermal growth factor receptor 2 targeting antibodies. J Nucl Med 2011; 52: 1778-1785.
18. Schmidt MM, Wittrup KD. A modeling analysis of the effects of molecular size and binding affinity on tumor targeting. Mol Cancer Ther 2009; 8: 2861-2871.

Nederlandse samenvatting

Hoewel de relatieve borstkankersterfte aanzienlijk is gedaald in de afgelopen decennia, is door een toename van het aantal borstkankerpatiënten het absolute aantal mensen wat aan deze ziekte overlijdt in Nederland stabiel gebleven. Uitzaaiingen zijn de oorzaak van de meeste kanker-gerelateerde sterfgevallen. Vroegdetectie en het chirurgisch verwijderen van tumoren die nog niet zijn uitgezaaid, zouden daarom de sterfte kunnen verminderen. Hiervoor zijn gevoelige beeldvormende technieken nodig die gebruikt kunnen worden voor het bevolkingsonderzoek en tijdens operaties. Helaas hebben de huidige beeldvormende technieken een beperkte specificiteit voor borstkanker, maken ze gebruik van ioniserende straling en/of zijn ze kostbaar.

Moleculaire beeldvorming, nucleair versus optisch

Traditionele beeldvormende technieken, zoals 'magnetic resonance imaging' (MRI), computer tomografie (CT) en echografie, maken gebruik van fysische en fysiologische eigenschappen voor contrastvorming en karakterisering van tumoren. Moleculaire beeldvorming is gebaseerd op deze technieken maar gebruikt, in plaats van (niet tumor-specifieke) fysische eigenschappen, specifieke moleculaire eigenschappen van tumoren (tumormarkers) voor het verkrijgen van contrast. Moleculaire beeldvorming is op te delen in twee soorten: nucleaire en optische moleculaire beeldvorming. Bij nucleaire moleculaire beeldvorming worden tumormarkers specifiek gebonden door agentia, zoals antilichamen of kleine moleculen ('small molecules'), die gelabeld zijn met radioactieve isotopen. Opname van deze agentia in de tumor wordt vervolgens gemeten door middel van positron emissie tomografie (PET) of 'single-photon emission computed tomography' (SPECT). Nucleaire beeldvorming is sensitief en heeft een grote penetratiediepte (wat belangrijk is voor detectie van diep liggende tumoren), echter de resolutie is beperkt, wat een probleem kan opleveren bij tumorkarakterisering en het plannen van de therapie. Andere nadelen zijn hoge kosten voor het produceren van de isotopen, ingewikkelde logistieke infrastructuur en de beschermende maatregelen die nodig zijn tegen de ioniserende straling.

Bij optische moleculaire beeldvorming wordt gebruik gemaakt van licht in plaats van ioniserende straling. Bovendien is de benodigde apparatuur minder duur en

heeft deze techniek een hoge resolutie. Echter, een beperkte penetratiediepte is een belangrijk probleem wat opgelost moet worden voordat deze techniek een plaats kan krijgen in de kliniek. Dit probleem kan deels opgelost worden door gebruik te maken van nabij-infrarood licht (NIR, 700-900 nm) wat het deel van het spectrum is tussen rood en infrarood. Deze golflengte wordt het minst geabsorbeerd door levend weefsel waardoor een optimale penetratiediepte verkregen kan worden.

Optische agentia, tumor gericht ('targeted') versus niet tumor gericht ('non-targeted')

In een eerder gepubliceerde studie leidde moleculaire beeldvorming met het aspecifieke NIR contrastmiddel Omocianine bij patiënten tot een beperkt signaal van de borsttumoren ten opzichte van omliggend weefsel. Dit suggereert dat tumor gerichte ('targeted') agentia nodig zijn om tumoren optimaal te kunnen detecteren. De ideale tumormarker waartegen deze stoffen gericht zouden moeten zijn, zou in 100% van de tumoren moeten worden geproduceerd ('geëxpresseerd') en niet aanwezig moeten zijn in normaal weefsel of in goedaardige tumoren. Expressie niveaus van veel bekende tumormarkers (zoals groeifactor receptoren) zijn in tumor en normaal borstweefsel van patiënten gemeten, maar ofwel de specificiteit voor tumorweefsel ofwel de expressie niveaus zijn beperkt. Tumormarkers die in tumoren met zuurstof tekort (hypoxie) tot expressie komen zijn interessante kandidaten. Hypoxie komt veel voor in tumoren en niet of nauwelijks in gezond (borst)weefsel en wordt veroorzaakt door snelle tumorgroei in combinatie met een inefficiënte doorbloeding. In hypoxische (zuurstof-arme) tumorcellen zorgt 'hypoxia-inducible factor 1α' (HIF-1 α) voor transcriptie van verschillende tumormarkers. In hoofdstuk 2 voerden wij een meta-analyse uit van in de literatuur gerapporteerde expressie niveaus van vier hypoxie-gerelateerde tumormarkers in normaal borstweefsel, goedaardige tumoren en borstkanker: carboxyl anhydrase IX (CAIX), glucose transporter 1 (GLUT1), C-X-C chemokine receptor type-4 (CXCR4) en 'insulin-like growth factor-1 receptor' (IGF1-R). GLUT1 had het hoogste expressie niveau in tumoren: 44%. Echter, geen van deze markers kwam vaak genoeg in tumoren tot expressie voor gebruik als individuele tumor marker. Daarom zochten wij in hoofdstuk 3 naar het minimale aantal gecombineerde tumormarkers om

het grootste gedeelte van alle kwaadaardige borsttumoren te kunnen detecteren. Ook keken wij naar het vermogen om met behulp van deze markers te kunnen discrimineren tussen normaal en kwaadaardig borstweefsel. We lieten zien dat van een combinatie van markers (CD44v6, GLUT1 (of CAIX), EGFR, HER2 en IGF1-R) er minstens één tot expressie komt in 80% van alle humane borstkankers, wat ze geschikt maakt om te worden getest als tumormarkers voor moleculaire beeldvorming. Omdat we met deze optimale combinatie nog steeds 20% van de borstkankers missen, zochten we in hoofdstuk 4 naar nieuwe tumormarkers die tot expressie komen in hypoxische weefsels. Hiervoor maakten we gebruik van een aangepaste 'phage-display' technologie. We beschreven de selectie van nanobodies die specifiek zijn voor hypoxische weefsels. Uit data van massaspectrometrie en bindingsproeven bleek dat nanobody A2A11 de hypoxie-gerelateerde tumormarker DAF bond. We hebben DAF ook als tumormarker getest in ons muismodel. De tumorsignalen van muizen die ingespoten waren met het DAF-specifieke nanobody waren significant hoger vergeleken met de tumorsignalen van muizen die waren ingespoten met het controle nanobody.

Moleculair gewicht van tumor gerichte ('targeted') agentia

Een reeks stoffen met verschillende moleculaire massa's, zoals IgG antilichamen, antilichaam-fragmenten (zoals nanobodies), 'small molecules' en nanodeeltjes, zijn voorheen door anderen preklinisch en klinisch getest voor moleculaire beeldvorming. Nanobodies zijn kleine gerichte ('targeted') agentia die afgeleid zijn van het variabele domein van 'heavy chain-only' antilichamen (VHH) die van nature voorkomen in kameelachtigen. In dit proefschrift testten wij de 'small molecules', nanobodies en IgG antilichamen als tumor-specifieke agentia voor optische moleculaire beeldvorming van hypoxische borstkanker. In hoofdstuk 5 beschrijven we de synthese van 'small molecule' 2-nitroimidazol en de conjugatie met de nabij-infrarode stof IRDye800CW (resulterend in het conjugaat '2-nitro-IR') voor detectie van borstkanker. Specificiteit voor hypoxische cellen was met behulp van een celkweek experiment bevestigd. Evaluatie in een muismodel voor borstkanker, toonde aan dat zowel tumor- als achtergrondsignalen van 2-nitro-IR hoger waren dan bij controle muizen, wat resulteerde in matig contrast. Chemische modificatie

(meer dan één fluorofoor per 2-nitroimidazol molecuul of meer dan één 2-nitroimidazol molecuul per fluorofoor) zou het fluorescente signaal kunnen versterken in toekomstige studies. Gebaseerd op onze huidige resultaten concluderen wij dat op antilichaam gebaseerde moleculen, in plaats van 'small molecules', nodig zijn voor een succesvolle detectie van hypoxische tumoren. Van oudsher worden voornamelijk IgG monoclonale antilichamen (met een moleculair gewicht van 150 kDa) gebruikt voor dergelijke toepassingen. In hoofdstuk 6 onderzochten wij moleculaire beeldvorming van borstkanker met een NIR fluorescent antilichaam gericht tegen CAIX (MabCAIX-IR) in een muis model. We lieten zien dat 24 uur na injectie van MabCAIX-IR, hypoxische borstkankertumoren succesvol kunnen worden gedetecteerd vóór en tijdens chirurgie. Deze techniek kan het wegsnijden van de complete tumor tijdens chirurgie vergemakkelijken. Met behulp van gevoelige fluorescentie scans van het tumorweefsel toonden wij, 96 uur na injectie, CAIX expressie aan rondom necrotische gebieden in de tumor, wat de specificiteit van MabCAIX-IR voor CAIX bevestigde. Verder suggereerden wij dat deze beeldvormende techniek ook gebruikt zou kunnen worden voor optimale fluorescentie-gestuurde weefsel preparatie op de pathologie afdeling.
In hoofdstuk 7 labelden we CD44v6-specifieke antilichamen met IRDye800CW en evalueerden tumor- en weefselopname in muizen met getransplanteerde CD44v6-positieve en -negatieve tumoren. Net zoals bij MabCAIX-IR werden optimale fluorescente signalen van dit antilichaam vanuit de tumoren vastgesteld vanaf 24 uur na injectie. We concluderen hieruit dat het gebruik van antilichamen als tumor gerichte moleculen voor optische moleculaire beeldvorming, door de langzame tumorpenetratie en renale klaring, resulteert in hoge achtergrond signalen en dus laag contrast gedurende de eerste 24 uur na injectie. Vanaf 24 uur tot wel enkele weken na injectie kunnen antilichamen een optimaal tumorsignaal afgeven. Om hoog contrast te verkrijgen gedurende de eerste dag na injectie, zijn tumor-specifieke moleculen nodig die snel in de tumor accumuleren. Aangezien grootte en affiniteit (bindingskracht) van invloed zijn op de tumorbinding van de meeste macromoleculen (grote moleculen), hebben kleinere moleculen een hoge affiniteit nodig om snelle uitwassing uit de tumor te voorkomen. In hoofdstuk 8 beschrijven we de ontwikkeling en toepassing van nieuwe CAIX-specifieke nano-

bodies die een snellere tumoropname hebben dan conventionele antilichamen en gebruikt kunnen worden voor snelle moleculaire beeldvorming van borstkanker. We selecteerden hoge affiniteit CAIX-specifieke nanobodies met een aangepaste phage display technologie en conjugeerden deze nanobodies aan IRDye800CW. Al na 2 uur werden relatief sterke tumorsignalen geobserveerd. We testten nanobody B9-IR in muizen en reeds 2 uur na injectie konden we hypoxische borsttumoren detecteren, zowel vóór als tijdens chirurgie. Net zoals bij MabCAIX-IR liet de stabiliteit van B9-IR toe dat CAIX eiwit zichtbaar gemaakt kon worden in plakjes tumorweefsel (moleculaire fluorescentie pathologie), wat resulteerde in sterkere signalen dan bij conventionele CAIX-immunohistochemische kleuring op de pathologie afdeling. Tot slot evalueren we in hoofdstuk 9 een cocktail van HER2- en CAIX-specifieke nanobodies voor dual-spectrale optische moleculaire beeldvorming van borstkankertumoren in muizen. We bepalen tegelijkertijd de expressie status van CAIX en HER2 in MCF10DCIS tumoren. In de toekomst kan het gebruik van nanobody cocktails voor moleculaire beeldvorming de detectie van tumoren, de afgrenzing van tumor weefsel tijdens chirurgie en de tumor karakterisering op de pathologie afdeling, optimaliseren.

Curriculum vitae

Aram van Brussel was born December 2nd, 1984 in Amsterdam. At the age of 3 he moved to Doorn. He attended primary school in Driebergen and high school (Gymnasium) at Revius Lyceum in Doorn. During this period he developed special interest in medicine and the subject of the final high school study project was 'gene therapy'. After graduating in 2003 he moved to Utrecht and started studying medicine. In this period, besides studying, he continued playing classical guitar, ballroom dancing and was an active member of students rowing club Orca, Utrecht. In the third year of medicine he was most interested in internal medicine. For an elective rotation on tropical medicine he went to Costa-Rica for 2 months. In 2006 he became member of triathlon club Hellas, Utrecht, where he met Femke. In the final year he did a 3 months elective rotation in internal medicine, Gelderse Vallei hospital, Ede, and in order to gain labwork experience, he completed his study with a research rotation at the Medical Oncology and Urology department, University Medical Center Utrecht. He worked on Von Hippel Lindau gene mutations, supervised by dr. Judith Jans. In that period he met prof. Elsken van der Wall who suggested applying for a PhD position at the Pathology Department of the University Medical Center Utrecht, with supervisor prof. Paul van Diest. He started his PhD in 2009 at the Cell Biology department, Kruyt building, Utrecht University, with dr. Paul van Bergen en Henegouwen as daily supervisor. During his PhD he married Femke and in 2011 their daughter Mare was born. In 2013 he completed his research for this thesis. From January 2014 he will work as resident at the department of internal medicine, Gelre hospital, Apeldoorn, and will continue his residency at the UMC Utrecht from 2016.

List of publications

1. **van Brussel AS***, Adams A*, Vermeulen JF, et al. Molecular imaging with a fluorescent antibody targeting carbonic anhydrase IX can successfully detect hypoxic ductal carcinoma in situ of the breast.
   Breast Cancer Res Treat 2013
2. **van Brussel AS***, Adams A*, Vermeulen JF, et al. The potential of hypoxia markers as target for breast molecular imaging – A systematic review and meta-analysis of human marker expression.
   BMC Cancer 2013
3. Vermeulen JF, **van Brussel AS**, Adams A, et al. Near-infrared fluorescence molecular imaging of ductal carcinoma in situ with CD44v6-specific antibodies in mice: a preclinical study.
   Mol Imaging Biol 2013
4. **van Brussel AS**, Adams A, Oliveira S, et al. Hypoxia-targeting fluorescent nanobodies for optical molecular imaging of pre-invasive breast cancer.
   2013, Submitted
5. **van Brussel AS**, Ramovs V, van der Welle R, et al. Subtractive panning of a nanobody phage library reveals DAF as a biomarker for hypoxic breast cancer.
   2013, Manuscript
6. **van Brussel AS**, van der Welle R, 't Hart P, et al. Hypoxia-specific optical imaging of ductal carcinoma of the breast with a near-infrared 2-nitroimidazole conjugate.
   2013, Manuscript
7. **van Brussel AS**, Kijanka M, van der Welle R, et al. Dual-spectral optical imaging of breast cancer with a combination of nanobodies targeting CAIX and HER2.
   2013, Manuscript

8. Vermeulen JF, **van Brussel AS**, van der Groep P, et al. Immunophenotyping invasive breast cancer: paving the road for molecular imaging.
BMC Cancer 2012
9. Emmerson CD, **van Brussel AS,** Roovers RC, et al. Low affinity anti-transferrin receptor reactive VHHs as efficient brain entry vehicle. 2012, Submitted
10. Kroeze SG, Vermaat JS, **van Brussel AS**, et al. Expression of nuclear FIH independently predicts overall survival of clear cell renal cell carcinoma patients.
Eur J Cancer 2010
11. Nordstrom-O'Brien M, van der Luijt RB, van Rooijen E, et al. Genetic analysis of von Hippel-Lindau disease.
Hum Mutat 2010

* Equal contributions

List of co-authors

Arthur Adams, Department of Radiology, University Medical Center Utrecht, Utrecht, The Netherlands

Paul M.P. van Bergen en Henegouwen, Division of Cell Biology, Department of Biology, Science Faculty, Utrecht University, Utrecht, The Netherlands

Peter Bult, Department of Pathology, Radboud University Nijmegen Medical Centre, Nijmegen, The Netherlands

Mirjam J.M.A. Damen, Biomolecular Mass Spectrometry and Proteomics Group, Utrecht Institute for Pharmaceutical Sciences and Bijvoet Center for Biomolecular Research, Utrecht University, Utrecht, The Netherlands

Patrick W.B. Derksen, Department of Pathology, University Medical Center Utrecht, Utrecht, The Netherlands

Paul J. van Diest, Department of Pathology, University Medical Center Utrecht, Utrecht, The Netherlands

Mohamed El Khattabi, QVQ BV, Utrecht, The Netherlands

Sjoerd G. Elias, Department of Radiology, University Medical Center Utrecht, Utrecht, The Netherlands and Julius Center of Health Sciences and Primary Care, University Medical Center, Utrecht, The Netherlands

Petra van der Groep, Department of Pathology, University Medical Center Utrecht, Utrecht, The Netherlands

Peter 't Hart, Department of Medicinal Chemistry & Chemical Biology, Utrecht Institute for Pharmaceutical Sciences, Faculty of Science, Utrecht University, Utrecht, The Netherlands

Marta Kijanka, Division of Cell Biology, Department of Biology, Science Faculty, Utrecht University, Utrecht, The Netherlands

Willem P.Th.M. Mali, Department of Radiology, University Medical Center Utrecht, Utrecht, The Netherlands

Nathaniel I. Martin, Department of Medicinal Chemistry & Chemical Biology, Utrecht Institute for Pharmaceutical Sciences, Faculty of Science, Utrecht University, Utrecht, The Netherlands

Folkert H.M. Morsink, Department of Pathology, University Medical Center Utrecht, Utrecht, The Netherlands

Sabrina Oliveira, Division of Cell Biology, Department of Biology, Science Faculty, Utrecht University, Utrecht, The Netherlands and Department of Pathology, University Medical Center Utrecht, Utrecht, The Netherlands

Veronika Ramovs, Division of Cell Biology, Department of Biology, Science Faculty, Utrecht University, Utrecht, The Netherlands

Monique Slijper, Biomolecular Mass Spectrometry and Proteomics Group, Utrecht Institute for Pharmaceutical Sciences and Bijvoet Center for Biomolecular Research, Utrecht University, Utrecht, The Netherlands

Jeroen F. Vermeulen, Department of Pathology, University Medical Center Utrecht, Utrecht, The Netherlands

Elsken van der Wall, Division of Internal Medicine and Dermatology, University Medical Center Utrecht, Utrecht, The Netherlands

Reini van der Welle, Division of Cell Biology, Department of Biology, Science Faculty, Utrecht University, Utrecht, The Netherlands

Dankwoord

Er zou weinig van mij overblijven als ik alles moest afstaan wat ik aan anderen te danken heb. - Goethe

Prof. dr. P.J. van Diest, beste Paul, je enthousiasme en werklust zijn aanstekelijk. Je bent een begeleider die kritisch is maar je tegelijkertijd de ruimte geeft. Ik hoop dat we in de toekomst weer eens kunnen samenwerken.
Prof. dr. E. van der Wall, beste Elsken, je bent een groot voorbeeld voor me als internist-oncoloog en als promotor. Ik hoop ooit met dezelfde 'drive' in het ziekenhuis te werken.
Dr. P.M.P. van Bergen en Henegouwen, beste Paul, je eindeloze vertrouwen in mijn onderzoeksresultaten zal me altijd bijblijven. En je had gelijk, ze binden!
Dr. S. Oliveira, beste Sabrina, misschien dat ik je ooit nog eens inroep als feilloze injectrice! Het was leuk om met je samen te werken en ik wens je veel succes met je wetenschappelijke loopbaan en natuurlijk met je Portugese voetbal-ster.
Dr. P.W.B. Derksen, beste Patrick, bedankt voor je kritische blik en voor je ondersteuning en advies rondom onze muisproeven.
Geachte leden van de beoordelingscommissie, prof. dr. P.R. Luijten, prof. dr. G. van Dongen, prof. dr. I.H.M. Borel Rinkes en prof. dr. C.C. Hoogenraad, hartelijk dank voor het doorlezen en beoordelen van mijn proefschrift. Geachte prof. dr. G.M. van Dam, beste Go, dank voor het beoordelen en ik kijk erg uit naar de eerst bevindingen uit de klinische studies met HER2 en CAIX nanobodies!

Raymond, Heukie, met jou heb ik het minst samengewerkt, maar het meest samen gewérkt! Je droge humor was (bijna altijd) welkom en ik hoop dat je nog vaak mijn Spotify inbox zal vol spammen.
Marta, inmiddels is je Nederlands vloeiend genoeg: Je was een fijne kamergenoot, we hebben veel gelachen, en ik wens je veel geluk met je familie en met Alicja!
Jeroen, bedankt voor je inzet en ondersteuning gedurende de eerste jaren.
Arthur, onze koffie-discussies hebben naast het gelach, ook vruchten afgeworpen. Het was goed een kritische blik vanuit de epidemiologie op onze studies te werpen.

Melissa, Veronika en Reini, jullie inzet heeft geleid tot mooie resultaten, veel succes de komende tijd in het (oncologie)onderzoek.

Jolien, Laurien, Stefanie, Wendy, Willy, Petra, Nathalie, Ton, Folkert en overige collega's van het UMC, bedankt voor de plezierige samenwerking en wellicht tot ziens.

Rachid, Alex en Bram, aan jullie om de celbiologie tradities voort te zetten, en veel succes bij Paul!
Smiriti, bedankt voor je hulp en geniet van het uitzicht daarboven.

Dr. N.I. Martin, dear Nathaniel, en beste Peter 't Hart, thanks for the interesting and pleasant collaboration on the 2-nitroimidazole project.
Dr. M. El Khattabi, beste Mohamed, beste overige collega's van QVQ, zonder jullie technische ondersteuning en advies op het gebied van nanobody productie hadden we het een stuk moeilijker gehad tijdens de muisstudies, dank daarvoor.
Dr. S. G. Elias, beste Sjoerd, dank voor de ondersteuning bij de statistiek. Ik hoop dat je inmiddels niet meer in de trein woont.
Dr. M. Slijper, beste Monique, en beste Mirjam Damen, hartelijk dank voor het uitvoeren van de massaspectrometrie en de hulp bij de data analyse. Het heeft geleid tot mooie resultaten.

Xiaoye, van angstaanjagende expedities door het oerwoud tot aan Mare in bad doen, we hebben het samen meegemaakt. Laten we onze diensten op elkaar afstemmen, dan blijven we elkaar ook de komende jaren regelmatig zien!
Tijmen, ik kijk uit naar de toekomstige uitjes met onze dochters naar de Moestuin en naar de fietsvakanties. Als jij naar Nijmegen gaat rijden, dan kan ik Apeldoorn ook wel aan, en LPG is het helemaal!

Ouders, lieve Willem en Rieneke, misschien een tegenvaller dat ik kanker niet heb weten uit te roeien, maar ik zie dat jullie veel waardering blijven hebben voor wat ik doe. Jullie zijn een geweldige stabiele rots in de branding, ook al slaan we om,

rammen we een havenmeesterskantoor, beweert Willem dat de mast wél onder de brug past, en blijft hij dat de tweede keer beweren, hangen we met de Sarah aan de sluismuur, gaan jullie zomaar voor maanden naar het Zuiden of verhuizen jullie opeens naar Wijk of Heusden.

Femke, lief, wat zijn er toch veel mooie dingen gebeurd sinds ik je aansprak op de sintelbaan! Hoewel die sintelbaan niet meer bestaat en de thee inmiddels sterke koffie is geworden, lachen we nog steeds zoveel als in het begin. Ik hoop dat we ook op ons 90ste nog dansen, fietsen, hardlopen, zwemmen, 'Agricola' spelen of wellicht rollator races houden. We gaan samen een geweldige toekomst tegemoet en ik vind het fantastisch te beseffen dat je altijd achter me zal staan (of vóór me zal lopen).

Mare, hier papa Wawam, ik geniet dagelijks van je karaktertje, ook als je me weer eens corrigeert. Ik hoop dat je die man die zondags (tenzij hij ook dán dienst heeft) de tofu snijdt nog steeds de beste papa zal blijven vinden van de hele Looierstraat. Ik kijk uit naar het moment dat je de 10 km voor het eerst onder de 40 minuten loopt en naar het moment dat je me onder de tafel klaverjast als een echte Visser en zegt: 'Papa, dat was een domme zet van je'. Van jou kan ik het hebben!